Safety assessment by limit analysis methods of non-axisymmetric masonry domes subjected to vertical and horizontal loads

by

Francesco Barsi

Submitted in partial fulfilment of the requirements for the degree of

Doctor of Philosophy

in the International Doctorate in Civil and Environmental Engineering (XXXIV cycle)
Università di Firenze, Dipartimento di Ingegneria Civile e Ambientale
Università di Pisa, Dipartimento di Ingegneria Civile e Industriale
Curriculum: Solid Fluid and Materials Mechanics, SSD: ICAR08

and

in the École Doctorale Ville, Transports et Territoires
Université Paris-Est, ENSA Paris-Malaquais, Laboratoire GSA
Spécialité du Doctorat Prépare: Architecture, section CNU 18

Defended on Tuesday, June 21, 2022

Supervisors: Stefano Bennati, Professor, Università di Pisa
Thierry Ciblac, Professor, ENSA Paris-Malaquais

Co-supervisor: Riccardo Barsotti, Associate Professor, Università di Pisa

Reviewers: Santiago Huerta, Professor, Universidad Politécnica de Madrid
Daniel Oliveira, Associate Professor, Universidade Do Minho

Examiners: Luciano Rosati, Professor, Università di Napoli Federico II (Chair)
Giovanna Ranocchiai, Associate Professor, Università degli Studi di Firenze
Anne-Sophie Colas, Ingénieure de recherche, Université Gustave Eiffel
Jean-Claude Morel, Directeur de recherche, EN des Travaux Publics de l'Etat
Pere Roca, Professor, Universidad Politécnica de Cataluña

May 9, 2022

Contents

List of Figures

List of Tables

List of Principal Symbols

$2h$	thickness of the shell
$\boldsymbol{\nu}$	external unit normal vector to $\partial\Pi$
$\boldsymbol{\omega}$	angular velocity
$\boldsymbol{\sigma}$	thermodynamic forces
$\boldsymbol{\varkappa}$	director curvature tensor
$\boldsymbol{\varphi}$	director rotation vector
$\boldsymbol{\xi}$	internal variables vector
$\boldsymbol{\zeta}$	proportionality vector between the branch lengths in form and force diagrams (in Chapter 2)
$\boldsymbol{\zeta}_{dof}$	degrees of freedom parameters (in Chapter 2)
$\boldsymbol{\zeta}_{unk}$	unknown parameters (in Chapter 2)
$\boldsymbol{C}$	branch-node connectivity matrix (in Chapter 2)
$\boldsymbol{C}_b$	branch-boundary node connectivity matrix (in Chapter 2)
$\boldsymbol{C}_i$	branch-internal node connectivity matrix (in Chapter 2)
$\boldsymbol{K}$	matrix gathering information on horizontal equilibrium equations (in Chapter 2)
$\boldsymbol{L_H}$	matrix of the horizontal length of the branches (in Chapter 2)
$\boldsymbol{p}_z$	vector of the vertical loads (in Chapter 2)
$\boldsymbol{U}, \boldsymbol{V}, \boldsymbol{W}$	diagonal matrices of $\boldsymbol{u}, \boldsymbol{v}, \boldsymbol{w}$ (in Chapter 2)
$\boldsymbol{u}, \boldsymbol{v}, \boldsymbol{w}$	vectors of the Cartesian components of the branches (in Chapter 2)
$\boldsymbol{z}_b$	position of the boundary nodes (in Chapter 2)
$\chi_{\alpha\beta}$	covariant components of the change of curvature tensor
$đ\mathcal{Q}$	heat increment
$đ\mathcal{I}$	internal work increment
$đ\mathcal{W}$	external work increment
$\delta^i_{.j}$	Kronecker symbol
δ	dissipation density
ϵ_{ijk}	Levi-Civita symbol
$\eta_{i\alpha}$	covariant components of the strain tensor
$\Gamma^{\lambda}_{\alpha\beta}$	Christoffel symbols
ι_R	inertia density in reference configuration
ι	inertia density in current configuration
$\kappa^{\alpha}_{.\beta}$	curvature tensor
$\kappa_{\alpha\beta}$	second fundamental form
$\mathbb{A}$	set of statically admissible generalised stress fields
$\mathbb{B}$	simple body

$\mathbb{D}$ set of kinematically admissible displacement fields
$\mathbb{E}^3$ Euclidean space
$\mathbb{H}$ stress range
$\mathbb{K}$ strain range
$\mathbb{P}$ part of a shell
$\mathbb{S}$ Cosserat surface body
$\mathbf{a}^i$ local contravariant base on the surface
$\mathbf{a}_3$ normal vector to the surface
$\mathbf{a}_i$ local covariant base on the surface
$\mathbf{b}$ body forces
$\mathbf{c}$ body couple forces
$\mathbf{d}$ director unit vector in current configuration
$\mathbf{e}_\alpha$ local covariant base in current configuration
$\mathbf{F}$ change of geometric configuration gradient
$\mathbf{f}$ change of geometric configuration
$\mathbf{G}$ change of director configuration gradient
$\mathbf{g}$ change in director configuration
$\mathbf{H}$ strain tensor
$\mathbf{h}$ director unit vector in reference configuration
$\mathbf{H}^e$ elastic part of the strain tensor
$\mathbf{H}^p$ plastic part of the strain tensor
$\mathbf{I}$ identity tensor
$\mathbf{i}_k$ Cartesian basis of the Euclidean space
$\mathbf{J}$ moment of inertia tensor
$\mathbf{j}$ entropy flux
$\mathbf{J}_F$ fibre second order moments tensor
$\mathbf{K}$ change of curvature tensor
$\mathbf{K}^e$ elastic part of the change of curvature tensor
$\mathbf{K}^p$ plastic part of the change of curvature tensor
$\mathbf{l}$ angular momentum density
$\mathbf{M}$ moment tensor
$\mathbf{m}$ contact couple forces
$\mathbf{m}_\partial$ known external boundary couple force vector
$\mathbf{N}$ surface part of $\mathbf{T}$
$\mathbf{p}$ momentum density
$\mathbf{Q}$ rotation tensor
$\mathbf{q}$ heat flux vector
$\mathbf{r}$ director displacement
$\mathbf{s}$ position of the generic point on the material fibre in Euclidean space
$\mathbf{T}$ force tensor
$\mathbf{t}$ contact forces
$\mathbf{t}_\partial$ known external boundary force vector
$\mathbf{u}$ geometric displacement
$\mathbf{v}$ velocity
$\mathbf{w}$ director velocity

$\mathbf{x}$ position vector of the genereic point in reference configuration
$\mathbf{y}$ position vector in current configuration
$\mathbf{z}$ position vector of the generic shell-like continuum
$\mathcal{D}$ total dissipation power
$\mathcal{E}$ internal energy
$\mathcal{P}_I$ internal power
$\mathcal{P}_Q$ heat power or heating
$\mathcal{P}_E$ external power
$\mathcal{S}$ entropy
$\mathcal{T}$ kinetic energy
$\mathfrak{E}$ extensive physical property
$\mathfrak{e}$ density of the extensive physical property $\mathfrak{E}$
$\mathfrak{f}$ geometric configuration
$\mathfrak{F}^m_{kl}$ solution of the equilibrium problem in which the coefficient $_{kl}$ in the series term of the redundant force component m^{11} is set equal to unity while all the others are set to zero, and the external loads and boundary conditions are homogeneous
$\mathfrak{F}^q_{rs}$ solution of the equilibrium problem in which the coefficient $_{rs}$ in the series term of the redundant force component t^{31} is set equal to unity while all the others are set to zero, and the external loads and boundary conditions are homogeneous
$\mathfrak{F}^t_{ij}$ solution of the equilibrium problem in which the coefficient $_{ij}$ in the series term of the redundant force component t^{11} is set equal to unity while all the others are set to zero, and the external loads and boundary conditions are homogeneous
$\mathfrak{F}_E$ solution of the effective equilibrium problem
$\mathfrak{F}_H$ solution of the equilibrium problem in which the horizontal force boundary condition is equal to unity and the external loads and boundary conditions are homogeneous
$\mathfrak{F}_M$ solution of the equilibrium problem in which the moment boundary condition is equal to unity and the external loads and boundary conditions are homogeneous
$\mathfrak{F}_z$ solution of the equilibrium problem in which only the external vertical loads at the internal and on the boundary are present
$\mathfrak{F}_x$ solution of the equilibrium problem in which only horizontal loads equal to the self-weight of the dome and applied in the x_1 direction are present
$\mathfrak{F}_y$ solution of the equilibrium problem in which only horizontal loads equal to the self-weight of the dome and applied in the x_2 direction are present
$\mathfrak{g}$ director configuration
$\mathfrak{L}$ angular momentum
$\mathfrak{M}$ resultant moment
$\mathfrak{P}$ momentum
$\mathfrak{R}$ resultant force
$\mathfrak{z}$ function describing the membrane parametrised *a la Monge* (in Chapter 2)
C_M elasticity tensor related to the moment tensor
C_T elasticity tensor related to the force tensor
D_M compliance tensor related to the moment tensor
D_T compliance tensor related to the force tensor
e alternating tensor
μ friction coefficient

Ω region in Euclidean space
$\overline{\mathbf{c}}$ body couple forces
$\overline{\mathbf{m}}$ contact couple forces
$\partial\Pi$ boundary of the region Π
$\partial\Sigma_D$ constrained boundary of the shell
$\partial\Sigma_N$ unconstrained boundary of the shell
ϕ Airy stress function (in Chapter 2), friction angle (in chapters 3, 4 and 5)
Π current geometric configuration of the part $\mathbb{P}$
ρ_R mass density in reference configuration
ρ mass density in current configuration
ρ_F fibre mass density
Σ surface region embedded in Euclidean space
σ_s entropy production
τ kinetic energy density
θ^α curvilinear coordinates
Θ coordinate domain
$\upsilon(\mathbf{y})$ number of fibres per unit area
ε internal energy density
$\varkappa^\beta_{.\alpha}$ director curvatures
ς entropy supply
ϑ absolute temperature
a determinant of the metric tensor
$a_{\alpha\beta}$ first fundamental form
BD bounded deformation function space
c cohesion
C^1 continuously differentiable function space
$d\mathbf{x}$ line element on the surface
$e(\boldsymbol{\nu})$ normal eccentricity referred to the $\boldsymbol{\nu}$ direction
L^2 square-integrable function space
m mass
$m^{\alpha\beta}$ contravariant components of the moment tensor
M_1 bounded Radon measures function space
m_F fibre mass
N_y normal space to the surface in current configuration
o origin in Euclidean space
p material point
q heat flux
r heat supply
s entropy density
t time
$t^{i\alpha}$ contravariant components of the force tensor
T_x tangent space to the surface in reference configuration
T_y tangent space to the surface in current configuration
u, v, w Cartesian components of the branches (in Chapter 2)
u^*, v^*, w^* dual quantities of u, v, z (in Chapter 2)

V vector space
x generic point in Euclidean space in reference configuration (in Chapter 3)
x, y, z Cartesian components of the nodes of the network (in Chapter 2)

List of Abbreviations

TNA	Thrust Network Analysis
TSA	Thrust Surface Analysis
SASF	Statically Admissible Shell Forces
GSF	Geometrical Safety Factor
TS1	Thrust Surface 1
TS2	Thrust Surface 2
TS3	Thrust Surface 3
P1	Problem 1: search for the minimum thickness
P2	Problem 2: search for the maximum load multiplier
M1	Heyman material model
M2	Material model with bounded shear strength
M3	Material model with bounded compressive strength
M4	Material model with bounded shear and compressive strength

Abstract

The research work described in the present thesis is addressed to an investigation of the analysis methods working within the framework of limit analysis for the stability assessment of masonry domes. The theoretical and numerical studies mainly focus on the development of an analysis method able to provide useful indications in the case a masonry dome is loaded upon by a system of vertical and horizontal loads, the latter somewhat representative of seismic loads.

The dome shapes considered in the thesis are not axisymmetric. This is motivated by the fact that, although throughout the centuries masonry domes have been usually built in the shape of solids of revolution, in the Romanesque period and later, during the Renaissance, builders began constructing new domed structures characterised by oval shapes. These structures, which have already received special attention from the historical point of view, undoubtedly deserve as much attention from the perspective of their mechanical response, which study is made even more complicated by their complex geometry.

The problem of determining the safety level of masonry domes with regard to structural collapse is an ancient one. Scholars involved in this issue effectively used graphical methods to assess the stability since the 18^{th} century, long before limit analysis was formalised in the modern terms we are used nowadays. For this reason, together with a brief synthesis of the modern literature, a historical perspective of the methods used in the past centuries for modelling and designing masonry domes is presented.

After a short survey of the historical methods, the thesis focuses on the investigation of different methods for the safety assessment of masonry domes by exploiting the static theorem of limit analysis. A suitable implementation of two methods widespread used and available in the literature, the "thrust network analysis (TNA)" and the "thrust surface analysis (TSA)" method, is illustrated. An expressly developed method for searching for statically admissible distributions of the internal forces is presented in which the dome is considered as a thin shell.

The thesis is composed of five chapters. The summary of the topics addressed in the thesis is recalled in the following.

Chapter 1 briefly outlines the state of the art on modelling methods used to study the load bearing capacity of masonry structures. A selection of the main historical contributions over the last three centuries aimed at assessing the safety level of masonry domes is also presented. These contributions have been revived in recent times, thanks to the fundamental contribution of Jacques Heyman, who has provided a common interpretation background to most of the historical techniques, by showing how they could be brought back within the framework of limit analysis.

In **Chapter 2**, the Thrust Network Analysis (TNA) and the Thrust Surface Analysis (TSA), which are two well-established methods for studying the stability of masonry domes used today are illustrated along with their hypotheses. The comparison between the two methods is performed in detail on a case study considering only the presence of vertical loads. The comparison, which represents one of the original parts of the thesis, highlights analogies and differences in the results obtained and constitutes a starting point for checking the feasibility in practice of a possible method combining thrust network and thrust surface. Finally, the applications of these two methods in case of horizontal loading are presented. In particular, it is highlighted how the two techniques present limitations which emerge clearly in case of horizontal loads. For these reasons, instead of focusing the attention on TNA and TSA, an alternative approach based on the thin shell model is developed in the following chapters.

In **Chapter 3** the classical thin shell model is recalled in detail. The fundamental static and kinematic theorems of limit analysis are reformulated, and an explicit proof is provided by specialising them to the case of shells. Different hypotheses on the failure criteria for the material are also discussed, which could be effectively used for modelling the ultimate limit state of masonry domes.

In **Chapter 4**, an original analysis method is illustrated for the safety assessment of a masonry dome. The procedure implemented in the method is inspired by the flexibility method used for determining internal forces in indeterminate beam systems. The dome is considered a thin shell, the dome stability is evaluated by the static theorem of limit analysis. In this regard, the method looks for optimal distributions of the internal forces, i.e., able to maximise the safety factor, by scanning a suitable set of statically admissible internal forces. The method is able to include information regarding the joints' orientation, as well as to cope with domes having a general shape. To ease the description the simple case of a conic shell is addressed before an illustration of the method is provided in the general case.

Finally, in **Chapter 5**, two case studies are presented. The first case study is a classical benchmark: the spherical dome. The second case is the dome of Pisa Cathedral, a dome with a peculiar oval plan and ogival profile. The results obtained are discussed in detail. The safety of the dome is assessed with and without horizontal loads. The influence of different material hypotheses on the results obtained is checked, as well as the effectiveness of the method to yield satisfactory estimates of the masonry dome safety level by suitably optimising the internal forces within the dome itself.

In conclusion, the thesis presents two main original contributions. The first one is a comparison between TNA and TSA, where similarities and differences between the two techniques are highlighted on a case study, as well as the feasibility in practice of a possible new method combining the two. The second one is the development of an original analysis methodology, for the analysis of the safety level of masonry domes against vertical and horizontal loads. The method, which is based on the thin shell model, is presented in detail and applied to two case studies. Remarkably, this new technique is able to overcome some major limitations of TNA and TSA. The change in the structural scheme from membrane to shell allows accounting for a wider set of resources for the masonry dome, otherwise neglected, that proved to be important when only vertical loads act on the structure and become crucial when horizontal loads are added to vertical ones.

Keywords: masonry domes, limit analysis, shell equilibrium, thrust surface, thrust network, convex optimisation

Sommario

Il lavoro di ricerca descritto nella presente tesi utilizza i metodi dell'analisi limite ed è rivolto alla valutazione della sicurezza delle cupole in muratura nei confronti del possibile collasso strutturale. L'attenzione si concentra, principalmente, sullo sviluppo di un nuovo metodo di analisi valido nel caso in cui sulla cupola in muratura agisca, oltre ai carichi gravitazionali, un sistema di carichi orizzontali ritenuto rappresentativo, in qualche senso da definire, delle azioni di origine sismica.

Nella tesi si considerano con particolare attenzione cupole la cui forma non è assialsimmetrica. Questa scelta trae la sua motivazione dal fatto che, sebbene durante i secoli passati le cupole in muratura siano state costruite quasi sempre nella forma di solidi di rivoluzione, nel periodo romanico e, successivamente, durante il Rinascimento, i costruttori iniziarono a realizzare cupole di nuova concezione, caratterizzate da forme ovali. Queste strutture, che hanno già ricevuto particolare attenzione dal punto di vista storico, senza dubbio meritano altrettanta attenzione dal punto di vista dello studio della loro risposta meccanica, studio che è reso ancora più complicato dalla loro particolare geometria.

La determinazione del livello di sicurezza delle cupole in muratura nei riguardi del collasso strutturale è un problema 'antico'. Gli studiosi che si sono occupati di queste tematiche hanno efficacemente utilizzato fin dal diciottesimo secolo metodi e strumenti propri dell'analisi limite, in forma grafica, molto prima che questa disciplina fosse formalizzata nei termini moderni ai quali siamo abituati oggi. Per questo motivo, insieme a una breve sintesi della letteratura moderna, viene presentato anche un resoconto sintetico dei principali metodi usati nei secoli passati per la verifica strutturale e la progettazione delle cupole in muratura.

Dopo una breve rassegna dei metodi storici, la tesi si concentra sull'indagine di alcuni metodi comunemente utilizzati per la valutazione della sicurezza delle cupole in muratura ricorrendo al teorema statico dell'analisi limite. Si illustra una specifica implementazione di due metodi ben noti in letteratura, il metodo della 'rete di spinta' (*thrust network*) e quello della 'superficie di spinta' (*thrust surface*). Viene inoltre presentato un metodo sviluppato *ad hoc* per la ricerca di distribuzioni di sollecitazioni staticamente ammissibili, nel quale la cupola è schematizzata come un guscio sottile.

La tesi è articolata in cinque capitoli. Gli argomenti affrontati sono richiamati sinteticamente nel seguito.

Il **Capitolo 1** illustra brevemente quello che è lo stato dell'arte per quanto riguarda gli schemi interpretativi utilizzati per lo studio del comportamento meccanico e del calcolo a rottura delle strutture in muratura. Viene inoltre presentata una selezione dei principali contributi storici che negli ultimi tre secoli sono stati proposti per valutare il livello di sicurezza delle cupole in muratura. Questi contributi sono stati ripresi in tempi recenti, grazie

al fondamentale lavoro di Jacques Heyman, che ha fornito uno sfondo interpretativo comune alla maggior parte dei metodi storici, mostrando come questi possano essere ricondotti nell'ambito dei metodi propri dell'analisi limite.

Nel **Capitolo 2** vengono presentati la "Thrust Network Analysis" (TNA) e la "Thrust Surface Analysis" (TSA), due metodi ormai consolidati e utilizzati correntemente per studiare la stabilità delle cupole in muratura; le ipotesi alla base dei due metodi sono inoltre discusse criticamente. Il capitolo esamina in dettaglio un loro confronto, effettuato su un caso di studio che considera la presenza di soli carichi verticali. Il confronto, che costituisce uno degli aspetti originali della tesi, mette in evidenza le analogie e le differenze nei risultati ottenuti e rappresenta uno spunto di riflessione per quanto riguarda la verifica della fattibilità, nella pratica, di un possibile metodo che combini le *reti di spinta* e le *superfici di spinta*. Infine, vengono presentate le applicazioni di questi due metodi al caso in cui siano presenti anche dei carichi orizzontali. In particolare, si evidenzia come le due tecniche presentino dei limiti che emergono in modo più evidente nel caso di carichi orizzontali. Per questi motivi, invece di focalizzare l'attenzione su TNA e TSA, nel seguito della tesi viene sviluppato un approccio alternativo nel quale la cupola è vista come un elemento strutturale identificabile come un 'guscio sottile'.

Nel **Capitolo 3** viene richiamato in dettaglio il modello classico di guscio sottile. I teoremi fondamentali, statico e cinematico, dell'analisi limite sono riformulati e ne viene fornita una dimostrazione esplicita specializzandoli al caso dei gusci. Si discutono anche diverse ipotesi sui criteri di rottura del materiale che possono essere utilizzati per schematizzare efficacemente il comportamento a rottura della muratura della cupola.

Nel **Capitolo 4** viene illustrato un metodo di analisi originale per la valutazione della sicurezza di una cupola in muratura. La procedura implementata nel metodo è ispirata dal metodo delle forze, utilizzato nell'ambito della teoria tecnica delle travi e nel quale i campi di sforzo staticamente ammissibili sono rappresentati in termini di un numero finito di parametri. La cupola è schematizzata come un guscio sottile e la sua stabilità è valutata utilizzando il teorema statico dell'analisi limite. Il metodo proposto prende in considerazione un opportuno insieme di campi di sforzo staticamente ammissibili e ricerca, al suo interno, una soluzione ottimale, ovvero tale da di rendere massimo un opportuno coefficiente di sicurezza. Il metodo è in grado di includere informazioni riguardanti l'orientamento dei giunti, così come di trattare cupole di forma generale. Per facilitare la descrizione, nel capitolo si affronta il caso semplice di un guscio conico prima di fornire un'illustrazione del metodo nel caso generale.

Infine, nel **Capitolo 5**, vengono presentati due casi studio. Il primo è un classico caso di riferimento: la cupola sferica. Il secondo caso studio è la cupola del duomo di Pisa, una cupola con una particolare pianta ovale e un profilo ogivale. I risultati ottenuti sono discussi in dettaglio. La sicurezza della cupola è valutata nei due casi in cui i carichi orizzontali sono, rispettivamente, presenti e assenti. Viene verificata l'influenza sui risultati ottenuti delle diverse ipotesi fatte sul materiale e l'efficacia del metodo nel produrre stime soddisfacenti del livello di sicurezza della cupola in muratura.

La tesi presenta due contributi ritenuti di maggiore interesse. Il primo è un confronto tra la TNA e la TSA, in cui si evidenziano le somiglianze e le differenze tra le due tecniche su un caso di studio, così come la reale fattibilità di un possibile nuovo metodo che combini reti e superfici delle spinte. Il secondo è lo sviluppo di una metodologia originale di analisi per

la valutazione del livello di sicurezza delle cupole in muratura soggette a carichi verticali e orizzontali. Il metodo, che si basa sul modello di guscio sottile, viene presentato in dettaglio e applicato a due casi di studio. Sorprendentemente, questa nuova tecnica si rivela in grado di superare alcune importanti limitazioni dei metodi basati sulla TNA e sulla TSA. Il cambiamento dello schema strutturale da membrana a guscio permette di far emergere alcune risorse resistenti delle cupole in muratura, altrimenti trascurate, che si rivelano importanti anche quando sulla struttura agiscono solo carichi verticali e risultano invece cruciali quando sono presenti carichi orizzontali oltre a quelli verticali.

Parole chiave: cupole in muratura, analisi limite, equilibrio di gusci, superficie di spinta, reticolo di spinta, ottimizzazione convessa

Résumé

Le travail de recherche décrit dans la présente thèse est consacré à l'étude des méthodes d'analyse s'inscrivant dans le cadre de l'analyse limite pour l'évaluation de la stabilité des dômes maçonnés. Les études théoriques et numériques se concentrent principalement sur le développement d'une méthode d'analyse capable de fournir des indications utiles dans le cas où un dôme en maçonnerie est chargé par un système de charges verticales et horizontales, ces dernières étant assez représentatives des charges sismiques.

Les formes de dôme considérées dans la thèse ne sont pas axisymétriques. Ceci est motivé par le fait que, bien qu'au cours des siècles les dômes en maçonnerie aient été généralement construits en forme de solides de révolution, à l'époque romane et plus tard, pendant la Renaissance, les constructeurs ont commencé à construire de nouvelles structures caractérisées par des formes ovales, que ce soit en plan ou en élévation. Ces structures, qui ont déjà reçu une attention particulière du point de vue historique, méritent sans aucun doute autant d'attention du point de vue de leur réponse mécanique, dont l'étude est rendue encore plus compliquée par leur géométrie complexe.

Le problème de la détermination du niveau de sécurité des dômes en maçonnerie relativement au risque d'effondrement est ancien. Les chercheurs impliqués dans cette question ont efficacement utilisé des méthodes graphiques pour évaluer la stabilité depuis le $18^{\text{ème}}$ siècle, bien avant que l'analyse des limites ne soit formalisée dans les termes modernes que nous utilisons aujourd'hui. Pour cette raison, en plus d'une brève synthèse de la littérature moderne, une perspective historique des méthodes utilisées au cours des siècles passés pour modéliser et concevoir les dômes en maçonnerie est présentée.

Après un bref aperçu des méthodes historiques, la thèse se concentre sur l'étude de différentes méthodes pour l'évaluation de la sécurité des dômes en maçonnerie en exploitant le théorème statique de l'analyse limite. Une implémentation appropriée de deux méthodes largement utilisées et disponibles dans la littérature, la méthode des "réseaux de forces" (TNA: *thrust network analysis*) et la méthode de la "surface de pression" (TSA: *thrust surface analysis*), est illustrée. Une méthode spécialement développée pour la recherche de distributions statiquement admissibles des forces internes est présentée dans laquelle le dôme est considéré comme une coque mince.

La thèse est composée de cinq chapitres. Le résumé des sujets abordés dans la thèse est rappelé dans ce qui suit.

Le **Chapitre 1** présente brièvement l'état de l'art sur les méthodes de modélisation utilisées pour étudier la capacité portante des structures en maçonnerie. Une sélection des principales contributions historiques des trois derniers siècles visant à évaluer le niveau de sécurité des dômes maçonnés est également présentée. Ces contributions ont été relancées

récemment, grâce à la contribution fondamentale de Jacques Heyman, qui a fourni un cadre d'interprétation commun à la plupart des techniques historiques, en montrant comment elles pouvaient être ramenées dans le champ de l'analyse limite.

Dans le **Chapitre 2**, l'analyse du réseau de forces (TNA : Thrust Network Analysis) et l'analyse de la surface de pression (TSA : Thrust Surface Analysis), qui sont deux méthodes bien établies pour étudier la stabilité des dômes en maçonnerie utilisées aujourd'hui, sont illustrées avec leurs hypothèses. La comparaison entre les deux méthodes est effectuée en détail sur une étude de cas considérant uniquement la présence de charges verticales. La comparaison, qui constitue une des parties originales de la thèse, met en évidence les analogies et les différences dans les résultats obtenus et établit un point de départ pour vérifier la faisabilité en pratique d'une éventuelle méthode combinant réseau de forces et surface de pression. Enfin, les applications de ces deux méthodes dans le cas d'un chargement horizontal sont présentées. En particulier, il est mis en évidence comment les deux techniques présentent des limitations qui apparaissent clairement dans le cas de charges horizontales. Pour ces raisons, au lieu de concentrer l'attention sur les réseaux de forces et les surfaces de pression (TNA et TSA), une approche alternative basée sur le modèle de coque mince est développée dans les chapitres suivants.

Dans le **Chapitre 3**, le modèle classique de coque mince est rappelé en détail. Les théorèmes statiques et cinématiques fondamentaux de l'analyse des limites sont reformulés, et une preuve explicite est fournie en les spécialisant au cas des coques. Différentes hypothèses sur les critères de rupture du matériau sont également discutées, qui pourraient être utilisées efficacement pour modéliser l'état limite ultime des dômes en maçonnerie.

Dans le **Chapitre 4**, une méthode d'analyse originale est illustrée pour l'évaluation de la sécurité d'un dôme en maçonnerie. La procédure mise en œuvre dans la méthode est inspirée de la méthode des forces utilisée pour déterminer les forces internes dans les systèmes de poutres indéterminées. Le dôme est considéré comme une coque mince, la stabilité du dôme est évaluée par le théorème statique de l'analyse limite. À cet égard, la méthode recherche des distributions optimales des forces internes, c'est-à-dire capables de maximiser le facteur de sécurité, en balayant un ensemble approprié de forces internes statiquement admissibles. La méthode est capable d'inclure des informations concernant l'orientation des joints, ainsi que de traiter les dômes ayant une forme générale. Pour faciliter la description, le cas simple d'une coque conique est abordé avant qu'une illustration de la méthode soit fournie dans le cas général.

Enfin, dans le **Chapitre 5**, deux études de cas sont présentées. Le premier cas est une référence classique : le dôme sphérique. Le second cas d'étude est le dôme de la cathédrale de Pise, un dôme à plan ovale particulier et un profil ogival. Les résultats obtenus sont discutés en détail. La stabilité du dôme est évaluée avec et sans charges horizontales. L'influence de différentes hypothèses de matériaux sur les résultats obtenus est vérifiée, ainsi que l'efficacité de la méthode pour produire des estimations satisfaisantes du niveau de sécurité du dôme en maçonnerie en optimisant de manière appropriée les forces internes dans le dôme lui-même.

En conclusion, la thèse présente deux contributions originales principales. La première est une comparaison des méthodes TNA et TSA, où les similitudes et les différences entre les deux techniques sont mises en évidence sur une étude de cas, ainsi qu'une étude de la faisabilité d'une nouvelle méthode combinant les deux. La seconde est le développement d'une méthodologie originale pour l'analyse du niveau de sécurité des dômes en maçonnerie

soumis à des charges verticales et horizontales. La méthode, basée sur le modèle de coque mince, est présentée en détail et appliquée à deux études de cas. De façon remarquable, cette nouvelle technique est capable de surmonter certaines limitations majeures des TNA et TSA. Le changement de schéma structurel de la membrane à la coque permet de prendre en compte un ensemble plus large de ressources de résistance des dômes en maçonnerie, autrement négligées, qui sont importantes lorsque seules des charges verticales agissent sur la structure et qui deviennent cruciales lorsque des charges horizontales sont ajoutées aux charges verticales.

Mots clés: dômes maçonnés, analyse limite, équilibre des coques, surface de pression, réseaux de forces, optimisation convexe

Chapter 1

Introduction

Historical masonry constructions, dating back to hundreds, in some cases to thousands, of years, strongly characterise the architectural heritage of European countries. In many cases, their same structural elements such as arches, vaults and domes hold great historical, artistic and architectural interest. Considerable and ever-increasing attention has been paid to their conservation, especially in recent decades. The focus of such efforts has been particularly on the need to develop effective analysis methods to assess their ability to resist vertical and, most notably, horizontal actions (as they are the most insidious) [Boothby, 2001]. This task is by no means an easy one, given the complex mechanical response of masonry, which is still far from being fully understood, as it is strongly dependent on a large number of mechanical and geometric parameters, such as, for example, the nature of the materials, and the texture and characteristic dimensions of the structure's constituent elements. Moreover, the skill of the builders and the construction methods, which are generally unknowable, affect the response of the masonry, thereby making the mechanical behaviour of historical masonry buildings even more unpredictable.

One property common to almost all masonry constructions is that they exhibit low tensile strength. This peculiar feature has, since antiquity, decisively influenced the shapes chosen for building such structures [Benvenuto, 1991], [Huerta, 2001], [Tralli et al., 2014]. In addition, masonry's limited capacity to transmit tensile stresses, and consequently the relative ease with which cracks can originate and propagate through the thickness of the masonry itself, has driven modern structural mechanics to develop various, specifically dedicated analysis methods, which also differ from each other in terms of the degree of detail and complexity. Many constitutive models have been proposed in the literature, nevertheless nowadays the problems inherent in analysing masonry structures are still far from being completely resolved, as a widely accepted approach for studying their stability is still missing [Tralli et al., 2014].

The following features give an idea of some complexities lying behind the modelling of masonry structures:

1. The construction technique and the quality of the masonry plays a crucial role in the mechanical behaviour, thus it's very unlikely to be able to define precise constitutive relations which apply to the generality of the masonry types.

2. Since masonry is generally made by an assemblage of blocks and mortar arranged

accordingly to a particular internal disposition, the material is anisotropic and inhomogeneous. However, as a first rough approximation, one can think of the behaviour to be linear elastic if the masonry is compressed up to a certain limit.

3. The material has an uncertain and generally low resistance to tensile stresses. Moreover, once the tensile strength is attained, no more tensile stresses can be transferred across that material element (formation of cracks) and thus some sort of 'damaging' and permanent deformations develop in the material. From a mechanical standpoint, this also means that the displacement field and the strain field can be discontinuous.

4. In addition to cracking, the material exhibits other permanent strains due to sliding and crushing, whose formation is a dissipative process.

In this context, searching for the 'true' displacement, strain and stress fields in the structure would require a precise characterisation of the materials and further information, such as the building technique adopted during construction and the internal arrangement of the masonry units (blocks of bricks), just to name a few.

As it is well known, the linear elastic analysis, which is the standard approach in structural mechanics, proves useless in the study of the mechanical behaviour of masonry structures (see for example [Huerta, 2001] and references therein). In the extensive literature aimed at defining possible strategies for studying the structural behaviour of masonry buildings, two main, well-known approaches have been followed: the nonlinear analysis and the limit analysis. Nonlinear analysis, which is the common approach in mechanics, aims to follow the evolution over time of the displacements and stress and strain fields in the structure. The solution depends on the particular boundary conditions and it requires precise characterisation of the body kinematics and constitutive laws. However, especially in the case of masonry structures, the results may be very sensitive to slight changes in the values of the material parameters and this issue is crucial given the uncertainties in the mechanical characterisation of the masonry. This reason is the main motivation justifying the use of limit analysis, whose aim, contrary to nonlinear analysis, is to determine the conditions that lead to a structure's collapse abandoning the claim to know the 'real' state of the structure, by determining the time evolution of displacements, stresses and deformations fields.

1.1 State of art: literature on masonry structures

The literature on the methods for assessing the mechanical response and load capacity of masonry structures is very rich. Many methods and techniques have been proposed and a full review is beyond the scope of this section. Modelling methodologies can be divided in several ways. For example, a first distinction distinguishes the methods that model the structure as a finite set of elements (blocks) from the methods that model the structure as a continuous body. In the first category falls the so-called *discrete element method* (DEM) [Cundall and Strack, 1979]. In recent years, Forgács et al. [Forgács et al., 2017] developed a model and estimated for the first time the minimum thickness of semi-circular skewed masonry arches with success. Beatini et al. [Beatini et al., 2017] numerically implemented a regularised non-smooth contact dynamics approach for the study of complex assemblies

of rigid blocks representative of real masonry structures. Simon and Bagi [Simon and Bagi, 2016] investigated the minimum thickness of domes with different geometries loaded by their self-weight. The DEM approach was used by the same authors to investigate the role of frictional resistance between masonry units on the stability of masonry domes [Simon and Bagi, 2016], [Beatini et al., 2018].

The methods belonging to the second group model the dome as a simple no-tension three-dimensional body, often referred to as a *masonry-like* continuum or *no-tension masonry material model*. The origins of this model can be dated back to the work of Signorini [Signorini, 1925b], [Signorini, 1925a]. Since the pioneering 1966 work of J. Heyman, there have been several attempts by many authors to adopt the masonry-like model as a first approximation for the mechanical behaviour of masonry structures [Di Pasquale, 1984], [Giaquinta and Giusti, 1985], [Anzellotti, 1985], [Fichera, 1973], [Panzeca and Polizzotto, 1988], [Del Piero, 1989], [Del Piero, 1998]. Within this context, the nonlinear elastic analysis approach, which follows the evolution of the stress and strain fields under increasing load is also used for the analysis of masonry arches. By way of example, Aita et al. [Aita et al., 2017a], [Aita et al., 2017b] presented some explicit solutions for both statically determinate and indeterminate problems and Barsotti et al. [Barsotti and Bennati, 2018] studied the static response of a masonry arch by way of a one-dimensional nonlinear elastic model in which masonry is regarded as a material with bounded tensile and compressive strengths.

Other widely used approaches are those making use of multi-scale continuum models. Two ways are followed here. The first one introduces the micro-scale in order to get information about the macroscopic properties of the masonry, such as, for example, the elastic constants. The aim is to determine the properties of a fictitious homogeneous continuum having a macroscopic structural response equal to the real heterogeneous composite continuum. The theories that allow the solution of this type of problem are called homogenisation theories. By way of example we cite [Milani et al., 2007], [Milani and Cecchi, 2013], [Peng et al., 2018]). It's worth observing that in these approaches the micro-problem is solved separately from the macro-problem since the micro-structure serves only to get the parameters for the macro-structure. The second way introduces additional internal variables and the solution of the problem involves the contemporary solution of both the micro- and macro-structures (these are the proper multi-scale approaches). We cite, by way of example, [Drougkas et al., 2016], [Petracca et al., 2017], [Salvatori and Spinelli, 2018].

1.2 Historical analysis methods for masonry domes

The problem of establishing mechanical rules capable of describing the structural response of masonry domes has been addressed also in past centuries. Here no claim is made to give a complete historical overview of all the methods adopted in the past, but focus is made on the main contributions. In this section, all contributions addressed to masonry arches have been excluded, focusing exclusively on those works explicitly addressing masonry domes. The interested reader can find excellent reviews on masonry arches, for example, in [Becchi and Foce, 2002] and [Aita, 2003]. An integral investigation of the historical evolution of analysis methods for vaulted structures can be also found in [Huerta, 2008]. Another reference source for historical perspective about the theory of structure is the book of Kurrer [Kurrer, 2018].

A review of historical approaches using graphical analysis devoted to the study of masonry domes can be found in [Fuentes, 2021].

Although a series of design rules and verification methods to determine the safety level of domes and vaults were developed several centuries ago, by most accounts a true theory of the static response of arches and domes seems to have been established in quantitative terms only in the late 17th century [Benvenuto, 1991]. Before the contributions of Philippe De la Hire and Bernard Forest de Belidor, the design of such structures was performed by means of a combination of empirical and geometric rules that reconciled the 'rules of art' with equally important aesthetic requirements. The first example of geometric dimensioning for the profile of masonry domes can be found in Carlo Fontana [Fontana, 1694] (see Figure 1.1).

It was instead Robert Hooke, who in 17th century first highlighted the analogy between the thrust line of a compressed arch and the shape of an inverted catenary, by writing the famous statement: *"Ut pendet continuum flexile, sic stabit contiguum rigidum inversum"* in the form of an anagram [Hooke, 1675].

In an attempt to give a framework to the various theories that have followed one another, the 19th century certainly constitutes a watershed. In fact, during this century, not only was the elasticity theory developed, which had a great influence on the methodologies for calculating masonry vaults and domes, but also the development of membrane analysis led to a change in the way mechanics of domes was seen. Before 19th century, all the theoretical contributions of Bouguer, Bossut, and Mascheroni, were more or less prefigurative of what will be called in 20th century the *slicing technique*. Membrane analysis, on the other hand, was a way to explicitly consider the two-dimensional behaviour of vaulted structures. However, this approach had the flaw to neglect the poor tensile strength of the masonry, by predicting tensile stresses. In an attempt to combine pre-19th century approaches with membrane analysis, notable are the contributions of Eddy, Lévy and Wolfe, all based on the same idea that the dome could be seen as having a double behaviour: an entirely reacting part in which there were stresses of compression-only and a cracked part, in which the mono-dimensional behaviour replaces the membrane one. One could say that the real first contributions on domes are these last three, as they have the merit to clearly distinguish the mechanical behaviour of domes from those of arches.

The contributions presented here are all based on the infinitely resistant rigid block model, which was the reference conceptual model for the calculations of masonry vaults until the development of the theory of elasticity. Even after 18th century, this approach has never been abandoned and it culminated in the nowadays well-established approach called *Thrust Network Analysis*, that is presented in the next chapter.

1.2.1 Bouguer, 1734 and Frézier, 1737

The contribution of Pierre Bouguer [Bouguer, 1734] can be considered the first true static theory of masonry domes. He explicitly tackles for the first time the problem of domes, distinguishing itself from previous contributions on simple arched vaults. He considers the stones making the dome as perfectly smooth, since a masonry domes that is stable under this hypothesis is surely stable also in the real situation of finite friction [cit.]. The main merit of Bouguer has been to extend to the bi-dimensional case a known result by Giacomo

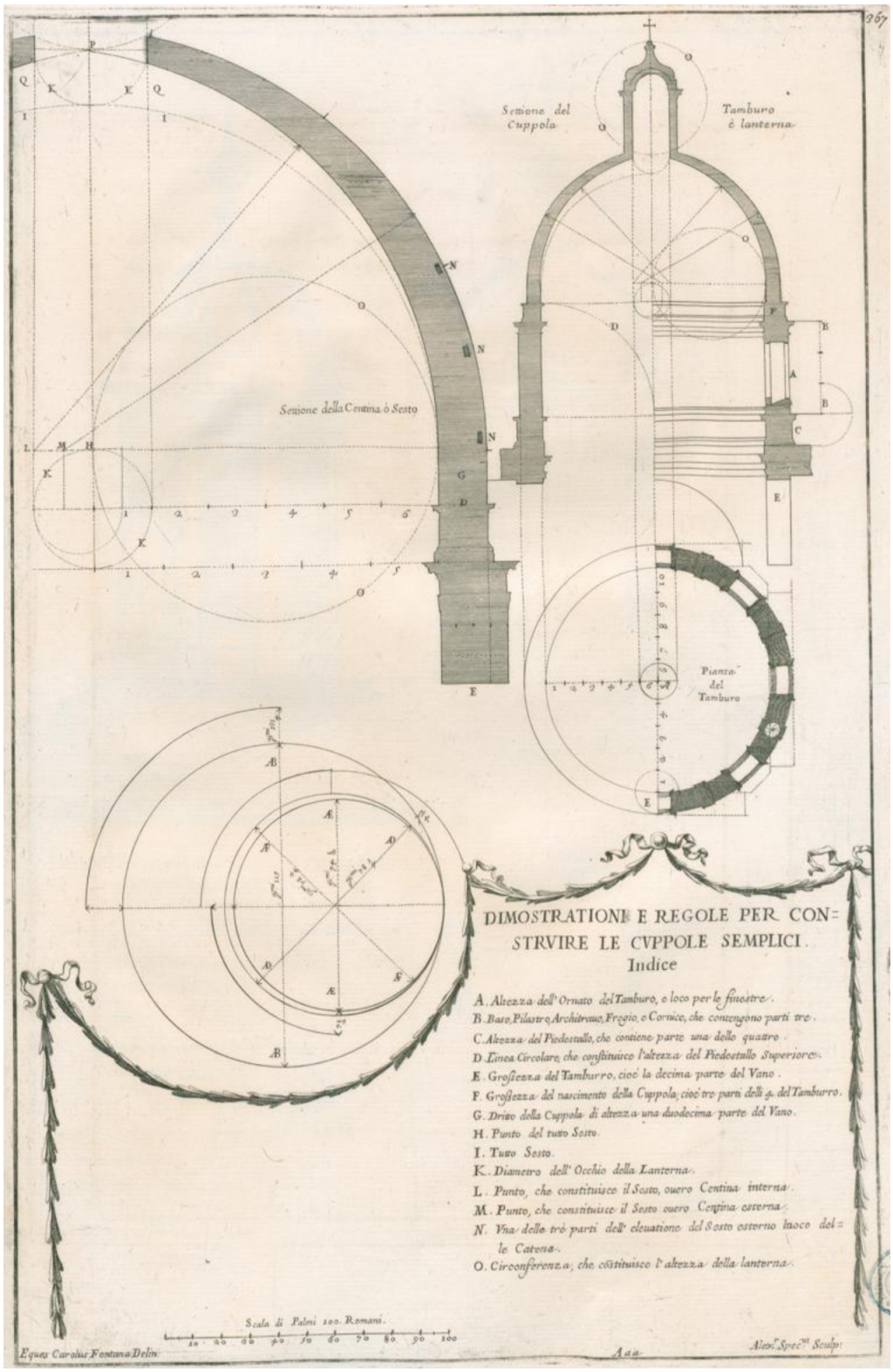

Figure 1.1: Geometrical rules for masonry domes, by Carlo Fontana.

Bernoulli who in 1704 proved that an arch shaped as a reversed catenary is capable of resist its weight whatever its thickness (from [Benvenuto, 1991]). Starting from the equation of the catenary he adapts it to the case of domes where the weight of the infinitesimal element increases towards the base. He comes to the equation describing the curve (see Figure 1.2)

$$xdx = \frac{\mathfrak{p}dy'}{\sqrt{1+y'^2}}, \tag{1.1}$$

where $\mathfrak{p}$ is a constant. By integrating equation (1.1) by series he comes to the description

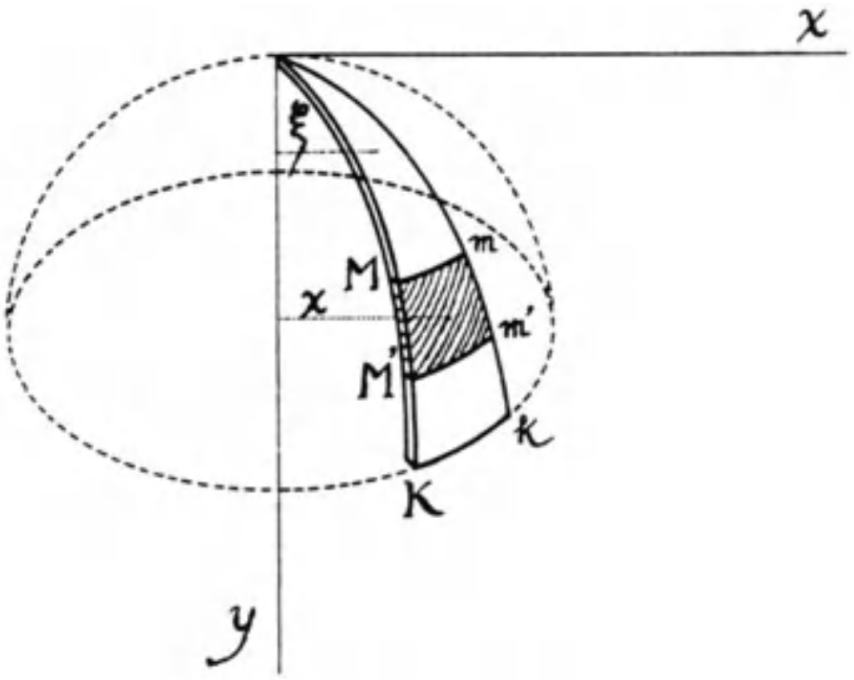

Figure 1.2: Surface of the dome generated by the rotation around vertical axis of the curve described by equation (1.1) (from [Benvenuto, 1991]).

by points of the homogeneous surface in equilibrium with its self-weight.

An important remark is that the shape obtained by integrating equation (1.1) is in equilibrium even if each lune interacts only with the opposite one in the vertex and not with the adjacent ones (this is the first example of the so-called *slicing technique*). On the other hand, if the dome is complete, the equilibrium is granted by every surfaces generated by curves whose equation satisfy

$$\mathfrak{p}y' \leq \int_0^x \xi dQ, \tag{1.2}$$

where Q is the weight of the portion above the section of coordinates (x, y) (see Figure 1.2). Therefore, if we take a curve of equation (1.1), widen its span and make it less convex everywhere, its rotation everywhere through 360 degrees still yields an equilibrated dome [Benvenuto, 1991]. This is an important aspect that hides a tacit hypothesis on the resistance of the material, as specified in the following.

While Bouguer implicitly applied the slicing technique for the study of masonry domes, Frézier [Frézier, 1737] explicitly put it in practice on different vaults and domes, although in a qualitative way.

1.2.2 Poleni, 1748

In 1748, Giovanni Poleni published a monumental treatise which represented a fairly complete synthesis of the knowledge of the time [Poleni, 1748]. Sadly, he seemed to be unaware of the works of Bouguer, as he explicitly stated *"It seems a marvellous thing to me, that either the difference between an arch and a sector of a cupola has not been proposed by anybody, or, if it has been proposed, that I have never met one among the many works of Architecture which I have seen"* (from [Benvenuto, 1991]). Among other things he gave a detailed history of the discovery of the damage to St. Peter's and the subsequent discussion in which he summarises the theoretical and experimental studies on the dome that he conducted starting from 1743. It is well know that in 1742 Pope Benedict XIV entrusted three famous mathematicians with the task of finding out the causes that leads to the damage of the dome of St. Peter's. Even if the conclusions they drew were wrong, the analyses carried out constituted a new and correct method for interpreting the behaviour of the dome, where they make a free use of the principle of virtual work. The discussion about the vicissitude was growing and Poleni was convened by the Pope and joined the debate. He came to the conclusion that the dome was not on immediate danger contrary to what was stated by the three mathematicians. He uses the Stirling's theory of spheres (see Figure 1.3) to the form of the dome to show that *"the form of the big vault is not bad at all"* (from [Benvenuto, 1991]). He then basically treated the dome as a series of slices on which a modified catenary analysis was performed.

Since Poleni was unaware of Bouguer's contributions, it can be said that he autonomously arrived at a formulation of the slicing technique. After all, the contributions on masonry arches were well known and the application of those same methods of analysis to the domes considered as a series of arches must have appeared as almost natural.

1.2.3 Bossut, 1770

Bossout's work on domes is the second of two dense studies published in 1778 [Bossut, 1778b], [Bossut, 1778a]. He deals with the problem of determining the shape of a vault capable of ensuring equilibrium even in absence of friction and cohesion between the blocks. In the case of an arch, he determines an equation relating the shape of the extrados curve, once the intrados curve and the forces acting on the arch are known. He considers both the case of finite dimension blocks and infinitesimal blocks carrying out the analysis in differential form (nowadays one could say: passing from a discrete model to a continuous one).

He tackles two specular problems: the first one consists in finding the shape of the vault when the distribution of the forces is known, and the second one consists in finding the distribution of the forces when the shape of the vault is known. He solves these problems in different cases. The extension to the case of domes is obtained in the hypothesis that the interaction between two adjacent lunes can be neglected (as was done also by Bouguer). Then, each lune is simply considered as an arch on varying width and the same analysis used for barrel vaults is applied (see Figure 1.4).

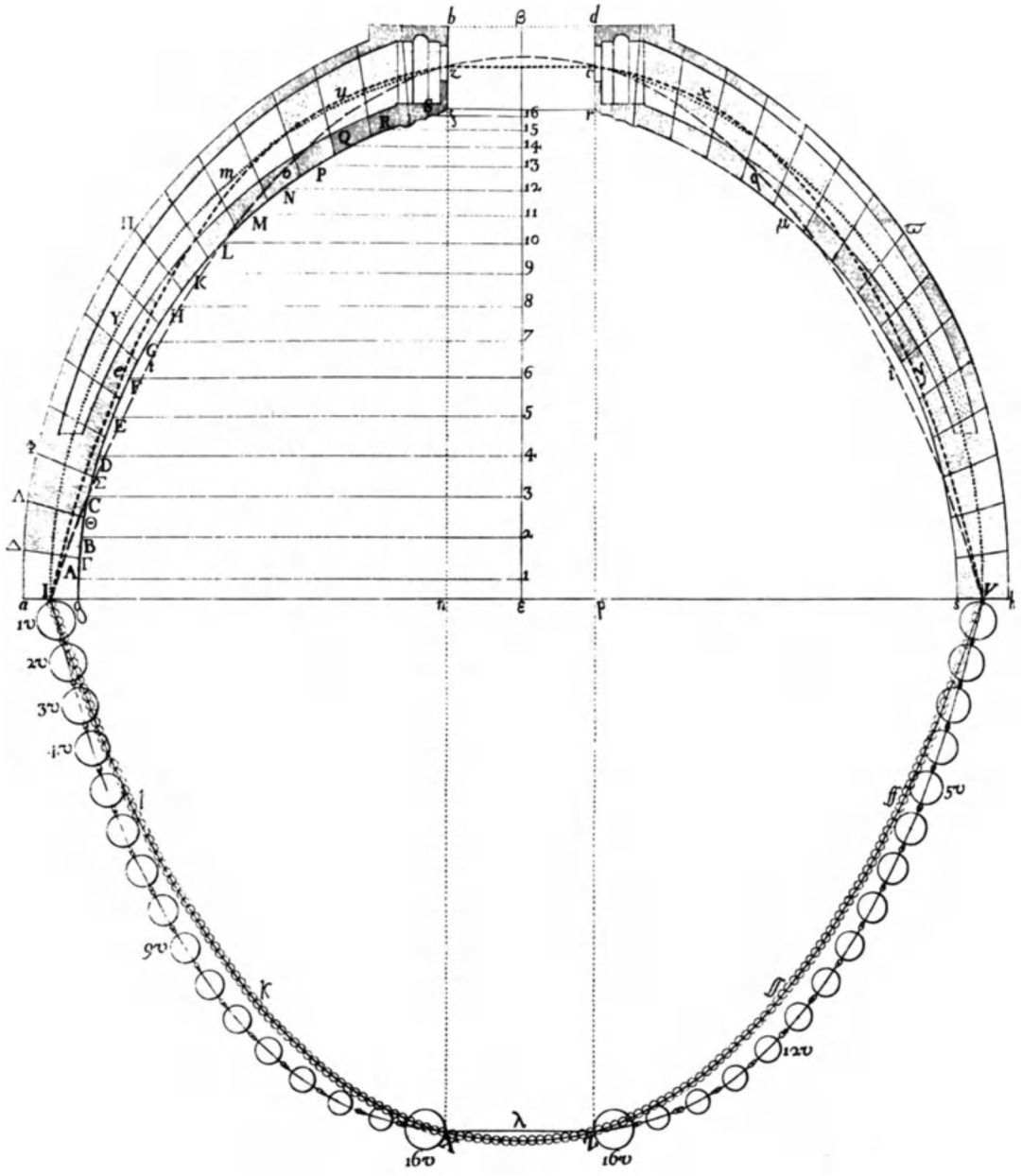

Figure 1.3: Poleni's experiment or ascertaining that the shape of the dome of St. Peter's was good (from [Benvenuto, 1991]).

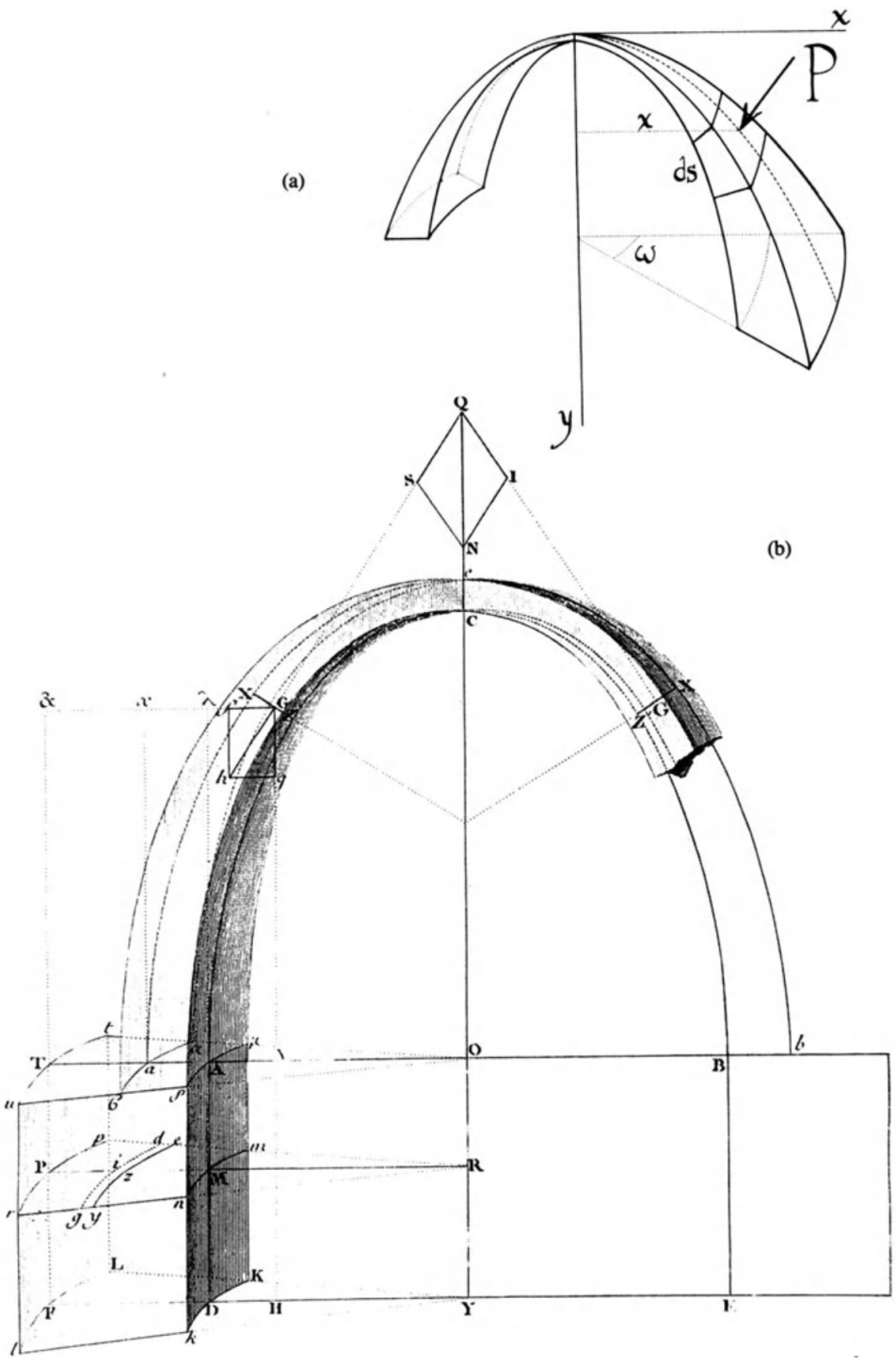

Figure 1.4: Bossut's studies on domes (from [Benvenuto, 1991]).

1.2.4 Mascheroni, 1785

In his treatise [Mascheroni, 1785], Lorenzo Mascheroni addresses the main problems involved in the design of the arches and vaults. One of them is the calculation of domes of finite thickness.

It is very interesting to observe, as reported by [Benvenuto, 1991], that during the 18^{th} century, a fundamental concept drove the calculations of masonry domes. In particular, before the cardinal work of Coulomb, friction and adhesion between voussoirs was constantly neglected. In these hypotheses, it was necessary to impose that the resultant on the generic joint of an arch be orthogonal to the joint itself in order to prevent sliding. For masonry domes it was sufficient to ensure that the resultant on the generic joint *"falls with steeper slope"* (see Figure 1.5), i.e.

$$\frac{Q}{P} > \tan \psi, \tag{1.3}$$

where P and Q are the horizontal and vertical components, respectively, of the resultant of the forces acting on the part above the generic section. This is due to the fact that

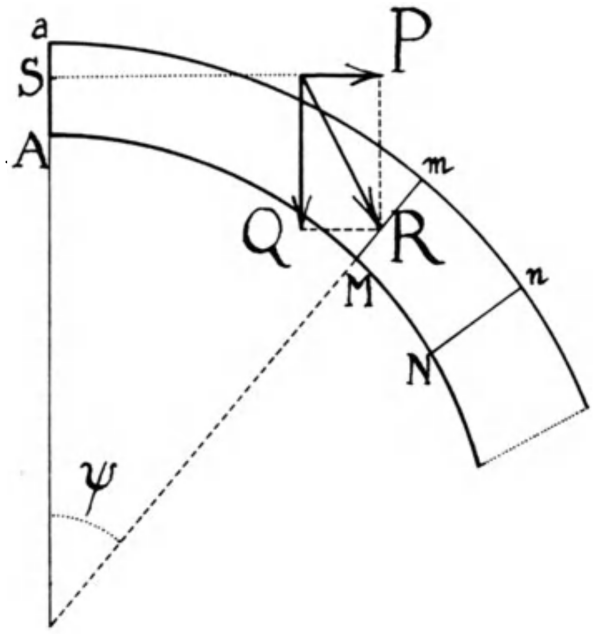

Figure 1.5: Fundamental concept in the design of domes (from [Benvenuto, 1991]).

circumferential forces can be present between two adjacent lunes and they must always be compressive. So equilibrium is ensured with compressive hoop forces whenever condition (1.3) is satisfied. The interesting aspect is that the ancient builders didn't worried about the magnitude of these forces, provided that they were compressive: the stone elements that made up the dome, often because of their superabundant dimensions, could be considered as they where infinitely resistant and thereby absolutely safe. This consideration has been recovered also by Jacques Heyman in 20^{th} century. Moreover, under these hypotheses, the problem of the safety of the dome came down to determining P and Q, a purely geometrical problem.

Mascheroni came to the equation

$$\frac{hxds}{\int hxds} > \frac{dy'}{y'}, \tag{1.4}$$

where h is the thickness of the dome, that allowed to solve the principal problems concerning masonry domes of small but finite thickness. In particular, when the intrados curve is known, the equation rules the size of the edges ensuring equilibrium in each point or, if the geometry is fully specified, it gives a criterion to judge on the safety of the dome.

Another interesting aspect of the treatise of Mascheroni is the application to spherical domes. In asking what conditions satisfy equilibrium for a round dome of constant thickness he came to the conclusion that a round dome cannot be hemispheric because its keystone cannot exceed $0,382R$, where R is the radius of the dome. In other words, the generating arch of the dome cannot be more than around 52°, a nowadays well know result from membrane theory.

1.2.5 Eddy, 1878 and Lévy, 1888

Eddy in 1878 [Eddy, 1878] and later Lévy 1888 [Lévy, 1888], proposed graphical methods to perform the equilibrium analysis of masonry domes. While all the previous contributions of Bouguer, Poleni, Bossut and Mascheroni regarded the dome as a set of one-dimensional masonry arches, these methods represent a step forward in the comprehension of the stability of masonry domes as they explicitly take into account the bi-dimensional behaviour.

It is recognised that the first to account explicitly the bi-dimensional behaviour of domes was J. Wilhelm Schwedler, who provided a detailed graphical solution to the problem [Schwedler, 1859], [Schwedler, 1863], [Schwedler, 1866]. The dome was separated in two parts: in the upper part, over a specific hoop, all hoops were considered compressed, while in the lower part the hoops were considered in tension. This somehow foresaw the result obtained by Beltrami through the membrane theory [Beltrami, 1882]. Two major issues are present in the work of Schwedler: actual masonry doesn't resist tractions and the inversion point of the hoop forces, that separate the upper from the lower part cannot be predetermined but is an unknown of the problem. This last point is addressed first by Eddy's work (see Figure 1.6).

Although Eddy considers spherical domes, its graphical construction can be, *de facto*, applied to any dome of revolution. He initially describes his graphical method for thin metallic domes, for which he applies the membrane behaviour hypothesis. The membrane hypothesis allows for the determination of the stresses in the circumferential direction. Exploiting the geometrical properties of spherical caps, he expressed the weights graphically by means of segments and found the magnitude of the internal forces ensuring equilibrium by searching the force polygon for each portion of the dome. By repeating the procedure for a certain number of lunes, he obtains a curve, whose vertical tangent identifies a joint at around 52°. The hoops in the part of the dome above this joint are compressed, while the rest are subjected to tensile stresses. This analysis even if correct for metallic domes, has to be modified for masonry domes given the zero tensile strength of the material. In the analysis of masonry domes, Eddy graphically divides the dome in a series of part having

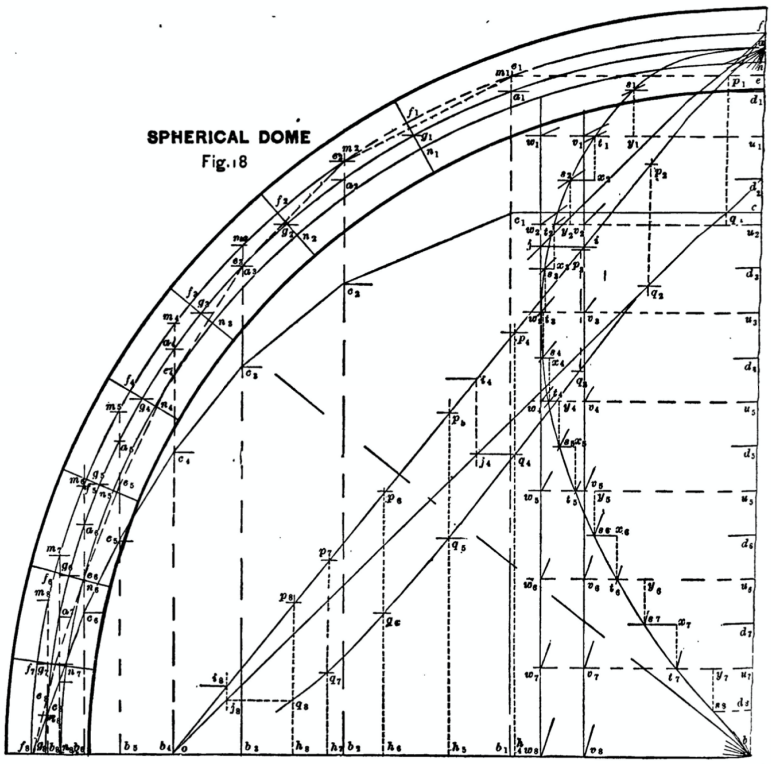

Figure 1.6: Eddy's graphical construction (from [Eddy, 1878]).

the same weight and, by exploiting the membrane analysis performed before and the geometrical properties of spherical sectors, the procedure finds the thrust line in the dome, in the hypothesis of null tensile strength. The methods allows to identify the 'neutral hoop' separating the upper portion, which behaves like a compressed membrane, from the lower part, which behaves as a series of one-dimensional, independent arches. In this way, the natural behaviour of masonry domes in which fractures along meridian planes in the lower part arise is accounted. In the procedure, it is assumed that the membrane coincides with the upper middle third limit, this fact denoting the influence of elasticity in the works of people dealing with masonry structures. In a certain sense, this method was the first to successfully put together the mono-dimensional approaches of the 18$^{\text{th}}$ century, which on the one hand neglected the bi-dimensional behaviour, with the membrane theory which, on the other hand, neglected the no-tension property of masonry.

Ten years later, Lévy extended Eddy's method to generic shaped domes of possibly varying thickness and with an oculus. Moreover, the loads acting on the structure could even include the weight of a lantern on top. In [Galassi et al., 2017] the procedure proposed by Lévy is accurately described and has been proposed in an analytical form. The method considers a lune comprised between two meridian planes and divided into an arbitrary number of blocks, evaluating the weights and the centroids by means of Guldin theorem (see Figure 1.7).

Lévy distinguished two steps: i) identification of the point of inversion then ii) drawing the thrust line in the lower part of the dome. In his procedure, which is not discussed here,

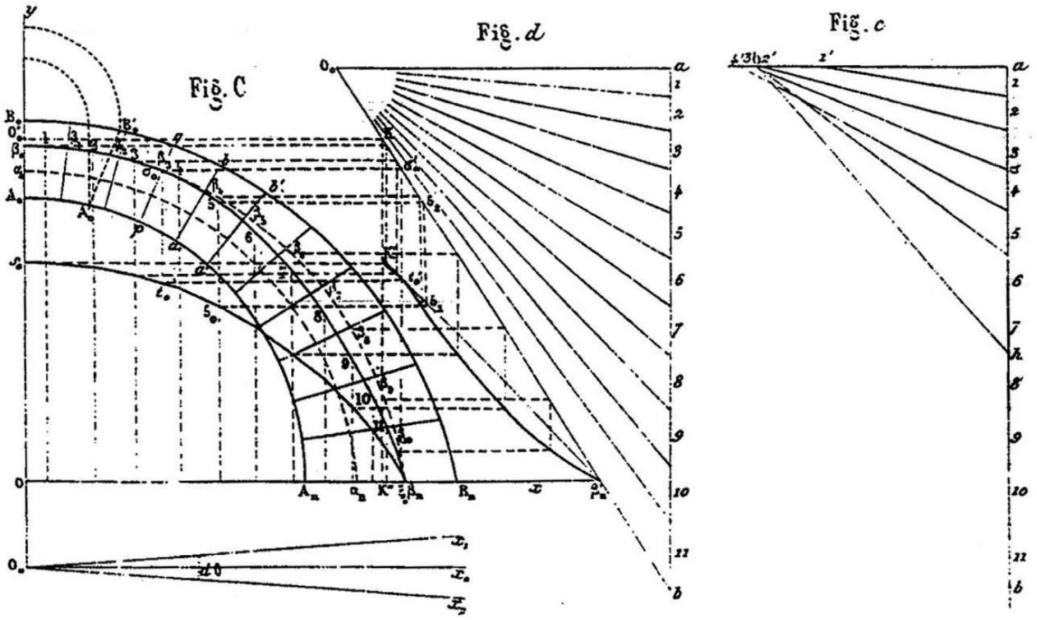

Figure 1.7: Lévy's graphical construction (from [Lévy, 1888]).

two hypotheses are made: the membrane in the upper part of the dome coincides with the exterior middle third limit (as for Eddy) and the thrust line passes through the exterior middle third point at the abutment.

1.2.6 Wolfe, 1921

In his treatise on graphic statics [Wolfe, 1921], Wolfe presents an analysis method to determine the stresses in masonry domes, that follows the same philosophy as Eddy and Lévy. He considers a spherical dome (see Figure 1.8) and divides it in a certain number of equally shaped lunes. Each lune is divided in an equal number of blocks, whose weight is estimated (approximately) through geometrical properties of the conical surface portion. Then, he graphically finds the 'neutral hoop' by assuming that the upper part of the dome behaves like a membrane that coincides with its middle surface (differently from Eddy and Lévy who assumed that the membrane coincides with the exterior middle third surface). He completes the analysis by finding the thrust line for the lower part (below the neutral hoop) and proposes design and verification criteria.

1.2.7 Heyman, 1966

With his 1966 fundamental work [Heyman, 1966] and in later publications dedicated to domes [Heyman, 1977], [Heyman, 2011], Jacques Heyman had the great merit of unifying under a single theory, that of limit analysis, all the historical contributions mentioned above. According to him, masonry is considered to behave according to three simple hypotheses: the material is unable to transmit tensile stresses, the compressive strength is unbounded and sliding failure cannot occur. The two last hypotheses find even greater justification in

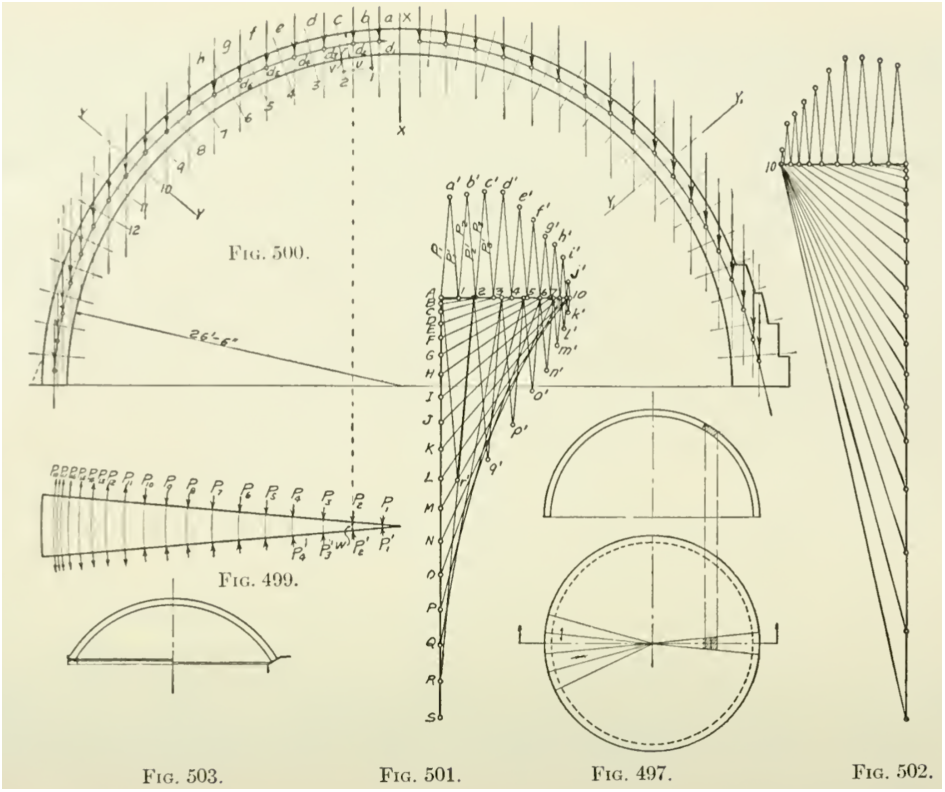

Figure 1.8: Wolfe's graphical construction (from [Wolfe, 1921]).

the case of historical monumental buildings, where the compressive levels are generally low compared to the strength of the material and where suitable construction techniques were usually adopted to avoid failure by sliding.

These assumptions on the material behaviour, which early builders already had an intuitive grasp of and which were endorsed at a more or less advanced level by the first static theories allow to prove the theorems of limit analysis. In particular, the static theorem of limit analysis states that: *"If any admissible equilibrium state can be found, that is, one for which a set of internal forces is in equilibrium with the external loads, and, further, for which every internal portion of the structure satisfies a strength criterion, then the structure is safe."*

This shed new light on the interpretation of the methods adopted in the past. Indeed, although some authors claimed to have found the 'real' state of a structure, by adopting subjective hypotheses to select a particular internal force distribution, the equilibrium state thus found is simply one of the possible equilibrium states for the structure. This means that, while the true state of the structure remains unknown, the existence of a statically admissible stress field enables to prove the safety of the masonry structure. The consequence is that every method adopted in the past is fully justified in their hypotheses and could be effectively exploited to check the safety of a masonry dome, by virtue of the static theorem.

1.3 Conclusive remarks

It is interesting to note how Heyman helped sparking new interest in the study of historical methods for the calculation of vaulted masonry structures. There are many recent contributions in which historical methods have been reinterpreted and translated into modern language, sometimes exploiting the possibilities offered by computers to perform otherwise excessively onerous operations, in order to propose their application in the analysis of real structures. In the already cited work of Galassi et al. [Galassi et al., 2017], the Lévy method is re-developed in analytical form and applied to some case studies. Another example is the Durand-Claye's method [Durand-Claye, 1866], [Durand-Claye, 1880], a graphical method aimed at determining the admissible values of the crown thrust magnitude and eccentricity, defining the so-called stability area. Aita et al. have proposed a modern version of Durand-Claye's method by translating the complex graphical construction into a suitable set of equations in terms of internal forces [Foce and Aita, 2003], [Aita et al., 2017c].

Methods based on the *Thrust Line Analysis* [Heyman, 1967], [Méry, 1840] have reached today the status of well-established methods for studying the stability of vaulted masonry structures which exploit the static theorem of limit analysis.

Although the lower bound theorem of limit analysis is a conservative approach to study masonry structures, the upper bound theorem of limit analysis is also exploited both for masonry arches (see for example [Di Carlo et al., 2018]) and for masonry vaults by using a Finite Element approach, as for example in [Milani et al., 2008]. Moreover, in [Tralli et al., 2014] limit analysis is acknowledged as the most reliable tool among the various modelling methods for masonry.

It is worth observing that historical methods for calculating masonry domes all refer, implicitly or explicitly, to axisymmetric domes. Although the most widespread form of masonry dome has, throughout history, been represented by the 'solid of revolution', in the Romanesque period and later, during the Renaissance, builders began constructing new domed structures with oval shapes, in either plan or elevation. These structures, which have already received special attention from the historical point of view [Huerta, 2007], [Chappuis, 1976], undoubtedly deserve as much attention from the perspective of their mechanical response - study made even more complicated by their complex geometry.

A final remark is in order here. Although all the historical methodologies for calculating vaulted masonry structures contributed to adding a piece of knowledge to the interpretation of the mechanics of masonry domes, it is interesting to observe how they never explicitly addressed the investigation of the structural response of domes subjected to vertical and horizontal loads, a topic that, most of the time, was completely ignored. This aspect, perhaps indicating the fact that the ancient builders did not care about this type of loads, is also interesting with regard to Heyman's hypotheses: if the hypotheses on the material made by Heyman find full justification for historical structures subject to their own weight and that of the elements they carry, the same thing cannot be said for certain when horizontal loads act on the construction.

Chapter 2

Analysis methods based on the safe theorem: the Thrust Network Analysis and the Thrust Surface Analysis

Within the framework of limit analysis, Thrust Network Analysis (TNA) and Thrust Surface Analysis (TSA) are two well established techniques that are used nowadays for effectively determining statically admissible stress fields in masonry vaults and domes. In this chapter, the two methods are presented, along with their hypotheses, and some considerations on their correlation and on the results obtained on a case study are discussed.

2.1 Discrete model: Thrust Network Analysis (TNA)

As already observed, all the historical approaches described in Chapter 1 are based on the infinitely resistant rigid block model. Since Heyman, several calculation methods have been brought back to the attention of the scientific community, and some of them received further development and extension also by exploiting the possibilities offered by modern computers. The case of *Thrust Network Analysis* (TNA) is probably the most emblematic. It is a discrete method that can be considered an extension of the Thrust Line Method, that is capable of accounting for the bi-dimensional behaviour of the structure.

The foundations of Thrust Network Analysis lie in the Force Density Method [Schek, 1974]. It was first formulated and applied to the study of masonry structures in 1999 by O'Dwyer [O'Dwyer, 1999] under the name of Force Network Method. The method has been further developed by P. Block in his Ph.D. thesis [Block, 2009] and in other works [Block and Ochsendorf, 2007], under the name of Thrust Network Analysis, by means of so-called reciprocal figures. The method has proven to be effective in analysing vaulted masonry structures and has been reformulated and extended in recent years, as well [Fantin and Ciblac, 2016], [Marmo and Rosati, 2017].

In the following, the TNA is presented according to the formulation of Fantin & Ciblac, which clearly highlights the mechanical interpretation of the thrust network. As said, the TNA models the dome as a system of rigid bodies, termed 'blocks', under unilateral contact conditions. Possible equilibrium states for the system are determined by looking for suitable

networks of compressed bars, the so-called thrust network (see Figure 2.1). The thrust network allows for graphically representing the system of forces acting on each block and can be considered fully analogous to the funicular polygon that is used to trace the thrust line for stability assessment of masonry arches. This issue is examined in following sections, as it is relevant for our investigation. Three hypotheses are commonly made in standard

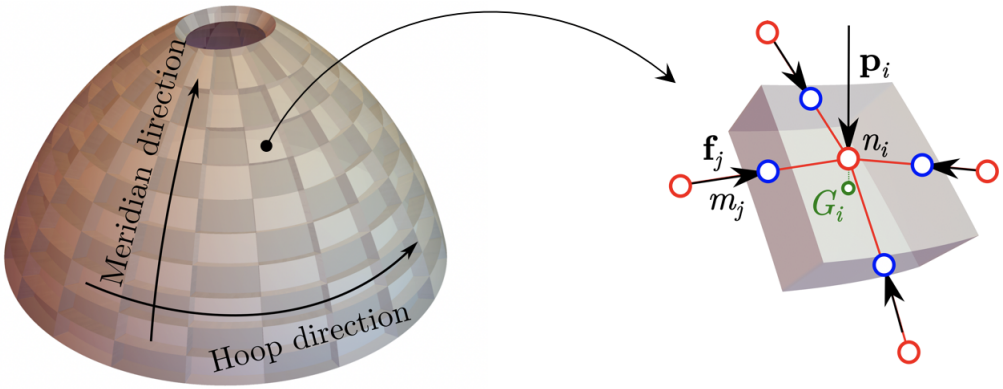

Figure 2.1: Rigid blocks model: equilibrium of a generic block. The red dots are the nodes of the network, the blue dots on the block's sides are the centres of pressure (defined later in the text).

TNA applications. The first is that all the forces acting on every single block meet at one point, that is, to each block there corresponds one node of the network. This assumption narrows the set of possible equilibrium states that are actually investigated but enables automatic fulfilment of the moment equations. The set of forces is required to fulfil Heyman's hypotheses only along the block interfaces, that is, it is required that a compressive force (nil at least) be transmitted across each joint and that the line of action of the force intersects the same joint. Moreover, no sliding between blocks is allowed since the joints' orientation and friction coefficient in real masonry are such that Coulomb criterion is generally satisfied for vertical loads.

The second hypothesis concerns the loads that may act on each network node. Each external nodal force is by hypothesis vertical, thus representing the weight of the block or some superposed element. In recent years, the method has been extended to the case of horizontal loads [Block, 2009], [Marmo and Rosati, 2017], but such extension requires some specific adaptations.

The third hypothesis is that the displacements are small enough so that equilibrium can be written in the reference configuration.

In the general case, an infinite number of different networks can be found that are in equilibrium with the same external loads. In order to select one particular network among all the possible choices an optimisation procedure is usually performed by choosing a suitable cost function. When dealing with safety level assessment of vaulted masonry structures that comply with the Heyman hypotheses, TNA can be successfully employed by choosing the *geometrical safety factor* (GSF) as the cost function to be maximised (the interested reader can refer to [Fantin and Ciblac, 2016] for the mathematical details). As is well known, the concept of a geometrical safety factor was first introduced by Heyman [Heyman, 1966] as a

measure of safety for masonry arches and is defined as the ratio between the actual thickness of the arch and the minimum thickness for which it is still possible to find at least one statically admissible stress field (that is, the minimum thickness within which at least one thrust line is contained). The notion of the geometrical safety factor is easily extended to the case of domes and is related to the distance of the centre of pressure from the dome mean surface.

2.1.1 Formulation of the method

Here the outline of the standard TNA is illustrated in a synthetic but complete way, as presented in [Fantin and Ciblac, 2016].

Geometry

The centroids of the blocks, in which the structure has been discretised, form a weighted point cloud, and are connected by a branch for each joint separating two blocks. The resulting network is what is called mass network. In this way, each branch connects the nodes of the adjacent blocks in contact at the corresponding joint. The contact force at the joint has the same direction as the branch. Contrary to the original formulation of Block, the connectivity of the network is deduced from the performed discretisation, and is not chosen a priori.

Equilibrium

Let x, y, z be the Cartesian components of the nodes and u, v, w the Cartesian components of the branches (the coordinate difference) and L_H their horizontal length (i.e. the length projected on the horizontal plane). Let $\boldsymbol{U}, \boldsymbol{V}, \boldsymbol{W}$ denote the diagonal matrices of $\boldsymbol{u}, \boldsymbol{v}, \boldsymbol{w}$. In this section a superscript * identifies all the dual quantities. For example, while u denotes the coordinate along x-axis of the generic branch, u^* denotes the x-components of the force in that branch. The matrix $\boldsymbol{C}$ denotes the $m \times n$ branch-node connectivity matrix, where m is the number of branches and n the number of nodes. This matrix can be separated in the $\boldsymbol{C}_i$ $m \times n_i$ and $\boldsymbol{C}_b$ $m \times n_b$ matrices, where n_i is the number of interior nodes and n_b is the number of boundary nodes, and where $\boldsymbol{C} = [\boldsymbol{C}_i | \boldsymbol{C}_b]$. Then, the equilibrium equations in the horizontal plane, respectively, along x and y axis can be written as

$$\begin{aligned} \boldsymbol{C}_i^\mathsf{T} \boldsymbol{u}^* &= \boldsymbol{0}, \\ \boldsymbol{C}_i^\mathsf{T} \boldsymbol{v}^* &= \boldsymbol{0}. \end{aligned} \tag{2.1}$$

Since the branches are parallel in the form diagram and the force diagram, let $\boldsymbol{\zeta}$ be the m-vector of proportionality between the branch lengths in form and force diagrams. Then the same horizontal equilibrium equations can be written as

$$\begin{bmatrix} \boldsymbol{C}_i^\mathsf{T} \boldsymbol{U} \boldsymbol{L}_{\boldsymbol{H}}^{-1} \\ \boldsymbol{C}_i^\mathsf{T} \boldsymbol{V} \boldsymbol{L}_{\boldsymbol{H}}^{-1} \end{bmatrix} \boldsymbol{\zeta} = \boldsymbol{K} \boldsymbol{\zeta} = \boldsymbol{0}. \tag{2.2}$$

Since there are $2n_i$ equilibrium equations and m unknown, the system in indeterminate. One can then choose $m_{dof} = m - r_K$ parameters, being r_K the rank of $\boldsymbol{K}$, that can be

called degrees of freedom of the system. After reordering the system in order to separate the parameters $\boldsymbol{\zeta}_{dof}$ from $\boldsymbol{\zeta}_{unk}$, the horizontal equilibrium can be written as follows

$$\boldsymbol{\zeta}_{unk} = \mathbf{K}_{unk}^{-1}\mathbf{K}_{dof}\boldsymbol{\zeta}_{dof} = \mathbf{0}. \tag{2.3}$$

The equilibrium along vertical direction z can also be written in matrix form as

$$\boldsymbol{C}_i^{\mathsf{T}}\boldsymbol{w}^* = -\boldsymbol{p}_z. \tag{2.4}$$

Moreover, it is possible to obtain the relations between the vertical loading $\boldsymbol{p}_z$ and the position of the boundary nodes $\boldsymbol{z}_b$, also be considerable as degrees of freedom

$$\boldsymbol{D}_i\boldsymbol{z}_i = -\boldsymbol{p}_z - \boldsymbol{D}_b\boldsymbol{z}_b, \tag{2.5}$$

where

$$\begin{aligned} \boldsymbol{D}_i &= \boldsymbol{C}_i^{\mathsf{T}}\boldsymbol{L}_H^{-1}\boldsymbol{L}_H^*\boldsymbol{C}_i, \\ \boldsymbol{D}_b &= \boldsymbol{C}_i^{\mathsf{T}}\boldsymbol{L}_H^{-1}\boldsymbol{L}_H^*\boldsymbol{C}_b. \end{aligned} \tag{2.6}$$

Optimisation procedure

Firstly, a set of values is chosen for the degrees of freedom of the branches $\boldsymbol{\zeta}_{dof}$ so that horizontal equilibrium equations give all horizontal forces in branches $\boldsymbol{\zeta}$. Then, another set of values is chosen for the degrees of freedom of the boundary nodes $\boldsymbol{z}_b$ so that also vertical equilibrium equations give the vertical positions of all nodes $\boldsymbol{z}$. Of course, an optimisation procedure must be enforced in order to choose the best value of the parameters according to a chosen cost function. The type of mathematical programming problem depends on the cost function chosen. For convenience, a quadratic function can be used for the cost function, linked to the concept of geometrical safety factor

$$cf = \sum(z_i^2 - z_m^2), \tag{2.7}$$

where z_m is the position of the mass network nodes. Obviously, the optimisation problem is constrained, since to enforce Heyman hypotheses it must be

$$z_i^{intrados} \leq z_i \leq z_i^{extrados} \tag{2.8}$$

in order for the nodes to be inside the masonry.

Implementation

For the applications described in the following, the TNA is carried out by exploiting the MaNACoH software (from `http://bestrema.fr/manacoh/`) [Fantin, 2017] to search for the network that maximises the geometrical safety factor under the constraint that all branches are compressed and inside the thickness of the masonry.

2.1.2 Some remarks on the method

As is well known, TNA can be conceived without explicitly referring to the blocks' arrangement within the dome. However, when considering thrust networks totally independent from the blocks' arrangement, the determination of a set of admissible compressive forces in all branches represents in general only a necessary condition for the stability of the dome. On the contrary, one of the strongest points of TNA as formulated by Fantin & Ciblac is the possibility of explicitly considering the joint orientations in the masonry as well as different strength criteria for the joints. This is an important point because, as mentioned, joints' orientation affects the geometrical safety factor and thus estimation of the safety level of the structure. In this regard, note that, while in the case of stone masonry the set of blocks as well as the orientation of the joints may closely follow the actual stereotomy of the construction, this is not usually possible when dealing with brick masonry. In this latter case, the number of blocks needed to accurately reproduce the brick pattern would generally be too large, and in common TNA applications a set of virtual blocks is used, each corresponding to a given portion of the brick masonry.

Apart from the explicit consideration of the joints in the formulation of TNA, the paper from Fantin & Ciblac [Fantin and Ciblac, 2016] proposes also an extension of the original method that is capable of removing a strong limitation. Indeed, by the introduction of partial branches, it overpasses the condition of the intersection of all forces in one point and thus extends the equilibrium possibilities for the structure. This point is not deepened here, but the interested reader can refer to [Fantin and Ciblac, 2016] and [Fantin, 2017].

2.2 Continuum model: Thrust Surface Analysis (TSA)

In the following, reference is made to the first works to present an exhaustive account of the method by Angelillo and co-workers [Angelillo and Fortunato, 2004], [Angelillo et al., 2013]. The method models the dome as a simple no-tension three-dimensional body, often referred

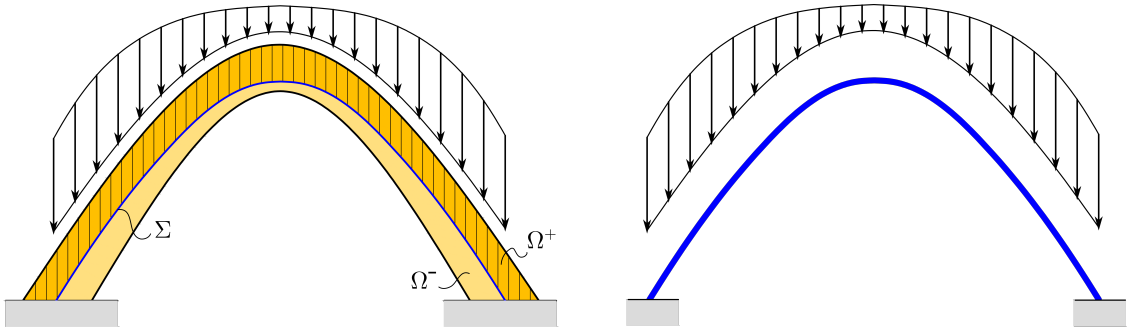

Figure 2.2: Continuum model: normal rigid no-tension material.

to as a *masonry-like* continuum or *no-tension masonry material model*, already presented in Chapter 1.

It is worth observing that, strictly speaking, in a 3D no-tension continuum an admissible stress state is represented by a negative semidefinite tensor. This is quite a limiting constraint, and strictly speaking, equilibrium under such a condition could be assured only

when very particular loading distributions are taken into consideration. Thus, in order to enable using the method, the actual load distribution is generally approximated by means of a suitable distribution that is considered equivalent to the actual one. More precisely, the body loads within the dome are set equal to zero and are replaced by a system of surface loads distributed on the 'extrados' of the structure; said system is statically equivalent to the body forces. In addition, stress discontinuities are allowed across a surface internal to the body, as is the development of singularity in the stress fields.

The discontinuity surface Σ (see Figure 2.2) ideally subdivides the dome into a reactive and a non-reactive part. In the reactive upper part, denoted by Ω^+, a uniaxial compressive state is present. The lower part, denoted by Ω^-, is stress-free and it is thought to be inert. The discontinuity surface is called the *thrust surface* and can be defined as the middle surface of a thin shell under a membrane stress state, wholly contained within the thickness of the masonry, and which in some sense represents the resistant part of the dome [Barsi et al., 2022]. The membrane is loaded by the jump in the body stress field across the two regions Ω^+ and Ω^-. In analogy to TNA, the method searches for a suitable thrust surface, wholly contained inside the dome thickness, that represents a membrane in equilibrium with the external loads. For the admissibility of the internal force field, the principal membrane forces must be compressive.

In the general case, an infinite number of admissible membranes can be found in equilibrium with the external loads. Hence, as happens in TNA, when performing TSA as well, some criterion has to be established in order to select one membrane from the many possible choices.

2.2.1 Formulation of the method

There are different solution strategies for finding an admissible thrust surface, most of which refer to the so-called Pucher formulation of the equilibrium problem of a membrane [Pucher, 1934]. While the thin shell model is described in detail in Chapter 3, only the equilibrium equations of a membrane, which are necessary for performing TSA, are recalled here. They can be written as (see [Angelillo and Fortunato, 2004])

$$\begin{cases} \dfrac{\partial(\sqrt{a}\,t^{xx})}{\partial x} + \dfrac{\partial(\sqrt{a}\,t^{xy})}{\partial y} + \sqrt{a}\,q^x = 0 \\ \dfrac{\partial(\sqrt{a}\,t^{xy})}{\partial x} + \dfrac{\partial(\sqrt{a}\,t^{yy})}{\partial y} + \sqrt{a}\,q^y = 0 \\ \sqrt{a}\,t^{xx}\dfrac{\partial^2 \mathfrak{z}}{\partial x^2} + 2\sqrt{a}\,t^{xy}\dfrac{\partial^2 \mathfrak{z}}{\partial x \partial y} + \sqrt{a}\,t^{yy}\dfrac{\partial^2 \mathfrak{z}}{\partial y^2} - \sqrt{a}\,\dfrac{\partial \mathfrak{z}}{\partial x}q^x - \sqrt{a}\,\dfrac{\partial \mathfrak{z}}{\partial y}q^y + \sqrt{a}\,q^z = 0, \end{cases} \tag{2.9}$$

where a is the determinant of the metric tensor, $t^{xx}, t^{xy} = t^{yx}, t^{yy}$ are the membrane force components with respect to a Cartesian reference system, q^x, q^y, q^z are the Cartesian components of the external load vector and $\mathfrak{z}(x, y)$ is the function describing the membrane parametrised *a la Monge* (i.e. x and y are the plane coordinates). Introducing the pseudo-forces, defined as $s^{xx} = \sqrt{a}\,t^{xx}$, $s^{xy} = s^{yx} = \sqrt{a}\,t^{xy}$, $s^{yy} = \sqrt{a}\,t^{yy}$, and denoting with $\mathbf{p} = \sqrt{a}\,\mathbf{q}$

the surface load per unit area on the projected surface, one can write

$$\begin{cases} \dfrac{\partial s^{xx}}{\partial x} + \dfrac{\partial s^{xy}}{\partial y} + p^x = 0 \\ \dfrac{\partial s^{xy}}{\partial x} + \dfrac{\partial s^{yy}}{\partial y} + p^y = 0 \\ s^{xx}\dfrac{\partial^2 \mathfrak{z}}{\partial x^2} + 2s^{xy}\dfrac{\partial^2 \mathfrak{z}}{\partial x \partial y} + s^{yy}\dfrac{\partial^2 \mathfrak{z}}{\partial y^2} - \dfrac{\partial \mathfrak{z}}{\partial x}p^x - \dfrac{\partial \mathfrak{z}}{\partial y}p^y + p^z = 0, \end{cases} \tag{2.10}$$

which represent the equilibrium equations of a membrane in *Pucher form*. The problem can be simplified by resorting to the well-known *Pucher stress function*, i.e., a proper potential function from which the pseudo-stresses can be derived. By restricting the analysis to the simpler case in which only vertical loads are present ($p^x = 0, p^y = 0, p^z = -p(x, y)$), the Pucher stress function reduces to the *Airy stress function*, $\phi(x, y)$, defined in terms of pseudo-stresses as

$$s^{xx} = \frac{\partial^2 \phi}{\partial y^2}, \quad s^{xy} = s^{yx} = -\frac{\partial^2 \phi}{\partial x \partial y}, \quad s^{yy} = \frac{\partial^2 \phi}{\partial x^2}. \tag{2.11}$$

By adopting the Airy stress function, the first two equilibrium equations reduce to identity, and the problem is fully described by the following second order partial differential equation

$$\frac{\partial^2 \mathfrak{z}}{\partial x^2}\frac{\partial^2 \phi}{\partial y^2} - 2\frac{\partial^2 \mathfrak{z}}{\partial x \partial y}\frac{\partial^2 \phi}{\partial x \partial y} + \frac{\partial^2 \mathfrak{z}}{\partial y^2}\frac{\partial^2 \phi}{\partial x^2} = p, \tag{2.12}$$

where $p(x, y)$ is the external vertical load. Among the solution strategies one can cite, without any claim to completeness, [Angelillo et al., 2013], [Fraddosio et al., 2020], [Barsi et al., 2022].

Implementation

In the applications that follow, the TSA is carried out by selecting a class of surfaces, whose analytical expression is chosen a priori and by performing the membrane analysis in order to obtain the membrane forces in equilibrium with the external loads. The admissibility conditions are then checked. If the internal force field thus determined results not compatible with the material hypotheses a different class of surface is selected and the procedure iterated.

For the numerical solution of the differential equations, either in form of equations (2.9) or equation (2.12), a finite difference scheme is exploited. The scheme, which is not illustrated here, follows the one presented in Subsection 4.4.3.

2.2.2 Some remarks on the method

Application of TSA is generally more involved than TNA, but it has the advantage of defining a generalised stress field that is statically admissible at any point of the continuum body. In other words, the constraints on the internal forces are enforced at every internal point of the structure, while in TNA they are imposed only along the interfaces between blocks.

It should be noted that TSA is unable to account for the actual texture of the masonry, as the method does not involve any explicit hypothesis about joints' orientation. For this reason,

in order to carry out a proper comparison between TNA and TSA, the joints' orientation in TNA must be suitably chosen, as will be explained in the following. Also note that in TNA the load distribution on the network nodes depends on the shape of the blocks, and thus on the orientation of the joints, while in TSA the load acting on each portion of the membrane is simply given by the weight of the corresponding portion of the continuum body overlying the membrane in the vertical direction.

2.3 Comparison between TNA and TSA

One question that arises spontaneously is whether these two methods are somehow related and, if so, under what hypotheses the correlation holds. Although this issue has already been addressed, even in recent years [Fraternali, 2010], [Marmo et al., 2018], [Nodargi and Bisegna, 2021], the relation between TNA and TSA is not fully understood, and these two methods are often considered in the literature as nearly equivalent without clearly specifying in what sense. In this section, the correlation between the two methods is analysed with reference to a case study, highlighting their similarities as well as their differences. The first objective is to examine the conditions under which it is effectively possible to establish a proper correlation between TNA and TSA. Moreover, since both methods search for statically admissible stress fields, the second objective is to investigate whether a method combining thrust network and thrust surface can be effectively set up to find equilibrium states for a given structure, as specified in the following. The study presented here is performed by referring to a real case study, the dome of Pisa Cathedral, on which some investigations of the mechanical response have recently been carried out [Aita et al., 2017d], [Aita et al., 2019], [Bennati et al., 2020], [Barsi et al., 2022]. This magnificent structure, which is characterised by a very peculiar shape, highlights the capability of the two methods to deal with complex geometries beyond axisymmetric domes.

2.3.1 Properly comparing TNA and TSA: what about joints' orientation?

A point that is seldom highlighted is that in order to properly perform a comparison between TNA and TSA, the joints' orientation assumed in the analysis cannot be set freely. The following delves more deeply into this statement, starting, for the sake of simplicity, with some preliminary considerations regarding the case of a masonry arch. Let's consider a plane masonry arch as a system of rigid blocks separated by a finite number of joints. As is well known, the *funicular polygon* is a simple graphic static construction that represents the system of forces acting on each block. The intersection points of each branch of the funicular polygon with the corresponding joint are called *centres of pressure* and represent the points of application of the internal forces acting on each block. If all the centres of pressure are inside the thickness of the masonry, no tensile stresses are needed to equilibrate the loads, and the structure can be considered safe. The polygon connecting all the centres of pressure is called the *polygon of the centres of pressure*. In the case the arch is stable, an infinite number of admissible funicular polygons may be traced. Note that the funicular polygon

may even exit the thickness of the masonry, provided that the centres of pressure all remain inside the joints.

According to Méry [Méry, 1840], the locus of the centres of pressure when the number of joints goes to infinite is the *thrust line* of the arch. At the same limit, the nodes of the funicular polygon become a curve as well, and is called *funicular curve*, which can be considered, by definition, a cable in equilibrium with the load distribution, this latter being known once and for all when the geometry of the blocks is known (whether their dimensions be finite or infinitesimal). These two curves are not necessarily coincident, as clearly pointed out also by Heyman [Heyman, 2009]. Indeed, due to the joints' orientation, the points of intersection between the funicular curve and the joints do not, in general, coincide with the centres of pressure (see Figure 2.3) and, as a consequence, the line of action of the force acting on each joint is not necessarily tangent to the thrust line. Milankovitch [Milankovitch, 1907] showed that the thrust line coincides with the funicular curve, and therefore the forces acting on each block are tangent to the thrust line if and only if the joints are vertical. By following the same line of reasoning, it can be shown that the thrust line coincides with the funicular curve if the joints have the same direction as the external loads. For an arch under gravitational loads, only if the joints are vertical can the thrust line be considered a cable in equilibrium with the same external loads as those acting on the arch (see Figure 2.4).

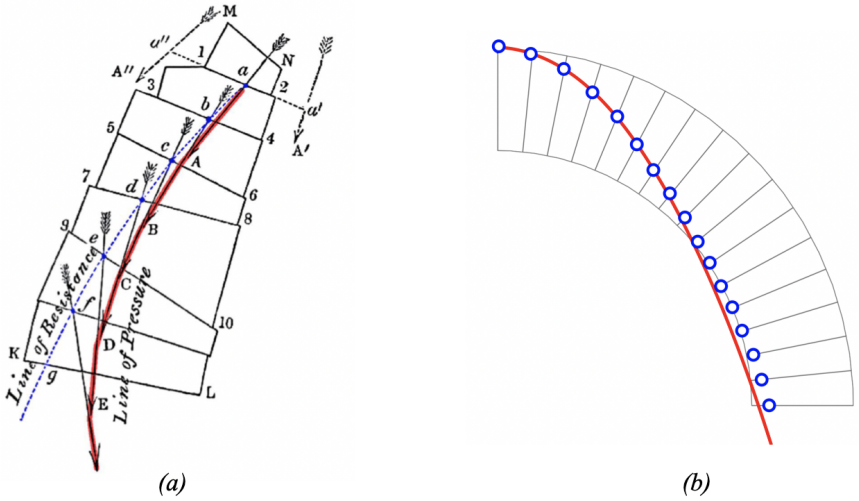

Figure 2.3: On the left, Moseley's example [Moseley, 1856] showing the difference between the funicular polygon (line of pressure) and the polygon of the centres of pressure (line of resistance). On the right, another case in which the funicular polygon (in red) and the centres of pressure (blue dots) are distinct near the springing; taken from [Fantin and Ciblac, 2016] (colours added to the originals).

Note that, unlike in TNA, for the arch no hypothesis is needed to assure that all the forces acting on each block intersect at one point, because it is always necessary for three forces to meet at one point in order for the equilibrium to be fulfilled. Hence, in the ideal limit case in which the number of blocks goes to infinity, any admissible distribution of internal forces corresponds to a line of thrust wholly contained within the arch. Also observe that, if the funicular polygon, which can be considered a plane truss carrying the external

load, is compressed, the axial force in the cable obtained by the limit operation will also be compressive.

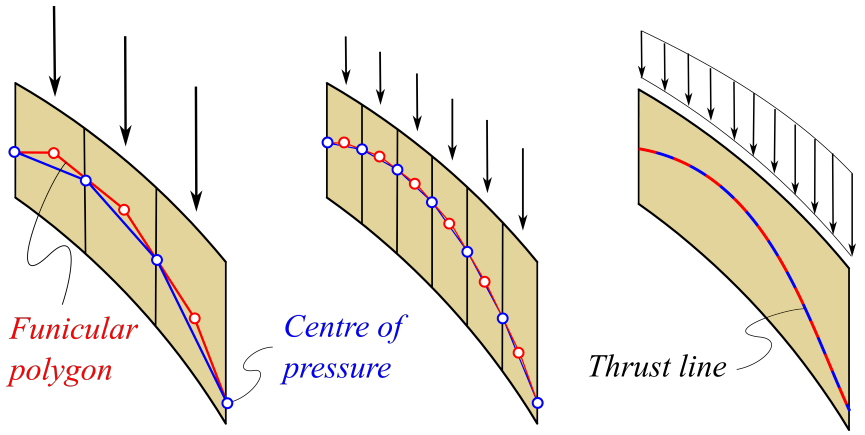

Figure 2.4: The *thrust line* is defined once the joints' orientations are chosen. In the case of vertical joints, the funicular polygon (red) and the polygon of the centres of pressure (blue) tends to a single curve when the number of the blocks increases: the thrust line.

In analogy to the plane arch, one can consider a masonry dome as a system of rigid blocks. As already stated, the thrust network is the extension to three dimensions of the funicular polygon [Fantin and Ciblac, 2016].

By keeping the hypothesis that all the forces acting on each block meet at one point, in the limit case of infinite blocks the nodes of the network will become a surface, which can be considered a membrane in equilibrium with the external loads, which are known once and for all when the geometry of the blocks is known. In the same limit operation, the centres of pressure will also become a surface, the thrust surface, which is, in general, different from the membrane (see Figure 2.5). It's worth observing that this definition of thrust surface is conceptually different by that given before in the case of TSA, as it refers to a different mechanical model (rigid blocks).

By reasoning fully analogous to that illustrated for the arch, it is not difficult to conclude that the two definitions of thrust surface coincide, and the thrust surface becomes a membrane when all the joints between the blocks are parallel to the external load. Moreover, only in such case can the membrane equilibrium of a thrust surface be formally described by the same set of equations used in TSA, and therefore the two methods coincide at limit. However, unlike the case of arches, even if the internal forces in the network are all compressive, it is by no means assured that the principal stresses in the corresponding membrane will be compressive. On the contrary, as long as all the joints are parallel to the load, an admissible thrust surface always corresponds to a statically admissible distribution of internal forces. In other terms, if it is possible to find a compressed membrane in equilibrium with the external loads that is entirely contained inside the thickness of the masonry, then the dome is safe.

An interesting aspect that deserves to be highlighted is that an admissible thrust surface defines a statically admissible distribution of internal forces not only in the limit case, but even in the case in which the dome is divided into a finite number of blocks. In other words,

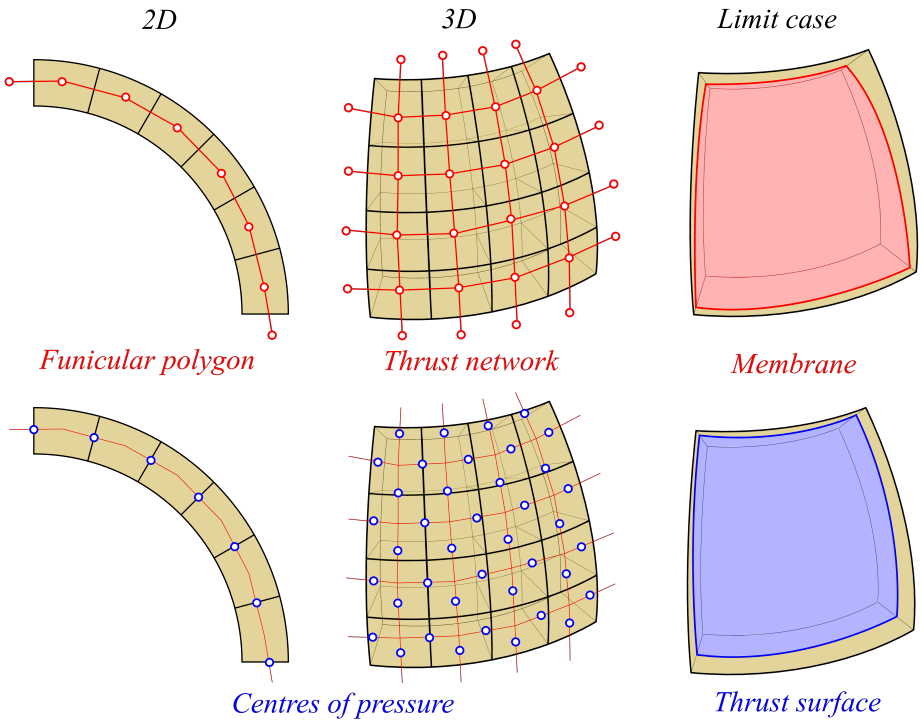

Figure 2.5: Difference between membrane and thrust surface.

if the dome is thought of as a system of blocks, the forces acting on each block can be evaluated by assessing the resultant of the membrane forces along the joints (see Figure 2.6). This offers a way to compare the internal force distributions evaluated by both TNA and TSA, as shown in the following section. It is also interesting to notice that, because of the curvatures the centres of pressure do not necessarily belong to the membrane (see the orange dots in Figure 2.6), as it is instead the case for infinitesimal blocks.

In conclusion, the important issue that deserves stressing is that, while the thrust network is a discretised version of a membrane, in general a thrust surface is not a membrane. Moreover, when gravitational loads are accounted for, such as for dome's self-weight, joints need to be considered vertical for the thrust surface to become a membrane and to be approached by the limit of a sequence of thrust networks. Hence, a proper comparison between TNA and TSA can be made if and only if the joints between the blocks are vertical.

2.3.2 Correlation between thrust network and thrust surface

The present section illustrates in some detail the correlation intervening between thrust networks and thrust surfaces. The comparison is performed by referring to a real case study: the dome of Pisa Cathedral.

The main goal of the comparison is to check the correspondence between the equilibrium states defined by thrust network and thrust surface. In particular, the aim is to investigate whether an admissible network, whose configuration is optimised by the TNA, can suggest the shape of an admissible thrust surface. Whether this could be effectively found, it would

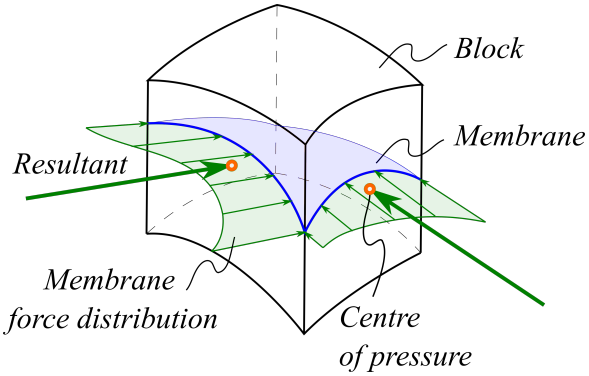

Figure 2.6: Membrane force resultants on joints.

be a good starting point for subsequent optimisation of the thrust surface by the TSA which usually requires the numerical solution of a partial differential equations set (see, for example, [De Chiara et al., 2019]). Based on the criterion that the surface is as close as possible to the network's centres of pressure, the procedure involves the following steps:

1. an optimised thrust network is determined by searching for the set of admissible networks by means of the TNA method;

2. three smooth surfaces, each belonging to a predetermined class (namely, elliptical paraboloid, hyperbolic cosine function and ellipsoid), are determined that are as close as possible to the centres of pressure of the optimised network;

3. the three approximating surfaces are considered as thrust surfaces, and their admissibility is checked by performing a membrane analysis;

4. the internal force distribution in the thrust surfaces is compared to that in the thrust network.

The case study: the dome of Pisa Cathedral

The analyses presented in the previous sections are now to be applied to the case of the dome of Pisa Cathedral, a 12^{th}-century masonry construction of singular historical and architectural value (see Figure 2.7). The dome has a peculiar shape, characterised by an oval base and pointed profile (see Figure 2.8), features that represent an original solution in coeval Romanesque architecture and make it an interesting case study with regard to building techniques and structural response. The interested reader can refer to [Sanpaolesi, 1959] and [Smith, 1984] for more information through an historical overview of the building's conception, design and construction. The dome has a total height of about 12 meters and its base can be inscribed in a rectangle of about 17 by 14 meters (see Figure 2.9).

In order to provide a suitable and reliable description of the complex geometry of the dome, the shape of both the intrados and extrados surfaces have been carefully reconstructed by means of laser-scanner survey and have been approximated by means of regular surfaces, allowing for as simple as possible analytical expressions [Bennati et al., 2020], [Barsi et al.,

Figure 2.7: Pisa Cathedral.

Figure 2.8: The dome of Pisa Cathedral.

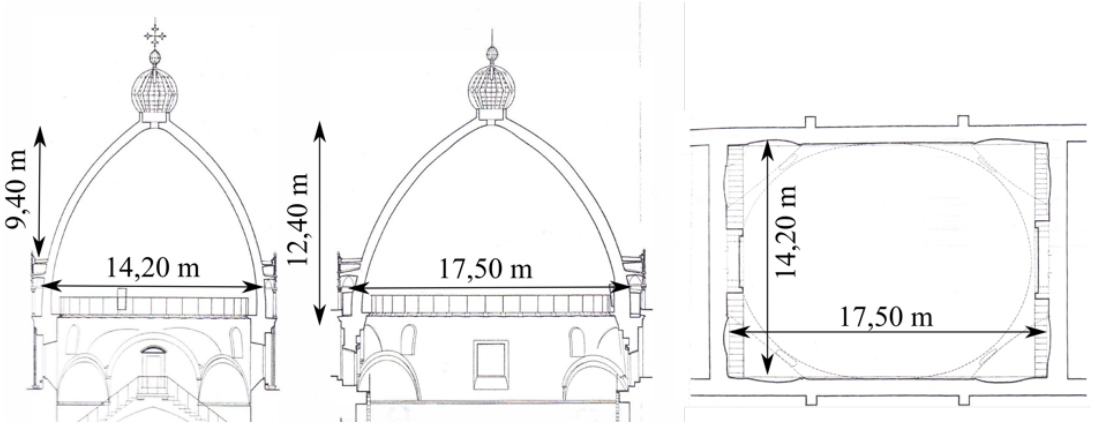

Figure 2.9: Dome geometry (from [Sanpaolesi, 1959], dimensions added to originals).

2022]. The parametric equations of the ideal surfaces are expressed in terms of the parameters (α, z) as follows:

$$\begin{cases} x_1(\alpha, z) = (d + \sqrt{e^2 - z^2}) \cos \alpha \\ x_2(\alpha, z) = (f + \sqrt{g^2 - z^2}) \sin \alpha \\ x_3(\alpha, z) = z \end{cases} \tag{2.13}$$

in which $0 \leq \alpha \leq 2\pi$ and $3\,\text{m} \leq z \leq 12\,\text{m}$. The constants d, e, f and g take different values for the intrados and the extrados surfaces.

In 1956, during the restoration works promoted by Sanpaolesi [Sanpaolesi, 1959] it was verified that the entire dome of Pisa Cathedral is made of four-head brick masonry and that each layer of bricks is almost normal to the dome's middle surface (see Figure 2.10-left). These findings have been confirmed by the visual inspections performed during the latest restoration works carried out between 2016 and 2018 [Aita et al., 2017d] (see Figure 2.10-right).

The TNA solution

As a first step of the investigation, an optimised admissible thrust network is determined using TNA. In this regard, as already specified, the MaNACoH software (from `http://bestrema.fr/manacoh/`) [Fantin, 2017] is exploited to search for the network that maximises the geometrical safety factor under the constraint that all branches are compressed. The dome is subdivided into 10 and 20 parts in the meridian and hoop direction, respectively. By using the equations (2.13) of the dome intrados and extrados, the shape of each block is easily determined. An overall number of 200 blocks and 360 branches is considered. Each block corresponds to some 500 bricks at the dome's base, and 250 bricks at its top. For the reason illustrated in the previous section, the joints between blocks are all vertical. The optimal admissible thrust network obtained in this way is shown in Figure 2.11 and corresponds to a geometrical safety factor equal to 1.93.

The vertical joints assumed in the TNA do not correspond to the actual joints in the masonry; nonetheless, this particular orientation has been assumed in order to assure proper

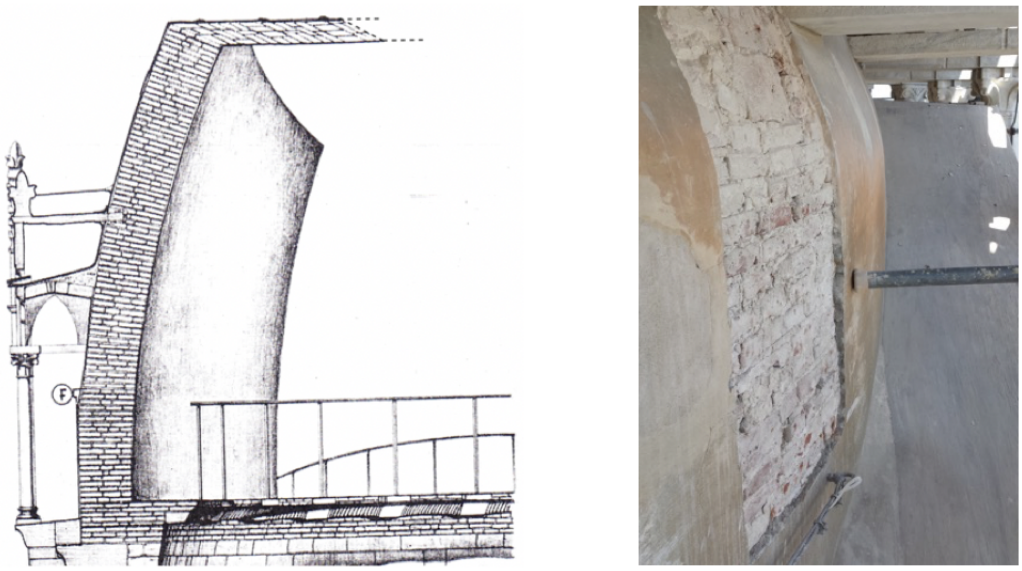

Figure 2.10: Joints' orientation inside the dome of Pisa Cathedral. On the left, a drawing adapted from [Sanpaolesi, 1959]. On the right, a photo taken by the author during the 2017 restoration works.

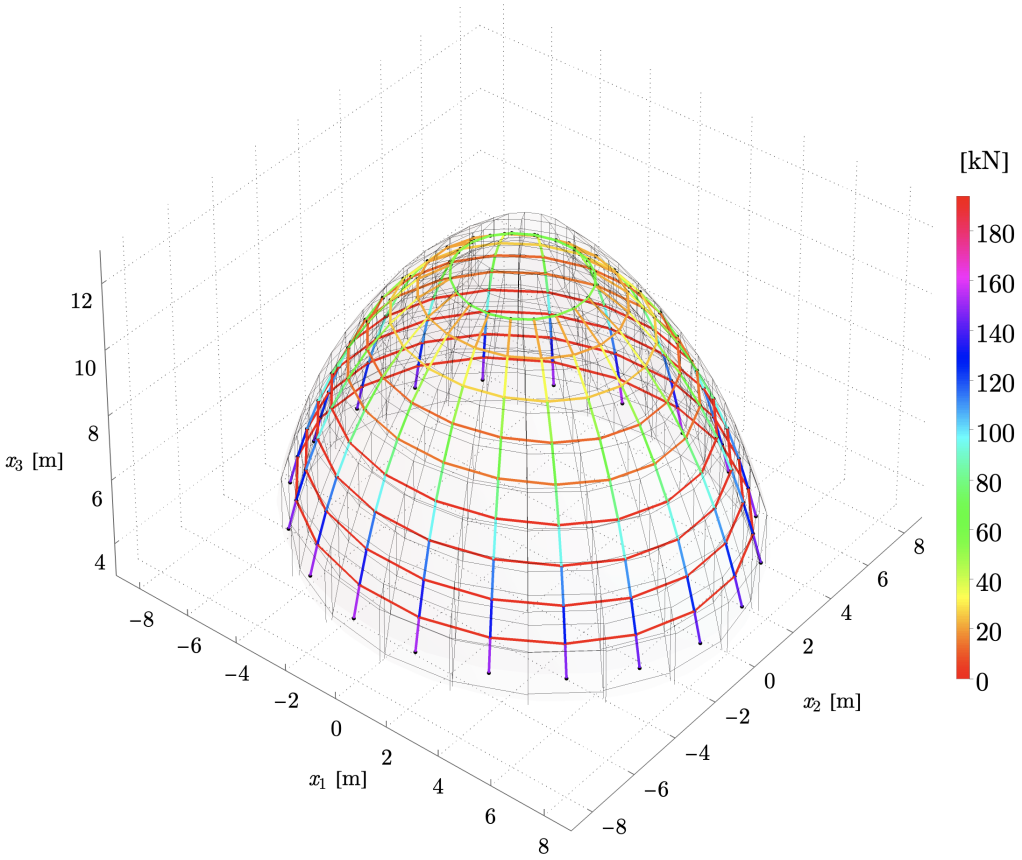

Figure 2.11: TNA: Thrust Network obtained with the MaNACoH software (vertical joints).

comparison between TNA and TSA. The vertical joints, rather than actual material interfaces, should be considered merely as ideal surfaces along which the admissibility conditions are checked for the internal forces. In this regard, it is worth noting that this procedure does not lead to an overestimation of dome safety: it is an easy task to verify that in the case at hand (although not in general) if the vertical joints are compressed, so will the actual joints.

As a last remark, naturally, different geometric safety factors could be obtained by considering different joints' inclinations in the TNA. By way of example, by assuming joints orthogonal to the dome middle surface, a slightly higher geometrical safety factor, equal to 2.21, would result. This difference, no matter how insignificant, could not be neglected if our aim were to evaluate the maximum geometric safety factor. However, as already stated, our aim here is to compare TNA with TSA, a task that can be done properly only if vertical joints are considered in the TNA.

The thrust surfaces suggested by TNA

The TNA solution described in the previous section is used as the starting point for obtaining a corresponding thrust surface. In this regard, the centres of pressure defined by the admissible thrust network are considered, and a suitable surface that best approximates the point cloud is searched. The best approximating surface is searched for amongst three predefined classes of smooth surfaces. In each class, some parameters c_k are left to be specified, and the best values of these parameters are obtained by minimising the sum of the squares of the distances between each centre of pressure and the corresponding point on the surface. The minimisation is performed numerically by means of the *Mathematica*® *"NMinimize"* function. As the geometric fitting problem is strongly nonlinear and computationally burdensome, in place of the true distance a close approximation is considered, which is easier to determine. Each centre of pressure P_i is projected vertically onto the surface to identify the corresponding point on the surface Q_i, and the objective function is then set equal to

$$h(c_k) = \sum_{i=1}^{n} |P_i - Q_i(c_k)|^2. \tag{2.14}$$

This approach can be considered acceptable for our aims since the real distance approaches zero when the vertical distance goes to zero. The three surface classes that have been chosen are:

1. elliptical paraboloids (TS1);
2. hyperbolic cosine functions (TS2);
3. ellipsoids (TS3).

All these surfaces have an elliptical horizontal section, just as the ideal surfaces representing the dome intrados and extrados. The first two classes, i.e., parabolas and hyperbolic cosines, have been selected by recalling that they can reproduce the shape of a cable carrying, respectively, a uniform distributed load and a load proportional to the cable self-weight, and so they are expected to have good chance of resulting in compressed membranes. The

third class is used because the ellipsoids' shape is able to cope well with the peculiar shape of the dome, while maintaining a relatively simple analytical expression.

For convenience, all the surfaces have been expressed in the same coordinate system as the ideal surfaces, equations (2.13), since the finite difference scheme set up works within the domain of those coordinates. The parametric expression for the general class of surfaces is

$$\mathbf{x} = rg(z)\cos\alpha\,\mathbf{i} + sg(z)\sin\alpha\,\mathbf{j} + z\,\mathbf{k} \tag{2.15}$$

where r and s are proportional to the semi-axes of the ellipse at the dome base, and $g(z)$ is a function of z that depends on the class of surfaces considered.

None of the three optimal surfaces identified by the minimisation routine has cost function equal to zero, which means that none of the surfaces exactly interpolates the cloud of the centres of pressure defined by the admissible network. However, the analyses illustrated below have the value of a counterexample as they highlight the main difficulties arising from a practical standpoint in setting up a method combining thrust network and thrust surface. The two main drawbacks, which will be illustrated in the following, are:

- surfaces very close to the network, as well as to admissible thrust surfaces, turn out to be not admissible;
- not negligible differences are observed in the equilibrium states defined by the thrust network and the thrust surface.

The admissibility of the internal forces is checked for each optimal thrust surface by performing a membrane analysis. To this aim, an ad-hoc finite difference scheme has been developed in *Mathematica*® to solve the differential equilibrium equations of a membrane. The corresponding results are described in the following.

Thrust surface TS1. The first class of surfaces, namely elliptical paraboloids, is described by the following expression for $g(z)$

$$g(z) = \sqrt{1 - \frac{z - z_c}{t}} \tag{2.16}$$

where t is a parameter, and $(0, 0, z_c)$ are the coordinates of the centre of the paraboloid. The best parameter values obtained from the optimisation procedure are $r = 10.35\,\mathrm{m}$, $s = 9.0\,\mathrm{m}$, $t = 14.49\,\mathrm{m}$, $z_c = -2.00\,\mathrm{m}$, and the minimum value of the cost function is equal to $h(r, s, t, zc) = 19.7\,\mathrm{m}^2$. Figure 2.12 shows a comparison between the centres of pressure and the optimal surface on a vertical section of the dome.

By performing the membrane analysis, the membrane forces turn out to be admissible everywhere. By way of example, the principal membrane forces, f_1 and f_2, evaluated on the vertical sections drawn by the major and minor axes of the dome are shown in Figure 2.13. For these two sections, because of symmetry, the principal membrane forces coincide with those along hoop and meridian directions respectively (the figure displays the curves interpolating the results of the finite difference method).

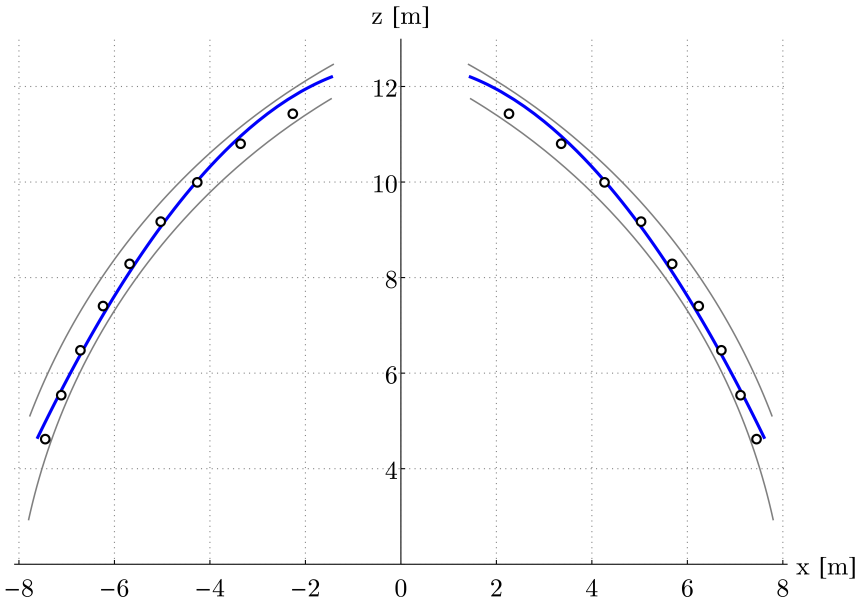

Figure 2.12: Vertical section on the dome's major semi-axis: (dots) centres of pressure obtained by the TNA, (blue line) optimal TS1 surface.

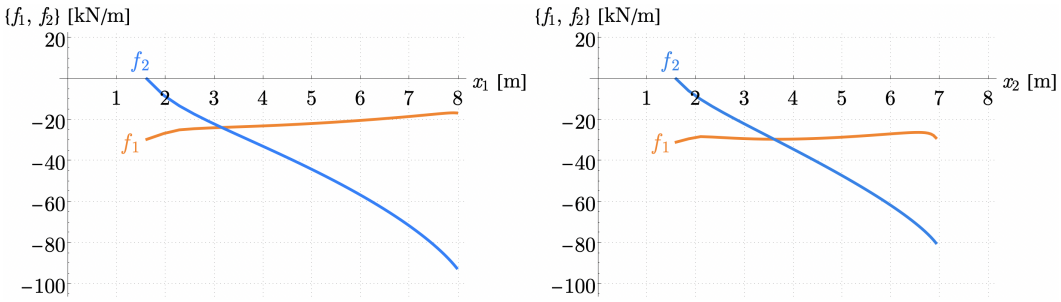

Figure 2.13: Principal forces (interpolation curves) on two vertical sections on $x_2 = 0$ (left) and on $x_1 = 0$ (right) for the TS1. For these sections only f_1 = hoop force and f_2 = meridian force.

Thrust surface TS2. The second class of surfaces, defined by hyperbolic cosine functions, is described by the following expression for $g(z)$

$$g(z) = \operatorname{arccosh}\left(1 - \frac{z - z_c}{t}\right) \tag{2.17}$$

where t is a parameter, and $(0, 0, z_c)$ are the centre coordinates. The best parameter values obtained from the optimisation procedure are $r = 3.57\,\text{m}$, $s = 3.12\,\text{m}$, $t = 2.35\,\text{m}$, $z_c = 12.00\,\text{m}$, and the minimum value of the cost function is equal to $h(r, s, t, zc) = 3.0\,\text{m}^2$. Figure 2.14 shows a comparison between the centres of pressure and the optimal surface on a vertical section of the dome.

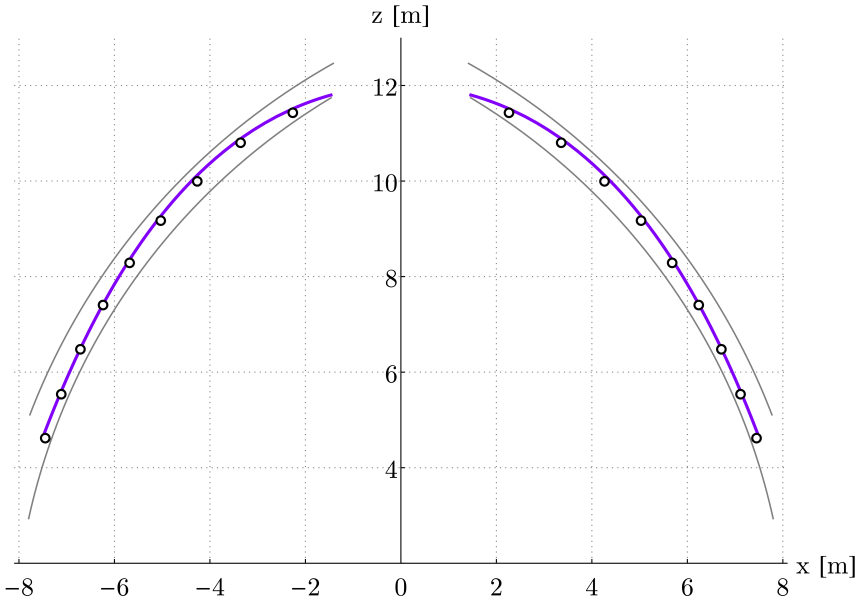

Figure 2.14: Vertical section on the dome's major semi-axis: (dots) centres of pressure obtained by the TNA, (blue line) optimal TS2 surface.

By performing the membrane analysis, the forces turn out to be admissible everywhere. By way of example, the principal membrane forces on two vertical sections are shown in Figure 2.15 (the figure displays the curves interpolating the results of the finite difference method).

Thrust surface TS3. The third class of surfaces, namely the ellipsoids, are described by the following expression for $g(z)$

$$g(z) = \sqrt{1 - \left(\frac{z - z_c}{t}\right)^2} \tag{2.18}$$

where t is a parameter, and $(0, 0, z_c)$ are the coordinates of the centre of the ellipsoid. The best parameter values obtained from the optimisation procedure are $r = 8.50\,\text{m}$, $s = 7.41\,\text{m}$, $t = 14.00\,\text{m}$, $z_c = -2.00\,\text{m}$, and the minimum value of the cost function is $h(r, s, t, zc) =$

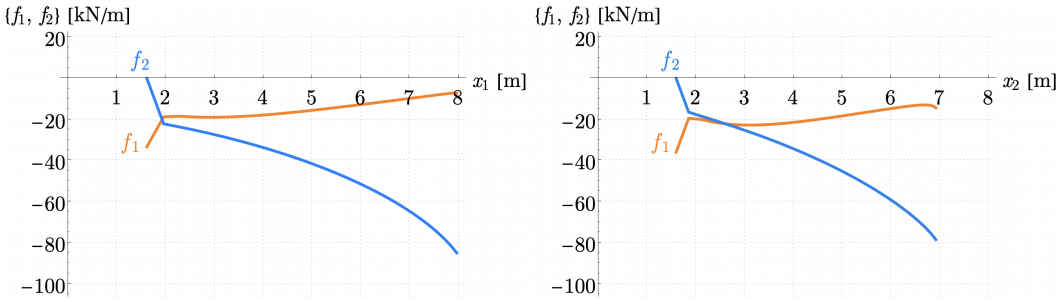

Figure 2.15: Principal forces (interpolation curves) on two vertical sections on $x_2 = 0$ (left) and on $x_1 = 0$ (right) for the TS2.

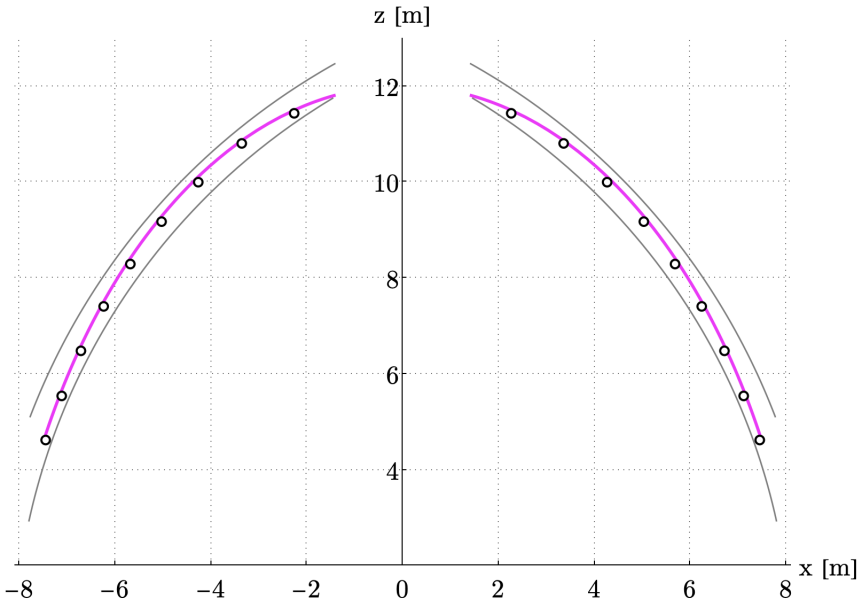

Figure 2.16: Vertical section on the dome's major semi-axis: (dots) centres of pressure obtained by the TNA, (blue line) optimal TS3 surface.

$2.7\,\mathrm{m}^2$. Figure 2.16 shows a comparison between the centres of pressure and the optimal surface on a vertical section of the dome.

In this case, by performing the membrane analysis, the forces turn out to be inadmissible in the lower region, where tensile forces arise. By way of example, the principal membrane forces on two vertical sections are shown in Figure 2.17 (the figure displays the curves interpolating the results of the finite difference method).

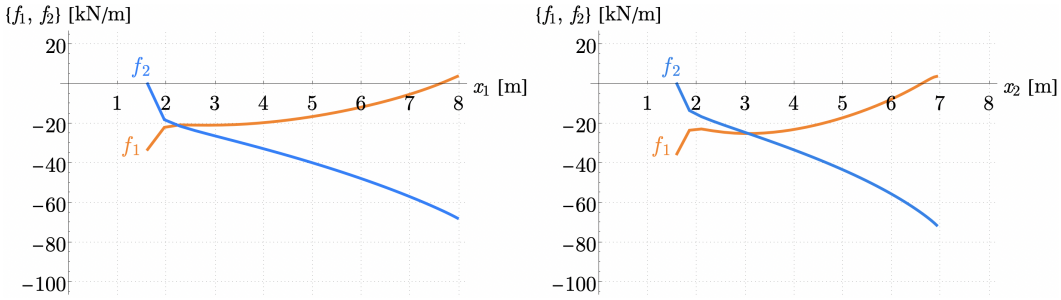

Figure 2.17: Principal forces (interpolation curves) on two vertical sections on $x_2 = 0$ (left) and on $x_1 = 0$ (right) for the TS3.

It is worth noting that the trend of the internal forces resembles that which develops inside a spherical shell under its self-weight. Although the load distribution is slightly different, this fact is not surprising, since an ellipsoid can be turned into a sphere by an affine transformation, and according to Rankine's theorem (1856) [Huerta, 2010], the stability of masonry structures subject to dead loads alone remain unaltered after an affine transformation.

Discussion of the results

The foregoing results show that, although a criterion based on the closeness of the surface to the centres of pressure seems to be reasonable, it leads to thrust surfaces that may or may not be admissible. The optimal TS2 and TS3 show no significant differences in shape; in fact, they nearly overlap, as shown in Figure 2.18. Nevertheless, the first is admissible, while the second it is not.

This is a crucial point to be made in the comparison between TNA and TSA. The case study considered clearly shows that it is by no means assured that the set of centres of pressure corresponding to an optimum thrust network furnished by TNA will lead to an admissible thrust surface. In the case study, thrust surface TS3 turned out to be inadmissible. Moreover, it is interesting to note that when the parameters defining each surface are changed slightly, TS3 remains inadmissible, while TS1 and TS2 continue to belong to the set of admissible thrust surfaces. In other terms, it seems that it is the surface class (and the geometrical properties defining it) that plays a central role in determining whether a given thrust surface will be admissible or not rather than its proximity to the thrust network. Such a finding is in keeping with the widespread belief that the admissibility of a thrust surface is governed mainly by its shape (i.e., the ratio between its curvatures).

By limiting the analysis to the first two surface classes, the optimal thrust network enables finding two admissible thrust surfaces: TS1 and TS2. In the following one shall focus on these and have a closer look at their internal forces, the aim being to compare

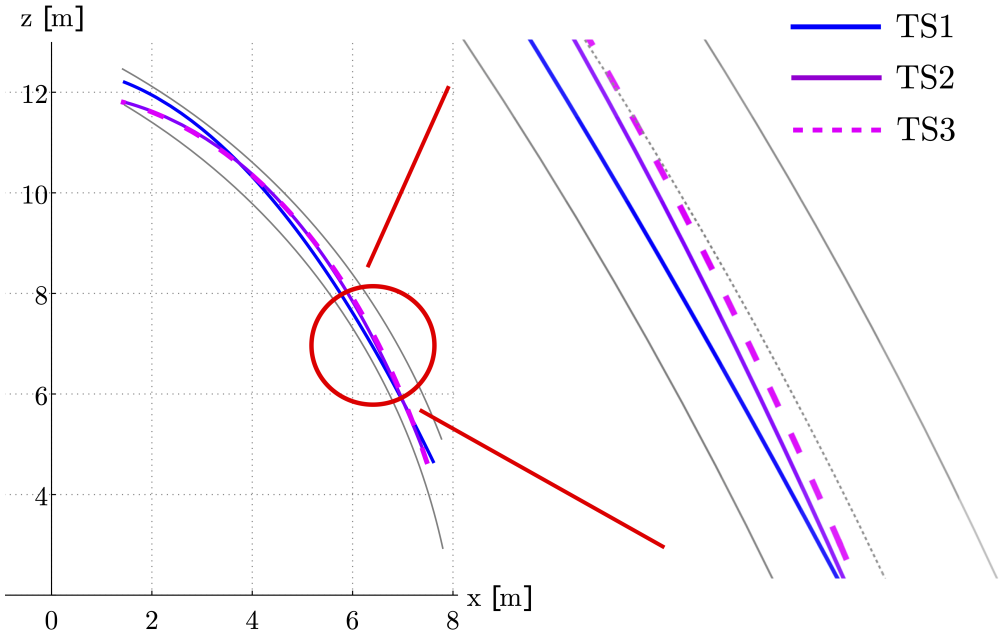

Figure 2.18: Comparison between the optimal surfaces on a vertical section on the dome's major semi-axis: the differences between TS2 and TS3 are very small.

the two distributions of membrane forces with that in the thrust network. In order to compare homogeneous quantities, in all cases one refers to the set of blocks the dome has been ideally subdivided into, and to the resultants acting on each block. Hence, starting with the membrane internal forces, the resultant forces acting on each block are evaluated by integration.

First, it should be pointed out that a necessary condition to be fulfilled by the TNA and TSA solutions in order for the two to be considered equivalent is that the lines of action of the resultant of the membrane forces acting on each block intersect at one point. However, this condition is not verified in the general case, and thus allows concluding that it is not possible, in general, to define a thrust network that is fully equivalent to a thrust surface (Figure 2.19). In the example at hand, the offsets between the lines of action of the forces acting on each block have been evaluated for the two admissible thrust surfaces found, TS1 and TS2. As far as TS1 is concerned, the results show that the mean of the distances between the lines of action of the forces acting on each block is 6 cm, with a maximum distance of 28 cm. When TS2 is considered, the offsets are even larger: the mean of the distances between the lines of action of the forces acting on each block is also 6 cm, with the maximum distance however reaching 84 cm. The greatest differences regard the line of action of the hoop forces, while the distances are generally almost negligible between the lines of action of the forces acting along the meridian directions. In conclusion, since there are considerable distances between the lines of action of the forces acting on the blocks, the thrust surfaces obtained cannot be considered fully equivalent to the thrust network.

As a final step in the comparison, let us compare the force distributions on the blocks furnished by TNA and TSA. Figure 2.20 shows the comparison between the magnitude of the forces acting on each block for TS1, while Figure 2.21 regards TS2 (the dashed lines

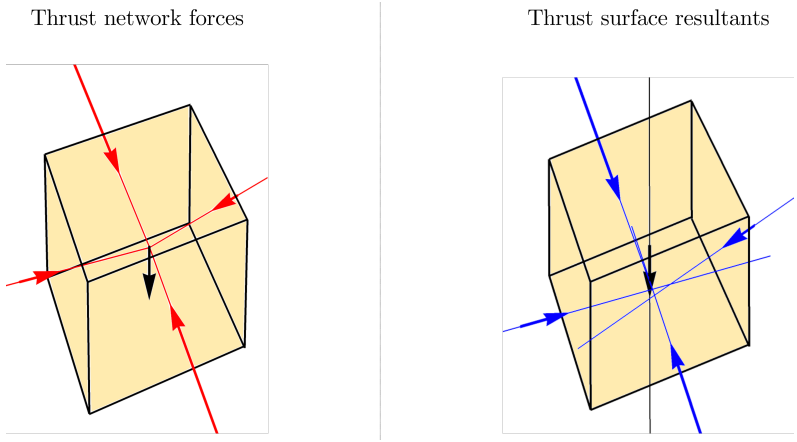

Figure 2.19: State of equilibrium of a generic block. The forces acting on the blocks in TSA do not, in general, intersect at one point.

mean that it is not a proper network, i.e. forces on a block do not meet at one point). By virtue of symmetry, both are limited to a quarter of the dome. Note that in this comparison one ignores the fact that the TSA forces acting on each block do not all meet at the same point, and that only the force magnitude is taken into consideration.

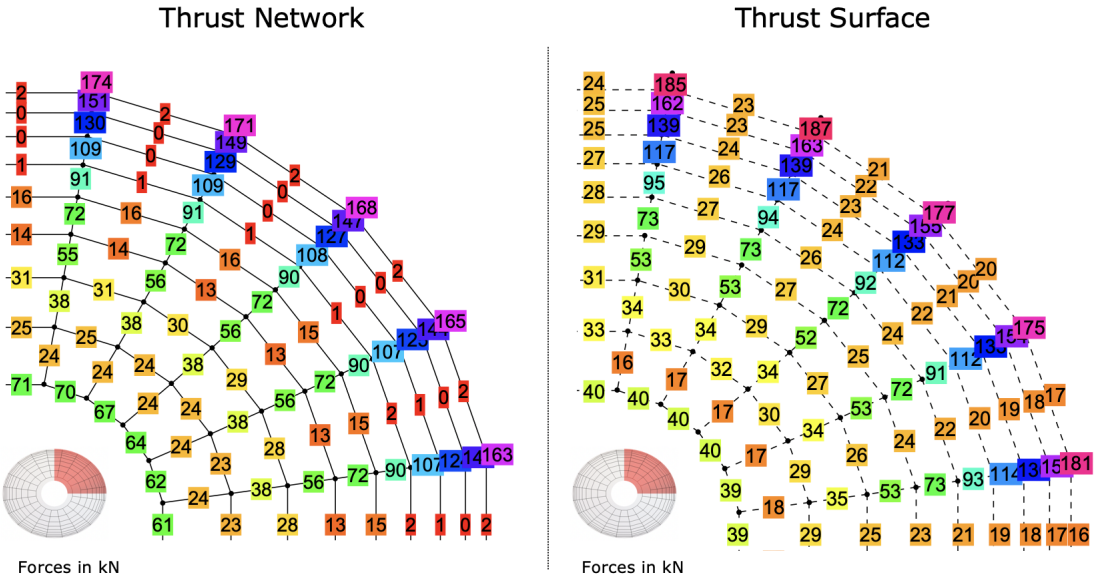

Figure 2.20: Comparison between the two force distributions for TS1 on a quarter of the dome.

In the TS1 solution the force distribution along the meridian directions is similar to that of TNA. However, the hoop compressions are almost constant while in TNA they decrease going towards the support structures. The force distribution in the meridian directions is also similar to TNA for TS2, but the hoop compressions still remain significantly different from those obtained via TNA. It is reasonable to expect that by suitably widening the set of surface classes, the two methods would yield more convergent results. However, in practice

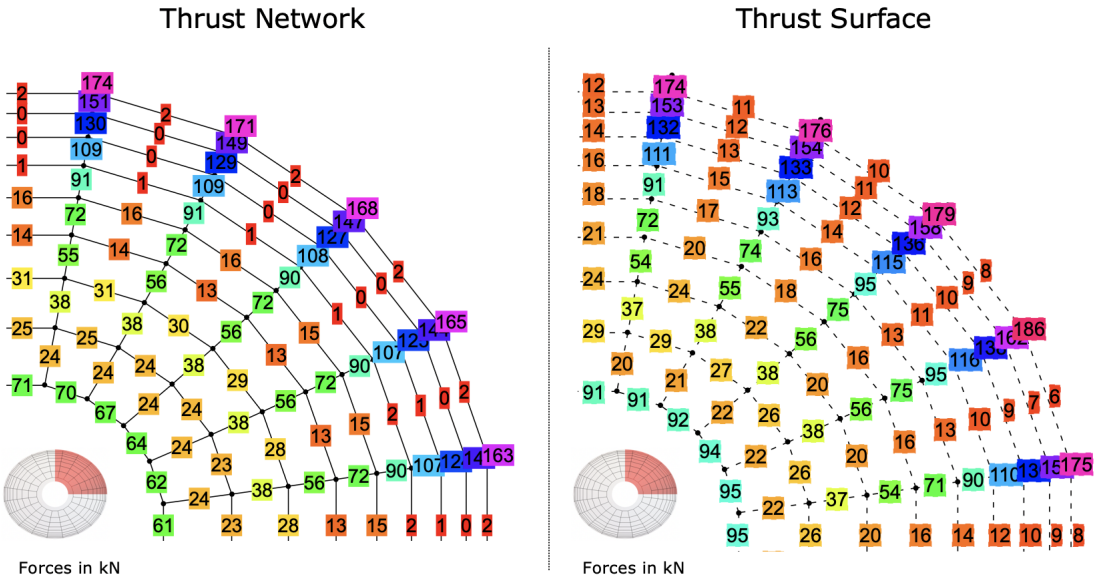

Figure 2.21: Comparison between the two force distributions for TS2 on a quarter of the dome.

it is not possible to allow a completely arbitrary membrane shape, and the choice of the most suitable parametric expressions is still an open issue.

2.4 TNA and TSA for the study of horizontal actions

The seismic assessment of masonry domes is an arduous task that goes beyond the purpose of this thesis work. Apart from the difficulty represented by the masonry itself, whose mechanical behaviour has not been completely understood yet, the second problem is linked to the nature of the seismic actions. First of all, the actions of seismic origin are dynamic and require a specific study that analyses the behaviour of the structure over time. Furthermore, while measurements and estimates of the actions that reach the structure through the ground are available, the evaluation of the actions that actually reach the dome is difficult to determine, as it would require a precise characterisation of the interactions between the dome, the underlying building and the ground. For these reasons, as a working hypothesis, reference is made to the problem in which the dome is isolated from the rest of the building and subjected to a system of vertical and horizontal static forces. The vertical loads are due to the self-weight of the structure and of the superimposed elements and are thus kept constant. The horizontal loads, which can represent, at least as a first approximation, the effect of an earthquake and which are assumed proportional to the self-weight (thus simulating inertial forces), are slowly increased over time, with the aim to evaluate the maximum lateral load multiplier before the structure reaches collapse. Under these hypotheses and assuming that the material satisfies Heyman's hypotheses, the problem can be considered equivalent to the problem of finding the maximum angle by which a structure placed on a tilting table can be rotated before it collapses. Even if these experimental tests are not able to reproduce the problem described, as the rotation of the structure leads to a progressive decrease of the

vertical actions, it is possible to demonstrate that the multiplier of the horizontal loads is the same. There are some examples in which this methodology has been applied to scale models of masonry panels (see, for example, [Trovalusci, 1992], [Grillanda et al., 2021]), masonry arches (see, for example, [Stockdale et al., 2020], [Misseri et al., 2018]), and masonry domes and vaults (see, for example, [Zessin, 2012], [Shapiro, 2012]).

TNA and TSA can also be used to study the stability of masonry domes subjected to vertical and horizontal loads. Although this doesn't require changes in the mechanical models or principles on which the two methodologies are based, some suitable adaptations are necessary in order to be able to effectively exploit the two techniques in presence of horizontal actions. Concerning the TNA, some adjustments are required in the numerical algorithm, as commented in [Block, 2009] and as fully developed in [Marmo and Rosati, 2017]. As for the TSA, since the selection of a class of surface is a crucial point, it's worth observing that, while it is possible to guess a good shape coping well with the dome geometry for vertical actions, the same is not straightforward when horizontal loads are involved. However, both these techniques can be applied in the standard way by ideally tilting the structure of a given angle related to the magnitude of the horizontal loads, without any further modification in the algorithm. One can observe that this is a first, quite rudimental way of employing TNA and TSA for the study of the stability when horizontal actions are involved, but it highlights well the main issues one can find when dealing with this problem.

The TNA has been applied via the MaNACoH software by defining a geometry which is tilted by a certain angle that simulates the horizontal loads. Since the aim of this analysis is not to compare thrust networks and thrust surfaces, the joints' orientation has been defined so as to follow the principal joints' directions of the brick pattern, i.e. orthogonal to the middle surface of the dome. The dome has been subdivided into 200 blocks, as for the previous analysis. The TSA has been employed by choosing the elliptical paraboloid as the class of surfaces because it is the surface that more than the others can rotate inside the structure without going beyond the limits of the masonry. Then, the membrane analysis is performed in presence of horizontal actions. The Figures 2.22 and 2.23 show the networks obtained for horizontal loads along the x_1 and x_2 axis, respectively. The maximum lateral load multipliers corresponding to the tilting angles are $\lambda_{x_1,max} = 0.05$ and $\lambda_{x_2,max} = 0.03$, respectively. The Figures 2.24 and 2.25 show the surfaces obtained for horizontal loads along the x_1 and x_2 axis, respectively. Even in this case, the maximum lateral load multipliers corresponding to the tilting angles are equal to $\lambda_{x_1,max} = 0.07$ and $\lambda_{x_2,max} = 0.05$, respectively.

In order to compare the results with lateral load multipliers of real earthquakes, reference is made to the maximum horizontal acceleration expected on the ground having a return period of 475 years and referred to the 50th percentile[1], which is equal to $a_g(475)_{rif} = 0.118g$, where g is the gravity acceleration. As $\lambda = a_g/g$ the maximum lateral load multipliers obtained by TNA and TSA are not satisfactory. Since the structure is very thin, both network and surface don't have much room to suitably reshape themselves in order to make equilibrium to the external loads and this may be the reason for the smallness of the load multipliers.

[1] https://www.regione.toscana.it/-/accelerogrammi-di-riferimento-provincia-di-pisa

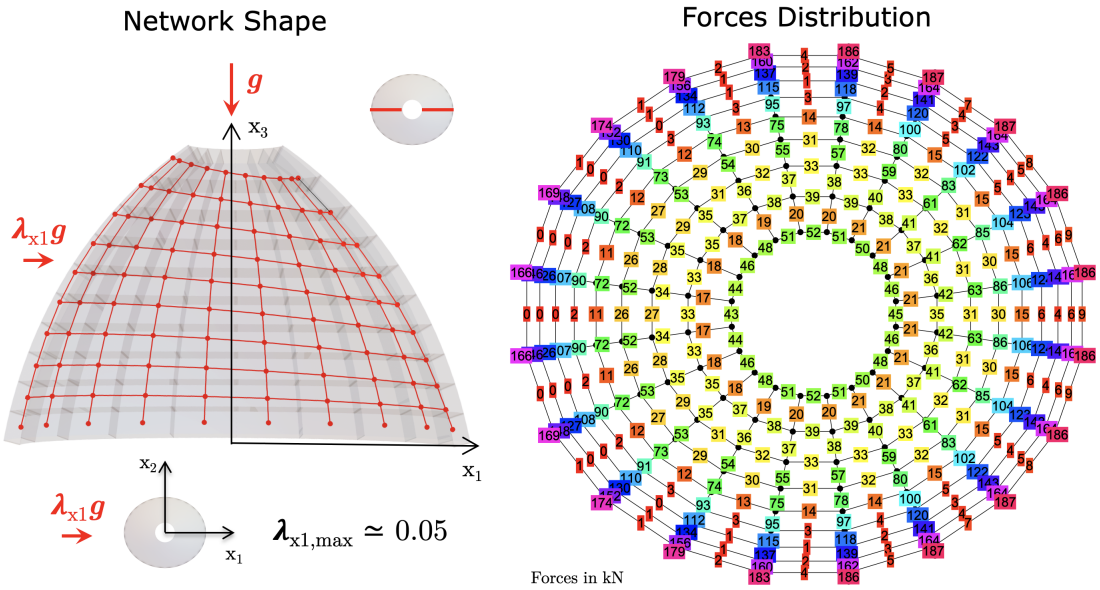

Figure 2.22: TNA solution with horizontal loads along the x_1 axis.

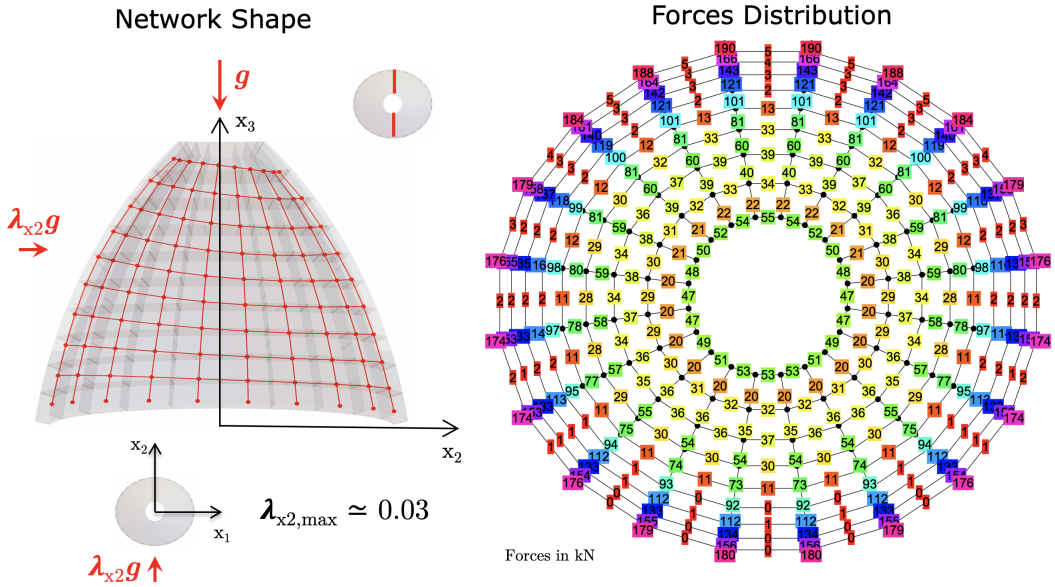

Figure 2.23: TNA solution with horizontal loads along the x_2 axis.

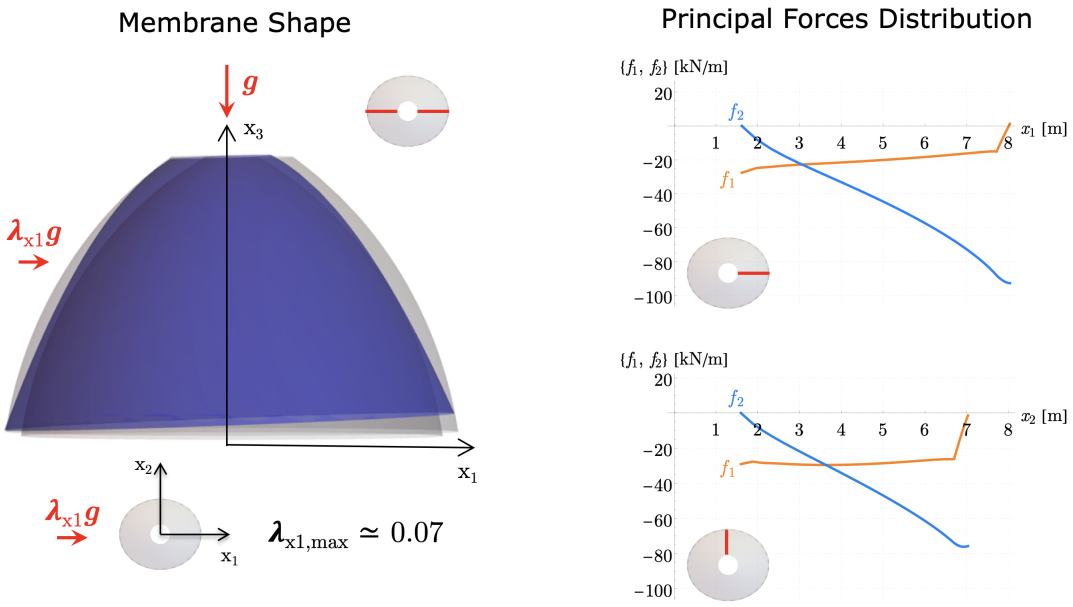

Figure 2.24: TSA solution with horizontal loads along the x_1 axis.

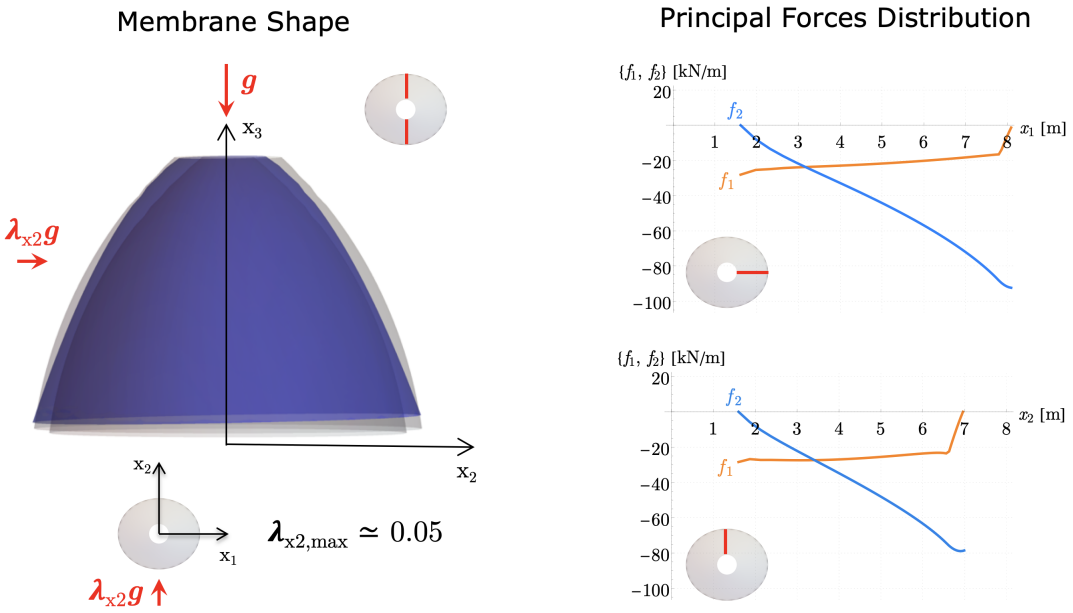

Figure 2.25: TSA solution with horizontal loads along the x_2 axis.

2.5 Summary and conclusive remarks

With reference to the limit analysis of masonry vaults and domes, nowadays Thrust Network Analysis and Thrust Surface Analysis are two well established techniques to find statically admissible stress fields. These two strategies are sometimes considered as somehow related. Nevertheless, the actual relation between TNA and TSA does not seem to be fully understood, even in their modern application, and further studies seem to be needed to clarify the correspondence between these two methods.

The chapter illustrates the results of a critical comparison between Thrust Network Analysis and Thrust Surface Analysis, with the aim of better understanding their mutual correlations. A necessary condition for establishing a proper correlation between the two methods is that vertical joints are considered when performing the TNA. Under this condition, the relation linking thrust network and thrust surface is investigated when considering a finite mesh size of the force network in the TNA. In particular, the centres of pressure of a thrust network determined by means of TNA are considered, and the surface closest to this set of points is determined by searching among a predefined class of surfaces.

The proposed methodology is applied to a real case study, the dome of the famous Pisa Cathedral. Three classes of surfaces are investigated: elliptical paraboloids, hyperbolic cosine functions and ellipsoids. When ellipsoids are used, the thrust surface corresponding to the thrust network is, among those tested, the closest to the centres of pressure, but at the same time it turns out to be inadmissible. Hence, it is by no means assured that a thrust surface close to the centres of pressure of a given admissible thrust network will in turn be admissible, and, as is widely assumed, a crucial role is played by the surface shape. Both methods, if applied separately, are able to find statically admissible generalised stress fields, and therefore are able to provide useful indication about the stability of a structure. However, by referring to the same ideal subdivision of the dome in blocks, what emerges is that there exist appreciable differences in the distribution of the internal forces yielded by the thrust surface and the thrust network, although the two are very close each other from a geometrical point of view.

The counterexample illustrated in the chapter appears to raise serious doubts about the actual possibility of establishing a correspondence between TNA and TSA. Although in the limit case, where the mesh size goes to zero, an admissible thrust network may approach an admissible thrust surface, the results emerging from the foregoing case study clearly show that for finite mesh size, it is by no means assured that an admissible thrust network is a good starting point to build an admissible thrust surface.

The first critical comparison discussed in the present chapter seems to show that it is not a simple matter to exploit the correspondence between TNA and TSA in practice. As a consequence, some care is advisable in deciding whether a possible method combining thrust network and thrust surface should be considered, since inadmissible thrust surfaces may result even very close to the centres of pressure of an admissible thrust network. The results obtained suggest the complementarity of the two techniques, rather than their combined use in investigating the stability of domes.

Although some crucial points on the relation between thrust networks and thrust surfaces have been highlighted, further in-depth analyses of the connections between the two methods are needed. In particular, the issue concerning discretised ('grid or network') vs continuous

(surface) model of masonry vaults is worth further discussing. Moreover, further studies could be devoted to checking whether a more refined criterion for the comparison, properly including the curvatures of the surface, could determine thrust surfaces that are closer to the network in terms of the equilibrium state defined. The influence of the choice of block discretisation on the correspondence between networks and surfaces is another issue to be faced. A comparison between optimised TNA and TSA solutions would also enable checking whether more accordant equilibrium states could be obtained.

The results obtained in the case horizontal loads are also considered highlight the limited effectiveness of TNA and TSA in the used form. The values of the statically admissible horizontal loads turn out to be quite low, and they are likely to be far from the actual ones. For this reasons other methods that could go beyond the critical issues exhibited by TNA and TSA are taken into consideration.

Chapter 3

The no-tension shell model

As it was already observed at the end of the previous chapter, the solutions obtained by both the TNA and TSA provide a satisfactory safety assessment when the dome is subjected to vertical loads. However, when horizontal loads also come into play, TNA and TSA do not seem able to provide reasonable estimations of the actual load capacity of the dome.

The limited effectiveness that both TNA and TSA show especially in the case horizontal loads are also considered as a consequence of the fact that both methods explore a narrow subset contained within the whole set of statically admissible internal forces. Hence, both methods yield lower bound estimates of the dome load capacity that are likely to be quite far from the true value.

The limitations revealed by TNA and TSA driven us towards the development of methods that would enable searching for more general distributions of statically admissible internal forces. In this regard, the natural extension of the analysis methods exploited in the previous chapter consists in modelling the dome as a thin shell, while accounting for general distribution of internal forces within the shell, allowing for both membrane and bending forces.

In this chapter the classical structural model for shells is recalled and suitably adapted to the case of masonry domes. The kinematic, equilibrium and constitutive issues, although not new, are explicitly illustrated for reader's convenience.

Firstly, the geometrical and kinematical hypotheses are introduced. In particular, the masonry dome is modelled as a shear deformable thin shell. Then, the balance laws are established, along with the hypotheses on the material. The shell is thought as made of a material endowed with an infinite compressive strength and a nil tensile strength. Estimations of the safety level against collapse are obtained by exploiting the theorems of limit analysis. In this regard, masonry is considered as a *standard material*. The fundamental theorems of limit analysis are reformulated, by specialising them to the case of a masonry shell. An explicit proof of both theorems in their specialised form is provided.

It is well known that the theory of shells can be developed directly by considering a 2d body or derived from the three-dimensional theory [Podio-Guidugli, 1991]. The interested reader can find the theory of shells, developed in parallel according to both ways, in [Naghdi, 1973] and [Truesdell and Toupin, 1960, sec. 60, 64, 212 and 213]. Here the direct formulation is adopted by regarding the shell as a *Cosserat surface* (see [Green et al., 1965] and [Cosserat and Cosserat, 1909]) because this formulation is more suitable to describe the influence of

the masonry joints' orientations on the internal forces and failure criterion adopted.

As will be shown in the following, masonry shear strength will be accounted for in the general case. In this regard, one observation is worth adding. Ancient builders usually paid close attention to vertical loads and ensured careful arrangement of the units and a good interlocking in historical masonry constructions so as to assure a good mechanical response with respect to these actions. Usually, units' arrangement is such that joints, which represent the weak surfaces in the masonry, are oriented so as to face the major compressive stress. Hence, the shear strength of the masonry is not an issue as far as vertical loads are concerned. On the contrary, when horizontal loads are considered, it is not excluded that the shear strength could play an important role in the collapse of historical construction. Large horizontal actions, like those of an earthquake, are likely to strongly modify the distribution of internal forces within the masonry and, for this reason, the influence on the limit load of a finite shear resistance is also investigated in our analysis. When only vertical loading is considered, the sliding failure is assumed prevented. This assumption, together with the previous ones, constitutes the adaptation to the case of shells of the famous Heyman hypotheses.

It is straightforward to recognise that masonry domes can be modelled as shells. The first obvious consideration to be made is that in general, their thickness is far smaller than their dimensions in plan or elevation. As an example, for the dome of Pisa cathedral, the study case that will be addressed in the following, the thickness is some 4% of the mean diameter, while the thickness of the internal shell in the St. Peter's cathedral in Rome is about 5% of the diameter [Como, 2013]. A second relevant consideration is the clever disposition of units, whether they are stone blocks or bricks, adopted by ancient builders in masonry domes. Usually, units' arrangement is such that joints, which represent the weak surfaces in the masonry, are oriented in the transversal direction, i.e., facing the major compressive stresses flowing from the top to the bottom of the dome. This arrangement is the rule in the case of single-layer brickwork (Figure 3.1), but it is also commonly adopted when courses are composed of mixed headers and stretchers, as in the case of the dome of Pisa cathedral (Figure 3.2). The arrangement of units in masonry domes makes it natural to consider the internal forces acting on the transversal surface elements, as it is usually done in shell theory. Moreover, failure criteria will account for tensile stresses transmitted over transversal elements (as the joint 1-1 in Figure 3.2), while tensile stresses acting within the units in the transversal direction will be neglected. In other terms, the tensile strength of the joints is assumed to be consistently lower than the traction needed to split up the bricks in the transversal direction. This can be considered a reasonable assumption provided that the interlocking between units is sufficient to prevent tensile failure across the thickness.

Before going into the details of the model two more observations are added. The first one concerns how the no-tension hypothesis is handled in the general case where the masonry is considered as a three-dimensional continuum body. As is well known, in the general case masonry is assumed unable to carry tensile stresses regardless of the direction, and this assumption characterises the so called *no-tension material* model developed in the last decades of the past century. This is a limit hypothesis: actually, although strongly dependent on the internal disposition of the constituent elements, almost all masonry structures have some tensile capacity, which should be taken into account [Chen and Bagi, 2020]. However, what is more important is that the standard form of no-tension hypothesis results to be

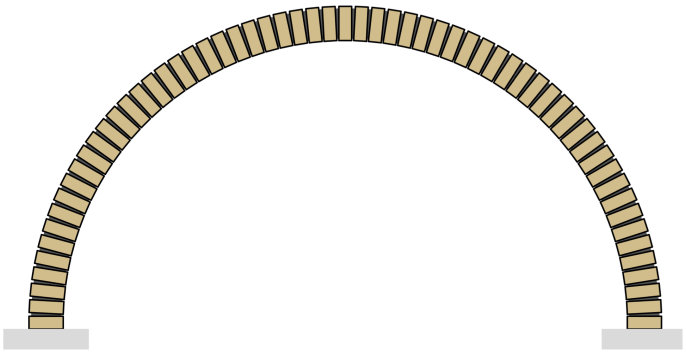

Figure 3.1: Single-layer brick dome. The bricks are assumed to be sufficiently strong in the transversal direction to neglect possible tensile failure.

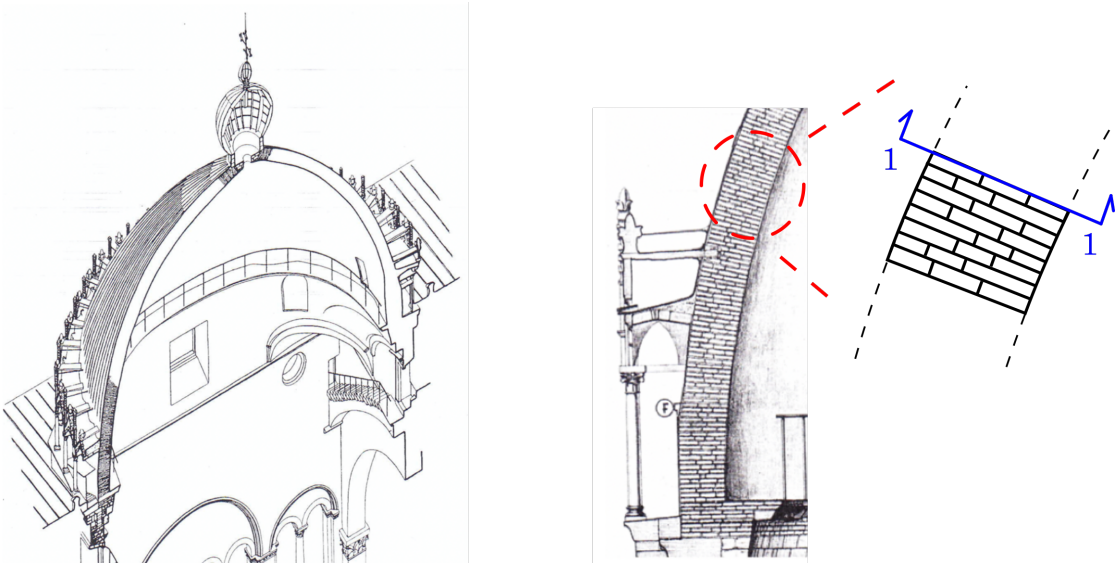

Figure 3.2: Typical internal brick arrangement in masonry domes (figure adapted from [Sanpaolesi, 1959]).

very restrictive and makes the search for statically admissible stress fields possible only for particular loading cases. In effect, in the case of masonry domes and vaults, the no-tension hypothesis in its classical form hampers determining admissible stress fields in equilibrium with the actual load distribution. This obstacle is generally overcome by requiring the stress fields to fulfil equilibrium only in some approximated sense. As an example, in the TSA in place of the actual load distribution a different suitable distribution that approximates the actual one is used. The second observation is that the mechanical behaviour of a masonry structure cannot be properly described simply by adopting suitable constitutive relations for the material. Masonry cannot be considered simply as a 'class of materials' since this approach lacks to catch essential aspects of masonry structures, related to the building techniques. Besides the mechanical characteristics of constitutive elements, also the structural typology and the internal disposition of the elements strongly contribute to determining the mechanical behaviour of masonry construction that, for this reason, should be regarded as a structural element rather than a simple continuum body. In other words, the approaches based uniquely on the no-tension assumption are not completely adequate to describe the mechanical behaviour of masonry domes and the proper description of different building elements, such as walls, towers, vaults and domes, having different internal structures, may require different treatments. For this reason, the field of application of the analysis approach developed in the next chapter is clearly recognised to be on masonry domes made of a series of organised bricks or regular pieces of stone. The elementary case that inspires the method is the single bricklayer masonry dome (see Figure 3.1). Looking at this simple case, since the building blocks, whether made of stones or bricks, usually have a certain tensile resistance, one can assume that some tensile stresses may arise in the direction of the thickness of the dome. As was done in the first analysis methodologies, the weak part is associated with the direction of the joints, whether they are filled with mortar or not and for this reason, we assume that no tensile stress can arise on the middle surface of the dome.

3.1 Geometry

To study the motion and the equilibrium of natural objects, one introduces the concept of *body* ([Villaggio, 2005]). Formally, a *simple body*[1] is defined as a set $\mathbb{B}$ whose elements have the property to occupy regions of the physical space, modelled as Euclidean three-dimensional space $\mathbb{E}^3$. The elements of $\mathbb{B}$ are called *material points*[2] and are here denoted by p . The geometric structure of the ambient space is the traditional one of classical mechanics: fixed a point $o \in \mathbb{E}^3$ as the *origin* and a Cartesian triplet of unit vectors $\{\mathbf{i}_k\}$, the generic point $x \in \mathbb{E}^3$ is identified with its position vector $\mathbf{x} = (x - o)$:

$$\mathbf{x} = x_k \mathbf{i}_k \tag{3.1}$$

which represents the translation that brings o to x (the summation over the repeated indexes is implicitly intended from now on). Let $V = \text{span}\{\mathbf{i}_k\}$ denote the vector space spanned by the base vectors on $\mathbb{E}^3$, also called *space of translations* on $\mathbb{E}^3$. One can establish in this way a correspondence between points $x \in \mathbb{E}^3$ and the elements of the vector space $\mathbf{x} \in V$, representing position vectors.

The injective function

$$\begin{aligned} \mathfrak{f} : \mathbb{B} &\to \Omega \in \mathbb{E}^3, \\ p &\mapsto \mathbf{x} = \mathfrak{f}(p), \end{aligned} \tag{3.2}$$

associates material points to the position vectors of the corresponding points in the Euclidean space and can thus be named *geometric configuration*. The vector $\mathbf{x}$ is the *position* occupied by the material point p in the geometric configuration $\mathfrak{f}$ and one says that the body $\mathbb{B}$ occupies a certain *region* Ω in the Euclidean space in the geometric configuration $\mathfrak{f}$. We assume that a bijective map between material points and a possible geometric configuration exists. We also require the geometric configuration function to be surjective so that each point of Ω belongs to $\mathfrak{f}(\mathbb{B})$. Commonly, we require the region Ω to be the closure of an open, regular and simply connected set. We further require the frontier $\partial\Omega$ to be locally Lipschitz continuous. For simplicity, we consider the frontier of class C^1 almost everywhere in the sense of measure theory so that the boundary of the region $\partial\Omega$ admits everywhere a normal vector except on a subset of measure zero.

In what follows, the common operations of scalar, vector and tensor product will be denoted, respectively, by $\cdot$, $\times$ and $\otimes$. The Einstein convention on summations is adopted and, unless otherwise stated, Latin indices take the values 1, 2 and 3 while Greek indices take the values 1 and 2.

3.1.1 The shell as a Cosserat surface

Intuitively, a shell can be seen as a continuum body in which one of its dimensions, called the *thickness*, is smaller than the other two and whose geometry can therefore be accurately described by means of a surface, called *model surface*. In this section, some well-known notions of the geometry of surfaces that will be useful in the following are recalled (see [Kreyszig, 1991]).

[1] The meaning of the term 'simple' will become clear later.

[2] Not to be confused with the concept of material points of classical mechanics [Abeyartne, 2012].

In this context, let $\mathbb{S}$ be a set such that $\Sigma = \mathfrak{f}(\mathbb{S})$ is a regular, compact and oriented surface embedded in the three-dimensional Euclidean space $\mathbb{E}^3$. We assume that the surface Σ admits a parametric representation in terms of two curvilinear coordinates θ^α

$$\Sigma: \quad \mathbf{x} = \mathbf{x}(\theta^\alpha), \qquad \theta^\alpha \in \Theta \subset \mathbb{R}^2, \tag{3.3}$$

where Θ is the coordinate domain (see Figure 3.3). We call *coordinate lines* the curves identified by the conditions $\theta^\alpha = const$, which are induced by (3.3). The parametrisation (3.3) provides a natural basis for the representation of the fields over Σ. We also assume that the function $\mathbf{x}(\theta^\alpha)$ is as regular as necessary for all the derivation operations that appear below to make sense. In the following, the partial derivatives with respect to θ^1 and θ^2 are denoted respectively by $\bullet_{,1}$ and $\bullet_{,2}$. The natural local covariant basis associated to this system of curvilinear coordinates is given by

$$\mathbf{a}_\alpha(\mathbf{x}) = \mathbf{x}_{,\alpha} \qquad (\text{with } \mathbf{a}_1 \times \mathbf{a}_2 \neq \mathbf{0} \text{ on } \Sigma) \tag{3.4}$$

and the local reference triad is completed by the surface unit normal vector $\mathbf{n}$ given by the *Gauss map*

$$\mathbf{n} = \mathbf{a}_3 = \frac{\mathbf{a}_1 \times \mathbf{a}_2}{\|\mathbf{a}_1 \times \mathbf{a}_2\|}. \tag{3.5}$$

The *tangent space* $T_x = \text{span}\{\mathbf{a}_\alpha(\mathbf{x})\}$ to Σ at $\mathbf{x}$ is spanned by the tangent vectors to the

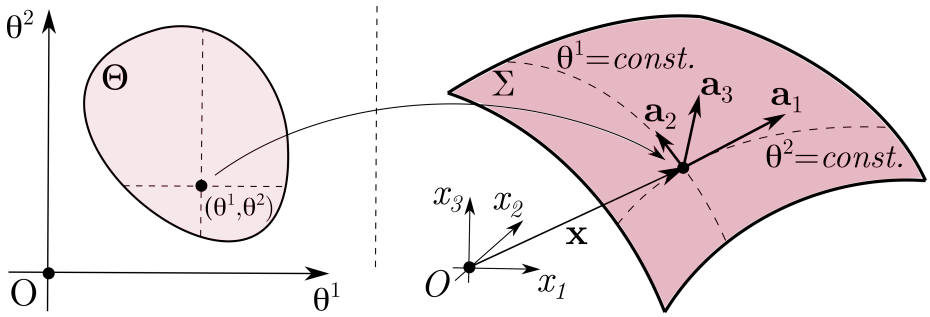

Figure 3.3: Geometry of the shell.

coordinate curves at that point. We also introduce the dual (contravariant) basis $\{\mathbf{a}^i\}$, defined by the orthogonality conditions

$$\mathbf{a}^i \cdot \mathbf{a}_j = \delta^i_{.j} \tag{3.6}$$

where $\delta^i_{.j}$ is the *Kronecker symbol*. In particular, since $\mathbf{a}_3$ is a unit vector and it's orthogonal to $\mathbf{a}_\alpha$, it follows that $\mathbf{a}^3 = \mathbf{a}_3$ and than $\mathbf{a}^\alpha$ are vectors contained in the tangent plane T_x.

The intrinsic surface metric in the chosen coordinate system is expressed as follows. The generic line element $d\mathbf{x}$ corresponding to the increments in the coordinates $d\theta^\alpha$ can be written as

$$d\mathbf{x} = \mathbf{a}_\alpha d\theta^\alpha \tag{3.7}$$

and its length is given by

$$\|d\mathbf{x}\|^2 = (\mathbf{a}_\alpha \cdot \mathbf{a}_\beta) d\theta^\alpha d\theta^\beta \tag{3.8}$$

which, by setting

$$a_{\alpha\beta} = \mathbf{a}_\alpha \cdot \mathbf{a}_\beta, \tag{3.9}$$

can be rewritten as

$$\|d\mathbf{x}\|^2 = a_{\alpha\beta} d\theta^\alpha d\theta^\beta. \tag{3.10}$$

This quadratic form is called *first fundamental form* of the surface and we can show (see [Kreyszig, 1991]) that the coefficients $a_{\alpha\beta}$ are the components of a tensor called *metric tensor*[3]. A generic vector or second order tensor field can be represented in terms of the natural basis $\{\mathbf{a}_i\}$, by means of their contravariant components as

$$\begin{aligned} \mathbf{u} &= u^\alpha \mathbf{a}_\alpha + u^3 \mathbf{a}_3 \\ \mathbf{T} &= t^{\alpha\beta} \mathbf{a}_\alpha \otimes \mathbf{a}_\beta + t^{3\alpha} \mathbf{a}_3 \otimes \mathbf{a}_\alpha + t^{\alpha 3} \mathbf{a}_\alpha \otimes \mathbf{a}_3 + t^{33} \mathbf{a}_3 \otimes \mathbf{a}_3. \end{aligned} \tag{3.12}$$

It is also possible to express the same vector or tensor fields in terms of the contravariant basis $\{\mathbf{a}^i\}$, by means of their covariant components[4]

$$\begin{aligned} \mathbf{u} &= u_\alpha \mathbf{a}^\alpha + u_3 \mathbf{a}^3 \\ \mathbf{T} &= t_{\alpha\beta} \mathbf{a}^\alpha \otimes \mathbf{a}^\beta + t_{3\alpha} \mathbf{a}^3 \otimes \mathbf{a}^\alpha + t_{\alpha 3} \mathbf{a}^\alpha \otimes \mathbf{a}^3 + t_{33} \mathbf{a}^3 \otimes \mathbf{a}^3. \end{aligned} \tag{3.13}$$

A vector field is called *superficial* if the only nonzero components are the u^α. Analogously we call a tensor field superficial if the only nonzero components are the $t^{\alpha\beta}$.

The generic surface element corresponding on Σ to the square of sides $d\theta^\alpha$ is identified by the vectors $\mathbf{a}_1 d\theta^1$ and $\mathbf{a}_2 d\theta^2$ and thus has area equal to

$$d\Sigma = \|\mathbf{a}_1 \times \mathbf{a}_2\| d\theta^1 d\theta^2. \tag{3.14}$$

Usually, we set

$$a = \|\mathbf{a}_1 \times \mathbf{a}_2\|^2 = \det(a_{\alpha\beta}) \tag{3.15}$$

so that

$$d\Sigma = \sqrt{a}\, d\theta^1 d\theta^2. \tag{3.16}$$

The scalar product

$$-\, d\mathbf{x} \cdot \mathbf{a}_3 = \kappa_{\alpha\beta} d\theta^\alpha d\theta^\beta \tag{3.17}$$

is called the *second fundamental form* of the surface. Being $\|\mathbf{a}_3\| = 1$, the derivatives $\mathbf{a}_{3,\beta}$ belong to the tangent plane and can thus be expressed by the *Weingarten formula*

$$\mathbf{a}_{3,\beta} = -\kappa^\alpha_{.\beta} \mathbf{a}_\alpha \tag{3.18}$$

being $\kappa^\alpha_{.\beta}$ the components of the *curvature tensor* of the surface. A curve on a surface Σ whose direction at every point is a principal direction of curvature is known as a *line of*

[3]We can introduce the metric tensor using the general notation as $\mathbf{A} = \mathbf{a}^\alpha \otimes \mathbf{a}_\alpha = \mathbf{a}_\alpha \otimes \mathbf{a}^\alpha$. In other words, the metric tensor is the linear function

$$\mathbf{A}: \quad d\mathbf{x} \cdot d\mathbf{x} = \mathbf{A} d\boldsymbol{\theta} \cdot d\boldsymbol{\theta}. \tag{3.11}$$

[4]In a similar way, one can define mixed-component vector or tensor fields, for which the reader can refer to the wide literature (e.g. [Itskov, 2007], [Green and Zerna, 1992]).

curvature of Σ (see [Kreyszig, 1991]). The derivatives $\mathbf{a}_{\alpha,\beta}$ are spatial vectors in general and can be expressed by the *Gauss formula*

$$\mathbf{a}_{\alpha,\beta} = \Gamma^{\lambda}_{\alpha\beta}\mathbf{a}_{\lambda} + \kappa_{\alpha\beta}\mathbf{a}_3 \tag{3.19}$$

where $\Gamma^{\lambda}_{\alpha\beta}$ are the *Christoffel symbols* with respect to the surface[5]. In the following we will make use of the covariant derivative with respect to θ^{α}, denoted by the symbol $|_{\alpha}$ and defined, respectively for a scalar, vector and second order contravariant tensor field as (see [Itskov, 2007] and [Davini, 1993])

$$\begin{aligned} &\varphi|_{\alpha} = \varphi_{,\alpha} \\ &u^{\alpha}|_{\beta} = u^{\alpha}{}_{,\beta} + u^{\lambda}\Gamma^{\alpha}_{\lambda\beta} \\ &t^{\alpha\beta}|_{\lambda} = t^{\alpha\beta}{}_{,\lambda} + t^{\alpha\rho}\Gamma^{\beta}_{\rho\lambda} + t^{\rho\beta}\Gamma^{\alpha}_{\rho\lambda}. \end{aligned} \tag{3.21}$$

We will use also the following definitions

$$\nabla\mathbf{u} = \mathbf{u}_{,i} \otimes \mathbf{a}^i = u_j|_i \mathbf{a}^j \otimes \mathbf{a}^i, \tag{3.22}$$

$$\operatorname{div}\mathbf{u} = \nabla\mathbf{u} \cdot \mathbf{A} = \mathbf{u}_{,i} \otimes \mathbf{a}^i \cdot \mathbf{a}^j \otimes \mathbf{a}_j = \mathbf{u}_{,i} \cdot \mathbf{a}^i = u^j|_i \mathbf{a}_j \cdot \mathbf{a}^i = u^i|_i, \tag{3.23}$$

$$\operatorname{div}\mathbf{T} = t^{ij}|_j \mathbf{a}_i, \tag{3.24}$$

where, in three dimensions, the covariant derivative becomes

$$t^{ij}|_k = t^{ij}{}_{,k} + t^{lj}\Gamma^{i}_{lk} + t^{il}\Gamma^{j}_{lk}. \tag{3.25}$$

To completely define a shell the model surface is not enough. Each point on the model surface is equipped with a transversal segment of given length, called *material fibre*. Hence, following the definition of body given before, a *shell-like* continuum is a 3d body whose points' positions $\mathbf{z}$ are faithfully representable by the pairs $(\mathbf{x}, \theta^3)$, being $\mathbf{x}$ a point on the model surface Σ and being θ^3 the distance from it:

$$\Omega = \{\mathbf{z} : \mathbf{z} = \mathbf{x} + \theta^3\mathbf{n},\ \mathbf{x} \in \Sigma,\ \theta^3 \in (-h_i, h_e)\} \tag{3.26}$$

where h_i and h_e are functions of $\mathbf{x}$ representing the distance from the model surface of the intrados and extrados respectively.

It should be noticed that, in order for the pair $(\mathbf{x}, \theta^3)$ to be an admissible representation for our aims, the orthogonal segments corresponding to different $\mathbf{x}$ must not intersect. This requisite is assured if the thickness $h_i + h_e$ is sufficiently small. It's also worth observing that the model surface doesn't necessarily have to be the so-called middle surface but it's sufficient for it to be inside the thickness of the body. Strictly speaking, the middle surface is defined as the locus of the centroids of the infinitesimal conoids normal to the middle

[5]For a general three-dimensional curvilinear coordinate system, the derivatives of the covariant basis vectors $\mathbf{a}_i = \mathbf{z}_{,i}$ define the Christoffel symbols

$$\mathbf{a}_{i,j} = \Gamma^{k}_{ij}\mathbf{a}_k. \tag{3.20}$$

Thus, we see that, for a surface, $\Gamma^{3}_{\alpha\beta} = \kappa_{\alpha\beta}$.

surface itself. In general, because of the curvature, the middle surface doesn't coincide with the middle surface in the geometric sense (i.e. the surface which has the same distance from the extrados and the intrados surfaces). Nevertheless, it is possible to demonstrate that, if the shell is homogeneous, Σ is the middle surface in the geometric sense if the thickness is small compared to the minimum radius of curvature [Davini, 1993]. This is the the case of the so-called *thin shells* for which $h_i = h$, $h_e = h$ and the total thickness is $2h$.

The use of the unit vector normal to the model surface, $\mathbf{n}$, is not mandatory. As is shown in the next section, in general, a unit vector in a suitable transversal direction may be used.

3.2 Kinematics of shells

The shell is not described only through the position of the points of its middle surface, as information about the thickness must be provided to characterise the behaviour of the three-dimensional body. Furthermore, one of our goal is to account for the arrangement of the masonry units and the joints' orientation in the model. These two needs can be dealt with by looking at the shell as a surface having an internal structure, which constitutes a case of a non-simple body. As it is done in the case of the theory of beams, where a cross-section is associated to each point of the line of axis, we associate to each point of the surface a material fibre. The material fibres are assumed to be straight so that a vector field, $\mathbf{h}$, is sufficient to describe them and we can thus resort to the so-called *director* theory (see [Ericksen, 1961], [Green and Laws, 1966]).

One can then define the injective function that associates material points to the director

$$\begin{aligned} \mathfrak{g} : \mathbb{S} &\to V, \\ p &\mapsto \mathbf{h} = \mathfrak{g}(p), \end{aligned} \tag{3.27}$$

and call it *director configuration*. In this context one calls *configuration* the couple $\{\mathfrak{f}, \mathfrak{g}\}$.

In order to identify a material point of the shell, it is often convenient to select one geometric configuration of the body, $\mathfrak{f}_R$, called *reference geometric configuration* and to use the unique position $\mathbf{x} = \mathfrak{f}_R(p)$ to label it. It should be noticed that the reference configuration has not to be necessarily the position occupied by the body in a certain instant.

To study the motion of a body it's necessary to describe the change of configuration in the time interval of interest $[t_0, t_1]$. In other words the motion of the body is known when all the configurations taken by the body in the time interval are known. If $\mathfrak{f}_R$ and $\mathfrak{f}$ are two geometric configurations such that

$$\mathbf{x} = \mathfrak{f}_R(p), \qquad \mathbf{y} = \mathfrak{f}(p) \tag{3.28}$$

and $\mathfrak{g}_R$ and $\mathfrak{g}$ are two director configurations such that

$$\mathbf{h} = \mathfrak{g}_R(p), \qquad \mathbf{d} = \mathfrak{g}(p) \tag{3.29}$$

then, given the bijectivity of the functions, the mappings

$$\begin{aligned} \mathbf{f} : \mathfrak{f}_R(\mathbb{S}) &\to \mathfrak{f}(\mathbb{S}), \\ \mathbf{x} &\mapsto \mathbf{y} = \mathfrak{f} \circ \mathfrak{f}_R^{-1}(\mathbf{x}) \end{aligned} \tag{3.30}$$

and

$$\begin{aligned} \mathbf{g} :\ & \mathfrak{g}_R(\mathbb{S}) \to \mathfrak{g}(\mathbb{S}), \\ & \mathbf{h} \mapsto \mathbf{d} = \mathfrak{g} \circ \mathfrak{g}_R^{-1}(\mathbf{h}) \end{aligned} \tag{3.31}$$

are induced. The couple $(\mathbf{f}, \mathbf{g})$ is called *change of configuration* of the shell from the reference configuration (see Figure 3.4). Clearly, $\mathbf{f}$ and $\mathbf{g}$ are bijective and their domains and codomains

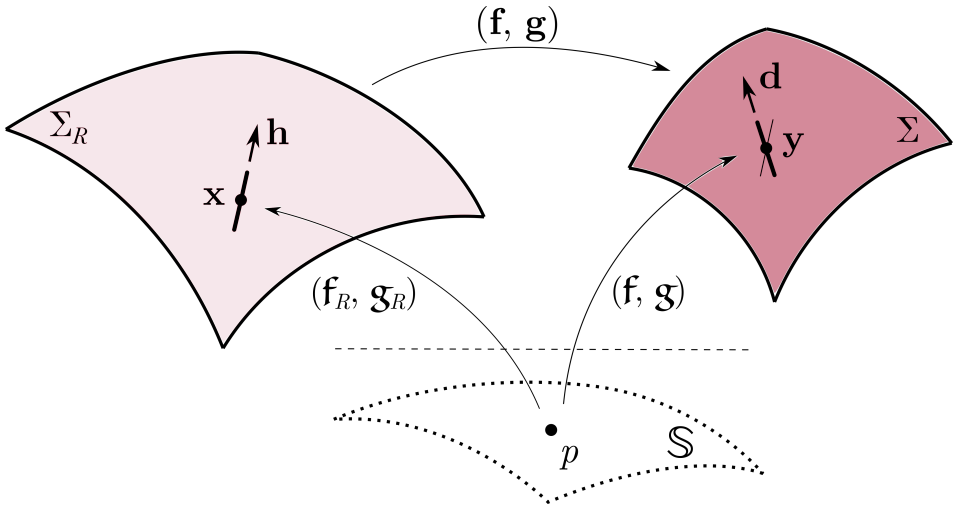

Figure 3.4: Change of configuration of the shell.

are subspace of $\mathbb{R}^3$ so that it makes sense to speak about continuity and differentiability. We require both the functions $\mathbf{f}$ and $\mathbf{g}$ to be at least C^1 diffeomorphisms and we require $\det \mathbf{F} > 0$, $\det \mathbf{G} > 0$, where $\mathbf{F} = \nabla \mathbf{f}$ and $\mathbf{G} = \nabla \mathbf{g}$. A change of configuration that satisfies the previous conditions is called a *deformation*. A *motion* of a shell is a smooth one-parameter family of deformations, the time t being the parameter [Gurtin et al., 2010], described by the functions

$$\begin{aligned} \mathbf{f} :\ & \Sigma_R \times [t_0, t_1] \to \mathbb{E}^3, \\ & (\theta^\alpha, t) \mapsto \mathbf{y}(\theta^\alpha, t), \end{aligned} \tag{3.32}$$

$$\begin{aligned} \mathbf{g} :\ & \Sigma_R \times [t_0, t_1] \to V, \\ & (\theta^\alpha, t) \mapsto \mathbf{d}(\theta^\alpha, t). \end{aligned} \tag{3.33}$$

So one can simply write

$$\mathbf{y}(\theta^\alpha, t_0) = \mathbf{x}(\theta^\alpha), \quad \mathbf{d}(\theta^\alpha, t_0) = \mathbf{h}(\theta^\alpha). \tag{3.34}$$

The current configuration, described by the fields $(\mathbf{y}, \mathbf{d})$, can be written

$$\mathbf{y} = \mathbf{x} + \mathbf{u}, \quad \mathbf{d} = \mathbf{h} + \mathbf{r}, \tag{3.35}$$

where $(\mathbf{u}, \mathbf{r})$ are the *generalised displacements*, that characterise the deformation. Since the reference configuration is fixed, the corresponding *generalised velocities* are

$$\dot{\mathbf{y}} = \dot{\mathbf{u}} = \mathbf{v}, \quad \dot{\mathbf{d}} = \dot{\mathbf{r}} = \mathbf{w}, \tag{3.36}$$

where the dot denotes the spatial time derivative.

It's worth observing that, although not specifically stated, it has been tacitly assumed that the material fibres remain straight during the motion so that they can be effectively described by a vector field. A stronger kinematical constraint that is introduced on the admissible motions is that the material fibre is perfectly rigid so that the director cannot change its length during the motion but can only rotate. This means that the material fibre is fully described just by the orientation of the director, which accordingly can be assumed to be a unit vector: $\|\mathbf{d}\| = 1$. It is easy to see that this restriction leads to the following

$$\dot{\mathbf{d}} \perp \mathbf{d}. \tag{3.37}$$

By virtue of the constraint, the director $\mathbf{d}$ is obtained from $\mathbf{h}$ by a rotation

$$\mathbf{d} = \mathbf{Q}\mathbf{h}, \qquad \mathbf{Q} \in \mathrm{SO}(3), \tag{3.38}$$

where SO(3) is the orthogonal special group (rotation group), and then

$$\mathbf{w} = \dot{\mathbf{Q}}\mathbf{h} = \dot{\mathbf{Q}}\mathbf{Q}^{\mathsf{T}}\mathbf{d} = \mathbf{\Omega}\mathbf{d}. \tag{3.39}$$

It is easy to show that $\mathbf{\Omega} \in$ Skw, being Skw the space of skew-symmetric second order tensors, so that we can write

$$\mathbf{w} = \boldsymbol{\omega} \times \mathbf{d} \tag{3.40}$$

where $\boldsymbol{\omega}$ is the axial vector of $\mathbf{\Omega}$. Therefore the vector $\mathbf{w}$ is orthogonal to the vector $\mathbf{d}$.

Definition of the local triad

One can find it convenient to refer to the local triad $\{\mathbf{a}_1, \mathbf{a}_2, \mathbf{h}\}$ to describe material fields. The quantities in the reference configuration, when needed, will be denoted by a subscript $\bullet_R$ while the quantities without the subscript are referred to the current configuration. The coordinate system $\{O, \theta^\alpha\}$ is convected, so that it constitutes a coordinate system also for the deformed surface, having the representation

$$\Sigma: \quad \mathbf{y} = \mathbf{y}(\theta^\alpha) = \mathbf{x}(\theta^\alpha) + \mathbf{u}, \quad \theta^\alpha \in \Theta \subset \mathbb{R}^2. \tag{3.41}$$

This parametrisation induces also on Σ a system of coordinate lines and furnishes the following natural basis for the representation of the surface spatial fields

$$\mathbf{e}_\alpha = \mathbf{y}_{,\alpha} = \mathbf{a}_\alpha + \mathbf{u}_{,\alpha}\,. \tag{3.42}$$

For the third vector completing the triad, instead of using the outward unit normal vector in the current configuration, given by

$$\mathbf{n} = \frac{\mathbf{e}_1 \times \mathbf{e}_2}{\|\mathbf{e}_1 \times \mathbf{e}_2\|}, \tag{3.43}$$

one can find it convenient to refer to the deformed director instead, $\mathbf{e}_3 = \mathbf{d}$. Since $\mathbf{e}_3$ is not constrained to be orthogonal to the tangent plane T_y then the contravariant basis vectors are not contained in the plane T_y. We call *normal space* (to the generic fibre) at point y

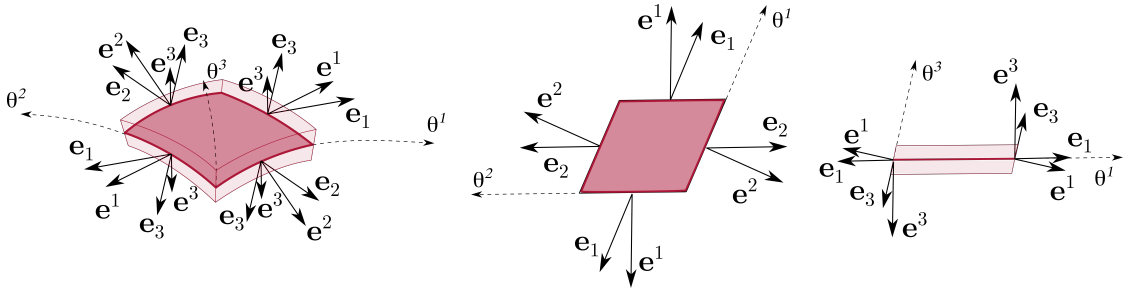

Figure 3.5: Covariant and contravariant basis vectors in current configuration.

the space $N_y = \text{span}\{\mathbf{e}^\alpha(\mathbf{y})\}$. The covariant and contravariant basis vectors are shown in Figure 3.5. We remark that, since $\|\mathbf{d}\| = 1$, then $\mathbf{e}_{3,\alpha} \perp \mathbf{e}_3$ and it can be written in general form as

$$\mathbf{e}_{3,\alpha} = -\varkappa^\beta_{.\alpha}\mathbf{e}_\beta, \tag{3.44}$$

where $\varkappa^\beta_{.\alpha}$ can be defined as *director curvatures* and are different from the surface curvatures $\kappa^\beta_{.\alpha}$ unless $\mathbf{d} \equiv \mathbf{n}$. In analogy with the geometric curvatures, we call a curve on a surface Σ whose direction at every point is a principal direction of director curvature a *line of director curvature* of Σ. The field of director vectors and the director curvatures (see Figure 3.6) enable describing the joints and specifying the failure criterion with reference to them. Moreover, since in general $\mathbf{e}_3$ is not the normal vector to the surface, we also put $\mathbf{e}_{\alpha,\beta} = \Gamma^\lambda_{\alpha\beta}\mathbf{e}_\lambda + \varkappa_{\alpha\beta}\mathbf{e}_3$, because, while $\kappa_{\alpha\beta}$ depends on the surface, $\varkappa_{\alpha\beta}$ depends on the orientation chosen for the director.

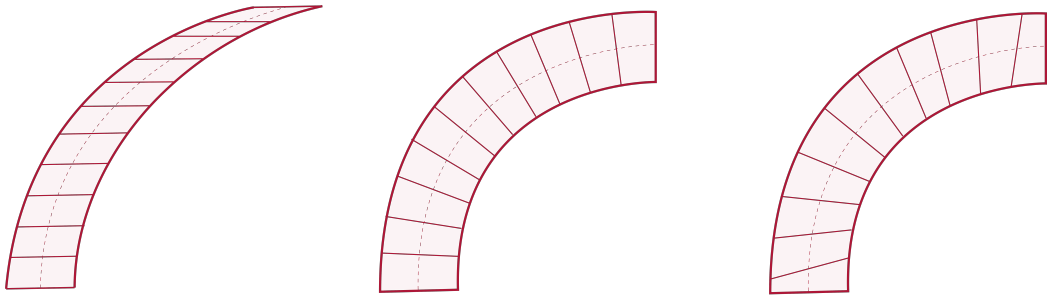

(a) (b) (c)

Figure 3.6: Difference between the curvatures and the director curvatures: the director curvatures are null while the curvatures are different from zero (a); the director curvatures coincide with the curvatures since $\mathbf{e}_3 = \mathbf{n}$ (b); the curvatures and the director curvatures are different from each other and both different from zero (c).

3.3 Balance laws for shells

In this section we deal with physical quantities that are associated to *parts* of the body, and not to material points. A *part* of a shell is a subset $\mathbb{P} \in \mathbb{S}$ with the same properties. We

denote with $\Pi \in \Sigma$ the image of the geometric configuration of the part $\mathbb{P}$. We say that $\mathfrak{E}$ is a (surface) *extensive* physical property if there is a function $\mathfrak{E}(\Pi)$ defined on the set $\mathfrak{s}$ of all parts of $\mathbb{S}$ such that

1. $\mathfrak{E}(\Pi_1 \cup \Pi_2) = \mathfrak{E}(\Pi_1) + \mathfrak{E}(\Pi_2)$ for all arbitrary disjoined parts Π_1 and Π_2;
2. $\mathfrak{E}(\Pi) \to 0$ as $area(\Pi) \to 0$.

Under these circumstances there exist a density $\mathfrak{e}(\mathbf{y})$ such that

$$\mathfrak{E}(\Pi) = \int_{\Pi} \mathfrak{e}(\mathbf{y})\, d\Sigma, \tag{3.45}$$

where $d\Sigma$ is the area element of the part Π.

Mass and micro inertia conservation laws

The inertial properties of the shell can be defined by considering the material fibre as a straight rigid rod endowed with a uniformly distributed mass ρ_F. The mass of the single fibre, with dimensions of mass per unit area, is given by

$$m_F = \int_{-h}^{h} \rho_F d\zeta = 2h\rho_F. \tag{3.46}$$

The centre of mass of the fibre is $\mathbf{y}$ because the first order moments vanish

$$\int_{-h}^{h} \rho_F \zeta \mathbf{d}\, d\zeta = \mathbf{0}. \tag{3.47}$$

Since the moment of inertia around the fibre axis is zero, the second order moments can be evaluated as

$$\mathbf{J}_F = \int_{-h}^{h} \rho_F \Big((\zeta\mathbf{d} \cdot \zeta\mathbf{d})\mathbf{I} - \zeta\mathbf{d} \otimes \zeta\mathbf{d} \Big)\, d\zeta = \frac{2}{3}\rho_F h^3 (\mathbf{I} - \mathbf{d} \otimes \mathbf{d}). \tag{3.48}$$

Considering the generic surface element pertaining to a point in the current configuration, and denoted by $\upsilon(\mathbf{y})$ the number of fibres per unit area, the total mass and total inertia of the surface element are then

$$dm(\mathbf{y}) = \upsilon(\mathbf{y}) m_F d\Sigma, \quad d\mathbf{J}(\mathbf{y}) = \upsilon(\mathbf{y}) \mathbf{J}_F d\Sigma. \tag{3.49}$$

The *mass* is a non-negative extensive quantity $m(\Pi)$ defined on each part of the shell that has the representation

$$m(\Pi) = \int_{\Pi} \rho\, d\Sigma \tag{3.50}$$

where $\rho = \upsilon(\mathbf{y}) m_F$ is a non-negative scalar function called *mass density*. The *moment of inertia* is a non-negative extensive quantity $\mathbf{J}(\Pi)$ defined on each part of the shell that has the representation

$$\mathbf{J}(\Pi) = \int_{\Pi} \iota(\mathbf{I} - \mathbf{d} \otimes \mathbf{d})\, d\Sigma \tag{3.51}$$

where $\iota = \frac{2}{3}\upsilon(\mathbf{y})\rho_F h^3$ is a non-negative scalar function called *inertia density*.

If there is no mass flux across the boundary $\partial\Pi$ and there is no mass supply in the domain Π, then the law of *conservation of mass* can be written as

$$\frac{d}{dt}\int_\Pi \rho\, d\Sigma = 0 \tag{3.52}$$

which must hold for each part. By applying the transport theorem we can write

$$\dot{m}(\Pi) = \int_\Pi (\dot{\rho} + \rho \operatorname{div}\mathbf{v})\, d\Sigma \tag{3.53}$$

and then

$$\dot{\rho} + \rho \operatorname{div}\mathbf{v} = 0 \tag{3.54}$$

which can be easily integrated giving

$$\rho = \rho_R \frac{1}{\det \mathbf{F}}, \tag{3.55}$$

where $\rho_R = \upsilon_R(\mathbf{x})m_F$ is the mass density in the reference configuration. Analogously, we state the law of *conservation of micro inertia*[6] as

$$\frac{d}{dt}\int_\Pi \iota\, d\Sigma = 0, \tag{3.56}$$

that gives

$$\iota = \iota_R \frac{1}{\det \mathbf{F}}, \tag{3.57}$$

where ι_R is the inertia density in the reference configuration.

Inertial properties of shells

Besides the mass, we introduce other two vectorial extensive quantities: the *momentum*

$$\mathfrak{P} = \int_\Pi \mathbf{p}\, d\Sigma, \tag{3.58}$$

where $\mathbf{p}$ is the momentum density, and the *angular momentum*

$$\mathfrak{L} = \int_\Pi \mathbf{l}\, d\Sigma, \tag{3.59}$$

where $\mathbf{l}$ is the angular momentum density. For a Cosserat surface the momentum density per unit area, can be written as

$$\mathbf{p} \triangleq \upsilon \int_{-h}^{h} \rho_F \dot{\mathbf{s}}\, d\zeta = \upsilon \int_{-h}^{h} \rho_F(\mathbf{v} + \zeta\mathbf{w})\, d\zeta = 2\upsilon h\rho_F\mathbf{v} + \int_{-h}^{h} \rho_F\zeta\mathbf{w} = \rho\mathbf{v} \tag{3.60}$$

[6] For a deepening on the concept of micro-inertia and on the nonlocal continuum field theories for bodies with micro-structure see for example [Eringen, 2002].

as the last integral vanishes because the function is odd. Here $\mathbf{s} = \mathbf{y} + \zeta\mathbf{d}$ denotes the position in $\mathbb{E}^3$ of the generic point on the material fibre in current configuration. The angular momentum density per unit area is defined as the moment of momentum of the material fibres

$$\begin{aligned}\mathbf{l} \triangleq \upsilon \int_{-h}^{h} (\mathbf{s} \times \rho_F \dot{\mathbf{s}})\, d\zeta = \upsilon \int_{-h}^{h} \Big((\mathbf{y} + \zeta\mathbf{d}) \times \rho_F (\mathbf{v} + \zeta\mathbf{w}) \Big)\, d\zeta = \\ = \upsilon \int_{-h}^{h} \Big(\mathbf{y} \times \rho_F \mathbf{v} + \zeta\mathbf{d} \times \rho_F \mathbf{v} + \mathbf{y} \times \zeta\mathbf{w} + \zeta^2 \mathbf{d} \times \rho_F \mathbf{w} \Big)\, d\zeta.\end{aligned} \tag{3.61}$$

The second and third term in the last integral vanish because they are linear in ζ and the integral is evaluated between $-h$ and h. We remark that the choice of a different model surface will cause those terms not to vanish. Since $\mathbf{w} = \boldsymbol{\omega} \times \mathbf{d}$ we have

$$\mathbf{d} \times \boldsymbol{\omega} \times \mathbf{d} = (\mathbf{d} \cdot \mathbf{d})\boldsymbol{\omega} - (\mathbf{d} \cdot \boldsymbol{\omega})\mathbf{d} = \boldsymbol{\omega} \tag{3.62}$$

and

$$\mathbf{l} = \mathbf{y} \times \rho\mathbf{v} + \upsilon\mathbf{d} \times \frac{2}{3}\rho_F h^3 \mathbf{w} = \mathbf{y} \times \rho\mathbf{v} + \mathbf{d} \times \iota\mathbf{w} = \mathbf{y} \times \rho\mathbf{v} + \iota\boldsymbol{\omega}. \tag{3.63}$$

Frequently, the last term is put in the form

$$\mathbf{d} \times \iota\mathbf{w} = \mathbf{J}\boldsymbol{\omega}. \tag{3.64}$$

In the same way used to derive the momentum and the angular momentum, we can introduce a scalar quantity, the *kinetic energy* which is a state function

$$\mathcal{T} = \int_{\Pi} \tau\, d\Sigma \tag{3.65}$$

where τ is the kinetic energy density per unit area, defined as follows

$$\begin{aligned}\tau \triangleq \frac{1}{2}\upsilon \int_{-h}^{h} \rho_F \dot{\mathbf{s}} \cdot \dot{\mathbf{s}}\, d\zeta = \frac{1}{2}\upsilon \int_{-h}^{h} \rho_F \Big((\mathbf{v} + \zeta\mathbf{w}) \cdot (\mathbf{v} + \zeta\mathbf{w}) \Big)\, d\zeta = \\ = \frac{1}{2}\upsilon \int_{-h}^{h} \rho_F \Big(\mathbf{v} \cdot \mathbf{v} + 2\zeta\mathbf{v} \cdot \zeta\mathbf{w} + \zeta^2 \mathbf{w} \cdot \mathbf{w} \Big)\, d\zeta.\end{aligned} \tag{3.66}$$

The second term in the integral vanishes because it is linear in ζ and the integral is evaluated between $-h$ and h, so the kinetic energy density is

$$\tau = \frac{1}{2}\rho\mathbf{v} \cdot \mathbf{v} + \frac{1}{2}\iota\mathbf{w} \cdot \mathbf{w}. \tag{3.67}$$

Balance of momentum and angular momentum

To model the interactions between the body and the environment we introduce the (generalised) forces, which are extensive quantities. It is usually assumed that there are two kind of forces: the *body* forces that act at each internal point in the domain of the generic part Π and the *contact* forces that act at points on the boundary of the domain of the generic part

$\partial\Pi$. To define a force we must say how it contributes to the resultant force, to the resultant moment and how it does work. For shells, we introduce the body forces $\mathbf{b}(\mathbf{y}, t)$ and the body couple forces $\overline{\mathbf{c}}(\mathbf{y}, t)$ both per unit surface acting at each interior point, and the contact forces $\mathbf{t}(\mathbf{y}, \boldsymbol{\nu}, t)$ and the contact couple forces $\overline{\mathbf{m}}(\mathbf{y}, \boldsymbol{\nu}, t)$ both per unit length acting at each point on the boundary having the external unit normal $\boldsymbol{\nu}$. The couple of forces are thought to act at the endpoints of the generic material fibre and we also assume that they belong to the normal space N_y. In this way, the choice of the director implies also the choice of what component of the couples is zero. This assumption is customary in shell theory and would deserve a further discussion, also in relation to the hypothesis of director in-extensibility, but we will not carry out such deepening in the present work. The generalised forces are shown in Figure 3.7 for clarity. The resultant force on the generic part is then

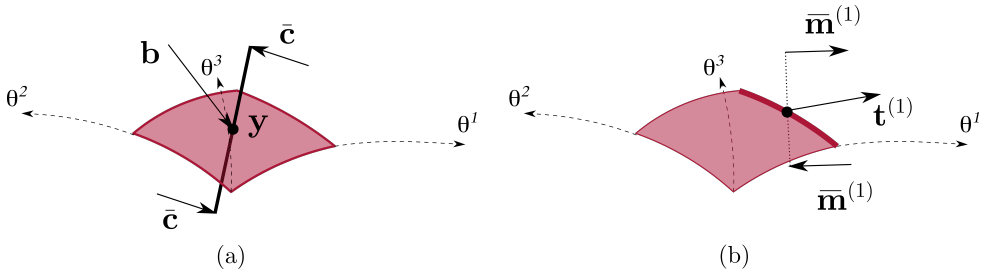

Figure 3.7: Body forces (a) and contact forces on the boundary of normal vector $\mathbf{e}^1$ (b).

$$\mathfrak{R} \triangleq \int_{\Pi} \mathbf{b}\, d\Sigma + \int_{\partial\Pi} \mathbf{t}\, d\Gamma, \tag{3.68}$$

where $\Gamma = \partial\Pi$ is the curve in the three-dimensional space bounding the region Π. The resultant moment is defined as

$$\begin{aligned} \mathfrak{M} &\triangleq \int_{\Pi} \Big(\mathbf{y} \times \mathbf{b} + 2(h\mathbf{d} \times \overline{\mathbf{c}})\Big)\, d\Sigma + \int_{\partial\Pi} \Big(\mathbf{y} \times \mathbf{t} + 2(h\mathbf{d} \times \overline{\mathbf{m}})\Big)\, d\Gamma = \\ &= \int_{\Pi} (\mathbf{y} \times \mathbf{b} + \mathbf{d} \times \mathbf{c})\, d\Sigma + \int_{\partial\Pi} (\mathbf{y} \times \mathbf{t} + \mathbf{d} \times \mathbf{m})\, d\Gamma, \end{aligned} \tag{3.69}$$

being $\mathbf{c} = 2h\overline{\mathbf{c}}$ and $\mathbf{m} = 2h\overline{\mathbf{m}}$, and can also be rewritten in the following way

$$\mathfrak{M} = \int_{\Pi} (\mathbf{y} \times \mathbf{b} + \mathfrak{c})\, d\Sigma + \int_{\partial\Pi} (\mathbf{y} \times \mathbf{t} + \mathfrak{m})\, d\Gamma, \tag{3.70}$$

by the introduction of $\mathfrak{c} = \mathbf{d} \times \mathbf{c}$ and $\mathfrak{m} = \mathbf{d} \times \mathbf{m}$ which are, respectively, the external body torque vector and the contact torque vector. Further, consequently to the kinematical hypotheses made, the work increment of the external loads can be defined as

$$\begin{aligned} đ\mathcal{W} &\triangleq \int_{\Pi} (\mathbf{b} \cdot d\mathbf{u} + 2h\overline{\mathbf{c}} \cdot d\mathbf{r})\, d\Sigma + \int_{\partial\Pi} (\mathbf{t} \cdot d\mathbf{u} + 2h\overline{\mathbf{m}} \cdot d\mathbf{r})\, d\Gamma = \\ &= \int_{\Pi} (\mathbf{b} \cdot \mathbf{v} + \mathbf{c} \cdot \mathbf{w})\, d\Sigma\, dt + \int_{\partial\Pi} (\mathbf{t} \cdot \mathbf{v} + \mathbf{m} \cdot \mathbf{w})\, d\Gamma\, dt, \end{aligned} \tag{3.71}$$

which again, by noticing that

$$\begin{aligned}\mathbf{c}\cdot\mathbf{w} &= \mathbf{c}\cdot\boldsymbol{\omega}\times\mathbf{d} = (\mathbf{d}\times\mathbf{c})\cdot\boldsymbol{\omega},\\ \mathbf{m}\cdot\mathbf{w} &= \mathbf{m}\cdot\boldsymbol{\omega}\times\mathbf{d} = (\mathbf{d}\times\mathbf{m})\cdot\boldsymbol{\omega},\end{aligned} \tag{3.72}$$

can be rewritten as

$$đ\mathcal{W} = \int_\Pi (\mathbf{b}\cdot\mathbf{v} + \mathfrak{c}\cdot\boldsymbol{\omega})\, d\Sigma\, dt + \int_{\partial\Pi} (\mathbf{t}\cdot\mathbf{v} + \mathfrak{m}\cdot\boldsymbol{\omega})\, d\Sigma\, dt. \tag{3.73}$$

In general, $đ\mathcal{W}$ is an inexact differential except in the case in which forces are conservative and the expressions in the integrals can be expressed as total differentials of potential scalar quantities (in that instance, the work increment will be denoted by $d\mathcal{W}$).

It's worth observing that, formally, $\mathbf{c}$ is a polar vector having the physical dimensions of a force while $\mathfrak{c}$ is an axial vector having the dimensions of a force times a length (torque). For our aims, it is convenient to keep working with the forces $\mathbf{c}$ and $\mathbf{m}$ instead of the couples $\mathfrak{c}$ and $\mathfrak{m}$.

The *external power* (or power of the external forces or rate of working) is defined as

$$\mathcal{P}_E = \int_\Pi (\mathbf{b}\cdot\mathbf{v} + \mathbf{c}\cdot\mathbf{w})\, d\Sigma + \int_{\partial\Pi} (\mathbf{t}\cdot\mathbf{v} + \mathbf{m}\cdot\mathbf{w})\, d\Gamma. \tag{3.74}$$

The balance laws for momentum and angular momentum state that

$$\mathfrak{R} = \frac{d\mathfrak{P}}{dt}, \quad \mathfrak{M} = \frac{d\mathfrak{L}}{dt}, \tag{3.75}$$

and, making the terms explicit, they are written as

$$\begin{aligned}&\frac{d}{dt}\int_\Pi \rho\mathbf{v}\, d\Sigma = \int_\Pi \mathbf{b}\, d\Sigma + \int_{\partial\Pi} \mathbf{t}\, d\Gamma,\\ &\frac{d}{dt}\int_\Pi (\mathbf{y}\times\rho\mathbf{v} + \mathbf{d}\times\iota\mathbf{w})\, d\Sigma = \int_\Pi (\mathbf{y}\times\mathbf{b} + \mathbf{d}\times\mathbf{c})\, d\Sigma + \int_{\partial\Pi} (\mathbf{y}\times\mathbf{t} + \mathbf{d}\times\mathbf{m})\, d\Gamma.\end{aligned} \tag{3.76}$$

3.3.1 Cauchy theorem

Let's consider the balance of a part Π in current configuration, bounded by the curve Γ. One can prove the following (see [Davini, 1993])

$$\int_{\partial\Pi} \boldsymbol{\nu}\, d\Gamma = \int_\Pi \varkappa^\alpha_{\cdot\alpha}\mathbf{e}_3\, d\Sigma. \tag{3.77}$$

Indeed, by divergence theorem

$$\int_{\partial\Pi} \nu_\alpha\mathbf{e}^\alpha\, d\Gamma = \int_\Pi \left(\mathbf{e}^\alpha{}_{,\alpha} + \Gamma^\beta_{\beta\alpha}\mathbf{e}^\alpha\right) d\Sigma. \tag{3.78}$$

We notice

$$\Gamma^\beta_{\beta\alpha} = \mathbf{e}_{\beta,\alpha}\cdot\mathbf{e}^\beta = \mathbf{e}_{\alpha,\beta}\cdot\mathbf{e}^\beta = -\mathbf{e}^\beta{}_{,\beta}\cdot\mathbf{e}_\alpha \tag{3.79}$$

and

$$\mathbf{e}^{\alpha}{}_{,\alpha} = (\mathbf{e}^{\alpha}{}_{,\alpha} \cdot \mathbf{e}_{\beta})\mathbf{e}^{\beta} + (\mathbf{e}^{\alpha}{}_{,\alpha} \cdot \mathbf{e}_{3})\mathbf{e}^{3} \tag{3.80}$$

and the first term in the right expression becomes

$$\int_{\Pi} \Big((\mathbf{e}^{\alpha}{}_{,\alpha} \cdot \mathbf{e}_{\beta})\mathbf{e}^{\beta} + (\mathbf{e}^{\alpha}{}_{,\alpha} \cdot \mathbf{e}_{3})\mathbf{e}^{3} - (\mathbf{e}^{\beta}{}_{,\beta} \cdot \mathbf{e}_{\alpha})\mathbf{e}^{\alpha} \Big)\, d\Sigma = \int_{\Pi} (\mathbf{e}^{\alpha}{}_{,\alpha} \cdot \mathbf{e}_{3})\mathbf{e}^{3}\, d\Sigma. \tag{3.81}$$

Remembering $\mathbf{e}^{\alpha}{}_{,\alpha} \cdot \mathbf{e}_{3} = -\mathbf{e}^{\alpha} \cdot \mathbf{e}_{3,\alpha} \equiv \varkappa^{\alpha}_{.\alpha}$ the thesis is obtained. If $\mathbf{e}_3 = \mathbf{n}$, then $\varkappa^{\alpha}_{.\alpha} = \kappa^{\alpha}_{.\alpha}$.

Cauchy theorem states that if the body forces and couples are bounded, there exist two second order tensors $\mathbf{T}(\mathbf{y})$ and $\mathbf{M}(\mathbf{y})$ such that the force and couple per unit length acting on a line element of unit normal $\boldsymbol{\nu}$ are given by

$$\mathbf{t} = \mathbf{T}\boldsymbol{\nu}, \quad \mathbf{m} = \mathbf{M}\boldsymbol{\nu}, \tag{3.82}$$

with

$$\mathbf{T} = \mathbf{t}^{\alpha} \otimes \mathbf{e}_{\alpha}, \quad \mathbf{M} = \mathbf{m}^{\alpha} \otimes \mathbf{e}_{\alpha}. \tag{3.83}$$

The proof is based on the standard argument ([Davini, 1993]). We consider a family of curvilinear triangle $\Delta\Pi$ on Π with two sides on the coordinate lines $\theta^{\alpha} = const$ and the third, having unit normal $\boldsymbol{\nu} = \nu_{\alpha}\mathbf{e}^{\alpha}$. We denote with ds_1 the length of the side along $\theta^2 = const$, with ds_2 the length of the side along $\theta^1 = const$ and with ds the length of the third side. By the mean value theorem and the (3.77) we have

$$\boldsymbol{\nu} ds - \frac{\mathbf{e}^1}{\|\mathbf{e}^1\|} ds_2 - \frac{\mathbf{e}^2}{\|\mathbf{e}^2\|} ds_1 = \mathbf{o}(ds), \tag{3.84}$$

where $\mathbf{o}(ds)$ is a vector with element being higher order infinitesimal in ds. Multiplying (3.77) by $\mathbf{e}_{\alpha}$ and keeping first order terms we find

$$\|\mathbf{e}^1\|(\boldsymbol{\nu} \cdot \mathbf{e}_1) ds = ds_2, \quad \|\mathbf{e}^2\|(\boldsymbol{\nu} \cdot \mathbf{e}_2) ds = ds_1. \tag{3.85}$$

Using $(3.76)_1$ on $\Delta\Pi$ together with the mean value theorem we get

$$\mathbf{t}(\boldsymbol{\nu}) ds + \mathbf{t}\Big(- \frac{\mathbf{e}^1}{\|\mathbf{e}^1\|}\Big) ds_2 + \mathbf{t}\Big(- \frac{\mathbf{e}^2}{\|\mathbf{e}^2\|}\Big) ds_1 = \mathbf{o}(ds). \tag{3.86}$$

On dividing by ds and passing to the limit $ds \to 0$ the preceding equation becomes

$$\mathbf{t}(\boldsymbol{\nu}) + \mathbf{t}\Big(- \frac{\mathbf{e}^{\alpha}}{\|\mathbf{e}^{\alpha}\|}\Big) \|\mathbf{e}^{\alpha}\|(\boldsymbol{\nu} \cdot \mathbf{e}_{\alpha}) = \mathbf{0}. \tag{3.87}$$

Assuming $\boldsymbol{\nu} = \mathbf{e}^{\beta}/\|\mathbf{e}^{\beta}\|$ we have the action-reaction principle

$$\mathbf{t}\Big(\frac{\mathbf{e}^{\beta}}{\|\mathbf{e}^{\beta}\|}\Big) = -\mathbf{t}\Big(-\frac{\mathbf{e}^{\beta}}{\|\mathbf{e}^{\beta}\|}\Big). \tag{3.88}$$

Therefore, we find that

$$\mathbf{t}(\boldsymbol{\nu}) = \mathbf{t}\Big(\frac{\mathbf{e}^{\alpha}}{\|\mathbf{e}^{\alpha}\|}\Big) \|\mathbf{e}^{\alpha}\|(\boldsymbol{\nu} \cdot \mathbf{e}_{\alpha}), \tag{3.89}$$

that is

$$\mathbf{t}(\boldsymbol{\nu}) = (\mathbf{t}^\alpha \otimes \mathbf{e}_\alpha)\boldsymbol{\nu} \tag{3.90}$$

being

$$\mathbf{t}^\alpha \equiv \mathbf{t}\big(\frac{\mathbf{e}^\alpha}{\|\mathbf{e}^\alpha\|}\big)\|\mathbf{e}^\alpha\|. \tag{3.91}$$

Analogously, one can repeat the preceding steps for the vector $\mathbf{m}$, obtaining

$$\mathbf{m}(\boldsymbol{\nu}) = (\mathbf{m}^\alpha \otimes \mathbf{e}_\alpha)\boldsymbol{\nu} \tag{3.92}$$

being

$$\mathbf{m}^\alpha \equiv \mathbf{m}\big(\frac{\mathbf{e}^\alpha}{\|\mathbf{e}^\alpha\|}\big)\|\mathbf{e}^\alpha\|. \tag{3.93}$$

3.3.2 Local momentum balance laws

Applying Cauchy's theorem to $(3.76)_1$ and using the conservation of mass yield

$$\int_\Pi \rho\dot{\mathbf{v}}\, d\Sigma = \int_\Pi \mathbf{b}\, d\Sigma + \int_{\partial\Pi} \mathbf{T}\boldsymbol{\nu}\, d\Gamma, \tag{3.94}$$

that can be rewritten as

$$\int_\Pi \rho\dot{\mathbf{v}}\, d\Sigma = \int_\Pi \mathbf{b}\, d\Sigma + \int_{\partial\Pi} (\mathbf{t}^\alpha \otimes \mathbf{e}_\alpha)\boldsymbol{\nu}\, d\Gamma. \tag{3.95}$$

By divergence theorem the equation becomes (see [Davini, 1993])

$$\int_\Pi \rho\dot{\mathbf{v}}\, d\Sigma = \int_\Pi \mathbf{b}\, d\Sigma + \int_\Pi \mathbf{t}^\alpha|_\alpha\, d\Sigma. \tag{3.96}$$

Since this equation must hold for each $\Pi \subset \Sigma$, if the integrand is continuous one can apply localisation lemma and get

$$\mathbf{t}^\alpha|_\alpha + \mathbf{b} = \rho\dot{\mathbf{v}}, \tag{3.97}$$

where

$$\mathbf{t}^\alpha|_\alpha = \mathbf{t}^\alpha{}_{,\alpha} + \mathbf{t}^\alpha\Gamma^\lambda_{\lambda\alpha}. \tag{3.98}$$

Applying the definition of covariant derivative,

$$\mathbf{t}^\alpha|_\alpha = (t^{\beta\alpha}|_\alpha - t^{3\alpha}\varkappa^\beta_{.\alpha})\mathbf{e}_\beta + (t^{3\alpha}|_\alpha + t^{\beta\alpha}\varkappa_{\alpha\beta})\mathbf{e}_3 \tag{3.99}$$

and remembering that, formally, $\Gamma^3_{\alpha\beta} = \varkappa_{\alpha\beta}$ and $\Gamma^\beta_{3\alpha} = -\varkappa^\beta_\alpha$, the balance equation can also be rewritten as

$$\operatorname{div}\mathbf{T} + \mathbf{b} = \rho\dot{\mathbf{v}}. \tag{3.100}$$

Analogously, applying Cauchy's theorem to $(3.76)_2$ and using the conservation of mass and micro inertia yield

$$\begin{aligned}\int_\Pi (\mathbf{y}\times\rho\dot{\mathbf{v}} + \mathbf{d}\times\iota\dot{\mathbf{w}})\, d\Sigma = \\ = \int_\Pi (\mathbf{y}\times\mathbf{b} + \mathbf{d}\times\mathbf{c})\, d\Sigma + \int_{\partial\Pi} (\mathbf{y}\times\mathbf{T}\boldsymbol{\nu} + \mathbf{d}\times\mathbf{M}\boldsymbol{\nu})\, d\Gamma,\end{aligned} \tag{3.101}$$

that can be rewritten as

$$\begin{aligned}\int_\Pi (\mathbf{y}\times\rho\dot{\mathbf{v}}+\mathbf{d}\times\iota\dot{\mathbf{w}})\,d\Sigma = \\ = \int_\Pi (\mathbf{y}\times\mathbf{b}+\mathbf{d}\times\mathbf{c})\,d\Sigma + \int_{\partial\Pi}\left(\mathbf{y}\times(\mathbf{t}^\alpha\otimes\mathbf{e}_\alpha)\boldsymbol{\nu}+\mathbf{d}\times(\mathbf{m}^\alpha\otimes\mathbf{e}_\alpha)\boldsymbol{\nu}\right)d\Gamma.\end{aligned} \tag{3.102}$$

By divergence theorem one obtains

$$\begin{aligned}\int_\Pi (\mathbf{y}\times\rho\dot{\mathbf{v}}+\mathbf{d}\times\iota\dot{\mathbf{w}})\,d\Sigma = \int_\Pi (\mathbf{y}\times\mathbf{b}+\mathbf{d}\times\mathbf{c})\,d\Sigma + \\ + \int_\Pi \left(\mathbf{y}_{,\alpha}\times\mathbf{t}^\alpha+\mathbf{y}\times\mathbf{t}^\alpha|_\alpha+\mathbf{d}_{,\alpha}\times\mathbf{m}^\alpha+\mathbf{d}\times\mathbf{m}^\alpha|_\alpha\right)d\Sigma.\end{aligned} \tag{3.103}$$

On using (3.97) the previous equation becomes

$$\int_\Pi \mathbf{d}\times\iota\dot{\mathbf{w}}\,d\Sigma = \int_\Pi \mathbf{d}\times\mathbf{c}\,d\Sigma + \int_\Pi (\mathbf{y}_{,\alpha}\times\mathbf{t}^\alpha+\mathbf{d}_{,\alpha}\times\mathbf{m}^\alpha+\mathbf{d}\times\mathbf{m}^\alpha|_\alpha)\,d\Sigma. \tag{3.104}$$

Remembering that $\mathbf{y}_{,\alpha}=\mathbf{e}_\alpha$, $\mathbf{d}=\mathbf{e}_3$ and since this equation must be valid for each $\Pi\subset\Sigma$, if the integrand is continuous one can apply localisation lemma and get

$$\mathbf{e}_3\times\mathbf{m}^\alpha|_\alpha+\mathbf{e}_{3,\alpha}\times\mathbf{m}^\alpha+\mathbf{e}_\alpha\times\mathbf{t}^\alpha+\mathbf{e}_3\times\mathbf{c}=\mathbf{e}_3\times\iota\dot{\mathbf{w}}. \tag{3.105}$$

Equation (3.105) can be rewritten in terms of the generalised force tensors by noticing that

$$\begin{aligned}\mathbf{e}_\alpha\times\mathbf{t}^\alpha=\mathbf{e}_\alpha\times\mathbf{T}\mathbf{e}^\alpha=\mathbf{e}_\alpha\times(t^{\beta\alpha}\mathbf{e}_\beta+t^{3\alpha}\mathbf{e}_3)=\epsilon_{3\alpha\beta}t^{\beta\alpha}\sqrt{e}\,\mathbf{e}^3+\epsilon_{3\beta\alpha}t^{3\alpha}\sqrt{e}\,\mathbf{e}^\beta= \\ =-\sqrt{e}\epsilon_{ijk}t^{jk}\mathbf{e}^i=-\mathsf{e}\mathbf{T},\end{aligned} \tag{3.106}$$

where e is the alternating tensor $\mathsf{e}=\epsilon_{ijk}\sqrt{e}\,\mathbf{e}^i\otimes\mathbf{e}^j\otimes\mathbf{e}^k$. Moreover

$$\mathbf{e}_{3,\alpha}\times\mathbf{m}^\alpha=\mathbf{e}_{3,\alpha}\times\mathbf{M}\mathbf{e}^\alpha=-\varkappa^\beta_{\cdot\alpha}\mathbf{e}_\beta\times m^{\lambda\gamma}(\mathbf{e}_\lambda\otimes\mathbf{e}_\gamma)\mathbf{e}^\alpha=-\varkappa^\beta_{\cdot\alpha}\mathbf{e}_\beta\times m^{\lambda\alpha}\mathbf{e}_\lambda=\varkappa^\beta_{\cdot\alpha}m^{\lambda\alpha}\epsilon_{3\lambda\beta}\sqrt{e}\mathbf{e}^3 \tag{3.107}$$

and given that

$$\boldsymbol{\varkappa}\mathbf{M}=\varkappa^\lambda_{\cdot\gamma}\mathbf{e}_\lambda\otimes\mathbf{e}^\gamma\,m^{\alpha\beta}\mathbf{e}_\alpha\otimes\mathbf{e}_\beta=\varkappa^\lambda_{\cdot\alpha}m^{\alpha\beta}\mathbf{e}_\lambda\otimes\mathbf{e}_\beta \tag{3.108}$$

one gets

$$\mathsf{e}\boldsymbol{\varkappa}\mathbf{M}=\sqrt{e}\epsilon_{ijk}k^j_{\cdot\alpha}m^{\alpha k}\mathbf{e}^i \tag{3.109}$$

and since $j,k\neq 3$ then $i=3$, $j,k=\alpha,\beta$, and one can write the term as

$$\mathsf{e}\boldsymbol{\varkappa}\mathbf{M}=\sqrt{e}\epsilon_{3\alpha\beta}\varkappa^\alpha_{\cdot\lambda}m^{\lambda\beta}\mathbf{e}^3. \tag{3.110}$$

Therefore

$$\mathbf{e}_{3,\alpha}\times\mathbf{m}^\alpha=-\mathsf{e}\boldsymbol{\varkappa}\mathbf{M}^\mathsf{T}, \tag{3.111}$$

and thus the balance equations (3.105) can be rewritten as

$$\mathbf{e}_3\times\operatorname{div}\mathbf{M}-\mathsf{e}(\mathbf{T}+\boldsymbol{\varkappa}\mathbf{M}^\mathsf{T})+\mathbf{e}_3\times\mathbf{c}=\mathbf{e}_3\times\iota\dot{\mathbf{w}}. \tag{3.112}$$

Equations (3.97) and (3.105) have to be completed with proper boundary conditions on the edges on which the external forces are known, that is

$$\begin{cases} \mathbf{t} = \mathbf{t}_\partial, \\ \mathbf{m} = \mathbf{m}_\partial \end{cases} \qquad \text{on } \partial\Sigma_N, \tag{3.113}$$

where $\mathbf{t}_\partial$ and $\mathbf{m}_\partial$ are the known external force and couple force vectors acting on the unconstrained boundary of the shell, denoted by $\partial\Sigma_N$.

The balance laws are now derived in components for later convenience. Remembering the representation $(3.12)_2$ the force vector and couple force vector can be written in contravariant components as

$$\begin{aligned} \mathbf{t}^\alpha &= t^{\beta\alpha}\mathbf{e}_\beta + t^{3\alpha}\mathbf{e}_3, \\ \mathbf{m}^\alpha &= m^{\beta\alpha}\mathbf{e}_\beta, \end{aligned} \tag{3.114}$$

since $\mathbf{m} \in N_y$. The contravariant components of the generalised forces represent the action, per unit length, exerted on a curvilinear unitary line element on the coordinate lines. The components are shown in Figure 3.8. Remembering the definition of covariant derivative and

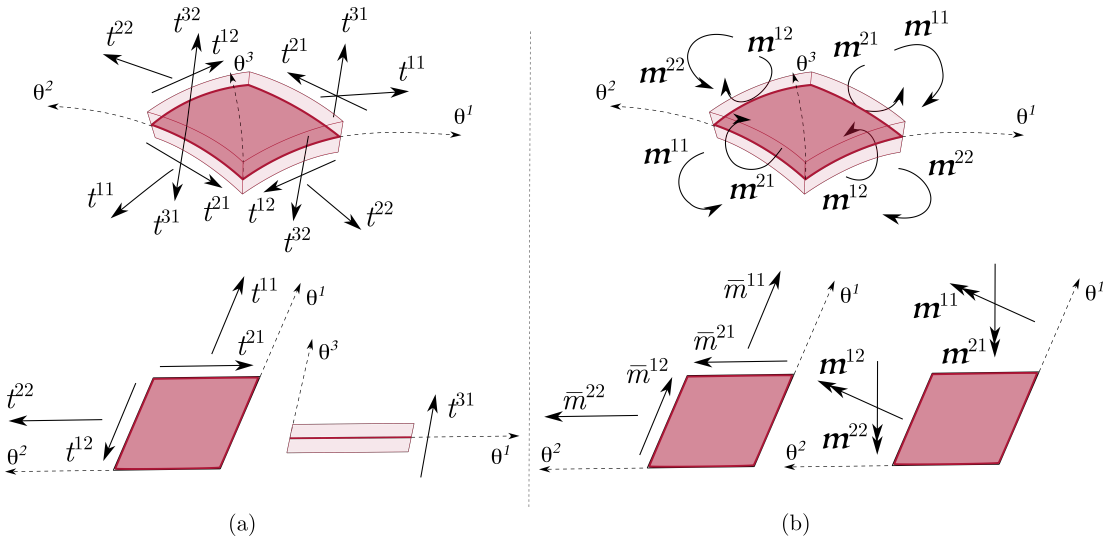

Figure 3.8: Force components (a) and couple force components with moments (b).

the definition of director curvatures (3.44) one can write

$$\begin{aligned} \mathbf{t}^\alpha|_\alpha &= (t^{\beta\alpha}|_\alpha - t^{3\alpha}\varkappa^\beta_{.\alpha})\mathbf{e}_\beta + (t^{3\alpha}|_\alpha + t^{\beta\alpha}\varkappa_{\beta\alpha})\mathbf{e}_3, \\ \mathbf{m}^\alpha|_\alpha &= m^{\beta\alpha}|_\alpha\mathbf{e}_\beta + m^{\beta\alpha}\varkappa_{\beta\alpha}\mathbf{e}_3. \end{aligned} \tag{3.115}$$

Using the previous expressions, the (3.97) can be written in term of the local covariant base as

$$(t^{\beta\alpha}|_\alpha - t^{3\alpha}\varkappa^\beta_{.\alpha})\mathbf{e}_\beta + (t^{3\alpha}|_\alpha + t^{\beta\alpha}\varkappa_{\beta\alpha})\mathbf{e}_3 + b^k\mathbf{e}_k = \rho\dot{v}^k\mathbf{e}_k. \tag{3.116}$$

Projection along $\mathbf{e}^\beta$ yields the first two scalar equations

$$t^{\beta\alpha}|_\alpha - t^{3\alpha}\varkappa^\beta_{.\alpha} + b^\beta = \rho\dot{v}^\beta, \tag{3.117}$$

and by projecting along $\mathbf{e}^3$ one gets the third scalar equation

$$t^{3\alpha}|_\alpha + t^{\beta\alpha}\varkappa_{\beta\alpha} + b^3 = \rho\dot{v}^3. \tag{3.118}$$

Analogously, the (3.105) can be written in terms of the local covariant base as

$$\begin{aligned}&\mathbf{e}_3 \times \left(m^{\beta\alpha}|_\alpha \mathbf{e}_\beta + m^{\beta\alpha}\varkappa_{\beta\alpha}\mathbf{e}_3\right) - \varkappa^\lambda_{.\alpha}\mathbf{e}_\lambda \times m^{\beta\alpha}\mathbf{e}_\beta + \mathbf{e}_\alpha \times \left(t^{\beta\alpha}\mathbf{e}_\beta + t^{3\alpha}\mathbf{e}_3\right) + \\ &+ \mathbf{e}_3 \times c^k\mathbf{e}_k = \mathbf{e}_3 \times \iota\dot{w}^k\mathbf{e}_k.\end{aligned} \tag{3.119}$$

Expanding the vector products, knowing that $\mathbf{e}_i \times \mathbf{e}_j = \sqrt{e}\epsilon_{ijk}\mathbf{e}^k$, one obtains an expression in terms of the contravariant local base vectors as follows

$$\begin{aligned}&\epsilon_{3\beta\lambda}\sqrt{e}m^{\beta\alpha}|_\alpha \mathbf{e}^\lambda + \epsilon_{3\lambda\beta}\sqrt{e}\varkappa^\lambda_{.\alpha}m^{\beta\alpha}\mathbf{e}^3 + \epsilon_{\beta 3\alpha}\sqrt{e}t^{\beta\alpha}\mathbf{e}^3 + \\ &+ \epsilon_{3\lambda\alpha}\sqrt{e}t^{3\alpha}\mathbf{e}^\lambda + \epsilon_{3\beta\lambda}\sqrt{e}c^\beta\mathbf{e}^\lambda = \epsilon_{3\beta\lambda}\sqrt{e}\iota\dot{w}^\beta\mathbf{e}^\lambda.\end{aligned} \tag{3.120}$$

Since the metric is invertible, it is $\sqrt{e} \neq 0$ and one can simplify it from the equation. By projecting along $\mathbf{e}_k$, observing that

$$\epsilon_{3\lambda\beta}\square^\beta \mathbf{e}^\lambda \cdot \mathbf{e}_\lambda = \square^{\lambda+1}, \quad \text{modulo } 2, \tag{3.121}$$

and renaming the dummy index $\lambda + 1 = \beta$ one obtains

$$m^{\beta\alpha}|_\alpha - t^{3\beta} + c^\beta = \iota\dot{w}^\beta \tag{3.122}$$

for the first two scalar equations (by projecting along $\mathbf{e}_\lambda$) and

$$\epsilon_{\alpha\beta}(t^{\alpha\beta} - \varkappa^\alpha_{.\lambda}m^{\beta\lambda}) = 0 \tag{3.123}$$

for the third one (by projecting along $\mathbf{e}_3$). The six balance equations are summarised in the following system

$$\begin{cases} t^{\beta\alpha}|_\alpha - t^{3\alpha}\varkappa^\beta_{.\alpha} + b^\beta = \rho\dot{v}^\beta, & \beta = 1,2 \\ t^{3\alpha}|_\alpha + t^{\beta\alpha}\varkappa_{\beta\alpha} + b^3 = \rho\dot{v}^3, & \\ m^{\beta\alpha}|_\alpha - t^{3\beta} + c^\beta = \iota\dot{w}^\beta, & \beta = 1,2 \\ \epsilon_{\alpha\beta}(t^{\alpha\beta} - \varkappa^\alpha_{.\lambda}m^{\beta\lambda}) = 0. & \end{cases} \tag{3.124}$$

By virtue of Cauchy theorem, the known values of the force vector and the couple force vector on the boundary are written as

$$\begin{aligned}\mathbf{t}_\partial &= t^{i\alpha}\nu_\alpha\mathbf{e}_i, \\ \mathbf{m}_\partial &= m^{\beta\alpha}\nu_\alpha\mathbf{e}_\beta.\end{aligned} \tag{3.125}$$

3.3.3 Equation of virtual powers

A fundamental result for the proof of the theorems of limit analysis is derived in this section. With reference to the generic part $\Pi \in \Sigma$, let's consider a virtual displacement field and the generalised velocities $(\mathbf{v}^*, \mathbf{w}^*)$. The external power is

$$\mathcal{P}^*_E = \int_\Pi (\mathbf{b}\cdot\mathbf{v}^* + \mathbf{c}\cdot\mathbf{w}^*)\, d\Sigma + \int_{\partial\Pi} (\mathbf{t}\cdot\mathbf{v}^* + \mathbf{m}\cdot\mathbf{w}^*)\, d\Gamma. \tag{3.126}$$

Using Cauchy's theorem and divergence theorem, and remembering the identity $\operatorname{div}(\mathbf{T}^{\mathsf{T}}\mathbf{v}^*) = \mathbf{T}\cdot\nabla\mathbf{v}^* + \mathbf{v}^*\cdot\operatorname{div}\mathbf{T}$ (see [Gurtin et al., 2010]), one can write

$$\begin{aligned}\mathcal{P}_E^* &= \int_\Pi (\mathbf{b}\cdot\mathbf{v}^* + \mathbf{c}\cdot\mathbf{w}^*)\,d\Sigma + \int_{\partial\Pi}(\mathbf{T}\boldsymbol{\nu}\cdot\mathbf{v}^* + \mathbf{M}\boldsymbol{\nu}\cdot\mathbf{w}^*)\,d\Gamma = \\ &= \int_\Pi (\mathbf{b}\cdot\mathbf{v}^* + \mathbf{c}\cdot\mathbf{w}^*)\,d\Sigma + \int_{\partial\Pi}(\mathbf{T}^{\mathsf{T}}\mathbf{v}^*\cdot\boldsymbol{\nu} + \mathbf{M}^{\mathsf{T}}\mathbf{w}^*\cdot\boldsymbol{\nu})\,d\Gamma = \\ &= \int_\Pi \Big((\mathbf{b}\cdot\mathbf{v}^* + \mathbf{c}\cdot\mathbf{w}^*) + \mathbf{T}\cdot\nabla\mathbf{v}^* + \mathbf{v}^*\cdot\operatorname{div}\mathbf{T} + \mathbf{M}\cdot\nabla\mathbf{w}^* + \mathbf{w}^*\cdot\operatorname{div}\mathbf{M}\Big)\,d\Sigma.\end{aligned} \tag{3.127}$$

By equation (3.97) one obtains

$$\mathcal{P}_E^* = \int_\Pi \Big(\rho\dot{\mathbf{v}}^*\cdot\mathbf{v}^* + \mathbf{c}\cdot\mathbf{w}^* + \mathbf{T}\cdot\nabla\mathbf{v}^* + \mathbf{M}\cdot\nabla\mathbf{w}^* + \mathbf{w}^*\cdot\operatorname{div}\mathbf{M}\Big)\,d\Sigma. \tag{3.128}$$

Using the fact that $\mathbf{w} = \boldsymbol{\omega}\times\mathbf{d}$ and the triple product rule some terms can be rewritten as

$$\mathcal{P}_E^* = \int_\Pi \Big(\rho\dot{\mathbf{v}}^*\cdot\mathbf{v}^* + \mathbf{T}\cdot\nabla\mathbf{v}^* + \mathbf{e}_3\times\mathbf{c}\cdot\boldsymbol{\omega}^* + \mathbf{M}\cdot\nabla\mathbf{w}^* + \mathbf{e}_3\times\operatorname{div}\mathbf{M}\cdot\boldsymbol{\omega}^*\Big)\,d\Sigma \tag{3.129}$$

and by virtue of equation (3.105)

$$\mathcal{P}_E^* = \int_\Pi \Big(\rho\dot{\mathbf{v}}^*\cdot\mathbf{v}^* + \mathbf{T}\cdot\nabla\mathbf{v}^* + \mathbf{M}\cdot\nabla\mathbf{w}^* + (\mathbf{e}_3\times\iota\dot{\mathbf{w}}^* - \mathbf{e}_\alpha\times\mathbf{T}\mathbf{e}^\alpha - \mathbf{e}_{3,\alpha}\times\mathbf{M}\mathbf{e}^\alpha)\cdot\boldsymbol{\omega}^*\Big)\,d\Sigma. \tag{3.130}$$

Remembering the mixed product rule one can compute

$$\mathbf{e}_3\times\iota\dot{\mathbf{w}}^*\cdot\boldsymbol{\omega}^* = \boldsymbol{\omega}^*\times\mathbf{e}_3\cdot\iota\dot{\mathbf{w}}^* = \iota\dot{\mathbf{w}}^*\cdot\mathbf{w}^*, \tag{3.131}$$

than can also be expressed in terms of $\boldsymbol{\omega}$ using the triple product rules and using the fact that $\|\mathbf{d}\| = 1$,

$$\begin{aligned}\dot{\mathbf{w}}\cdot\mathbf{w} &= (\dot{\boldsymbol{\omega}}\times\mathbf{e}_3 + \boldsymbol{\omega}\times\dot{\mathbf{e}}_3)\cdot(\boldsymbol{\omega}\times\mathbf{e}_3) = (\dot{\boldsymbol{\omega}}\times\mathbf{e}_3)\cdot(\boldsymbol{\omega}\times\mathbf{e}_3) + \Big(\boldsymbol{\omega}\times(\boldsymbol{\omega}\times\mathbf{e}_3)\Big)\cdot(\boldsymbol{\omega}\times\mathbf{e}_3) = \\ &= (\dot{\boldsymbol{\omega}}\cdot\boldsymbol{\omega})(\mathbf{e}_3\cdot\mathbf{e}_3) - (\dot{\boldsymbol{\omega}}\cdot\mathbf{e}_3)(\mathbf{e}_3\cdot\boldsymbol{\omega}) + \Big((\boldsymbol{\omega}\cdot\mathbf{e}_3)\boldsymbol{\omega} - (\boldsymbol{\omega}\cdot\boldsymbol{\omega})\mathbf{e}_3\Big)\cdot(\boldsymbol{\omega}\times\mathbf{e}_3) = \dot{\boldsymbol{\omega}}\cdot\boldsymbol{\omega}.\end{aligned} \tag{3.132}$$

It is possible to recognise the time derivative of the *kinetic energy* associated with the virtual displacement field as

$$\dot{\mathcal{T}}^* = \int_\Pi \left(\rho\dot{\mathbf{v}}^*\cdot\mathbf{v}^* + \iota\dot{\boldsymbol{\omega}}^*\cdot\boldsymbol{\omega}^*\right)d\Sigma, \tag{3.133}$$

so it is possible to write

$$\mathcal{P}_E^* = \dot{\mathcal{T}}^* + \int_\Pi \left(\mathbf{T}\cdot\nabla\mathbf{v}^* + \mathbf{M}\cdot\nabla\mathbf{w}^* - (\mathbf{e}_\alpha\times\mathbf{T}\mathbf{e}^\alpha + \mathbf{e}_{3,\alpha}\times\mathbf{M}\mathbf{e}^\alpha)\cdot\boldsymbol{\omega}^*\right)d\Sigma. \tag{3.134}$$

The first term in the interior parenthesis becomes

$$\mathbf{e}_\alpha\times\mathbf{T}\mathbf{e}^\alpha = \mathbf{e}_\alpha\times(t^{\beta\alpha}\mathbf{e}_\beta + t^{3\alpha}\mathbf{e}_3) = \epsilon_{3\alpha\beta}t^{\beta\alpha}\sqrt{e}\,\mathbf{e}^3 + \epsilon_{3\beta\alpha}t^{3\alpha}\sqrt{e}\,\mathbf{e}^\beta, \tag{3.135}$$

and, given $\omega^3 = 0$, we have

$$-(\mathbf{e}_\alpha \times \mathbf{T}\mathbf{e}^\alpha) \cdot \boldsymbol{\omega}^* = -\epsilon_{3\beta\alpha}\sqrt{e}\, t^{3\alpha}\omega^{*\beta}. \tag{3.136}$$

Since the gradient of a vector field is defined as (see [Itskov, 2007] and Equation (3.22))

$$\nabla\mathbf{v} = \mathbf{v}_{,i} \otimes \mathbf{e}^i = v_j|_i \mathbf{e}^j \otimes \mathbf{e}^i, \tag{3.137}$$

it is possible to write

$$\mathbf{T} \cdot \nabla\mathbf{v}^* = (t^{\beta\alpha}\mathbf{e}_\beta \otimes \mathbf{e}_\alpha + t^{3\alpha}\mathbf{e}_3 \otimes \mathbf{e}_\alpha) \cdot (v_j^*|_i\, \mathbf{e}^j \otimes \mathbf{e}^i) = t^{\beta\alpha}v_\beta^*|_\alpha + t^{3\alpha}v_3^*|_\alpha \tag{3.138}$$

and then

$$\begin{aligned} \mathbf{T} \cdot \nabla\mathbf{v}^* - (\mathbf{e}_\alpha \times \mathbf{T}\mathbf{e}^\alpha) \cdot \boldsymbol{\omega}^* &= t^{\beta\alpha}v_\beta^*|_\alpha + t^{3\alpha}v_3^*|_\alpha - \epsilon_{3\beta\alpha}\sqrt{e}\, t^{3\alpha}\omega^{*\beta} = \\ &= t^{\beta\alpha}v_\beta^*|_\alpha + t^{3\alpha}(v_3^*|_\alpha - \epsilon_{3\beta\alpha}\sqrt{e}\,\omega^{*\beta}). \end{aligned} \tag{3.139}$$

Defining the tensor $\mathbf{L} = \nabla\mathbf{v} + \mathbf{e}\boldsymbol{\omega}$, of components

$$l_{\beta\alpha} = v_\beta|_\alpha, \quad l_{3\alpha} = v_3|_\alpha - \sqrt{e}\epsilon_{3\beta\alpha}\omega^\beta, \quad l_{k3} = 0, \tag{3.140}$$

we have

$$\mathbf{T} \cdot \nabla\mathbf{v}^* - (\mathbf{e}_\alpha \times \mathbf{T}\mathbf{e}^\alpha) \cdot \boldsymbol{\omega}^* = t^{ij}\dot{l}_{ij} = \mathbf{T} \cdot \mathbf{L}^*, \tag{3.141}$$

where the tensor $\mathbf{L}$ has the following representation

$$\mathbf{L} = l_{ij}\, \mathbf{e}^i \otimes \mathbf{e}^j. \tag{3.142}$$

The last term in (3.134) is computed starting from

$$\mathbf{e}_{3,\alpha} \times \mathbf{M}\mathbf{e}^\alpha = -\varkappa_{.\alpha}^\beta \mathbf{e}_\beta \times m^{\lambda\gamma}(\mathbf{e}_\lambda \otimes \mathbf{e}_\gamma)\mathbf{e}^\alpha = -\varkappa_{.\alpha}^\beta \mathbf{e}_\beta \times m^{\lambda\alpha}\mathbf{e}_\lambda = \varkappa_{.\alpha}^\beta m^{\lambda\alpha}\epsilon_{3\lambda\beta}\sqrt{e}\mathbf{e}^3, \tag{3.143}$$

so that $-(\mathbf{e}_{3,\alpha} \times \mathbf{M}\mathbf{e}^\alpha) \cdot \boldsymbol{\omega}^* = 0$. Even if a power conjugate tensor to $\mathbf{M}$ in terms of $\mathbf{w}$ can be straightforwardly defined, we decide to give it in terms of $\boldsymbol{\omega}$ as done for $\mathbf{L}$. In particular, since

$$\begin{aligned} \nabla\mathbf{w} &= \nabla(\boldsymbol{\omega} \times \mathbf{e}_3) = (\boldsymbol{\omega} \times \mathbf{e}_3)_{,i} \otimes \mathbf{e}^i = (\boldsymbol{\omega}_{,i} \times \mathbf{e}_3 + \boldsymbol{\omega} \times \mathbf{e}_{3,i}) \otimes \mathbf{e}^i = \\ &= (\boldsymbol{\omega}_{,\alpha} \times \mathbf{e}_3) \otimes \mathbf{e}^\alpha + (\boldsymbol{\omega} \times \mathbf{e}_{3,\alpha}) \otimes \mathbf{e}^\alpha = (\omega^\beta|_\alpha \mathbf{e}_\beta \times \mathbf{e}_3 - \omega^\lambda \mathbf{e}_\lambda \times \varkappa_{.\alpha}^\beta \mathbf{e}_\beta) \otimes \mathbf{e}^\alpha = \\ &= (\epsilon_{3\lambda\beta}\sqrt{e}\omega^\beta|_\alpha \mathbf{e}^\lambda - \epsilon_{3\lambda\beta}\sqrt{e}\omega^\lambda \varkappa_{.\alpha}^\beta \mathbf{e}^3) \otimes \mathbf{e}^\alpha, \end{aligned} \tag{3.144}$$

and given that $m^{3\alpha} = 0$, one gets

$$\mathbf{M} \cdot \nabla\mathbf{w}^* = m^{\lambda\alpha}\epsilon_{3\lambda\beta}\sqrt{e}\omega^{*\beta}|_\alpha. \tag{3.145}$$

By defining the tensor $\mathbf{D} = -\mathbf{e}_3 \times \nabla\boldsymbol{\omega}$, where

$$-\mathbf{e}_3 \times \nabla\boldsymbol{\omega} \triangleq -\omega^\beta|_\alpha(\mathbf{e}_3 \times \mathbf{e}_\beta) \otimes \mathbf{e}^\alpha = \epsilon_{3\lambda\beta}\sqrt{e}\omega^\beta|_\alpha \mathbf{e}^\lambda \otimes \mathbf{e}^\alpha. \tag{3.146}$$

and whose components are

$$d_{\beta\alpha} = \epsilon_{3\lambda\beta}\sqrt{e}\omega^\lambda|_\alpha, \quad d_{3\alpha} = 0, \quad d_{k3} = 0, \tag{3.147}$$

we can write

$$\mathbf{M}\cdot\nabla\mathbf{w}^* - (\mathbf{e}_{3,\alpha}\times\mathbf{M}\mathbf{e}^\alpha)\cdot\boldsymbol{\omega}^* = m^{\alpha\beta}d^*_{\alpha\beta} = \mathbf{M}\cdot\mathbf{D}^*, \tag{3.148}$$

where the tensor $\mathbf{D}$ has the following representation

$$\mathbf{D} = d_{\alpha\beta}\mathbf{e}^\alpha\otimes\mathbf{e}^\beta. \tag{3.149}$$

It is now possible to define the *internal power* as

$$\mathcal{P}^*_I = \int_\Pi \left(\mathbf{T}\cdot\mathbf{L}^* + \mathbf{M}\cdot\mathbf{D}^*\right) d\Sigma, \tag{3.150}$$

and so we proved the virtual power theorem (sometimes called work-energy theorem)

$$\mathcal{P}^*_E = \dot{\mathcal{T}}^* + \mathcal{P}^*_I. \tag{3.151}$$

It is interesting to notice that theorem (3.151) can be considered as an extension of the kinetic energy theorem for rigid systems where the kinetic energy increment is not given simply by the external power but also by the contribution (negative in sign) of the deformability of the system. The previous result can also be written in incremental form as

$$đ\mathcal{W}^* = d\mathcal{T}^* + đ\mathcal{I}^*, \tag{3.152}$$

where $đ\mathcal{I}^*$ is called *internal work increment*. It's worth observing that, while in general both $đ\mathcal{W}$ and $đ\mathcal{I}$ are inexact differential as they depend on the path, the kinetic energy increment $d\mathcal{T}$ is an exact differential since the kinetic energy is a state function.

Definition of the strain measures

In dealing with the statics of masonry domes, we assume that the displacements are small compared to both the characteristic dimension of the shell and its minimum radius of curvature and hence we also assume that the balance equations can be written in the initial (reference) configuration. In addition, we assume the strains to be small, so that it is possible to refer to the linearised theory also referred to as small strain and small displacement regime (sometimes called small perturbations regime).

In the foregoing hypotheses, the external work on the generic part Π can be written as

$$\mathcal{W}^* = \int_\Pi (\mathbf{b}\cdot\mathbf{u}^* + \mathbf{c}\cdot\mathbf{r}^*)\, d\Sigma + \int_{\partial\Pi} (\mathbf{t}\cdot\mathbf{u}^* + \mathbf{m}\cdot\mathbf{r}^*)\, d\Gamma. \tag{3.153}$$

Analogously, the internal work can be expressed as

$$\mathcal{I}^* = \int_\Pi \left(\mathbf{T}\cdot\mathbf{H}^* + \mathbf{M}\cdot\mathbf{K}^*\right) d\Sigma \tag{3.154}$$

where the strain tensor $\mathbf{H}$ and the change of curvature tensor $\mathbf{K}$ have been defined such that $\mathbf{L} = \dot{\mathbf{H}}$ and $\mathbf{D} = \dot{\mathbf{K}}$. As a consequence the strain tensor can be defined as $\mathbf{H} = \nabla\mathbf{u} + \mathsf{e}\boldsymbol{\varphi}$, whose components are

$$\eta_{\beta\alpha} = u_\beta|_\alpha, \quad \eta_{3\alpha} = u_3|_\alpha - \sqrt{e}\epsilon_{3\beta\alpha}\varphi^\beta, \quad \eta_{k3} = 0, \tag{3.155}$$

and the change of curvature tensor can be defined as $\mathbf{K} = -\mathbf{e}_3 \times \nabla\boldsymbol{\varphi}$, whose components are

$$\chi_{\beta\alpha} = \epsilon_{3\lambda\beta}\sqrt{e}\varphi^{\lambda}|_{\alpha}, \quad \chi_{3\alpha} = 0, \quad \chi_{k3} = 0, \tag{3.156}$$

having the following representations $\mathbf{H} = \eta_{ij}\,\mathbf{e}^i \otimes \mathbf{e}^j$, $\mathbf{K} = \chi_{\alpha\beta}\mathbf{e}^{\alpha} \otimes \mathbf{e}^{\beta}$. The tensors $\mathbf{H}$ and $\mathbf{K}$ assume the meaning of strain measures work-conjugate to the force measures $\mathbf{T}$ and $\mathbf{M}$.

It is not difficult to recognise that, analogously to the case of a three-dimensional continuum body, the components η_{ij} represent the stretching in the direction of the covariant base, as shown in Figure 3.9. The stretching in a generic direction $\boldsymbol{\nu}$ is expressed as $\eta_{\nu} = \mathbf{H}\boldsymbol{\nu} \cdot \boldsymbol{\nu}$, indeed, for instance, it is $\mathbf{H}\mathbf{e}_1 \cdot \mathbf{e}_1 = \eta_{ij}\,(\mathbf{e}^i \otimes \mathbf{e}^j)\mathbf{e}_1 \cdot \mathbf{e}_1 = \eta_{11}$.

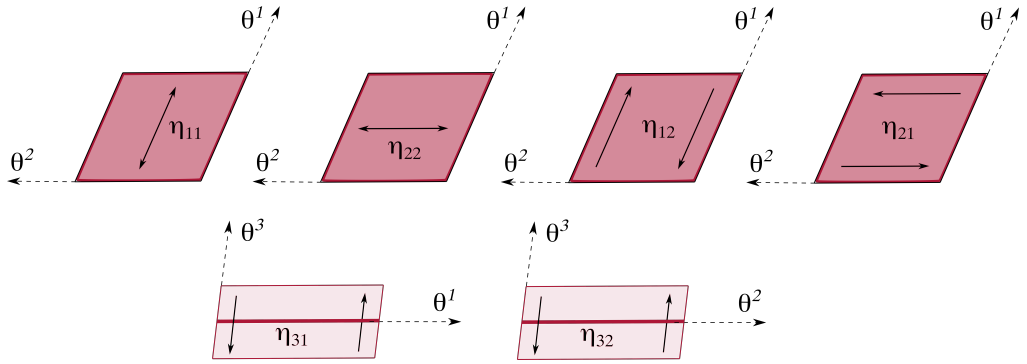

Figure 3.9: Covariant components of the stretching.

3.3.4 Conservation of Energy

As already done for forces, it is assumed that the *heating* of the generic part Π of the shell is due to two sources: the heat supply which is provided throughout Π (ex. radiation, chemical reactions, etc.) and the heat flux, entering into Π across its boundary $\partial\Pi$. The heating is here considered to be positive if entering the body, and the total rate of heat of Π is

$$đ\mathcal{Q} = \int_{\Pi} r(\mathbf{y}, t)\, d\Sigma\, dt + \int_{\partial\Pi} q(\mathbf{y}, t, \boldsymbol{\nu})\, d\Gamma\, dt, \tag{3.157}$$

which is an inexact differential. The heat supply depends on the point and on the instant while the heat flux depends also on the unit normal vector to the generic surface, in analogy of what is done for the forces. The *First Principle of Thermodynamics* states that it exists a state function $\mathcal{E}(\Pi, \mathbf{y}, t)$, called *internal energy*, which is the energy a body possesses other than it's kinetic energy and such that

$$d\mathcal{E} + d\mathcal{T} = đ\mathcal{W} + đ\mathcal{Q}. \tag{3.158}$$

The internal energy is an extensive quantity which possesses a density, so that

$$d\mathcal{E} = \int_{\Pi} \rho\varepsilon\, d\Sigma\, dt. \tag{3.159}$$

In differential form, the first law (3.158) can be written as

$$\dot{\mathcal{E}} + \dot{\mathcal{T}} = \mathcal{P}_E + \mathcal{P}_Q, \tag{3.160}$$

where the heating $\mathcal{P}_Q$ is

$$\mathcal{P}_Q = \int_\Pi r(\mathbf{y}, t)\, d\Sigma + \int_{\partial\Pi} q(\mathbf{y}, t, \boldsymbol{\nu})\, d\Gamma. \tag{3.161}$$

Applying the equation of virtual powers, we obtain the part-wise first law for shells

$$\dot{\mathcal{E}} = \mathcal{P}_I + \mathcal{P}_Q, \tag{3.162}$$

expressed by

$$\frac{d}{dt}\int_\Pi \rho\varepsilon\, d\Sigma = \int_\Pi r\, d\Sigma + \int_{\partial\Pi} q\, d\Gamma + \int_\Pi \left(\mathbf{T}\cdot\dot{\mathbf{H}} + \mathbf{M}\cdot\dot{\mathbf{K}}\right) d\Sigma. \tag{3.163}$$

With the same argument used to prove the Cauchy theorem, one can show that (3.163) implies that the heat flux depends linearly on $\boldsymbol{\nu}$, that is, it exists a vector $\mathbf{q}(\mathbf{y}, t)$, called heat flux vector, such that

$$q(\mathbf{y}, t, \boldsymbol{\nu}) = \mathbf{q}(\mathbf{y}, t)\cdot\boldsymbol{\nu}. \tag{3.164}$$

Rewriting (3.163) as

$$\frac{d}{dt}\int_\Pi \rho\varepsilon\, d\Sigma = \int_\Pi r\, d\Sigma + \int_{\partial\Pi} \mathbf{q}\cdot\boldsymbol{\nu}\, d\Gamma + \int_\Pi \left(\mathbf{T}\cdot\dot{\mathbf{H}} + \mathbf{M}\cdot\dot{\mathbf{K}}\right) d\Sigma, \tag{3.165}$$

and applying the divergence theorem and the localisation lemma, by the conservation of mass, we state the point-wise energy field equation as

$$\rho\dot{\varepsilon} = r + \operatorname{div}\mathbf{q} + \mathbf{T}\cdot\dot{\mathbf{H}} + \mathbf{M}\cdot\dot{\mathbf{K}}. \tag{3.166}$$

3.4 Constitutive equations for elasto-plastic shells

A crucial role in thermodynamics is played by the concept of equilibrium. We can say that a thermodynamical system is in equilibrium if the variables that describe its state remain unchanged in time. Equilibrium (or classical) thermodynamics deals essentially with the study of macroscopic properties of matter at equilibrium and can be applied also to the description of reversible processes, that represent a special class of idealised processes considered as a continuum sequence of equilibrium states. The theory of solids undergoing permanent deformations falls within the framework of irreversible thermodynamics which is a large, modern and fully alive field of research, concerning physical processes that goes beyond equilibrium. The main difficulty in dealing with non-equilibrium processes is that concepts like temperature and entropy are not univocally defined outside equilibrium. Several theories exist, each of which has advantages and disadvantages and the choice of the theory to adopt depends on what physical phenomenon is described. For inelastic solids, one of the most

fruitful approaches is the theory of internal state variable of which we recall here only some main concepts, leaving the complete treatment to the vast literature[7].

The theory of internal variables postulates that the thermodynamic state of a material medium at a given point and instant is completely defined by the knowledge of the local equilibrium variables (observable) $\mathbf{H}$, $\mathbf{K}$ and a certain number of internal variables (hidden) $\boldsymbol{\xi}$. The presence of additional variables in the constitutive relations requires additional evolution equations, which for rate-dependent inelastic body are given assuming that the rate of evolution of the internal variables is determined by the local state

$$\dot{\boldsymbol{\xi}} = \dot{\boldsymbol{\xi}}(\mathbf{H}, \mathbf{K}, \vartheta, \boldsymbol{\xi}), \tag{3.167}$$

where ϑ denotes the absolute temperature. In the context of Thermomechanics of inelastic continuum bodies with internal variables, a local state is an equilibrium local state if $\dot{\boldsymbol{\xi}}(\mathbf{H}, \mathbf{K}, \vartheta, \boldsymbol{\xi}) = \mathbf{0}$. The theory is based on the *accompanying state axiom*. The essence of this postulate is that to each non-equilibrium state corresponds an accompanying equilibrium state, and to every irreversible process is associated an accompanying "reversible" process, so that the usual definitions of temperature and entropy can be accepted. By this axiom we can accept the existence of an 'accompanying' entropy, that is a function of the whole set of state variables $\mathcal{S}(\mathcal{E}, \mathbf{H}, \mathbf{K}, \boldsymbol{\xi})$, that, as the internal energy, is an extensive quantity which possesses a density, $\rho s(\varepsilon, \mathbf{H}, \mathbf{K}, \boldsymbol{\xi})$. This definition of entropy refers to a fictitious equilibrium state, and then, the usual definition of entropy applies $d\mathcal{S} = \vartheta^{-1} đ\mathcal{Q}_{rev}$. The part-wise rate of change of entropy may be written as

$$\frac{d}{dt}\int_{\Pi} \rho s \, d\Sigma = \int_{\partial\Pi} \mathbf{j} \cdot \boldsymbol{\nu} \, d\Gamma + \int_{\Pi} (\varsigma + \sigma_s) \, d\Sigma, \tag{3.168}$$

where $\mathbf{j}$ is the entropy flux, ς is the entropy supply and σ_s is the entropy production, whose expressions depend on the model. It has been assumed, as done for the heating, that the entropy inflow is due to two sources: the entropy internal supply per unit volume (or simply entropy supply) which is provided throughout Π and the entropy flux, entering into Π across it's boundary $\partial\Pi$. For the present model, we assume that the entropy flux is given by $\mathbf{j} = \mathbf{q}/\vartheta$ and the entropy supply is given by $\varsigma = r/\vartheta$, so that by applying the divergence theorem and localisation lemma, also given the conservation of mass, the point-wise balance of entropy can be written as

$$\rho \dot{s} = \operatorname{div}\left(\frac{\mathbf{q}}{\vartheta}\right) + \frac{r}{\vartheta} + \sigma_s. \tag{3.169}$$

The *Second Principle of Thermodynamics* states that the entropy production σ_s is zero for reversible processes or at equilibrium and it is strictly positive for irreversible processes, that is $\sigma_s \geq 0$. Plugging the definition of entropy into the first law (3.158) yields

$$d\mathcal{S} = \vartheta^{-1} d\mathcal{E} - \vartheta^{-1} d\mathcal{I}. \tag{3.170}$$

In the small perturbation regime, using the conservation of mass, the above expression can be written as

$$\dot{s} = \vartheta^{-1}\dot{\varepsilon} - (\rho\vartheta)^{-1}\mathbf{T} \cdot \dot{\mathbf{H}} - (\rho\vartheta)^{-1}\mathbf{M} \cdot \dot{\mathbf{K}}, \tag{3.171}$$

[7]For a review of the theories of irreversible thermodynamics and for a deepening in the theory with internal variables see [Lebon et al., 2008]

which is known under the name of Gibbs' equation in rate form. On the other hand, by differentiating the entropy one gets

$$\dot{s} = \frac{\partial s}{\partial \varepsilon}\dot{\varepsilon} + \frac{\partial s}{\partial \mathbf{H}} \cdot \dot{\mathbf{H}} + \frac{\partial s}{\partial \mathbf{K}} \cdot \dot{\mathbf{K}} + \frac{\partial s}{\partial \boldsymbol{\xi}} \cdot \dot{\boldsymbol{\xi}} \tag{3.172}$$

and since at equilibrium $\dot{\boldsymbol{\xi}} = \mathbf{0}$, in absence of internal constraints, we have the following constitutive equations

$$\frac{1}{\vartheta} = \frac{\partial s}{\partial \varepsilon}, \quad \mathbf{T} = -\rho\vartheta \frac{\partial s}{\partial \mathbf{H}}, \quad \mathbf{M} = -\rho\vartheta \frac{\partial s}{\partial \mathbf{K}}. \tag{3.173}$$

In an irreversible process, plugging the entropy balance equation in rate form into the first law and remembering that

$$\operatorname{div}\left(\frac{\mathbf{q}}{\vartheta}\right) = \vartheta^{-1} \operatorname{div} \mathbf{q} + \mathbf{q} \cdot \nabla \vartheta^{-1}, \tag{3.174}$$

one obtains

$$\dot{s} = \vartheta^{-1}\dot{\varepsilon} - (\rho\vartheta)^{-1}\mathbf{T} \cdot \dot{\mathbf{H}} - (\rho\vartheta)^{-1}\mathbf{M} \cdot \dot{\mathbf{K}} + \rho^{-1}\mathbf{q} \cdot \nabla \vartheta^{-1} + \rho^{-1}\sigma_s. \tag{3.175}$$

Since we will be dealing with very slow processes (pseudo-static processes) it is justified to assume that the forces acting in the actual physical space are equal to those acting in the fictitious reversible process. On using the constitutive relations, the entropy production can be written as

$$\rho \frac{\partial s}{\partial \boldsymbol{\xi}} \cdot \dot{\boldsymbol{\xi}} - \mathbf{q} \cdot \nabla \vartheta^{-1} = \sigma_s \geq 0. \tag{3.176}$$

This inequality must hold in any process and at any state, so that we get the heat-conduction inequality

$$-\mathbf{q} \cdot \nabla \vartheta^{-1} \geq 0 \tag{3.177}$$

along with the Kelvin inequality

$$\boldsymbol{\sigma} \cdot \dot{\boldsymbol{\xi}} \geq 0 \tag{3.178}$$

where

$$\boldsymbol{\sigma} = \rho \frac{\partial s}{\partial \boldsymbol{\xi}} \tag{3.179}$$

are the thermodynamic forces or affinity (also known as configurational or Eshelby force in some branches of solid mechanics) conjugated to $\boldsymbol{\xi}$. The general theory that describes materials undergoing permanent deformation (i.e. deformations that remain after the external load is removed) is the theory of visco-plasticity. Here we assume that viscous effects can be neglected and we refer to rate-independent materials, i.e. materials whose response is linearly proportional to the adopted time scale (that, for this reason, needs not to be the physical time). In the following, the influence of temperature is omitted by considering ϑ as a constant and uniform field, referring to an isothermal setting so that the total dissipation is given by equation (3.178).

3.4.1 Masonry material and limit analysis

Under the hypothesis that the strains are small enough, it is almost universally assumed that the strain tensor can be decomposed additively into an elastic strain and an inelastic strain (see [Lubliner, 2008]) . For shells this assumption particularises as

$$\mathbf{H} = \mathbf{H}^e + \mathbf{H}^p, \qquad \mathbf{K} = \mathbf{K}^e + \mathbf{K}^p, \tag{3.180}$$

being ^{e} and ^{p} the superscripts denoting, respectively, the elastic parts and the permanent parts of the strain tensors. We assume that the generalised forces depend linearly on the elastic part of the strains. For simplicity, here we adopt the following (decoupled) relations

$$\mathbf{T} = \mathsf{C}_T \mathbf{H}^e, \quad \mathbf{M} = \mathsf{C}_M \mathbf{K}^e, \tag{3.181}$$

where C_T and C_M are two fourth-order positive definite tensors. Moreover, we assume $\boldsymbol{\sigma}_T = \vartheta^{-1}\mathbf{T}$ and $\boldsymbol{\sigma}_M = \vartheta^{-1}\mathbf{M}$ the thermodynamic forces conjugated to $\mathbf{H}^p$ and $\mathbf{K}^p$ respectively. By the positive definiteness of the elasticity tensors it follows that the previous equations can be inverted

$$\mathbf{H}^e = \mathsf{D}_T \mathbf{T}, \quad \mathbf{K}^e = \mathsf{D}_M \mathbf{M}, \tag{3.182}$$

where $\mathsf{D}_T = \mathsf{C}_T^{-1}$, $\mathsf{D}_M = \mathsf{C}_M^{-1}$ are the compliance tensors. Although the theorems of limit analysis hold in general for work-hardening materials, their application when the elastic range varies during the evolution is complex. For this reason, wanting to exploit the static theorem of limit analysis from now on we refer to elastic-perfectly plastic materials, thus the only internal variables are the permanent part of the strain tensors.

We assume the existence of a convex set $\mathbb{H}$, called the set of *admissible generalised stresses* or *stress range*[8], of all the possible stress states that satisfy certain failure criteria. A stress state belonging to the interior of the stress range is called *safe* generalised stress state and a stress state belonging to the boundary of the stress range is called a limit generalised stress state. The set of *statically admissible generalised stress fields* is

$$\begin{aligned}\mathbb{A}(\mathbb{H}) = \Big\{ &(\mathbf{T}, \mathbf{M}) \in L^2(\Sigma, \mathrm{Lin}) \times L^2(\Sigma, \mathrm{Lin}) : (\mathbf{T}, \mathbf{M}) \in \mathbb{H}, \text{ and} \\ &\operatorname{div} \mathbf{T} + \mathbf{b} = \mathbf{0},\ \mathbf{e}_3 \times \operatorname{div} \mathbf{M} - \mathsf{e}(\mathbf{T} + \boldsymbol{\varkappa}\mathbf{M}^{\mathsf{T}}) + \mathbf{e}_3 \times \mathbf{c} = \mathbf{0} \quad \text{on } \Sigma, \\ &\mathbf{T}\boldsymbol{\nu} = \mathbf{t}_\partial,\ \mathbf{M}\boldsymbol{\nu} = \mathbf{m}_\partial \quad \text{on } \partial\Sigma_N \Big\},\end{aligned} \tag{3.183}$$

that are the admissible stresses which are also in equilibrium with the external loads and that represent all the stress states attainable by the structure. A generalised stress field belonging to $\mathbb{A}(\mathrm{Int}(\mathbb{H}))$ is called a *statically safe generalised stress field*. In the following, we use the notation

$$(\mathbf{T}^a, \mathbf{M}^a) \in \mathbb{H}, \quad (\mathbf{T}^s, \mathbf{M}^s) \in \mathrm{Int}(\mathbb{H}), \quad (\mathbf{T}, \mathbf{M}) \in \partial\mathbb{H}, \tag{3.184}$$

and

$$\mathbb{A}^s = \mathbb{A}(\mathrm{Int}(\mathbb{H})), \quad \partial\mathbb{A} = \mathbb{A}(\partial\mathbb{H}). \tag{3.185}$$

[8] In the rest of this chapter we use the term *stress* as a synonym of generalised forces.

For a rate-independent elasto-plastic material we provide a law for the evolution of the internal state variable, namely the permanent part of the strains, and we usually set the following associate flow rule related to a single criterion plasticity (since the flux rate $\dot{\xi}$ is the same for the two strain tensors)

$$\begin{aligned} \dot{\mathbf{H}}^p = \mathbf{0}, \quad \dot{\mathbf{K}}^p = \mathbf{0} \qquad & \text{if } f(\mathbf{T},\mathbf{M}) < 0, \\ \dot{\mathbf{H}}^p = \dot{\xi}\frac{\partial f}{\partial \mathbf{T}}, \quad \dot{\mathbf{K}}^p = \dot{\xi}\frac{\partial f}{\partial \mathbf{M}} \qquad & \text{if } f(\mathbf{T},\mathbf{M}) = 0, \end{aligned} \tag{3.186}$$

where $f(\mathbf{T},\mathbf{M}) = 0$ is the *yield surface*, defined by the stress range by the conditions

$$\mathbb{H} = \{(\mathbf{T},\mathbf{M}) : f(\mathbf{T},\mathbf{M}) \leq 0\}, \quad \partial\mathbb{H} = \{(\mathbf{T},\mathbf{M}) : f(\mathbf{T},\mathbf{M}) = 0\}. \tag{3.187}$$

An equivalent way of expressing the normality rule is to set the normal flow rule

$$\dot{\mathbf{H}}^p = \dot{\xi}\frac{\partial f}{\partial \mathbf{T}}, \quad \dot{\mathbf{K}}^p = \dot{\xi}\frac{\partial f}{\partial \mathbf{M}} \tag{3.188}$$

along with the set of Karush-Kuhn-Tucker conditions (see [Karush, 2014], [Kuhn, 1982])

$$\dot{\xi} \geq 0, \quad f \leq 0, \quad \dot{\xi} f = 0. \tag{3.189}$$

The specific dissipation, defined by $\delta = \vartheta\sigma_s$, is then

$$\delta = \mathbf{T}\cdot\dot{\mathbf{H}}^p + \mathbf{M}\cdot\dot{\mathbf{K}}^p \tag{3.190}$$

and it satisfies the Kelvin inequality since $f(\mathbf{T},\mathbf{M})$ is convex.

Let $\mathbb{K}$ denote the set of *compatible* strains or strain range of all the strains attainable by the system, which is, similarly to the stress range, a material feature. The set of *kinematically admissible displacement fields* is

$$\begin{aligned} \mathbb{D}(\mathbb{K}) = \Big\{ & (\mathbf{u},\boldsymbol{\varphi}) \in BD(\Sigma,V)\times BD(\Sigma,V) : \mathbf{H} = \nabla\mathbf{u} + \mathsf{e}\boldsymbol{\varphi},\ \mathbf{K} = -\mathbf{e}_3\times\nabla\boldsymbol{\varphi}, \\ & (\mathbf{H},\mathbf{K}) \in \mathbb{K}, \quad \text{and } \mathbf{u} = \mathbf{u}_\partial,\ \boldsymbol{\varphi} = \boldsymbol{\varphi}_\partial \quad \text{on } \partial\Sigma_D \Big\}, \end{aligned} \tag{3.191}$$

which are the displacement fields that are also compatible with the constraints. The function space BD, introduced in [Matthies et al., 1979] and studied in [Temam and Strang, 1980], [Kohn and Temam, 1983] is the subset of $L^1(\Sigma)$ such that the strains $\mathbf{H}$ and $\mathbf{K}$ associated to $\mathbf{u}$ and $\boldsymbol{\varphi}$ belong to $M_1(\Sigma,\mathrm{Lin})$, which is the function space of bounded Radon measures. The choice of this function space is motivated by the fact that [Temam and Strang, 1980] shows that the space BD seems to be the correct space for the displacement field in the problems of perfect plasticity. The choice of the space L^2 for the stress fields is the classical one used both in linear elasticity and plasticity[9]. In the following, we denote by a superscript ^{k} the kinematically admissible displacement fields, i.e. $(\mathbf{u}^k,\boldsymbol{\varphi}^k) \in \mathbb{D}$.

[9]Unlike what is done for the NRNT material, while the strains can be reasonably represented as singular measures as they may comprise concentrated jumps in the displacement field, the use of singular stresses for the description of the internal state of the material appears to be more controversial from a conceptual standpoint and it will not be adopted in our setting.

We define a state of impending plastic *collapse* as one in which a non-vanishing strain rate occurs under constant loads. In other words the collapse is the phenomenon for which, once a particular external load condition is reached $(\mathbf{b}, \mathbf{c}, \mathbf{t}_\partial, \mathbf{m}_\partial)$, called the *limit load*, the displacements and deformations of the structure, or a part of it, increase indefinitely while the load cannot increase. We call *collapse mechanism* the part of the displacement fields and their shape that increase indefinitely. Provided that the set $\mathbb{H}$ is convex and the strain increments obey an associate flow rule it is possible to prove the theorems of limit analysis.

If the set $\mathbb{H}$ is convex then, following [Lubliner, 2008], we can write

$$f(t\mathbf{T} + (1-t)\mathbf{T}^a, t\mathbf{M} + (1-t)\mathbf{M}^a) \leq tf(\mathbf{T}, \mathbf{M}) + (1-t)f(\mathbf{T}^a, \mathbf{M}^a) \tag{3.192}$$

for any admissible $(\mathbf{T}, \mathbf{M})$ and $(\mathbf{T}^a, \mathbf{M}^a)$ and any t such that $0 \leq t \leq 1$. It follows that

$$\left.\frac{\partial f}{\partial \mathbf{T}}\right|_{\mathbf{T}} \cdot (\mathbf{T} - \mathbf{T}^a) + \left.\frac{\partial f}{\partial \mathbf{M}}\right|_{\mathbf{M}} \cdot (\mathbf{M} - \mathbf{M}^a) \geq f(\mathbf{T}, \mathbf{M}) - f(\mathbf{T}^a, \mathbf{M}^a). \tag{3.193}$$

Thus, given the associate flow rule, for any $(\mathbf{T}^a, \mathbf{M}^a)$ such that $f(\mathbf{T}^a, \mathbf{M}^a) \leq f(\mathbf{T}, \mathbf{M})$, we have

$$(\mathbf{T} - \mathbf{T}^a) \cdot \dot{\mathbf{H}}^p + (\mathbf{M} - \mathbf{M}^a) \cdot \dot{\mathbf{K}}^p \geq 0, \tag{3.194}$$

known as the *maximum dissipation inequality*[10]. Moreover, since the set $\mathbb{H}$ is convex, we have

$$(\mathbf{T} - \mathbf{T}^s) \cdot \dot{\mathbf{H}}^p + (\mathbf{M} - \mathbf{M}^s) \cdot \dot{\mathbf{K}}^p > 0, \quad \forall (\mathbf{T}^s, \mathbf{M}^s). \tag{3.196}$$

Another consequence of (3.194) is the Drucker stability condition, written in terms of the second order plastic work. Following [Bigoni, 2012], dividing (3.194) by the time increment dt and taking the limit for $dt \to 0$ we get

$$\dot{\mathbf{T}} \cdot \dot{\mathbf{H}}^p + \dot{\mathbf{M}} \cdot \dot{\mathbf{K}}^p \geq 0. \tag{3.197}$$

To prove the lower bound theorem we need the following lemma

Lemma 3.5. *The elastic strain increments and the stress increments are null at collapse:*

$$\dot{\mathbf{T}} = \mathbf{0}, \quad \dot{\mathbf{M}} = \mathbf{0}, \quad \dot{\mathbf{E}}^e = \mathbf{0}, \quad \dot{\mathbf{X}}^e = \mathbf{0}, \quad \dot{\mathbf{E}} = \dot{\mathbf{E}}^p, \quad \dot{\mathbf{X}} = \dot{\mathbf{X}}^f. \tag{3.198}$$

Proof. The virtual work equation for the load increments at impending collapse writes as

$$\begin{aligned} \int_\Sigma (\dot{\mathbf{b}} \cdot \mathbf{v} + \dot{\mathbf{c}} \cdot \mathbf{w})\, d\Sigma + \int_{\partial\Sigma_N} (\dot{\mathbf{t}}_\partial \cdot \mathbf{v} + \dot{\mathbf{m}}_\partial \cdot \mathbf{w})\, d\Gamma = 0 \\ = \int_\Sigma \left(\dot{\mathbf{T}}(\dot{\mathbf{H}}^p + \mathsf{C}_T^{-1}\dot{\mathbf{T}}) + \dot{\mathbf{M}}(\dot{\mathbf{K}}^p + \mathsf{C}_M^{-1}\dot{\mathbf{M}})\right) d\Sigma. \end{aligned} \tag{3.199}$$

[10] The name is due to the fact that the associate flow rule can be deduced by requiring the dissipation (3.178) to be maximum under the constraint $f(\boldsymbol{\sigma}) \leq 0$. The problem can be written as

$$\min_{\dot{\boldsymbol{\xi}}} (\dot{\xi} f(\boldsymbol{\sigma}) - \boldsymbol{\sigma} \cdot \dot{\boldsymbol{\xi}}), \tag{3.195}$$

where $\dot{\xi}$ is a Lagrange multiplier. Taking the first variation with respect to $\boldsymbol{\sigma}$ yields the normality rule (3.188) along with the KKT conditions (3.189).

Since the elasticity tensors are positive definite, $\mathsf{C}_T^{-1}\dot{\mathbf{T}}\cdot\dot{\mathbf{T}} > 0$ and $\mathsf{C}_M^{-1}\dot{\mathbf{M}}\cdot\dot{\mathbf{M}} > 0$ unless $\dot{\mathbf{T}} = \mathbf{0}$ and $\dot{\mathbf{M}} = \mathbf{0}$. This fact together with the (3.197) implies that at impending collapse or incipient plastic flow the stress rates vanish so that the elastic strain increments vanish. □

It's worth observing that the previous result holds true also for any kinematically admissible displacement field $(\mathbf{u}^k, \boldsymbol{\varphi}^k)$. In view of Lemma 3.5, it is noticed that, for kinematically admissible displacement fields, the internal power reduces to the so-called *total dissipation power* (or simply total dissipation)

$$\mathcal{P}_I = \int_\Sigma \left(\mathbf{T}\cdot\dot{\mathbf{H}}^p + \mathbf{M}\cdot\dot{\mathbf{K}}^p\right) d\Sigma = \int_\Sigma \delta\, d\Sigma = \mathcal{D}. \tag{3.200}$$

We are now in the position to prove the static theorem of limit analysis.

Theorem 3.6 (Static theorem)**.** *The existence of a safe stress field, that is $\mathbb{A}^s \neq \emptyset$, is a sufficient condition for the collapse not to occur.*

Proof. To prove the static theorem of limit analysis we suppose by absurd that a safe stress state exists for the structure in presence of the collapse loads. Then, it also exists the stress field in equilibrium with the external loads. Writing the virtual power equation for the field $(\mathbf{T}-\mathbf{T}^s, \mathbf{M}-\mathbf{M}^s)$, which is self-equilibrated, and for the real collapse strain increments, yields

$$\int_\Sigma \left((\mathbf{T}-\mathbf{T}^s)\cdot\dot{\mathbf{H}}^p + (\mathbf{M}-\mathbf{M}^s)\cdot\dot{\mathbf{K}}^p\right) d\Sigma = 0 \tag{3.201}$$

in contrast with the convexity of the safe stress domain, which can be expressed as

$$(\mathbf{T}-\mathbf{T}^s)\cdot\dot{\mathbf{H}}^p + (\mathbf{M}-\mathbf{M}^s)\cdot\dot{\mathbf{K}}^p > 0. \tag{3.202}$$

□

In the applications of the static theorem of limit analysis we assume that the final configuration is so close to the reference one that the equilibrium can be written in the initial geometry of the structure and that, whatever the stress and strain history the shell undergoes, the stress range remains the same and it is known at time t_0.

We can also prove the kinematic theorem of limit analysis.

Theorem 3.7 (Kinematic theorem)**.** *The existence of a kinematically admissible displacement field, that is $\mathbb{D} \neq \emptyset$, for which $\mathcal{P}_E > \mathcal{D}$ is a sufficient condition for the collapse to occur.*

Proof. By absurd, we suppose that a kinematically admissible displacement field exists for a stable structure (i.e. for which the collapse doesn't occur). Then, it also exists a stress field in equilibrium with the external loads $(\mathbf{b}, \mathbf{c}, \mathbf{t}_\partial, \mathbf{m}_\partial)$, such that

$$\int_\Sigma (\mathbf{b}\cdot\mathbf{v}^k + \mathbf{c}\cdot\mathbf{w}^k)\, d\Sigma + \int_{\partial\Sigma} (\mathbf{t}\cdot\mathbf{v}^k + \mathbf{m}\cdot\mathbf{w}^k)\, d\Gamma = \int_\Sigma \left(\mathbf{T}\cdot\dot{\mathbf{H}}^k + \mathbf{M}\cdot\dot{\mathbf{K}}^k\right) d\Sigma. \tag{3.203}$$

Since $(\mathbf{T}, \mathbf{M})$ is statically admissible it must be

$$\int_\Sigma \left((\mathbf{T}^k-\mathbf{T})\cdot\dot{\mathbf{H}}^k + (\mathbf{M}^k-\mathbf{M})\cdot\dot{\mathbf{K}}^k\right) d\Sigma > 0, \tag{3.204}$$

where $(\mathbf{T}^k, \mathbf{M}^k)$ is the stress field associated to $(\dot{\mathbf{H}}^k, \dot{\mathbf{K}}^k)$ by the flow rule, not necessarily in equilibrium with the collapse loads. Then, it follows

$$\int_\Sigma \left(\mathbf{T}^k \cdot \dot{\mathbf{H}}^k + \mathbf{M}^k \cdot \dot{\mathbf{K}}^k\right) d\Sigma \geq \int_\Sigma \left(\mathbf{T} \cdot \dot{\mathbf{H}}^k + \mathbf{M} \cdot \dot{\mathbf{K}}^k\right) d\Sigma. \tag{3.205}$$

But, since $(\mathbf{v}^k, \mathbf{w}^k)$ is unstable,

$$\begin{aligned}\int_\Sigma (\mathbf{b} \cdot \mathbf{v}^k + \mathbf{c} \cdot \mathbf{w}^k)\, d\Sigma + \int_{\partial\Sigma} (\mathbf{t} \cdot \mathbf{v}^k + \mathbf{m} \cdot \mathbf{w}^k)\, d\Gamma > \int_\Sigma \left(\mathbf{T}^k \cdot \dot{\mathbf{H}}^k + \mathbf{M}^k \cdot \dot{\mathbf{K}}^k\right) d\Sigma \geq \\ \geq \int_\Sigma \left(\mathbf{T} \cdot \dot{\mathbf{H}}^k + \mathbf{M} \cdot \dot{\mathbf{K}}^k\right) d\Sigma\end{aligned} \tag{3.206}$$

that is $\mathcal{P}_E[\mathbf{b}, \mathbf{c}, \mathbf{t}_\partial, \mathbf{m}_\partial] > \mathcal{P}_I[\mathbf{T}, \mathbf{M}, \dot{\mathbf{H}}^k, \dot{\mathbf{K}}^k]$ which is in contrast with equation (3.203). □

Some simple classes of materials are used in the analyses of the case studies and are thus examined in the following. In the previous hypotheses and with the aim of exploiting the static theorem of limit analysis, it is sufficient for their characterisation to specify the convex set of the admissible stresses $\mathbb{H}$ and the compatible strain range $\mathbb{K}$.

3.7.1 M1: Heyman material

This material model is an adaptation to the case of shells of that proposed by Heyman. The hypotheses are:

1. the shell has a null tensile strength in any direction contained in the tangent plane to the middle surface;
2. the shell compressive strength is unbounded;
3. the shear strength is unbounded.

The only feature of such a material is the null resistance to tractions. This material model is non-dissipative as fractures nucleates and propagates at zero stress. To define the stress range it is useful to introduce the concept of *normal eccentricity*[11], or simply eccentricity, as the ratio

$$e(\boldsymbol{\nu}) \triangleq \frac{\mathbf{m}(\boldsymbol{\nu}) \cdot \boldsymbol{\nu}}{\mathbf{t}(\boldsymbol{\nu}) \cdot \boldsymbol{\nu}} = \frac{\mathbf{M}\boldsymbol{\nu} \cdot \boldsymbol{\nu}}{\mathbf{T}\boldsymbol{\nu} \cdot \boldsymbol{\nu}}, \tag{3.207}$$

where the last expression is a consequence of Cauchy theorem. For the internal stresses to be only compressive the condition $-h \leq e(\boldsymbol{\nu}) \leq h$ must hold $\forall\, \boldsymbol{\nu}$. Since $\boldsymbol{\nu} \in T_x$, we can also rewrite this requirement as

$$h\mathbf{N}\boldsymbol{\nu} \cdot \boldsymbol{\nu} + |\mathbf{M}\boldsymbol{\nu} \cdot \boldsymbol{\nu}| \leq 0, \tag{3.208}$$

[11] Although one can define different concepts of eccentricity, using other components of the force vector and the couple force vector, here we are interested in the eccentricity of the internal actions acting on the normal space N_x and orthogonally to the generic coordinate line. The physical justification for this choice lies in the fact that in order to formulate a failure criterion based on Heyman's hypotheses, we focus the attention on material 'joints' of height $2h$, and base $d\theta^\alpha$ which are considered incapable of carrying tensile stresses.

where $\mathbf{N} \in \text{Sym}$ is the surface part of $\mathbf{T}$[12]. In these hypotheses, the stress range can be expressed independently from $\boldsymbol{\nu}$ as

$$\mathbb{H}(\mathbf{y}) = \left\{(\mathbf{N}, \mathbf{M}) \in \text{Sym} \times \text{Sym} : |\mathbf{M}| + h(\mathbf{y})\mathbf{N} \in \text{Sym}^-\right\}. \tag{3.209}$$

It can be easily verified that the set $\mathbb{H}$ is convex. We observe that the condition can also be expressed by

$$h(\mathbf{y})\mathbf{N} + \mathbf{M} \in \text{Sym}^- \quad \text{and} \quad h(\mathbf{y})\mathbf{N} - \mathbf{M} \in \text{Sym}^- \tag{3.210}$$

which also imply $\mathbf{N} \in \text{Sym}^-$ (as shown in [Lucchesi et al., 1999]). The first dissipative term can be decomposed as follow

$$\mathbf{T} \cdot \dot{\mathbf{H}}^p = t^{\alpha\beta}\dot{\xi}_{\alpha\beta} + t^{3\alpha}\dot{\xi}_{3\alpha}. \tag{3.211}$$

Moreover, since the shear strength is unbounded, there is just the elastic part of the shear strains $\dot{\xi}_{3\alpha} = 0$. It is observed that the only parameter that determines the stress range is the thickness of the shell.

Following [Lucchesi et al., 1999] since the compressive strength is unbounded, the fracture strains satisfy the following relations

$$\mathbf{E}^p + h\mathbf{K}^p \in \text{Sym}^+, \quad \mathbf{E}^p - h\mathbf{K}^p \in \text{Sym}^+, \tag{3.212}$$

where $\mathbf{E}$ denotes the surface part of $\mathbf{H}$. Then we have

$$\mathbb{K}(\mathbf{y}) = \left\{(\mathbf{H}, \mathbf{K}) \in \text{Sym} \times \text{Sym} : \mathbf{E} + h|\mathbf{K}| \in \text{Sym}^+\right\}, \tag{3.213}$$

and the dissipative term is zero, as the following orthogonality condition holds

$$\delta = \mathbf{N} \cdot \dot{\mathbf{E}}^p + \mathbf{M} \cdot \dot{\mathbf{X}}^p = 0. \tag{3.214}$$

Denoted by N, T and M the normal force, shear force and bending moment on the generic joint respectively, the admissible domain in the N, T, M space is shown in Figure 3.10.

3.7.2 M2: Material with finite shear resistance

While for masonry domes under gravitational loads the shear resistance is generally not an issue, things can be different when the shell is subjected to horizontal actions too. In that case, particular attention should be paid to checking the maximum magnitude of the shear forces in order to verify the no-sliding hypothesis. For this reason, in order to relax the Heyman hypotheses by considering finite shear strength, a modification to the previous M1 model is analysed. An extension of the Heyman hypotheses has been already made in [Angelillo et al., 2010], by adopting a mixed non-linear elastic and plastic model, considering a NENT material in traction and a plastic material with finite compressive strength in compression. In the same spirit of that work, we instead specialise the material model to the case of shells having a finite shear resistance.

[12] It's worth observing that it is explicitly required, as a constitutive assumption, that the tensors $\mathbf{N}$ and $\mathbf{M}$ are symmetric. Different assumptions for the material are also possible but they will not be treated in the present thesis.

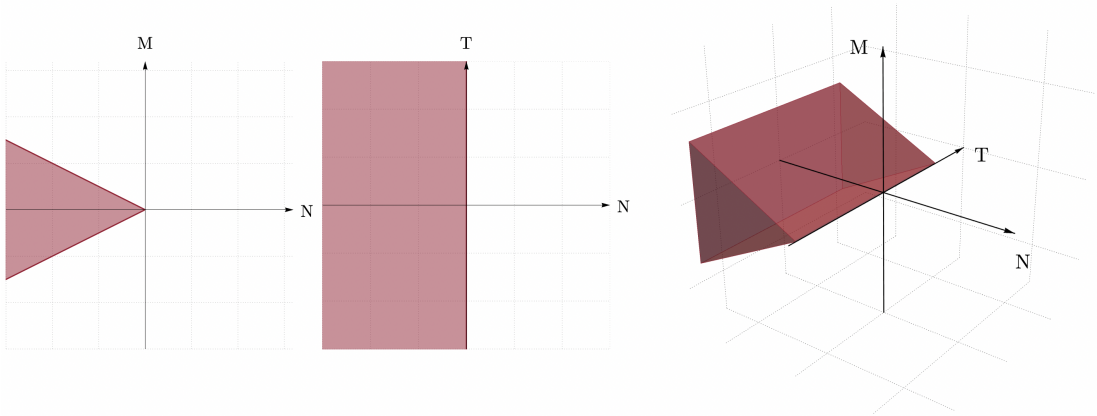

Figure 3.10: Admissible domain for M1 model.

Defining a suitable shear strength criterion for masonry is not a fully resolved issue, especially when the effect of masonry texture must be considered (see, e.g., [Mousavian and Casapulla, 2020]). The easiest way to approach the problem is to refer to the Mohr-Coulomb law for the shear resistance. Thus, with reference to the generic joint's interface, we write

$$|T| \leq c - \tan\phi N \tag{3.215}$$

with $\phi > 0$ the friction angle and $c \geq 0$ the cohesion, where

$$|T| = \sqrt{\mathbf{T}^\intercal \mathbf{T}\boldsymbol{\nu}\cdot\boldsymbol{\nu} - (\mathbf{T}\boldsymbol{\nu}\cdot\boldsymbol{\nu})^2}, \quad N = \mathbf{T}\boldsymbol{\nu}\cdot\boldsymbol{\nu}. \tag{3.216}$$

Since the tensor $\mathbf{T}$ is not symmetric, this condition cannot be expressed independently of $\boldsymbol{\nu}$, as in the case of M1 model[13].

The intersection of the limitations on tensile and shear strength yields the stress range for M2 material

$$\begin{aligned}\mathbb{H} = \Big\{ &(\mathbf{T},\mathbf{M}) \in \text{Lin}\times\text{Sym} : |\mathbf{M}| + h(\mathbf{y})\mathbf{N} \in \text{Sym}^-, \\ &\sqrt{\mathbf{T}^\intercal \mathbf{T}\boldsymbol{\nu}\cdot\boldsymbol{\nu} - (\mathbf{T}\boldsymbol{\nu}\cdot\boldsymbol{\nu})^2} + \mu\,\mathbf{T}\boldsymbol{\nu}\cdot\boldsymbol{\nu} - c \leq 0, \quad \forall\boldsymbol{\nu}\Big\},\end{aligned} \tag{3.218}$$

with $\mu = \tan\phi$ the friction coefficient. It can be proved that this is a convex set since it's the intersection of two convex cones. In this case, the only parameters characterising the failure criterion are the thickness, the friction angle and the cohesion. The energy dissipation rate in this case is different from zero, and equal to

$$\delta = \mathbf{T}\cdot\dot{\mathbf{H}}^p \geq 0. \tag{3.219}$$

The admissible domain in the N, T, M space is shown in Figure 3.11.

[13] In the case of a 3d body, since $\mathbf{T} \in \text{Sym}$, by exploiting the Cayley-Hamilton theorem (see, for example, [Itskov, 2007]), it is shown in [Lucchesi et al., 2021] that the stress range can be written independently from $\boldsymbol{\nu}$ as

$$\mathbb{H}^s = \left\{ \mathbf{T} \in \text{Lin} : \|\mathbf{T} - \bar{c}\,\mathbf{I}\|^2 - \frac{1+\sin^2\phi}{2}\big(\text{tr}(\mathbf{T} - \bar{c}\,\mathbf{I})\big)^2 \leq 0, \quad \text{tr}(\mathbf{T} - \bar{c}\,\mathbf{I}) \leq 0 \right\} \tag{3.217}$$

with $\bar{c} = c/\tan\phi$. The set $\mathbb{H}^s$ is a convex cone.

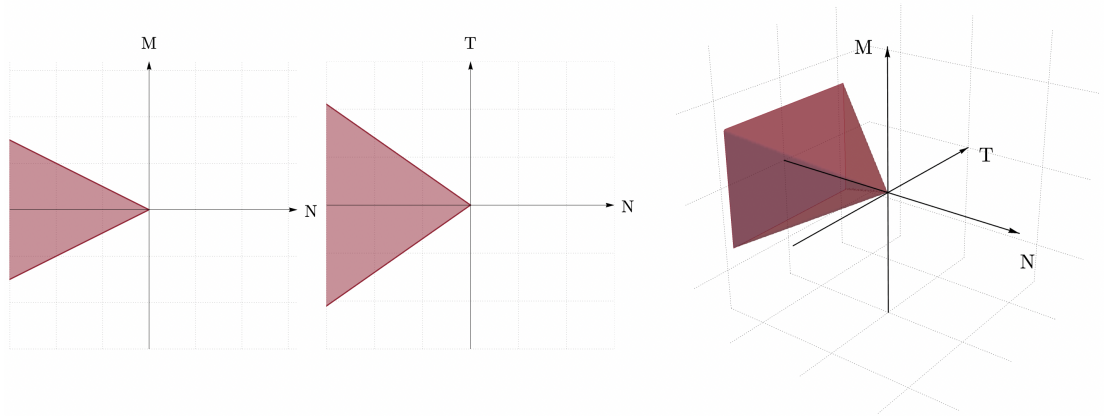

Figure 3.11: Admissible domain for M2 model.

Considerations about the shear strength: influence of the texture

Since the cohesion is generally difficult to estimate, and since it is generally assumed null on the joints as a conservative assumption, one is tempted to search for a stress field compatible with the hypothesis that the cohesion is zero everywhere. However, finding a stress field with such restriction may be very challenging as the assumption of zero cohesion is often overly limiting from a mechanical standpoint.

To give an example, let's consider a generic dome, where the bricks are disposed by horizontal layering and with half running bond pattern, as shown in Figure 3.12 (a). Moreover, let's consider a null cohesion on mortar joints. It is recognised that in the meridian direction, which is a weak direction for the shear strength as mortar joints are uninterrupted (see Figure 3.12 (b)), the Mohr-Coulomb failure criterion needs to be satisfied with zero cohesion. On the other hand, if we consider the circumferential direction or any direction between the meridian and the circumferential one, a sliding surface can form either by intersecting different mortar joints (blue line in Figure 3.12 (c) and (d)) or by cracking the bricks (red line in Figure 3.12 (c) and (d)). If bricks are cracked, considering the cohesion equal to zero would be excessively conservative, as the resistant elements surely have some strength that needs to be considered. If the mortar joints are met, then it is seen how the surfaces of the bricks in the meridian direction would contribute to the shear resistance (purple lines in Figure 3.12 (c) and (d)).

These remarks highlight that the issue of the shear failure is not banal, and simply adopting the Morh-Coulomb criterion with null cohesion could lead to overly cautious estimates of dome safety. In what follows, when the shear strength needs to be taken into account, we adopt a criterion that limits the shear force only along what we call *weak shear directions*, that can be identified based on the texture of the bricks (or blocks).

A remark on the dilatancy effect

Adopting the M2 model implies the so-called dilatancy effect, i.e. the presence of normal strain together with the shear strain in order to maintain the normality hypothesis. Although the dilatancy effect is sometimes seen in masonry, it is not necessarily linked to

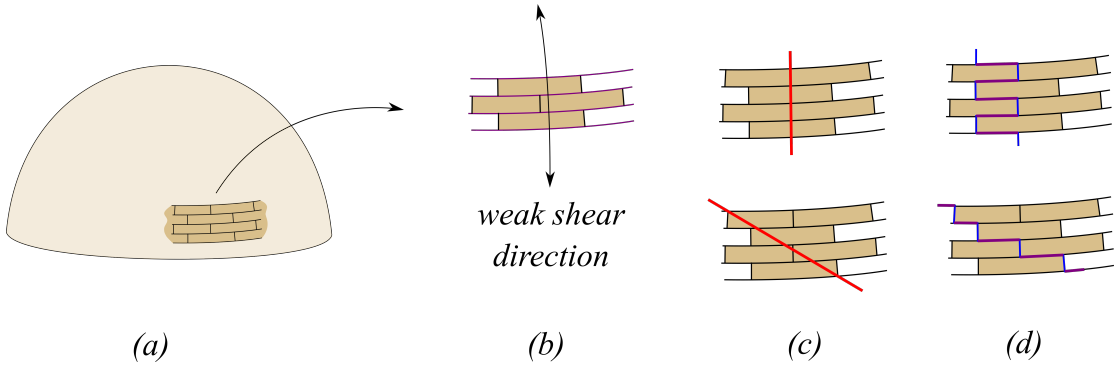

Figure 3.12: Texture effect on shear resistance.

the friction angle, but rather to the internal masonry units disposition. In order to keep physical coherence and still be able to apply the static theorem of limit analysis, we can exploit Radenkovic theorems for nonstandard materials (see for example [Lubliner, 2008]). The second Radenkovic's theorem is based on the existence of a convex subset $\hat{\mathbb{H}} \subset \mathbb{H}$ which has the property that to any $(\mathbf{T}, \mathbf{M}) \in \partial\mathbb{H}$ there correspond a $(\hat{\mathbf{T}}, \hat{\mathbf{M}}) \in \partial\hat{\mathbb{H}}$ such that

1)
$$\dot{\mathbf{H}}^p = \dot{\xi}\frac{\partial g}{\partial \mathbf{T}}\bigg|_{\hat{\mathbf{T}}}, \quad \dot{\mathbf{K}}^p = \dot{\xi}\frac{\partial g}{\partial \mathbf{M}}\bigg|_{\hat{\mathbf{M}}}, \tag{3.220}$$

where $g(\mathbf{T}, \mathbf{M})$ is defined by the conditions

$$\hat{\mathbb{H}} = \left\{(\mathbf{T}, \mathbf{M}) : g(\hat{\mathbf{T}}, \hat{\mathbf{M}}) \leq 0\right\}, \quad \partial\hat{\mathbb{H}} = \left\{(\mathbf{T}, \mathbf{M}) : g(\hat{\mathbf{T}}, \hat{\mathbf{M}}) = 0\right\}, \tag{3.221}$$

2)
$$(\mathbf{T} - \hat{\mathbf{T}}) \cdot \dot{\mathbf{H}}^p + (\mathbf{M} - \hat{\mathbf{M}}) \cdot \dot{\mathbf{K}}^p \geq 0, \quad \forall (\hat{\mathbf{T}}, \hat{\mathbf{M}}) \in \hat{\mathbb{H}} \tag{3.222}$$

where inequality holds strictly for safe stress states $(\hat{\mathbf{T}}^s, \hat{\mathbf{M}}^s) \in \mathrm{Int}(\hat{\mathbb{H}})$.

In other words, it exists a fictitious standard material associated to the real non standard one, whose convex stress range is entirely contained inside the real stress range and for which an associated flow rule holds. Once such material can be identified, we are able to prove

Theorem 3.8 (Radenkovic's second theorem)**.** *The existence of a safe stress field for the fictitious standard material, that is $\hat{\mathbb{A}}^s \neq \emptyset$, is a sufficient condition for the collapse not to occur.*

Proof. The proof retrace the one for the static theorem of limit analysis. Let's suppose that a safe stress state $(\hat{\mathbf{T}}^s, \hat{\mathbf{M}}^s)$ exists for the fictitious standard material in presence of collapse. Then, it also exists the real stress field in equilibrium with the external loads. By the virtual power theorem written for the fields $(\mathbf{T} - \hat{\mathbf{T}}^s, \mathbf{M} - \hat{\mathbf{M}}^s)$, which is self-equilibrated, and for the real collapse strain increments, yields

$$\int_\Sigma \left((\mathbf{T} - \hat{\mathbf{T}}^s) \cdot \dot{\mathbf{H}}^p + (\mathbf{M} - \hat{\mathbf{M}}^s) \cdot \dot{\mathbf{K}}^p\right) d\Sigma = 0, \tag{3.223}$$

and by localisation

$$(\mathbf{T} - \hat{\mathbf{T}}^s) \cdot \dot{\mathbf{H}}^p + (\mathbf{M} - \hat{\mathbf{M}}^s) \cdot \dot{\mathbf{K}}^p = 0. \tag{3.224}$$

Since $(\hat{\mathbf{T}}^s, \hat{\mathbf{M}}^s)$ is statically admissible, and since $\hat{\mathbb{H}}$ is convex, it holds the inequality

$$(\hat{\mathbf{T}} - \hat{\mathbf{T}}^s) \cdot \dot{\mathbf{H}}^p + (\hat{\mathbf{M}} - \hat{\mathbf{M}}^s) \cdot \dot{\mathbf{K}}^p > 0. \tag{3.225}$$

But, by adding the previous to the inequality (3.222) we get

$$(\mathbf{T} - \hat{\mathbf{T}}^s) \cdot \dot{\mathbf{H}}^p + (\mathbf{M} - \hat{\mathbf{M}}^s) \cdot \dot{\mathbf{K}}^p > 0, \tag{3.226}$$

in contrast with equation (3.224). □

We notice that the auxiliary subset $\hat{\mathbb{H}}$ is not unique. The closer $\hat{\mathbb{H}}$ is to $\mathbb{H}$ the best estimation of the lower bound one can get. However, since the two sets do not coincide, it follows that the lower and upper bounds on the limit loading, being based on two different standard materials, cannot be made to coincide. The correct limit loading in the nonstandard material cannot, therefore, be determined in general. This result is consistent with the absence of a uniqueness proof for the stress field in a body made of a nonstandard perfectly plastic material ([Lubliner, 2008]).

Radenkovic's second theorem allows us to somehow 'avoid' the problem of dilatancy. Indeed, let's assume that an admissible stress field is identified, for which the permanent strain increment is normal to the stress range. Given the shape of the domain, for every such a stress field, we can identify a convex fictitious stress range, which is entirely contained in the real one, and for which an associated flow rule can be defined that doesn't foresee dilatancy, as shown in Figure 3.13. It can be shown that the normality rule holds true if the strain increment belongs to the normal cone (grey cone in Figure 3.13) in the corner point Q. Since such a fictitious domain can always be identified in this way, we can always refer to the nonstandard material which doesn't foresee dilatancy and apply the static theorem for the standard fictitious material.

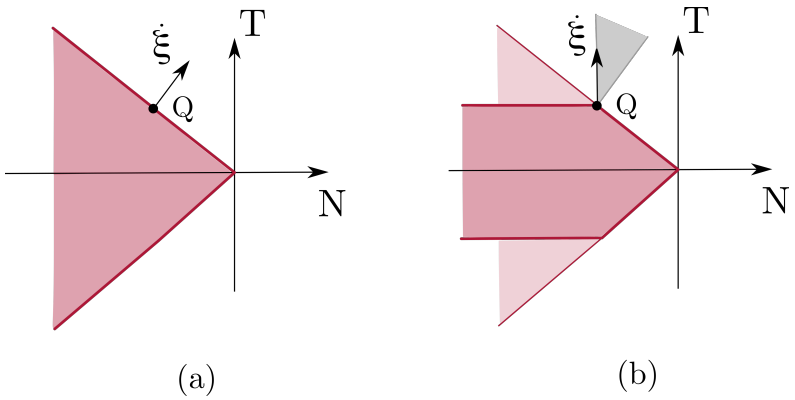

(a) (b)

Figure 3.13: Modification to the stress range in order to avoid dilatancy effect: (a) standard material with permanent strain increment normal to the stress range; (b) modified stress range.

3.8.1 M3, M4: Material with bounded compressive strength

If one wants to account for a limited compressive strength, say f_c, it can be assumed that the internal forces are distributed according to a stress-block law in the real 3d body, as shown in Figure 3.14. Considering the single fibre, of height $2h$ and infinitesimal width ds,

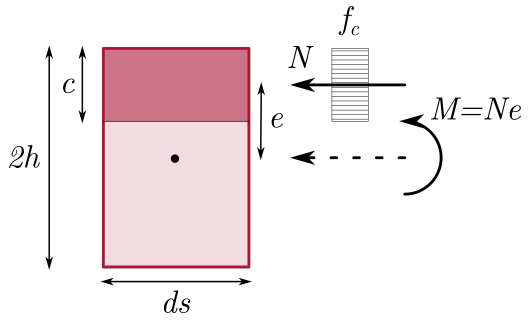

Figure 3.14: Assuming a stress-block distribution, a finite compressive strength can be accounted in the material model.

for the translational equilibrium we have $N = -xf_c$. It can be easily shown that the bending moment has to satisfy the following condition

$$|M| \leq -N\left(h + \frac{N}{2f_c}\right). \tag{3.227}$$

In this way, we can define two additional material models: the first one, termed M3 material, is a modification of material M1, with a finite compressive strength, whose stress range is

$$\mathbb{H}(\mathbf{y}) = \left\{(\mathbf{N},\mathbf{M}) \in \text{Sym} \times \text{Sym} : |\mathbf{M}| + \mathbf{N}\left(h(\mathbf{y})\mathbf{I} + \frac{\mathbf{N}}{2f_c}\right) \in \text{Sym}^-\right\}. \tag{3.228}$$

It can be shown that this set is still convex although it is not a cone. For the generic material element, the admissible domain in N, T, M space is shown in Figure 3.15.

If the limitation on compressive strength is added to the M2 material we identify the second additional model, termed M4 material, whose stress range is

$$\begin{aligned}\mathbb{H} = \Bigg\{(\mathbf{T},\mathbf{M}) \in \text{Lin} \times \text{Sym} :& |\mathbf{M}| + \mathbf{N}\left(h(\mathbf{y})\mathbf{I} + \frac{\mathbf{N}}{2f_c}\right) \in \text{Sym}^-, \\ & \sqrt{\mathbf{T}^\intercal\mathbf{T}\boldsymbol{\nu}\cdot\boldsymbol{\nu} - (\mathbf{T}\boldsymbol{\nu}\cdot\boldsymbol{\nu})^2} + \mu\,\mathbf{T}\boldsymbol{\nu}\cdot\boldsymbol{\nu} - c \leq 0, \quad \forall\boldsymbol{\nu}\Bigg\}.\end{aligned} \tag{3.229}$$

This domain is a convex set, since it is the intersection of convex sets. In the space N, T, M, the admissible domain is shown in Figure 3.16.

3.9 Summary and conclusive remarks

In this chapter, the classical thin shell model used to study the statics of masonry domes is recalled, and all hypotheses and governing equations are presented in detail. The classical

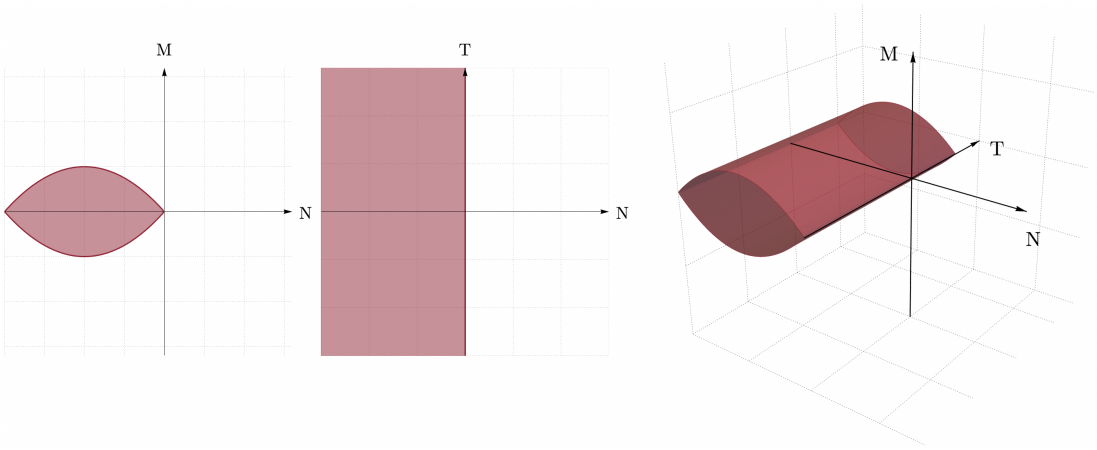

Figure 3.15: Admissible domain for M3 model.

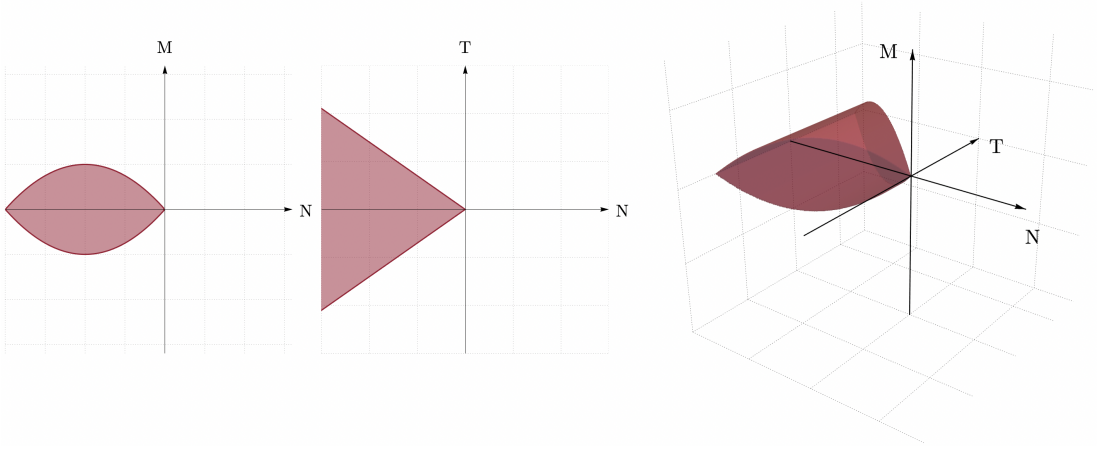

Figure 3.16: Admissible domain for M4 model.

theorems of limit analysis are specialised to the case of masonry shells and explicit proofs are provided. In the following we make use of the static theorem of limit analysis to carry out stability analysis of masonry domes subjected to vertical and horizontal loads. In doing so, it has been shown how the set of statically admissible generalised stress fields $\mathbb{A}(\mathbb{H})$ is sufficient to characterise the material for our purpose. The analyses that will be carried out will make use mainly of the M1 material, although it remains proven that the existence of a stress field in the case of M2, M3 and M4 materials will ensure stability since every one of these sets is convex and thus the static theorem holds.

Chapter 4

Statically admissible shell internal forces for safety assessment of masonry domes

This chapter traces a methodology for the safety level assessment with respect to collapse of unreinforced masonry domes having a generic shape, subjected to vertical and horizontal loads. The lower bound theorem of limit analysis enables us to perform conservative estimation of the limit load of a masonry structure by simply looking at the set $\mathbb{A}(\mathbb{H})$, checking for the existence of generalised force fields which are both in equilibrium with the external given loads and compatible with the material resistance. In general, several different stress states are possible for the structure, so the method selects one equilibrium state by means of a specifically developed optimisation procedure. Two kinds of problems will be addressed:

(P1): Under a given vertical loads distribution, find the minimum theoretical thickness of the dome which allows finding at least one statically admissible generalised force field;

(P2): For the real thickness of the structure, find the maximum horizontal loads that can be added to the vertical loads and for which it is possible to find at least one statically admissible generalised force field.

The first problem is addressed when vertical loads act on the dome and one wants to evaluate the (static) safety level. As already mentioned in Chapter 2, under Heyman hypotheses on the material, one of the measures that is commonly adopted to evaluate the safety level of the structure is the *geometrical safety factor*. As well known, the concept of a geometrical safety factor was first introduced by Heyman [Heyman, 1966] as a measure of safety for masonry arches but it can also be extended to masonry vaults. In particular, the geometrical safety factor is defined as the ratio between the actual thickness of the dome and the minimum thickness that would allow finding at least one statically admissible generalised force field. This safety factor is purely conventional and takes on meaning only in Heyman's hypotheses, that is to say, for the M1 material. In any case, the minimum thickness gives us useful evidence on how suitable the shape chosen for a particular dome is: if the minimum thickness is much smaller than the thickness of the dome it means that the structure could balance external loads with a stress regime which doesn't differ much from the membrane one (which is optimal for masonry).

The second problem deals with the evaluation of the maximum 'lateral load multiplier' in seismic (pseudo-static) analyses. In this second case, the aim is to evaluate the maximum lateral loads that can act on the structure before collapse, that is, the maximum horizontal actions for which it is possible to find at least one statically admissible generalised force field.

A first version of the technique can be found in [Barsotti et al., 2017] and later developed in [Barsotti et al., 2021]. A more similar procedure to that presented here was first applied, although in a simplified form, in [Barsi et al., 2019] in studying a sail vault. Then, in [Nodargi and Bisegna, 2021] an analogous method for axisymmetric domes subjected to vertical loads is fully developed. The approach presented here differs from the previous in some aspects. First, the method is not limited to axisymmetric domes, but it is capable of tackling domes having a generic shape. The equilibrium problem is numerically solved in its strong differential formulation by means of the collocation method and hence the generalised force components determined have smooth analytical expressions with global support. This allows for an accurate evaluation of the error made in the numerical solution of the equilibrium equations as well as for checking the material conditions everywhere within the domain and not just on a finite subset of point. Moreover, since the solution is analytical, the computation of every other mechanical quantity from the force field is straightforward. It is also capable of accounting for different joints' orientation as well as a limited shear resistance, which is a crucial aspect when horizontal loads are present.

4.1 The equilibrium problem of a shell

At equilibrium $\mathbf{v} = \mathbf{0}$ and $\boldsymbol{\omega} = \mathbf{0}$, so the balance system of equations (3.124) reduces to

$$\begin{cases} t^{\beta\alpha}|_\alpha - t^{3\alpha}\varkappa^\beta_{\cdot\alpha} + b^\beta = 0, \\ t^{3\alpha}|_\alpha + t^{\beta\alpha}\varkappa_{\beta\alpha} + b^3 = 0, \\ m^{\beta\alpha}|_\alpha - t^{3\beta} + c^\beta = 0, \\ \epsilon_{\alpha\beta}(t^{\alpha\beta} - \varkappa^\alpha_{\cdot\lambda} m^{\beta\lambda}) = 0, \end{cases} \tag{4.1}$$

and the problem is completed with the boundary conditions (3.125)

$$\begin{aligned} &\mathbf{t}_\partial = t^{i\alpha}\nu_\alpha \mathbf{e}_i, \\ &\mathbf{m}_\partial = m^{\beta\alpha}\nu_\alpha \mathbf{e}_\beta. \end{aligned} \qquad \text{on } \partial\Sigma_N. \tag{4.2}$$

Expanding the covariant derivatives, the same system can be rewritten in the following form

$$\begin{cases} t^{11}{}_{,1} + 2t^{11}\Gamma^1_{11} + t^{21}\Gamma^1_{12} + t^{12}\Gamma^1_{12} + t^{21}{}_{,2} + t^{11}\Gamma^2_{21} + t^{21}\Gamma^2_{22} + t^{21}\Gamma^1_{21} + t^{22}\Gamma^1_{22} + \\ \quad - \varkappa^1_{\cdot 1} t^{31} - \varkappa^1_{\cdot 2} t^{32} + b^1 = 0, \\ t^{12}{}_{,1} + t^{12}\Gamma^1_{11} + t^{22}\Gamma^1_{12} + t^{11}\Gamma^2_{11} + t^{12}\Gamma^2_{12} + t^{22}{}_{,2} + t^{12}\Gamma^2_{21} + 2t^{22}\Gamma^2_{22} + t^{21}\Gamma^2_{21} + \\ \quad - \varkappa^2_{\cdot 1} t^{31} - \varkappa^2_{\cdot 2} t^{32} + b^2 = 0, \\ t^{11}\varkappa_{11} + t^{12}\varkappa_{12} + t^{21}\varkappa_{21} + t^{22}\varkappa_{22} + t^{31}{}_{,1} + t^{31}\Gamma^1_{11} + t^{32}\Gamma^1_{21} + t^{32}{}_{,2} + t^{31}\Gamma^2_{12} + \\ \quad + t^{32}\Gamma^2_{22} + b^3 = 0, \\ m^{11}{}_{,1} + 2m^{11}\Gamma^1_{11} + m^{21}\Gamma^1_{12} + m^{12}\Gamma^1_{12} + m^{21}{}_{,2} + m^{11}\Gamma^2_{21} + m^{21}\Gamma^2_{22} + m^{21}\Gamma^1_{21} + m^{22}\Gamma^1_{22} + \\ \quad - t^{31} + c^1 = 0, \\ m^{12}{}_{,1} + m^{12}\Gamma^1_{11} + m^{22}\Gamma^1_{12} + m^{11}\Gamma^2_{11} + m^{12}\Gamma^2_{12} + m^{22}{}_{,2} + m^{12}\Gamma^2_{21} + 2m^{22}\Gamma^2_{22} + m^{21}\Gamma^2_{21} + \\ \quad - t^{32} + c^2 = 0, \\ t^{12} - t^{21} + m^{11}\varkappa^2_{\cdot 1} - m^{12}\varkappa^1_{\cdot 1} + m^{21}\varkappa^2_{\cdot 2} - m^{22}\varkappa^1_{\cdot 2} = 0. \end{cases} \tag{4.3}$$

It can be noticed that both the surface geometry (via the Christoffel symbols) and the joints' orientation (via the director's curvatures) play an important role in the equilibrium system.

The constitutive prescriptions of the material models require the surface part of the force tensor $\mathbf{T}$ and the couple force tensor $\mathbf{M}$ to be symmetric. Keeping in mind that also the Christoffel symbols are symmetric with respect to the lower indices $\Gamma^\alpha_{\beta\lambda} = \Gamma^\alpha_{\lambda\beta}$, the equilibrium system (4.3) reduces to

$$\begin{cases} t^{11}{}_{,1} + 2\Gamma^1_{11}t^{11} + 3\Gamma^1_{12}t^{12} + t^{12}{}_{,2} + \Gamma^2_{12}t^{11} + \Gamma^2_{22}t^{12} + \Gamma^1_{22}t^{22} - \varkappa^1_{\cdot 1}t^{31} - \varkappa^1_{\cdot 2}t^{32} + b^1 = 0, \\ t^{12}{}_{,1} + \Gamma^1_{11}t^{12} + \Gamma^1_{12}t^{22} + \Gamma^2_{11}t^{11} + 3\Gamma^2_{12}t^{12} + t^{22}{}_{,2} + 2\Gamma^2_{22}t^{22} - \varkappa^2_{\cdot 1}t^{31} - \varkappa^2_{\cdot 2}t^{32} + b^2 = 0, \\ \varkappa_{11}t^{11} + 2\varkappa_{12}t^{12} + \varkappa_{22}t^{22} + t^{31}{}_{,1} + \Gamma^1_{11}t^{31} + \Gamma^1_{12}t^{32} + t^{32}{}_{,2} + \Gamma^2_{12}t^{31} + \Gamma^2_{22}t^{32} + b^3 = 0, \\ m^{11}{}_{,1} + 2\Gamma^1_{11}m^{11} + 3\Gamma^1_{12}m^{12} + m^{12}{}_{,2} + \Gamma^2_{12}m^{11} + \Gamma^2_{22}m^{12} + \Gamma^1_{22}m^{22} - t^{31} + c^1 = 0, \\ m^{12}{}_{,1} + \Gamma^1_{11}m^{12} + \Gamma^1_{12}m^{22} + \Gamma^2_{11}m^{11} + 3\Gamma^2_{12}m^{12} + m^{22}{}_{,2} + 2\Gamma^2_{22}m^{22} - t^{32} + c^2 = 0, \\ \varkappa^2_{\cdot 1}m^{11} + (\varkappa^2_{\cdot 2} - \varkappa^1_{\cdot 1})m^{12} - \varkappa^1_{\cdot 2}m^{22} = 0. \end{cases} \tag{4.4}$$

Equations (4.4) represent a statically not determined equilibrium problem and sundry methods can be enforced to make it determined. The classical approach is to suitably characterise the elastic constants and solving the incremental problem, but this has the disadvantage of requiring a precise characterisation of all the relevant data for the problem, such as the material's parameters, the internal disposition of the units and the auto-stress state due to the history of building, only to cite some. Usually it's very difficult, if not impossible, to get all this information for masonry structures. Other approaches, based on limit analysis, consist of a priori choosing some of the generalised force functions and solving the equations in terms of the remaining ones. This approach, although often adopted in the past, has the disadvantage of limiting the possibilities of the structure to balance the loads. In the next section, two special of such choices are discussed.

In concluding this section it is worth observing that if the coordinate lines on the surface are also curvature lines, the mixed curvatures are null. Therefore, when $\varkappa^1_1 \neq \varkappa^2_2$ the $(4.4)_6$

yields $m^{12} = 0$. This means that, except in the particular case where $\varkappa_1^1 = \varkappa_2^2$, the moment tensor has the same principal directions as the curvature tensor. Hence the geometry of the shell partially determines the moment tensor regardless of the loads.

4.2 Some comments on two historical methods

Before going to the proposed method for the determination of statically admissible internal force distributions and the safety level assessment of masonry domes, it is worth to briefly address two methods, both working within the framework of limit analysis, which deserve to be recalled for their historical importance: the *slicing technique* and the *membrane analysis*.

4.2.1 The slicing technique

The so-called slicing technique is a well renowned method that dates to the 18$^{\text{th}}$ century [Poleni, 1748]. It consists in ideally subdividing a masonry dome into a series of plane arches thought as independent from each other. If a statically admissible distribution of internal forces can be determined within each arch, the whole dome is safe. Usually, the arched sub-structures are identified with a 'lunar slicing' method, by ideally cutting the dome along the meridians. Here the method is presented in the framework of shell theory, by assuming that a family of curves, that represents the axes of the arched structures, can be identified to be coincident with a family of coordinate lines, for example, the coordinate lines $\theta^1 = const.$ Let's assume that each spatial arch doesn't interact with the adjacent one, so that the only force components different from zero are $\{t^{22}, t^{32}, m^{22}\}$, and let's also assume that no external couple act on the dome, that is $c^\beta = 0$. In the given hypotheses the equilibrium equations become

$$\begin{cases} \Gamma^1_{22} t^{22} - \varkappa^1_{.2} t^{32} + b^1 = 0, \\ \Gamma^1_{12} t^{22} + t^{22}{}_{,2} + 2\Gamma^2_{22} t^{22} - \varkappa^2_{.2} t^{32} + b^2 = 0, \\ \varkappa_{22} t^{22} + \Gamma^1_{12} t^{32} + t^{32}{}_{,2} + \Gamma^2_{22} t^{32} + b^3 = 0, \\ \Gamma^1_{22} m^{22} = 0, \\ \Gamma^1_{12} m^{22} + m^{22}{}_{,2} + 2\Gamma^2_{22} m^{22} - t^{32} = 0, \\ -\varkappa^1_{.2} m^{22} = 0. \end{cases} \tag{4.5}$$

If $m^{22} = 0$, from $(4.5)_5$ we have $t^{32} = 0$, and the reduced system, which is statically underdetermined, describes the equilibrium of a cable. On the contrary, when $m^{22} \neq 0$, for the $(4.5)_6$ to be fulfilled we conclude that $\varkappa^1_{.2} = 0$, which means that, if the director is normal to Σ and then $\varkappa^1_{.2} = \kappa^1_{.2} = 0$ the coordinate lines must be lines of curvature. If the director is generally oriented this requirement is not compulsory, for example, in a false dome $\varkappa^\alpha_{.\beta} = 0$ and $(4.5)_6$ always holds. For the $(4.5)_4$ to be fulfilled, it's required that $\Gamma^1_{22} = 0$, which means that the coordinate lines $\theta^1 = const.$ must be plane curves. Finally, from $(4.5)_1$ we see that $b^1 = 0$, that is the load direction must be contained in the plane identified by the coordinate lines $\theta^1 = const.$ The above restrictions yield the notable result that strictly speaking the slicing technique is applicable only to axisymmetric domes if the external load is vertical. Moreover, if horizontal loads are also present, the slicing technique can be applied

to spherical domes only. The restrictions on the slicing technique are essentially due to the fact that the moment tensor is superficial. This means that if the slicing technique is applied to domes of general shape, the set of arches in which the shell is ideally subdivided should be considered as a set of spatial beams in which all internal force and moment components are present, rather than as parts of a shell.

4.2.2 The membrane analysis

Setting $t^{3\alpha} = 0$ and $m^{\alpha\beta} = 0$, the system (4.5) reduces to three equations describing the equilibrium of a membrane along with the compatibility conditions on the loads, that require $c^{\beta} = 0$. This kind of analysis is generally not suitable for assessing the safety level of a dome, since a membrane solution that involves only compressive stresses is seldom found, but it provides an efficient way to define the best shape to be given to a dome, once the external loads are given, in order to avoid tensile stresses.

An analysis method that is somewhat linked to the membrane equilibrium solutions is the Thrust Surface Analysis, which is sometimes thought as an extension of the membrane solution for the shell. Roughly speaking, TSA searches for the membranes wholly contained within the thickness of the dome, not necessarily coinciding with its middle surface, able to make equilibrium to the external loads by compressive forces only. The eccentricity of the membrane forces from the dome middle surface introduces bending moments along the meridian and hoop direction, and so thrust surfaces can be seen as an extension of the set of statically admissible distributions of internal forces for the dome with respect to the pure membrane solution.

As a matter of fact, this is exactly true only if at any point on the middle surface the joints are parallel to the load, otherwise transport couples would act on the membrane thus violating the compatibility conditions on loads.

In the case of the real Thrust Surface Analysis, the model on which such technique is based, at least in one of its formulations, is not the thin shell but the 3d Normal Rigid No-Tension (NRNT) simple continuum body (see references in Chapter 2), and the thrust surface is the support of a discontinuity in the stress field. In such a case the mechanical meaning of the thrust surface is deeply different from that of a shell solution

4.3 Statically admissible shell forces (SASF): the first simple case study of the conic shell

The historical methods mentioned in the previous section assess the safety level of masonry domes by searching for equilibrium solutions in suitable subsets of statically admissible internal forces. The simplification introduced by restricting the set of possible equilibrium states explored entails that in general the actual load bearing capacity of the dome is underestimated. This section presents a method for assessing the safety level of masonry domes modelled as shells that can greatly reduce this limitation. The idea of the method is first introduced with a simple example in which calculations can be carried out analytically. Then, the method is explained in detail, as well as its implementation.

Let's consider an axisymmetric shell of uniform thickness $2h$ having a middle surface shaped like a straight cone of height H and basis radius R (see Figure 4.1). The shell is

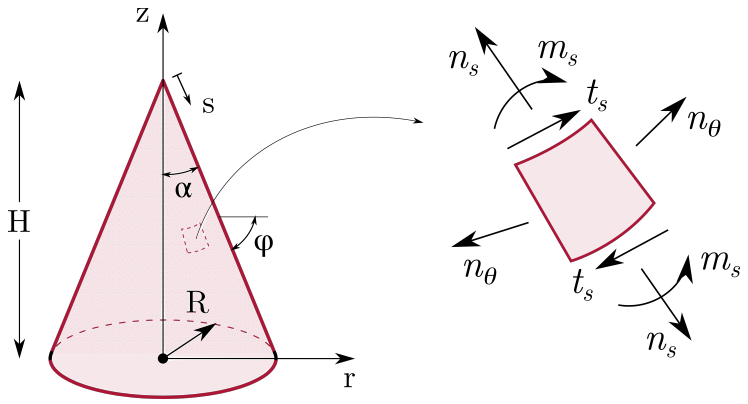

Figure 4.1: The conic shell.

made of a homogeneous material having a given specific weight γ and subjected exclusively to its self-weight. For simplicity, we consider the presence of a small hole at the top, whose diameter tending to zero and we assume that the shell is clamped at the base. Let's assume the material to be M1 (Heyman-like), that is, incapable of carrying tensile stresses but with infinite compressive strength and capable of opposing any relative sliding motion. The goal is to find the minimum thickness granting the stability, i.e., by virtue of the static theorem, the aim is to find for what thickness it is possible to find at least one statically admissible generalised force field. Given the symmetry of the structure, it is assumed that the best force field is axisymmetric[1]. The equilibrium equations for an axisymmetric shell and axisymmetric generalised forces reduces to a system of three equations in five unknowns, given by

$$\begin{cases} (rn_s)_{,s} - \dfrac{rt_s}{\rho} - n_\theta \cos\varphi + rp_s = 0, \\ (rt_s)_{,s} + \dfrac{rn_s}{\rho} + n_\theta \sin\varphi + rp_n = 0, \\ (rm_s)_{,s} - rt_s - m_\theta \cos\varphi = 0, \end{cases} \tag{4.6}$$

where $s \in [0, L]$ and $\theta \in [0, 2\pi]$ are the curvilinear coordinates and the force components are referred to the natural covariant base. For the conic shell we have

$$\begin{aligned} &L = \sqrt{R^2 + H^2}, \quad \cos\varphi = \frac{R}{L}, \quad \sin\varphi = \frac{H}{L}, \\ &\rho \to \infty, \quad r = s\sin\alpha, \quad \sin\alpha = \cos\varphi, \quad \cos\alpha = \sin\varphi, \end{aligned} \tag{4.7}$$

[1] Although a statically admissible force field need not to be axisymmetric, it can be easily seen that, since we are interested in optimised force fields, the best solution is one that satisfies symmetry conditions given by the geometry and the distribution of external loads.

and then, the equilibrium equations simplifies in

$$\begin{cases} (sn_s)_{,s} - n_\theta + sp_s = 0, \\ (st_s)_{,s} + n_\theta \dfrac{H}{R} + sp_n = 0, \\ (sm_s)_{,s} - st_s - m_\theta = 0. \end{cases} \tag{4.8}$$

It can be observed that a solution of the system exists for whatever value of the components n_θ and m_θ, so the equilibrium problem is two times statically not determined. By restricting ourselves to the case in which $m_\theta = 0$ and by defining the force components in an *equivalent beam* as

$$N = sn_s, \quad T = st_s, \quad M = sm_s, \tag{4.9}$$

it is possible to rewrite the equilibrium equations in the following way

$$\begin{cases} N_{,s} + \overline{p}_s = 0, \\ T_{,s} + \overline{p}_n = 0, \\ M_{,s} - T = 0, \end{cases} \tag{4.10}$$

which is formally identical to the set of equations describing the equilibrium of a straight beam and where the component n_θ appears as an additional external load

$$\overline{p}_s = sp_s - n_\theta, \qquad \overline{p}_n = sp_n + \frac{H}{R} n_\theta. \tag{4.11}$$

For a conic shell under its self-weight we have

$$p_s = \gamma \sin\varphi = \gamma \frac{H}{L}, \qquad p_n = \gamma \cos\varphi = \gamma \frac{R}{L}, \tag{4.12}$$

and then

$$\overline{p}_s = \gamma \frac{H}{L} s - n_\theta, \qquad \overline{p}_n = \gamma \frac{R}{L} s + \frac{H}{R} n_\theta. \tag{4.13}$$

Assuming the force components to be sufficiently differentiable, from the $(4.10)_3$ it is $T = M_{,s}$ and the differential problem becomes

$$\begin{cases} N' + \overline{p}_s = 0, \\ M'' + \overline{p}_n = 0, \\ N(0) = 0,\ M'(0) = 0,\ M(0) = 0, \end{cases} \tag{4.14}$$

where the boundary conditions are imposed by the infinitesimal hole at the top. The admissibility conditions for the M1 require that

$$\begin{cases} N(s) \leq 0, \\ -h \leq e(s) \leq h, \end{cases} \qquad \forall s \in [0, L], \tag{4.15}$$

that is the normal force has to be compressive and the eccentricity diagram (thrust line) has to be contained inside the shell's thickness. In addition it is required that $n_\theta \leq 0$, $\forall s \in$

$[0, L]$. Since the meridian and hoop directions are principal directions of forces and bending moments and since $m_\theta = 0$ the admissibility conditions are only those just given.

If $n_\theta = 0$ the problem is statically determined, the force components being

$$N = -\frac{\gamma H}{2L}s^2, \quad M = -\frac{\gamma R}{6L}s^3, \quad T = -\frac{\gamma R}{2L}s^2, \tag{4.16}$$

and the eccentricity is $e = -Rs/3H$ whose absolute value is maximum in $s = L$ and equal to $|e(L)| = RL/3H$. The minimum half-thickness that the cone should have to contain the thrust line is then $h_{min} = RL/3H$. A solution of (4.14) can be obtained for every function n_θ. We now wonder if it is possible to find a distribution of compressive n_θ and its intensity such to minimise the maximum of the absolute value of the eccentricity. In other words, we ask if it's possible to select, among the infinite functions n_θ, the one for which the minimum thickness of the shell is the smallest possible (or, equivalently, the geometric safety factor is the greatest possible). With this purpose, we initially limit ourself to the simplest distribution considering the class of constant functions $n_\theta = const.$, and we search for the best value of that constant such to minimise $\max|e(s)|$. Solving the equilibrium equations one gets

$$N = -\frac{\gamma H}{2L}s^2 + n_\theta s, \quad M = -\frac{\gamma R}{6L}s^3 - \frac{H n_\theta}{2R}s^2, \quad T = -\frac{\gamma R}{2L}s^2 - \frac{H n_\theta}{R}s, \tag{4.17}$$

and then

$$e = \frac{s(\gamma R^2 s + 3HLn_\theta)}{6LRn_\theta - 3RH\gamma s}. \tag{4.18}$$

By expressing n_θ as

$$n_\theta = -\frac{\gamma R^2}{HL}c, \tag{4.19}$$

with c being a positive constant (having the dimension of a length) and by introducing the dimensionless quantity $\mu = R/H = \tan\alpha > 0$, the eccentricity becomes

$$e = -\frac{\mu}{3}\left(\frac{s^2 - 3cs}{2\mu^2 c + s}\right). \tag{4.20}$$

The eccentricity can have an extremum either where the first derivative is null or at the boundaries. The first derivatives is

$$\frac{de}{ds} = -\frac{\mu}{3}\left(\frac{s^2 + 4\mu^2 cs - 6\mu^2 c^2}{(2\mu^2 c + s)^2}\right). \tag{4.21}$$

The only acceptable solution of the equation $e_{,s} = 0$ is

$$\overline{s} = \mu c\big(-2\mu + \sqrt{6 + 4\mu^2}\big). \tag{4.22}$$

Therefore,

$$\begin{cases} e(s = 0) = 0, \\ e(s = L) = -\dfrac{\mu}{3}\left(\dfrac{L^2 - 3cL}{2\mu^2 c + L}\right), \\ e(s = \overline{s}) = \dfrac{\mu c}{3}\left(3 + 4\mu^2 - 2\mu\sqrt{6 + 4\mu^2}\right). \end{cases} \tag{4.23}$$

One then needs to solve the following optimisation problem

$$\min_c \{\max\{|e(L)|, |e(\overline{s})|\}\}. \tag{4.24}$$

There may be two cases; the first one is the case for which

$$e(\overline{s}) = e(L), \tag{4.25}$$

whose unique solution is

$$c_1 = \frac{L}{6\mu}(2\mu + \sqrt{6+4\mu^2}). \tag{4.26}$$

The second case is

$$e(\overline{s}) = -e(L), \tag{4.27}$$

which is an equation with two solutions, only one of which is acceptable since it's the only positive one

$$c_2 = \frac{L}{3+2\mu^2-\mu\sqrt{6+4\mu^2}+\sqrt{-(3+4\mu^2)\big[-3+2\mu(-2\mu+\sqrt{6+4\mu^2})\big]}}. \tag{4.28}$$

For $c = c_1$ it is $\overline{s}|_{c=c_1} = L$ and the eccentricity is

$$e(L)|_{c=c_1} = \frac{L}{6}\big(-2\mu+\sqrt{6+4\mu^2}\big) > 0. \tag{4.29}$$

For $c = c_2$ it is, with the position $\Delta = -(3+4\mu^2)\big[-3+2\mu(-2\mu+\sqrt{6+4\mu^2})\big]$,

$$\begin{aligned} e(\overline{s})|_{c=c_2} &= \frac{L}{6\mu}\bigg(-3+\mu(-2\mu+\sqrt{6+4\mu^2})+\sqrt{\Delta}\bigg) > 0, \\ e(L)|_{c=c_2} &= -e(\overline{s})|_{c=c_2} < 0. \end{aligned} \tag{4.30}$$

It can be proven that

$$e(\overline{s})|_{c=c_1} > e(\overline{s})|_{c=c_2} \tag{4.31}$$

and then the optimal value of c which always minimise the maximum of the absolute value of the eccentricity is

$$c^O = \frac{L}{3+2\mu^2-\mu\sqrt{6+4\mu^2}+\sqrt{-(3+4\mu^2)\big[-3+2\mu(-2\mu+\sqrt{6+4\mu^2})\big]}}. \tag{4.32}$$

The hoop normal force, constant with s, is

$$n_\theta^O = -\gamma R\frac{\mu}{3+2\mu^2-\mu\sqrt{6+4\mu^2}+\sqrt{-(3+4\mu^2)\big[-3+2\mu(-2\mu+\sqrt{6+4\mu^2})\big]}} \tag{4.33}$$

and the minimum half-thickness is

$$h_{min} = \frac{L}{6\mu}\bigg(-3+\mu(-2\mu+\sqrt{6+4\mu^2})+\sqrt{\Delta}\bigg). \tag{4.34}$$

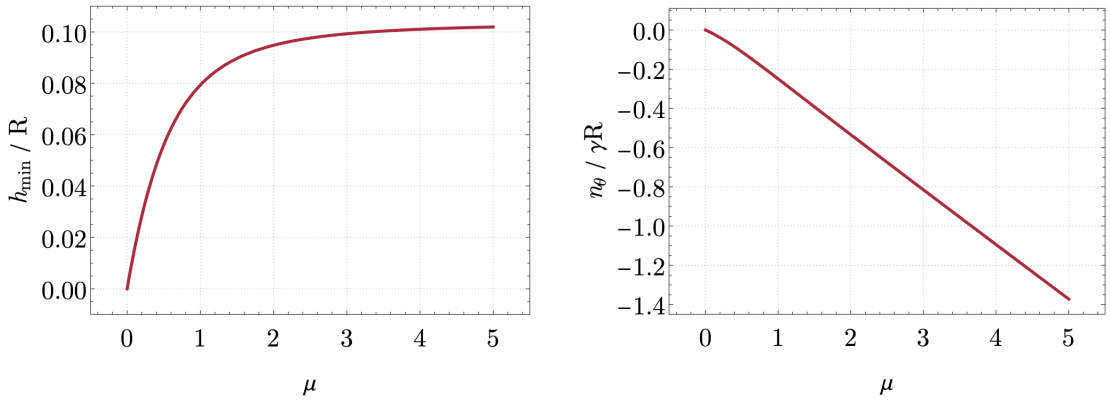

Figure 4.2: Plot of the dimensionless minimum half-thickness and the dimensionless optimum hoop normal force.

Figure 4.2 shows h_{min}/R and $n_\theta/\gamma R$ as functions of μ.

The value found for n_θ is the one that optimise the eccentricity for the problem at hand only with reference to the class of constant functions. In this case it is possible to carry out the calculations by hand, but for more complex cases, in which the class of functions is richer, the procedure leads naturally to mathematical optimisation problems. It's worth observing that, if one was able to explore all possible functions, one could find the absolute minimum thickness of the shell. Of course, the richer the class of functions considered, the closer the minimum thickness found will be to the real one.

4.4 Statically admissible shell forces (SASF): outline of the method

The method searches for the equilibrium state that maximise the safety level within the set of statically admissible internal forces. The adopted strategy is very simple and it is borrowed from the well-known flexibility method, used in the mechanics of beams. It consists of the following steps:

Step 1: Let E be the number of equilibrium equations (4.4), and U the number of unknown internal force components. As $U > E$ the system is statically undetermined. One can choose a set of $X = U - E$ functions, called *redundant generalised forces*, and express each of them as a linear combination of known basis functions, chosen a priori, leaving the coefficients unspecified. By doing so the system of equations becomes determinate;

Step 2: One can thus solve the linear system of equations with respect to the other $U - X$ internal force components, which are linear in the coefficients. In this way, the equilibrium equations are satisfied whatever the values of the coefficients of the linear combinations;

Step 3: One can finally solve a constrained optimisation problem that searches for the minimum of a suitable cost function related to the inverse of the safety level.

The independent variables of the optimisation problem are the coefficients of the linear combinations of known basis functions used for the redundant generalised forces while the constraints are the admissibility conditions for the material.

The various aspects of the illustrated procedure are analysed in detail below.

4.4.1 The choice of the redundant generalised force components

Regarding the first step, for a surface having a generic geometry and generic joints' disposition, it is $U = 8$ and $E = 6$ so that $X = 2$ redundant force functions have to be chosen. However, there are cases where the sixth equilibrium equation turns out to be an identity. The first example is the case in which the joints are 'spherically arranged' (in the simplest of such cases, the surface is a sphere with normal joints), for which $\varkappa^1_{.2} = \varkappa^2_{.1} = 0$ and $\varkappa^1_{.1} = \varkappa^2_{.2}$. Moreover, also in the case where all the joints have the same direction it is $\varkappa^\alpha_{.\beta} = 0$ (a simple case would be vertical joints, although there are no domes built with such a joints' disposition for evident building reasons). We refer to these special cases as the *spherical joints* case and the *flat joints* case, respectively. In these instances, the sixth equation is always an identity and the equilibrium equations reduce to a system of five differential equations so $U = 8$, $E = 5$ and $X = 3$ redundant force functions have to be chosen.

Concerning the choice of the redundant forces, a question arises whether they may be chosen freely among any component of the internal forces. The issue is not trivial since not every choice of redundant forces is admissible. To show this statement let's assume components t^{31} and m^{11} are chosen as redundant forces and try to solve the equilibrium equations when they are set to zero. From $(4.4)_6$ we see that where the lines of director curvature coincide with the coordinate lines $\varkappa^1_{.2} = 0$ and since, in general, the principal curvature are distinct $\varkappa^1_{.1} \neq \varkappa^2_{.2}$, we have $m^{12} = 0$. Then, if $\Gamma^1_{22} = 0$ the $(4.4)_4$ becomes an identity and the system is underdetermined. Instead, if $\Gamma^1_{22} \neq 0$ then $(4.4)_4$ implies $m^{22} = 0$ so that $m^{\alpha\beta} = 0$ and $t^{3\alpha} = 0$ and we fall back to the membrane solution. It is trivial to verify that also other choices of redundant forces are not admissible. The redundant force components selection is also linked to the parametrisation used to describe the middle surface. To this aim, a cylindrical coordinate system is adopted to describe the shell's geometry, and it is assumed that the surface admits the parametric expression

$$\mathbf{x}(\alpha, z) = \mathfrak{h}(\alpha, z)\cos\alpha\,\mathbf{i}_1 + \mathfrak{h}(\alpha, z)\sin\alpha\,\mathbf{i}_2 + z\,\mathbf{i}_3 \tag{4.35}$$

in which $0 \leq \alpha \leq 2\pi$ and $z_0 \leq z \leq z_1$, and and $\mathfrak{h}(\alpha, z)$ is a function that depends on the shape. This parametric expression is quite general because is able to closely approximate not only axisymmetric domes but also elliptical and oval base domes, which together constitute the vast majority of existing shapes. Moreover, the coordinate domain Θ is always rectangular and both the dome's base and the central opening on top (where the lantern is usually placed) are easily identified by the coordinate lines $z = z_0$ and $z = z_1$ respectively. The following considerations, although specialised to the case at hand, can be also extended to other classes of surfaces.

Although other choices of redundant forces may be also appropriate, one choice that has proven to be suitable is to select the contravariant components t^{11} and m^{11}, which are linked

to the normal force and bending moment in the hoops' direction, as redundant forces. Such choice has been verified to lead to a stable numerical solution scheme.

One reason that led to this choice is the fact that all the components whose values are known on the upper boundary, i.e. $t^{12}, t^{22}, t^{32}, m^{12}, m^{22}$, are kept in the system and five over six of the boundary conditions can be directly specified on those components (Dirichlet-type boundary conditions). As for the last boundary condition on the component t^{31}, equation $(4.4)_4$ can be used where a partial derivative of m^{12} appears. In this way the differential problem is set with Robin-type boundary conditions (see [Salsa, 2016]).

In the cases of spherical joints or flat joints, the third redundant force component to be added has been chosen to be t^{31}, which is linked to the transverse shear force in hoops' direction. In this case, there are Dirichlet-type boundary conditions only on the unknown force components $t^{12}, t^{22}, t^{32}, m^{12}, m^{22}$.

4.4.2 The choice of the basis functions

The necessity to specify the basis functions and to express the redundant force components in terms of them arises from the requirement that the generalised force components have to be L^2 fields. Unlike the case of beams systems, the statically indeterminacy of system (4.4) is due to an excessive number of unknown functions and not to an excess number of boundary conditions on constraints reactions (which are scalars). For this reason, a procedure that identifies the value of a function in the same way as the flexibility method for beam systems is not possible. However, one can choose to reduce the class of functions explored by referring to a linear combination of known functions, called basis functions (or coordinate functions). As is frequent in plasticity, the square integrable functions, which is a Hilbert space, is chosen as the function space for forces, that is we set

$$t^{ij} \in L^2(\Sigma, \mathbb{R}), \quad m^{\alpha\beta} \in L^2(\Sigma, \mathbb{R}). \tag{4.36}$$

A priori, it's not possible to give the expression of the redundant forces that minimise a certain cost function. Anyhow, from the theory of PDE we know that an orthonormal basis of L^2 are the trigonometric functions and thus, any element of L^2 can be expressed as a Fourier series. This guaranties the uniform convergence of the series to the function almost everywhere. For this reason, we choose the trigonometric functions as the series functions, precisely because this choice doesn't restrict much the class of functions explored. For example, if the best trend of the normal forces along the hoop directions is piecewise constant, the Fourier series is able to approximate that function with arbitrary precision, contrary for example to the case in which polynomial approximation is used. As a downside, this could come at a cost of computation time, because a high number of series functions could be needed. For this reason, in order to speed up computations, sine, cosine and constant functions are used. Let's consider the column vectors of functions

$$\underset{\sim}{\boldsymbol{f}} = \{1, \sin\alpha, \sin 2\alpha, \dots, \sin n\alpha, \cos\alpha, \cos 2\alpha, \dots, \cos n\alpha\}^{\mathsf{T}}, \tag{4.37}$$

and

$$\underset{\sim}{\boldsymbol{g}} = \left\{1, \sin\left(\pi\frac{z-z_0}{z_1-z_0}\right), \sin\left(2\pi\frac{z-z_0}{z_1-z_0}\right), \ldots, \sin\left(m\pi\frac{z-z_0}{z_1-z_0}\right), \cos\left(\pi\frac{z-z_0}{z_1-z_0}\right), \cos\left(2\pi\frac{z-z_0}{z_1-z_0}\right), \ldots, \cos\left(m\pi\frac{z-z_0}{z_1-z_0}\right)\right\}^{\mathsf{T}}. \tag{4.38}$$

Here and in the following bold italics letters with an underscore 'tilde' symbol are used to distinguish the column vectors and matrices used in the numerical computations from the vectors and tensors, used in the formalisation of the structural model, and denoted with bold normal font without underscore. The redundant force contravariant components can then be written as

$$t^{11} = \underset{\sim}{\boldsymbol{f}}^{\mathsf{T}}\underset{\sim}{\boldsymbol{U}}\underset{\sim}{\boldsymbol{g}}, \quad m^{11} = \underset{\sim}{\boldsymbol{f}}^{\mathsf{T}}\underset{\sim}{\boldsymbol{V}}\underset{\sim}{\boldsymbol{g}}, \tag{4.39}$$

where $\underset{\sim}{\boldsymbol{U}}$ and $\underset{\sim}{\boldsymbol{V}}$ are the matrices collecting the coefficients of the linear combinations of basis functions, whose constant components have to be determined. Each redundant force component is expressed as a series of $C = (1+2n)(1+2m)$ terms in which every known basis function is multiplied by an unknown coefficient. Hence, the total number of unknown coefficients to be determined is $2C$.

In the special cases of spherical joints or flat joints, the third redundant force component can be written as

$$t^{31} = \underset{\sim}{\boldsymbol{f}}^{\mathsf{T}}\underset{\sim}{\boldsymbol{W}}\underset{\sim}{\boldsymbol{g}}, \tag{4.40}$$

where $\underset{\sim}{\boldsymbol{W}}$ is a matrix collecting the coefficients of the linear combination of basis functions, whose constant components have to be determined. In this case, the total number of unknown coefficients to be determined is $3C$.

4.4.3 Solution of the equilibrium problem

The redundant force components can be considered as additional known loading terms, which then assume the form

$$\begin{aligned}
\bar{b}^1 &= b^1 + t^{11},_1 + 2\Gamma^1_{11}t^{11} + \Gamma^2_{12}t^{11},\\
\bar{b}^2 &= b^2 + \Gamma^2_{11}t^{11},\\
\bar{b}^3 &= b^3 + \varkappa_{11}t^{11},\\
\bar{c}^1 &= c^1 + m^{11},_1 + 2\Gamma^1_{11}m^{11} + \Gamma^2_{12}m^{11},\\
\bar{c}^2 &= c^2 + \Gamma^2_{11}m^{11},\\
\bar{c}^3 &= \varkappa^2_{\cdot 1}m^{11},
\end{aligned} \tag{4.41}$$

and the equilibrium system of equations is reduced to the following

$$\begin{cases} 3t^{12}\Gamma^1_{12} + t^{12}{}_{,2} + t^{12}\Gamma^2_{22} + t^{22}\Gamma^1_{22} - \varkappa^1_{.1}t^{31} - \varkappa^1_{.2}t^{32} + \bar{b}^1 = 0, \\ t^{12}{}_{,1} + t^{12}\Gamma^1_{11} + t^{22}\Gamma^1_{12} + 3t^{12}\Gamma^2_{12} + t^{22}{}_{,2} + 2t^{22}\Gamma^2_{22} - \varkappa^2_{.1}t^{31} - \varkappa^2_{.2}t^{32} + \bar{b}^2 = 0, \\ 2\varkappa_{12}t^{12} + \varkappa_{22}t^{22} + t^{31}{}_{,1} + t^{31}\Gamma^1_{11} + t^{32}\Gamma^1_{12} + t^{32}{}_{,2} + t^{31}\Gamma^2_{12} + t^{32}\Gamma^2_{22} + \bar{b}^3 = 0, \\ 3m^{12}\Gamma^1_{12} + m^{12}{}_{,2} + m^{12}\Gamma^2_{22} + m^{22}\Gamma^1_{22} - t^{31} + \bar{c}^1 = 0, \\ m^{12}{}_{,1} + m^{12}\Gamma^1_{11} + m^{22}\Gamma^1_{12} + 3m^{12}\Gamma^2_{12} + m^{22}{}_{,2} + 2m^{22}\Gamma^2_{22} - t^{32} + \bar{c}^2 = 0, \\ m^{12}(\varkappa^2_{.2} - \varkappa^1_{.1}) - \varkappa^1_{.2}m^{22} + \bar{c}^3 = 0. \end{cases} \tag{4.42}$$

Given the linearity of the problem, the solution of the system of equations (4.42), $\mathfrak{F}_E$, can be expressed as the linear combination of the solutions of $2C+3$ auxiliary subsystems:

$$\mathfrak{F}_E = \mathfrak{F}_z + \lambda_x\mathfrak{F}_x + \lambda_y\mathfrak{F}_y + \sum_{i,j} \underset{\sim}{U}_{ij}\mathfrak{F}^t_{ij} + \sum_{k,l} \underset{\sim}{V}_{kl}\mathfrak{F}^m_{kl}. \tag{4.43}$$

In equation (4.43) $\mathfrak{F}_z$ denotes the solution of the equilibrium problem in which only the external vertical loads at the internal and on the boundary are present. $\mathfrak{F}_x$ and $\mathfrak{F}_y$ denote the solutions of the equilibrium problem in which only horizontal loads equal to the self-weight of the dome and applied respectively in the x_1 and x_2 directions are present and the boundary conditions are homogeneous.

$\mathfrak{F}^t_{ij}$ and $\mathfrak{F}^m_{kl}$, with $i,k = 1,\dots,2n+1$ and $j,l = 1,\dots,2m+1$, denote the solutions of the equilibrium problems in which the coefficient $_{ij}$ and $_{kl}$ in the series term of the redundant force components t^{11} and m^{11}, respectively, is set equal to unity while all the others are set to zero, and the external loads and boundary conditions are homogeneous. In this way, the second step of the method consists of solving $3+2C$ equilibrium systems of equations, different one from each other only for the loading term. Once the solutions of all the subsystems have been obtained, all the generalised force components in the effective system can be expressed as a linear combination of the solutions of the subsystems. For instance, the meridian normal force can be formally written as

$$(t^{22})_E = (t^{22})_z + \lambda_x(t^{22})_x + \lambda_y(t^{22})_y + \sum_{i,j} \underset{\sim}{U}_{ij}(t^{22})^t_{ij} + \sum_{k,l} \underset{\sim}{V}_{kl}(t^{22})^m_{kl}. \tag{4.44}$$

To apply the preceding strategy, one needs to solve $3+2C$ statically determinate equilibrium problems, for which a numerical method is required. In the following, two different solution strategies are set up: the finite difference method and the collocation method.

The case of spherical joints. In this special case, remembering that $\varkappa^1_{.2} = \varkappa^2_{.1} = 0$ and $\varkappa^1_{.1} = \varkappa^2_{.2}$ the additional loading terms assume the form

$$\begin{aligned}
\bar{b}^1 &= b^1 + t^{11},_1 + 2\Gamma^1_{11}t^{11} + \Gamma^2_{12}t^{11} - \varkappa^1_{.1}t^{31},\\
\bar{b}^2 &= b^2 + \Gamma^2_{11}t^{11},\\
\bar{b}^3 &= b^3 + \varkappa_{11}t^{11} + t^{31},_1 + \Gamma^1_{11}t^{31} + \Gamma^2_{12}t^{31}\\
\bar{c}^1 &= c^1 + m^{11},_1 + 2\Gamma^1_{11}m^{11} + \Gamma^2_{12}m^{11} - t^{31},\\
\bar{c}^2 &= c^2 + \Gamma^2_{11}m^{11},
\end{aligned} \tag{4.45}$$

and the equilibrium equations can be written as

$$\begin{cases}
3t^{12}\Gamma^1_{12} + t^{12},_2 + t^{12}\Gamma^2_{22} + t^{22}\Gamma^1_{22} + \bar{b}^1 = 0,\\
t^{12},_1 + t^{12}\Gamma^1_{11} + t^{22}\Gamma^1_{12} + 3t^{12}\Gamma^2_{12} + t^{22},_2 + 2t^{22}\Gamma^2_{22} - \varkappa^2_{.2}t^{32} + \bar{b}^2 = 0,\\
\varkappa_{22}t^{22} + t^{32}\Gamma^1_{12} + t^{32},_2 + t^{32}\Gamma^2_{22} + \bar{b}^3 = 0,\\
3m^{12}\Gamma^1_{12} + m^{12},_2 + m^{12}\Gamma^2_{22} + m^{22}\Gamma^1_{22} + \bar{c}^1 = 0,\\
m^{12},_1 + m^{12}\Gamma^1_{11} + m^{22}\Gamma^1_{12} + 3m^{12}\Gamma^2_{12} + m^{22},_2 + 2m^{22}\Gamma^2_{22} - t^{32} + \bar{c}^2 = 0.
\end{cases} \tag{4.46}$$

The auxiliary subsystems are $3C + 3$ and the effective solution can be expressed as

$$\mathfrak{F}_E = \mathfrak{F}_z + \lambda_x\mathfrak{F}_x + \lambda_y\mathfrak{F}_y + \sum_{i,j} \underset{\sim}{U}_{ij}\mathfrak{F}^t_{ij} + \sum_{k,l} \underset{\sim}{V}_{kl}\mathfrak{F}^m_{kl} + \sum_{r,s} \underset{\sim}{W}_{rs}\mathfrak{F}^q_{rs}, \tag{4.47}$$

where $\mathfrak{F}^q_{rs}$ with $r = 1, \ldots, 2n+1$ and $s = 1, \ldots, 2m+1$, denotes the solution of the equilibrium problem in which the coefficient $_{rs}$ in the series term of the redundant force component t^{31} is set equal to unity while all the others are set to zero, and the external loads and boundary conditions are homogeneous.

The case of flat joints. If the joints' curvatures are all equal to zero, the additional loading terms simplifies as

$$\begin{aligned}
\bar{b}^1 &= b^1 + t^{11},_1 + 2\Gamma^1_{11}t^{11} + \Gamma^2_{12}t^{11},\\
\bar{b}^2 &= b^2 + \Gamma^2_{11}t^{11},\\
\bar{b}^3 &= b^3 + t^{31},_1 + \Gamma^1_{11}t^{31} + \Gamma^2_{12}t^{31}\\
\bar{c}^1 &= c^1 + m^{11},_1 + 2\Gamma^1_{11}m^{11} + \Gamma^2_{12}m^{11} - t^{31},\\
\bar{c}^2 &= c^2 + \Gamma^2_{11}m^{11},
\end{aligned} \tag{4.48}$$

and the equilibrium equations can be written as

$$\begin{cases} 3t^{12}\Gamma^1_{12} + t^{12},_2 + t^{12}\Gamma^2_{22} + t^{22}\Gamma^1_{22} + \bar{b}^1 = 0, \\ t^{12},_1 + t^{12}\Gamma^1_{11} + t^{22}\Gamma^1_{12} + 3t^{12}\Gamma^2_{12} + t^{22},_2 + 2t^{22}\Gamma^2_{22} + \bar{b}^2 = 0, \\ t^{32}\Gamma^1_{12} + t^{32},_2 + t^{32}\Gamma^2_{22} + \bar{b}^3 = 0, \\ 3m^{12}\Gamma^1_{12} + m^{12},_2 + m^{12}\Gamma^2_{22} + m^{22}\Gamma^1_{22} + \bar{c}^1 = 0, \\ m^{12},_1 + m^{12}\Gamma^1_{11} + m^{22}\Gamma^1_{12} + 3m^{12}\Gamma^2_{12} + m^{22},_2 + 2m^{22}\Gamma^2_{22} - t^{32} + \bar{c}^2 = 0, \end{cases} \tag{4.49}$$

while the effective solution can still be expressed with equation (4.47).

Special geometries. So far, some special cases concerning joints' orientation have been analysed. However, it is noted that the equilibrium equations do depend on the orientation of the joints, but also on the geometry of the middle surface. This means that other simplifications of the problem are possible in some particular cases, in which the shape of the middle surface takes on particular characteristics. However, in this chapter, no other particular cases, besides those already treated, are analysed.

The case of a reinforcing ring. If a strengthening ring is present near the oculus, an horizontal force component and a bending moment can be provided at the boundary $z = z_1$, assuming that the ring is strong enough to sustain circumferential compressions of any magnitude. In this case, two additional redundant unknowns are present. This components are functions of α in general and could be written as a linear combination of basis functions just as the other redundant components. In this work and in the following applications, these components are assumed constant, H_0 and M_0 respectively, so that the effective solution can be written as

$$\mathfrak{F}_E = \mathfrak{F}_z + H_0\mathfrak{F}_H + M_0\mathfrak{F}_M + \lambda_x\mathfrak{F}_x + \lambda_y\mathfrak{F}_y + \sum_{i,j} \underset{\sim}{U}_{ij}\mathfrak{F}^t_{ij} + \sum_{k,l} \underset{\sim}{V}_{kl}\mathfrak{F}^m_{kl}, \tag{4.50}$$

where $\mathfrak{F}_H$ and $\mathfrak{F}_M$ denote the solutions obtained by setting the external loads to zero and the horizontal force boundary condition or the moment boundary condition equal to unity, respectively. If the joints are spherically arranged, the sum $\sum_{r,s} \underset{\sim}{W}_{rs}\mathfrak{F}^q_{rs}$ has to be added.

Solution of the statically determinate equilibrium sub-problems: numerical solution via finite difference method

Having adopted the cylindrical parameters, for domes with the upper oculus, the coordinate domain is rectangular, and can be discretised by finite difference as shown in Figure 4.3. The rectangular domain is divided in $n_\alpha \times n_z$ points. We do not impose directly the periodicity conditions on $i = n_\alpha$ but we write unknown and equations on $n_\alpha - 1$ points and we impose periodicity conditions when writing the partial derivative with respect to α. Let $N =$

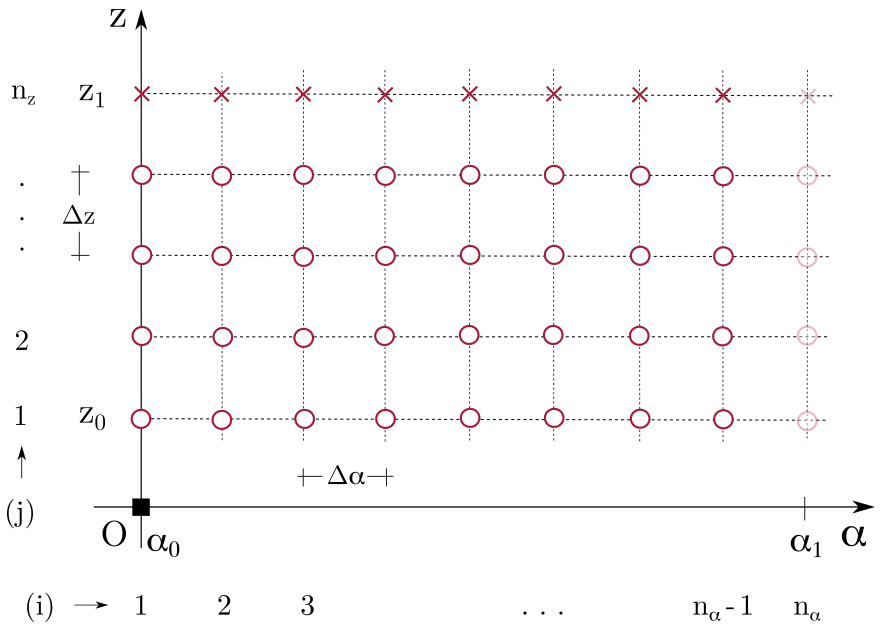

Figure 4.3: The finite difference grid.

$(n_\alpha - 1)n_z$ denote the number of grid nodes. The unknowns are written in a vector $\underset{\sim}{\boldsymbol{u}} \in \mathbb{R}^{6N\times 1}$ with the following ordering

$$\underset{\sim}{\boldsymbol{u}} = \{\underset{\sim}{\boldsymbol{t}}^{12}, \underset{\sim}{\boldsymbol{t}}^{22}, \underset{\sim}{\boldsymbol{t}}^{31}, \underset{\sim}{\boldsymbol{t}}^{32}, \underset{\sim}{\boldsymbol{m}}^{12}, \underset{\sim}{\boldsymbol{m}}^{22}\}^{\mathsf{T}}, \tag{4.51}$$

where, for example, $\underset{\sim}{\boldsymbol{t}}^{12} \in \mathbb{R}^{N\times N}$ is the collection of all the values of t^{12} computed on the grid points and ordered as follows

$$\underset{\sim}{\boldsymbol{t}}^{12} = \{t^{12}_{1,1}, t^{12}_{1,2}, \ldots, t^{12}_{1,n_z}, t^{12}_{2,1}, t^{12}_{2,2}, \ldots, t^{12}_{2,n_z}, \ldots, t^{12}_{(n_\alpha-1),n_z}\}^{\mathsf{T}}. \tag{4.52}$$

The $6N$ linear equilibrium equations can be written in matrix form as

$$\underset{\sim}{\boldsymbol{A}}\underset{\sim}{\boldsymbol{u}} = \underset{\sim}{\boldsymbol{d}}, \tag{4.53}$$

where $\underset{\sim}{\boldsymbol{A}} \in \mathbb{R}^{6N\times 6N}$, $\underset{\sim}{\boldsymbol{u}} \in \mathbb{R}^{6N\times 1}$ and $\underset{\sim}{\boldsymbol{d}} \in \mathbb{R}^{6N\times 1}$. The matrix $\underset{\sim}{\boldsymbol{A}}$ can be decomposed as the sum of three matrices, two of them associated to the finite difference and one to the coefficients, as follows:

$$\underset{\sim}{\boldsymbol{A}} = \underset{\sim}{\boldsymbol{B}}_\alpha + \underset{\sim}{\boldsymbol{C}}_z + \underset{\sim}{\boldsymbol{D}}. \tag{4.54}$$

The partial derivatives are approximated by forward/backward finite difference as follows

$$\partial_\alpha = \begin{cases} \dfrac{f_{i+1,j} - f_{i,j}}{\Delta\alpha} & \text{if} \quad i \neq n_\alpha - 1 \\ \dfrac{f_{1,j} - f_{i,j}}{\Delta\alpha} & \text{if} \quad i = n_\alpha - 1, \end{cases} \qquad \partial_z = \begin{cases} \dfrac{f_{i,j+1} - f_{i,j}}{\Delta z} & \text{if} \quad j \neq n_z \\ \dfrac{f_{i,j} - f_{i,j-1}}{\Delta z} & \text{if} \quad j = n_z. \end{cases} \tag{4.55}$$

To find expressions of matrices $\underset{\sim}{\boldsymbol{B}}_\alpha$ and $\underset{\sim}{\boldsymbol{C}}_z$ we consider for example the vector $\underset{\sim}{\boldsymbol{t}}^{12}$. It's easy to verify that, in this case, the finite difference matrices $\underset{\sim}{\boldsymbol{T}}_\alpha \in \mathbb{R}^{N\times N}$ and $\underset{\sim}{\boldsymbol{T}}_z \in \mathbb{R}^{N\times N}$ are

$$\underset{\sim}{\boldsymbol{T}}_\alpha = \frac{1}{\Delta\alpha}\begin{bmatrix} -\underset{\sim}{\mathbf{1}} & \underset{\sim}{\mathbf{1}} & \underset{\sim}{\mathbf{0}} & \dots & \underset{\sim}{\mathbf{0}} & \underset{\sim}{\mathbf{0}} \\ \underset{\sim}{\mathbf{0}} & -\underset{\sim}{\mathbf{1}} & \underset{\sim}{\mathbf{1}} & \dots & \underset{\sim}{\mathbf{0}} & \underset{\sim}{\mathbf{0}} \\ \vdots & & & \ddots & & \vdots \\ \underset{\sim}{\mathbf{0}} & \dots & & & -\underset{\sim}{\mathbf{1}} & \underset{\sim}{\mathbf{1}} \\ \underset{\sim}{\mathbf{1}} & \underset{\sim}{\mathbf{0}} & \dots & & \underset{\sim}{\mathbf{0}} & -\underset{\sim}{\mathbf{1}} \end{bmatrix}, \quad \underset{\sim}{\boldsymbol{T}}_z = \frac{1}{\Delta z}\begin{bmatrix} \underset{\sim}{\boldsymbol{T}}_z^0 & \underset{\sim}{\mathbf{0}} & \underset{\sim}{\mathbf{0}} & \dots & \underset{\sim}{\mathbf{0}} & \underset{\sim}{\mathbf{0}} \\ \underset{\sim}{\mathbf{0}} & \underset{\sim}{\boldsymbol{T}}_z^0 & \underset{\sim}{\mathbf{0}} & \dots & \underset{\sim}{\mathbf{0}} & \underset{\sim}{\mathbf{0}} \\ \vdots & & \ddots & & & \vdots \\ \underset{\sim}{\mathbf{0}} & \dots & & & \underset{\sim}{\boldsymbol{T}}_z^0 & \underset{\sim}{\mathbf{0}} \\ \underset{\sim}{\mathbf{0}} & \dots & & & \underset{\sim}{\mathbf{0}} & \underset{\sim}{\boldsymbol{T}}_z^0 \end{bmatrix} \tag{4.56}$$

where the sub-matrix $\underset{\sim}{\boldsymbol{T}}_z^0 \in \mathbb{R}^{n_z\times n_z}$

$$\underset{\sim}{\boldsymbol{T}}_z^0 = \begin{bmatrix} -1 & 1 & 0 & 0 & \dots & 0 \\ 0 & -1 & 1 & 0 & \dots & 0 \\ \vdots & & \ddots & \ddots & & \vdots \\ 0 & \dots & & 0 & -1 & 1 \\ 0 & \dots & & 0 & -1 & 1 \end{bmatrix} \tag{4.57}$$

is such that

$$\partial_z \underset{\sim}{\boldsymbol{t}}_{1,j}^{12} = \underset{\sim}{\boldsymbol{T}}_z^0 \underset{\sim}{\boldsymbol{t}}_{1,j}^{12}, \tag{4.58}$$

being $\underset{\sim}{\mathbf{0}} \in \mathbb{R}^{n_z\times n_z}$ the zero matrix and $\underset{\sim}{\mathbf{1}} \in \mathbb{R}^{n_z\times n_z}$ the identity matrix. Matrices $\underset{\sim}{\boldsymbol{B}}_\alpha \in \mathbb{R}^{6N\times 6N}$ and $\underset{\sim}{\boldsymbol{C}} \in \mathbb{R}^{6N\times 6N}$ are block matrices that can be assembled by putting $\underset{\sim}{\boldsymbol{T}}_\alpha$ and $\underset{\sim}{\boldsymbol{T}}_z$ in the (k,l) place such that the derivative with respect to α or z respectively of the unknown of index l appears in equation k and by putting $\underset{\sim}{\boldsymbol{O}}$ otherwise, where $\underset{\sim}{\boldsymbol{O}} \in \mathbb{R}^{N\times N}$ is the zero matrix. In particular,

$$\underset{\sim}{\boldsymbol{B}}_\alpha = \begin{bmatrix} \underset{\sim}{\boldsymbol{O}} & \underset{\sim}{\boldsymbol{O}} & \underset{\sim}{\boldsymbol{O}} & \underset{\sim}{\boldsymbol{O}} & \underset{\sim}{\boldsymbol{O}} & \underset{\sim}{\boldsymbol{O}} \\ \underset{\sim}{\boldsymbol{T}}_\alpha & \underset{\sim}{\boldsymbol{O}} & \underset{\sim}{\boldsymbol{O}} & \underset{\sim}{\boldsymbol{O}} & \underset{\sim}{\boldsymbol{O}} & \underset{\sim}{\boldsymbol{O}} \\ \underset{\sim}{\boldsymbol{O}} & \underset{\sim}{\boldsymbol{O}} & \underset{\sim}{\boldsymbol{T}}_\alpha & \underset{\sim}{\boldsymbol{O}} & \underset{\sim}{\boldsymbol{O}} & \underset{\sim}{\boldsymbol{O}} \\ \underset{\sim}{\boldsymbol{O}} & \underset{\sim}{\boldsymbol{O}} & \underset{\sim}{\boldsymbol{O}} & \underset{\sim}{\boldsymbol{O}} & \underset{\sim}{\boldsymbol{O}} & \underset{\sim}{\boldsymbol{O}} \\ \underset{\sim}{\boldsymbol{O}} & \underset{\sim}{\boldsymbol{O}} & \underset{\sim}{\boldsymbol{O}} & \underset{\sim}{\boldsymbol{O}} & \underset{\sim}{\boldsymbol{T}}_\alpha & \underset{\sim}{\boldsymbol{O}} \\ \underset{\sim}{\boldsymbol{O}} & \underset{\sim}{\boldsymbol{O}} & \underset{\sim}{\boldsymbol{O}} & \underset{\sim}{\boldsymbol{O}} & \underset{\sim}{\boldsymbol{O}} & \underset{\sim}{\boldsymbol{O}} \end{bmatrix}, \quad \underset{\sim}{\boldsymbol{C}}_z = \begin{bmatrix} \underset{\sim}{\boldsymbol{T}}_z & \underset{\sim}{\boldsymbol{O}} & \underset{\sim}{\boldsymbol{O}} & \underset{\sim}{\boldsymbol{O}} & \underset{\sim}{\boldsymbol{O}} & \underset{\sim}{\boldsymbol{O}} \\ \underset{\sim}{\boldsymbol{O}} & \underset{\sim}{\boldsymbol{T}}_z & \underset{\sim}{\boldsymbol{O}} & \underset{\sim}{\boldsymbol{O}} & \underset{\sim}{\boldsymbol{O}} & \underset{\sim}{\boldsymbol{O}} \\ \underset{\sim}{\boldsymbol{O}} & \underset{\sim}{\boldsymbol{O}} & \underset{\sim}{\boldsymbol{O}} & \underset{\sim}{\boldsymbol{T}}_z & \underset{\sim}{\boldsymbol{O}} & \underset{\sim}{\boldsymbol{O}} \\ \underset{\sim}{\boldsymbol{O}} & \underset{\sim}{\boldsymbol{O}} & \underset{\sim}{\boldsymbol{O}} & \underset{\sim}{\boldsymbol{O}} & \underset{\sim}{\boldsymbol{T}}_z & \underset{\sim}{\boldsymbol{O}} \\ \underset{\sim}{\boldsymbol{O}} & \underset{\sim}{\boldsymbol{O}} & \underset{\sim}{\boldsymbol{O}} & \underset{\sim}{\boldsymbol{O}} & \underset{\sim}{\boldsymbol{O}} & \underset{\sim}{\boldsymbol{T}}_z \\ \underset{\sim}{\boldsymbol{O}} & \underset{\sim}{\boldsymbol{O}} & \underset{\sim}{\boldsymbol{O}} & \underset{\sim}{\boldsymbol{O}} & \underset{\sim}{\boldsymbol{O}} & \underset{\sim}{\boldsymbol{O}} \end{bmatrix}. \tag{4.59}$$

The $\underset{\sim}{\boldsymbol{D}}$ matrix collects all coefficients and can be expressed in the following way

$$\underset{\sim}{\boldsymbol{D}} = \begin{bmatrix} \underset{\sim}{\boldsymbol{D}}_1 & \underset{\sim}{\boldsymbol{D}}_2 & \underset{\sim}{\boldsymbol{D}}_3 & \underset{\sim}{\boldsymbol{D}}_4 & \underset{\sim}{\boldsymbol{O}} & \underset{\sim}{\boldsymbol{O}} \\ \underset{\sim}{\boldsymbol{D}}_7 & \underset{\sim}{\boldsymbol{D}}_8 & \underset{\sim}{\boldsymbol{D}}_5 & \underset{\sim}{\boldsymbol{D}}_6 & \underset{\sim}{\boldsymbol{O}} & \underset{\sim}{\boldsymbol{O}} \\ \underset{\sim}{\boldsymbol{D}}_9 & \underset{\sim}{\boldsymbol{D}}_{10} & \underset{\sim}{\boldsymbol{D}}_{11} & \underset{\sim}{\boldsymbol{D}}_{12} & \underset{\sim}{\boldsymbol{O}} & \underset{\sim}{\boldsymbol{O}} \\ \underset{\sim}{\boldsymbol{O}} & \underset{\sim}{\boldsymbol{O}} & -\underset{\sim}{\boldsymbol{I}} & \underset{\sim}{\boldsymbol{O}} & \underset{\sim}{\boldsymbol{D}}_1 & \underset{\sim}{\boldsymbol{D}}_2 \\ \underset{\sim}{\boldsymbol{O}} & \underset{\sim}{\boldsymbol{O}} & \underset{\sim}{\boldsymbol{O}} & -\underset{\sim}{\boldsymbol{I}} & \underset{\sim}{\boldsymbol{D}}_7 & \underset{\sim}{\boldsymbol{D}}_8 \\ \underset{\sim}{\boldsymbol{O}} & \underset{\sim}{\boldsymbol{O}} & \underset{\sim}{\boldsymbol{O}} & \underset{\sim}{\boldsymbol{O}} & \underset{\sim}{\boldsymbol{D}}_6 + \underset{\sim}{\boldsymbol{D}}_3 & \underset{\sim}{\boldsymbol{D}}_4 \end{bmatrix} \tag{4.60}$$

where $\underset{\sim}{\boldsymbol{I}} \in \mathbb{R}^{N\times N}$ is the identity matrix and the diagonal $\underset{\sim}{\boldsymbol{D}}_i \in \mathbb{R}^{N\times N}$ matrices all have the form

$$\underset{\sim}{\boldsymbol{D}}_i = \mathrm{diag}\big(\{f^i_{1,1}, f^i_{1,2}, \ldots, f^i_{1,n_z}, f^i_{2,1}, \ldots, f^i_{2,n_z}, \ldots, f^i_{(n_\alpha-1),n_z}\}^{\mathsf{T}}\big) \tag{4.61}$$

being the functions f^i the following

$$\begin{aligned}
&f^1 = 3\Gamma^1_{12} + \Gamma^2_{22}, \quad f^2 = \Gamma^1_{22}, \quad f^3 = -\varkappa^1_{.1}, \quad f^4 = -\varkappa^1_{.2},\\
&f^5 = -\varkappa^2_{.1}, \quad f^6 = -\varkappa^2_{.2}, \quad f^7 = \Gamma^1_{11} + 3\Gamma^2_{12}, \quad f^8 = \Gamma^1_{12} + 2\Gamma^2_{22},\\
&f^9 = 2\varkappa_{12}, \quad f^{10} = \varkappa_{22}, \quad f^{11} = \Gamma^1_{11} + \Gamma^2_{12}, \quad f^{12} = \Gamma^1_{12} + \Gamma^2_{22}.
\end{aligned} \tag{4.62}$$

Finally, the vector of the external known forces writes as

$$\underset{\sim}{\boldsymbol{d}} = \{-\underset{\sim}{\boldsymbol{b}}^1, -\underset{\sim}{\boldsymbol{b}}^2, -\underset{\sim}{\boldsymbol{b}}^3, -\underset{\sim}{\boldsymbol{c}}^1, -\underset{\sim}{\boldsymbol{c}}^2, -\underset{\sim}{\boldsymbol{c}}^3\}^{\mathsf{T}}, \tag{4.63}$$

where $\underset{\sim}{\boldsymbol{b}}^i \in \mathbb{R}^{N\times 1}$ are vectors ordered as the others following the scheme below

$$\underset{\sim}{\boldsymbol{b}}^1 = \{b^1_{1,1}, b^1_{1,2}, \ldots, b^1_{1,n_z}, b^1_{2,1}, \ldots, b^1_{(n_\alpha-1),n_z}\}^{\mathsf{T}}. \tag{4.64}$$

Once all matrices are assembled we need to insert the boundary conditions by suitably modifying some elements of $\underset{\sim}{\boldsymbol{A}}$ and $\underset{\sim}{\boldsymbol{d}}$. In our case, all boundary conditions are imposed on the (i, n_z) points. Hence, we need to replace equilibrium equations written in the points (i, n_z) with equations like

$$\begin{aligned}
t^{12}_{i,n_z} &= \widehat{t}^{12}_{i,n_z}, \quad i \in [1, n_\alpha - 1],\\
t^{22}_{i,n_z} &= \widehat{t}^{22}_{i,n_z}, \quad i \in [1, n_\alpha - 1],\\
t^{31}_{i,n_z} &= \widehat{t}^{31}_{i,n_z}, \quad i \in [1, n_\alpha - 1],\\
t^{32}_{i,n_z} &= \widehat{t}^{32}_{i,n_z}, \quad i \in [1, n_\alpha - 1],\\
m^{12}_{i,n_z} &= \widehat{m}^{12}_{i,n_z}, \quad i \in [1, n_\alpha - 1],\\
m^{22}_{i,n_z} &= \widehat{m}^{22}_{i,n_z}, \quad i \in [1, n_\alpha - 1],
\end{aligned} \tag{4.65}$$

where the quantities denoted by $\widehat{\square}$ are known quantities. To do this, we replace the $k-1)N+in_z$ rows for $k \in [1, 6]$ and $i \in [1, n_\alpha - 1]$ with rows having 1 in the place corresponding to unknown u_{1,n_z} and zero elsewhere. In this way we identify a sub-matrix $\underset{\sim}{\boldsymbol{A}}_{bc} \in \mathbb{R}^{6(n_\alpha-1)\times 6N}$ that is assembled by 6×6 blocks $\underset{\sim}{\boldsymbol{A}}^0_{bc} \in \mathbb{R}^{(n_\alpha-1)\times N}$

$$\underset{\sim}{\boldsymbol{A}}_{bc} = \begin{bmatrix}
\underset{\sim}{\boldsymbol{A}}^0_{bc} & \underset{\sim}{\boldsymbol{0}} & \underset{\sim}{\boldsymbol{0}} & \underset{\sim}{\boldsymbol{0}} & \underset{\sim}{\boldsymbol{0}} & \underset{\sim}{\boldsymbol{0}}\\
\underset{\sim}{\boldsymbol{0}} & \underset{\sim}{\boldsymbol{A}}^0_{bc} & \underset{\sim}{\boldsymbol{0}} & \underset{\sim}{\boldsymbol{0}} & \underset{\sim}{\boldsymbol{0}} & \underset{\sim}{\boldsymbol{0}}\\
\underset{\sim}{\boldsymbol{0}} & \underset{\sim}{\boldsymbol{0}} & \underset{\sim}{\boldsymbol{A}}^0_{bc} & \underset{\sim}{\boldsymbol{0}} & \underset{\sim}{\boldsymbol{0}} & \underset{\sim}{\boldsymbol{0}}\\
\underset{\sim}{\boldsymbol{0}} & \underset{\sim}{\boldsymbol{0}} & \underset{\sim}{\boldsymbol{0}} & \underset{\sim}{\boldsymbol{A}}^0_{bc} & \underset{\sim}{\boldsymbol{0}} & \underset{\sim}{\boldsymbol{0}}\\
\underset{\sim}{\boldsymbol{0}} & \underset{\sim}{\boldsymbol{0}} & \underset{\sim}{\boldsymbol{0}} & \underset{\sim}{\boldsymbol{0}} & \underset{\sim}{\boldsymbol{A}}^0_{bc} & \underset{\sim}{\boldsymbol{0}}\\
\underset{\sim}{\boldsymbol{0}} & \underset{\sim}{\boldsymbol{0}} & \underset{\sim}{\boldsymbol{0}} & \underset{\sim}{\boldsymbol{0}} & \underset{\sim}{\boldsymbol{0}} & \underset{\sim}{\boldsymbol{A}}^0_{bc}
\end{bmatrix} \tag{4.66}$$

where

$$\underset{\sim}{\boldsymbol{A}}^0_{bc} = \begin{bmatrix} 0 & \dots & \overset{(n_z)}{1} & 0 & \dots & 0 & \dots & 0 \\ 0 & \dots & 0 & \dots & \overset{(2n_z)}{1} & 0 & \dots & 0 \\ \vdots & & & \ddots & \ddots & & & \vdots \\ 0 & \dots & 0 & \dots & 0 & \dots & 0 & \overset{((n_\alpha-1)n_z)}{1} \end{bmatrix}. \tag{4.67}$$

Finally, we need to replace also the $(k-1)N + in_z$ rows for $k \in [1,6]$ and $i \in [1, n_\alpha - 1]$ of the vector $\underset{\sim}{\boldsymbol{d}}$ with the value of the correct boundary conditions. In the simple yet interesting case in which the free edge, where boundary conditions are imposed, is identified by $z = z_1$, and adopting the same system of coordinates, the boundary curve $\Gamma : \mathbf{x}(\alpha, z_1)$ is a plane curve. The tangent, binormal and normal unit vectors are, respectively,

$$\boldsymbol{\tau}(\alpha) = \frac{\mathbf{x}'(\alpha, z_1)}{\|\mathbf{x}'(\alpha, z_1)\|}, \quad \boldsymbol{\beta}(\alpha) = \mathbf{k}, \quad \boldsymbol{\nu}(\alpha) = \boldsymbol{\beta}(\alpha) \times \boldsymbol{\tau}(\alpha), \tag{4.68}$$

with $\nu_3 = 0$ and $\tau_3 = 0$ because Γ is plane. The force vector on the surface element having unit normal vector $\boldsymbol{\nu}$ can be expressed by Cauchy theorem as

$$\mathbf{t}^\nu = \mathbf{T}\boldsymbol{\nu} = \left[t^{\alpha\beta}\mathbf{a}_\alpha \otimes \mathbf{a}_\beta + t^{3\alpha}\mathbf{a}_3 \otimes \mathbf{a}_\alpha \right] \cdot \nu_\gamma \mathbf{a}^\gamma = t^{\alpha\gamma}\nu_\gamma \mathbf{a}_\alpha + t^{3\gamma}\nu_\gamma \mathbf{a}_3. \tag{4.69}$$

It's worth observing that, for surfaces parametrised by the particular coordinate system adopted, $\boldsymbol{\nu}$ is always normal to $\mathbf{a}_1$ as the first is orthogonal to Γ by definition while the second is tangent to the curve. Thus, $\nu_1 = \boldsymbol{\nu} \cdot \mathbf{a}_1 = 0$. On the other hand, $\boldsymbol{\nu}$ could be not parallel to $\mathbf{a}_2$, because $\mathbf{a}_1$ and $\mathbf{a}_2$ are not orthogonal (or, in other words, $\mathbf{a}_2$ could not be orthogonal to Γ). The boundary conditions impose that $\mathbf{t}^\nu = \mathbf{t}_\partial$, namely

$$\begin{aligned} t^{12} &= \frac{t^1_\partial}{\nu_2}, \quad \text{with} \quad t^1_\partial = \mathbf{t}_\partial \cdot \mathbf{a}^1,\ \nu_2 = \boldsymbol{\nu} \cdot \mathbf{a}_2, \\ t^{22} &= \frac{t^2_\partial}{\nu_2}, \quad \text{with} \quad t^2_\partial = \mathbf{t}_\partial \cdot \mathbf{a}^2,\ \nu_2 = \boldsymbol{\nu} \cdot \mathbf{a}_2, \\ t^{32} &= \frac{t^3_\partial}{\nu_2}, \quad \text{with} \quad t^3_\partial = \mathbf{t}_\partial \cdot \mathbf{a}^3,\ \nu_2 = \boldsymbol{\nu} \cdot \mathbf{a}_2. \end{aligned} \tag{4.70}$$

In the case in which the boundary couples are due to an eccentricity in the external load $\mathbf{t}_\partial$ with respect to the middle surface, the remaining boundary conditions are written as

$$\begin{aligned} m^{12} &= e_\partial \frac{t^1_\partial}{\nu_2}, \quad \text{with} \quad t^1_\partial = \mathbf{t}_\partial \cdot \mathbf{a}^1,\ \nu_2 = \boldsymbol{\nu} \cdot \mathbf{a}_2, \\ m^{22} &= e_\partial \frac{t^2_\partial}{\nu_2}, \quad \text{with} \quad t^2_\partial = \mathbf{t}_\partial \cdot \mathbf{a}^2,\ \nu_2 = \boldsymbol{\nu} \cdot \mathbf{a}_2. \end{aligned} \tag{4.71}$$

Convergence of the numerical scheme. The convergence of the finite difference scheme is investigated on the $\mathfrak{F}_z$ equilibrium system for the case of the dome of Pisa cathedral. The rate of convergence depends on the ratio chosen for the discretisation grid (i.e. $r = n_z/n_\alpha$),

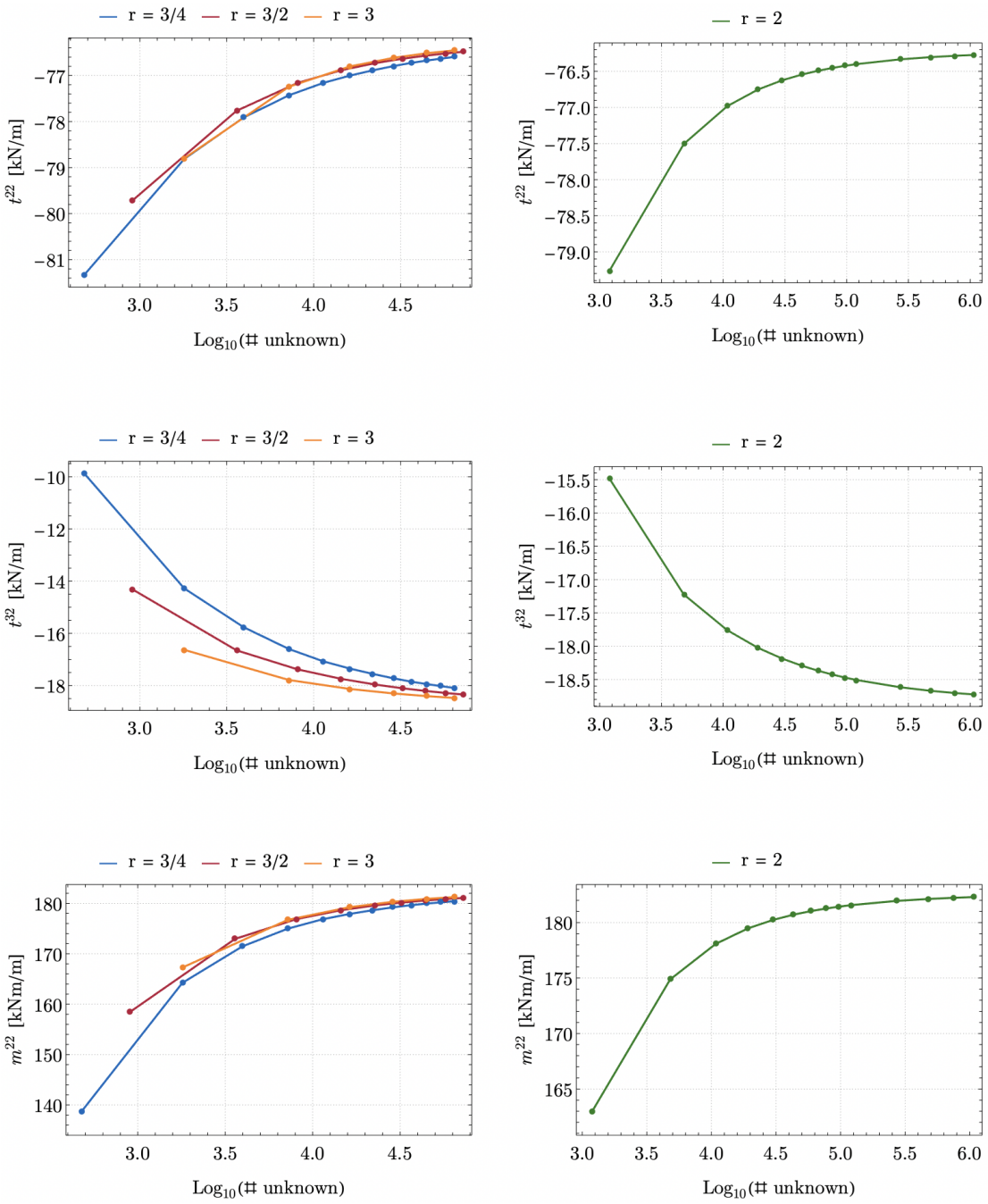

Figure 4.4: Convergence of the finite difference scheme with varying r.

as shown in Figure 4.4 (left column). It is observed how higher values of r correspond to higher convergence rates. In order to achieve a good spacing between the grid points, a value $r = 2$ is chosen in order to perform further convergence analyses with more unknowns. Figure 4.4 (right column) shows the convergence rate achieved by the numerical method. In the following, the results obtained with the finite difference scheme are compared with those obtained by other numerical techniques.

Solution of the statically determinate equilibrium sub-problems: numerical solution via collocation method

The finite difference method is a standard and simple numerical scheme that can be used effectively to solve systems of differential equations. Other frequently used options are the finite element method and the finite volume method. However, since our aim is to define a proper generalised force field, that is a set of analytical functions that can be evaluated everywhere in the domain, we chose to adopt a collocation method (see for example [Quarteroni and Quarteroni, 2009]) to numerically solve the equilibrium problem in its strong formulation. Differently from the other techniques, the collocation method has the advantage of giving the solution in terms of smooth functions with global support. This allows us to evaluate the error, as well as checking the fulfilment of the admissibility conditions on the material everywhere in the domain and not just in a finite subset of points. In this regard, it is worth pointing out that, although it is possible to verify that the equilibrium and material admissibility conditions are met at any point within the domain, it is generally not operationally possible to prove that they are met everywhere. However, admissibility checks can be conducted at a sufficiently large number of points such that the physical distance between two points is less than the smaller dimension of the resisting elements. In this way, it is possible to employ a sparse mesh grid for solving the problem and a dense mesh grid for admissibility checks. This is the procedure followed in applications. Based on the above considerations, in the following, it will be implicitly understood that the expression 'everywhere in the domain' means 'in a sufficiently large number of points'.

The collocation method consists in writing the generic unknown function, u, as a linear combination of known basis functions

$$u = \underset{\sim}{\boldsymbol{f}}^{\mathsf{T}} \underset{\sim}{\boldsymbol{Z}}^{u} \underset{\sim}{\boldsymbol{g}} \tag{4.72}$$

where the same basis functions (4.37) and (4.38) used to write the redundant generalised force components are adopted. The matrix $\underset{\sim}{\boldsymbol{Z}}^{u}$ collects the coefficients of the linear combinations of basis functions, whose constant components have to be determined. Thus, each unknown function is expressed as a series of $D = (1 + 2k)(1 + 2l)$ terms in which every known basis function is multiplied by an unknown coefficient. Hence, the total number of unknown coefficients to be determined is, in general, $6D$. Then, equilibrium equations and boundary conditions are imposed in a finite number of points on the domain in order to find the coefficients of the series. We choose a number of equally spaced collocation points on the domain. Having adopted the cylindrical parameters, for domes with the upper oculus, the coordinate domain is rectangular, and can be discretised in the same way as in the finite difference method (the Figure 4.5 is shown again for reader's convenience) by dividing the rectangular domain in $n_\alpha \times n_z$ points. Then, six equilibrium equations at each internal

point and six boundary conditions at the free boundary are imposed. Periodicity conditions

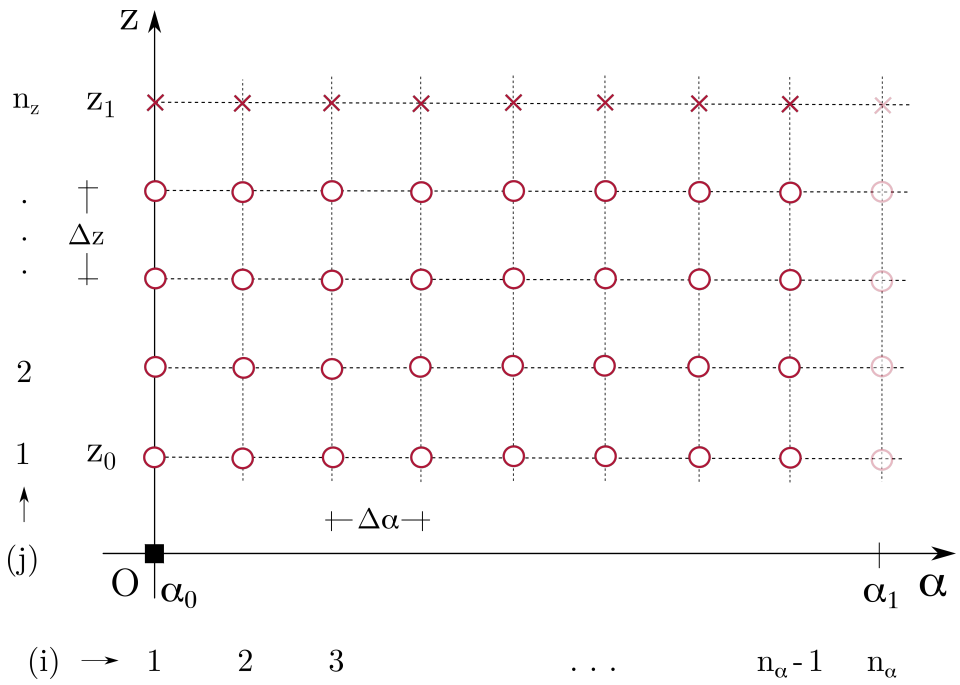

Figure 4.5: Collocation grid. The circles are the points on which equilibrium equations are imposed. The crosses are points on which boundary conditions are imposed. The periodicity along α is satisfied by the choice of the basis functions.

on $i = n_\alpha$ are not enforced directly, as the choice of the basis functions lead to automatic fulfilment of this condition, but unknowns and equations are written on $n_\alpha - 1$ points along direction α. Once k and l are chosen, we set $n_\alpha = 2 + 2k$ and $n_z = 1 + 2l$ in order for the number of unknown to be equal to the number of equations, i.e. $6 \times n_\alpha \times n_z$. It's worth observing that the values of k and l chosen for the unknowns may differ from the values chosen for the redundant forces (the latter could also be zero for an equilibrium solution to be found, as in the case of the $\mathfrak{F}_z$ subsystem). The resulting algebraic system can be solved with a classical technique, such as direct LU decomposition methods.

Comparison between the numerical methods

As for the case of the finite difference scheme, a comparison between the numerical methods in order to check their accuracy is performed, again on the $\mathfrak{F}_z$ equilibrium system for the case of the dome of Pisa cathedral. The equilibrium system is solved with the finite difference method, the collocation method and also the finite element method made available by *Wolfram Mathematica*® in the *NDSolve* routine. As shown in Figure 4.6 the numerical methods give solutions which are practically coincident. A final remark on efficiency is in order here. Obviously, all three methods lead the original problem back to the solution of a linear algebraic system of equations, which, for the finite difference and finite element methods, is represented by a sparse matrix, while for the collocation method it is represented by a dense matrix. This implies that, for the same size of representative matrices, the collocation

method is slower than the other two. However, in the applications, the collocation method is employed for its capability to give the solution in terms of analytical functions with global support. In the following chapter, the analysis of the error in the solution of the equilibrium equations is carried out.

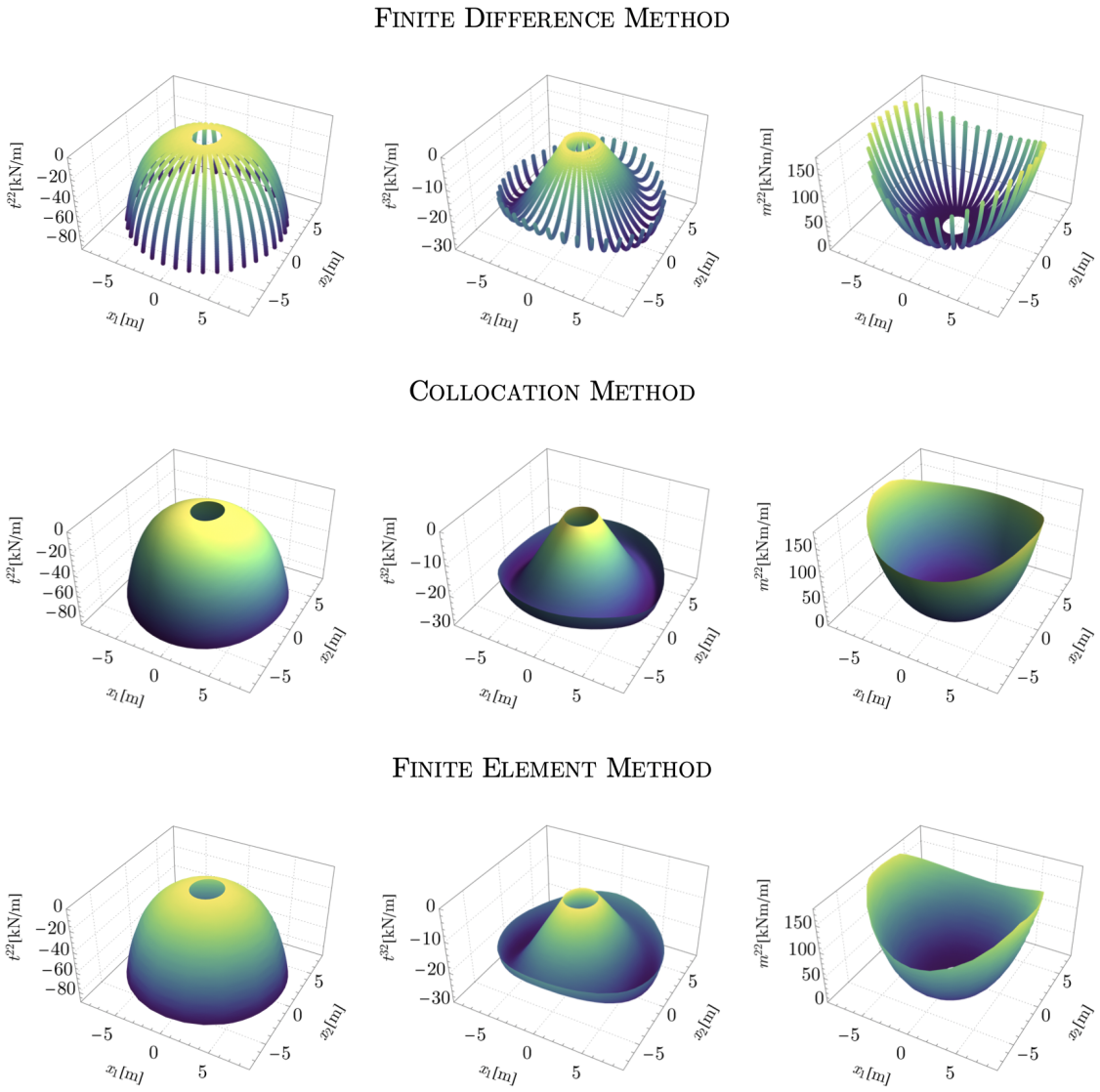

Figure 4.6: Comparison between the solutions obtained via finite difference, collocation and finite element methods on components t^{22}, t^{32} and m^{22} for system $\mathfrak{F}_z$.

4.4.4 Optimisation of the parameters

Once the solution of the system of equations has been expressed in terms of the parameters $\underset{\sim}{U}_{ij}$, $\underset{\sim}{V}_{ij}$, λ_x and λ_y (and possibly $\underset{\sim}{W}_{rs}$, H_0 and M_0 in special cases), the last step of the method consists in choosing those values such that a certain cost function is minimised under the

constraint that the admissibility conditions are satisfied. Here we distinguish between the two problems P1 and P2 and we refer to the case of generically oriented joints since the extension of the procedure to one of the special cases illustrated above is straightforward.

P1: analysis with only vertical loads

For problem P1 we have $\lambda_x = 0$ and $\lambda_y = 0$ and, as anticipated in the previous section, the safety level assessment is performed by maximising the geometric safety factor. To this aim, one searches for the minimum thickness and thus for the minimum eccentricity of the internal actions. However, setting the absolute value of the maximum eccentricity as the cost function would lead to a nonlinear optimisation problem with respect to the parameters of the series. For this reason, a procedure that searches for the minimum thickness of the dome iteratively is adopted. The strategy is as follows:

1. We start by defining a suitable linear cost function;
2. We solve a convex semidefinite optimisation problem;
3. If an admissible solution is found, the thickness is reduced and the procedure is iterated from point 1).

For the choice of the linear cost function, it is interesting to notice that there is no need for a specific choice as long as it is linear in the coefficients. Indeed, the interest is only in checking for the existence of a feasible solution, no matter which. Having said this, two choices appear natural though: minimise or maximise the sum of the meridian forces evaluated at the base of the dome, as this is related to the overall thrust of the dome.

In this way, the solution consists in solving a series of convex optimisation problems for which fast and reliable minimisation routines exist. Although for every material model, M1, M2, M3 and M4, a specific convex optimisation problem could be set up, we will refer exclusively to the M1 model (satisfying Heyman's hypotheses). This is necessary for problem P1, as the geometrical safety factor finds its justification only within these assumptions. For M1, the optimisation problem is semidefinite, as the constraints are those on the eccentricity, given by equation (3.210). In particular, for the applications we made use of the *SemidefiniteOptimization* routine, made available by *Wolfram Mathematica*®, that implements the DSDP algorithm. The DSDP software is a free open source implementation of an interior-point method for semidefinite programming. It provides primal and dual solutions, exploits low-rank structure and sparsity in the data, and has relatively low memory requirements for an interior-point method. It allows feasible and infeasible starting points and provides approximate certificates of infeasibility when no feasible solution exists. The dual-scaling algorithm implemented in this package has a convergence proof and worst-case polynomial complexity under mild assumptions on the data (from https://www.mcs.anl.gov/hs/software/DSDP/).

The minimisation problem can be stated as

$$\begin{aligned} \min_{\underset{\sim}{U},\underset{\sim}{V}} \quad & \{\mathfrak{l}(\underset{\sim}{U},\underset{\sim}{V})\}, \\ s.t. \quad & h\underset{\sim}{N} + \underset{\sim}{M} \in \mathrm{Sym}^{-} \\ & h\underset{\sim}{N} - \underset{\sim}{M} \in \mathrm{Sym}^{-}, \end{aligned} \tag{4.73}$$

where $\underset{\sim}{\boldsymbol{N}}$ and $\underset{\sim}{\boldsymbol{M}}$ denote the matrices of the physical components of the membrane force tensor $\mathbf{N}$ and the moment tensor $\mathbf{M}$ respectively, given in terms of the contravariant components, by

$$t^{\langle\alpha\beta\rangle} = t^{\alpha\beta}\sqrt{a_{\alpha\alpha}}\sqrt{a_{\beta\beta}}, \quad t^{\langle 3\alpha\rangle} = t^{3\alpha}\sqrt{a_{\alpha\alpha}}, \quad m^{\langle\alpha\beta\rangle} = m^{\alpha\beta}\sqrt{a_{\alpha\alpha}}\sqrt{a_{\beta\beta}}, \tag{4.74}$$

$\mathfrak{l}(\underset{\sim}{\boldsymbol{U}}, \underset{\sim}{\boldsymbol{V}})$ can be any linear function of the parameters and where the constraints on the eccentricity are convex cones. It is again stressed the fact that, in order to find the minimum thickness required to evaluate the geometrical safety factor, only the constraints of the optimisation problem matter, so the only thing one should check is the feasibility, provided that the objective function is a linear one. The optimisation problem has to be discretised in a finite subset of points of the domain. To this end, another grid is adopted where the constraint conditions are imposed. However, given the regularity of the solution, the optimised generalised force field satisfying the constraints on the grid will turn out to be admissible in every point of the domain, as for the case studies shown in the next chapter.

P2: analysis with both vertical and horizontal loads

For problem P2, since the lateral load multipliers λ_x and λ_y are related by the direction of the seismic action, one can express them as a function of a single lateral load multiplier once a particular direction has been chosen. With reference to the Cartesian coordinate system, let's denote by $\underset{\sim}{\boldsymbol{k}} = \{\cos\beta, \sin\beta\}^{\mathsf{T}}$ the column vector identifying the plan direction of the horizontal action, where β is the angle between x_1 and the direction of the load. Thus

$$\lambda_x = \lambda\cos\beta, \quad \lambda_y = \lambda\sin\beta. \tag{4.75}$$

Since the goal is to find the maximum horizontal load that can act on the dome, once the direction is identified, the following minimisation problem for M1 is set

$$\begin{aligned} \min_{\lambda, \underset{\sim}{\boldsymbol{U}}, \underset{\sim}{\boldsymbol{V}}} \quad & \{-\lambda\}, \\ s.t. \quad & h\underset{\sim}{\boldsymbol{N}} + \underset{\sim}{\boldsymbol{M}} \in \mathrm{Sym}^{-} \\ & h\underset{\sim}{\boldsymbol{N}} - \underset{\sim}{\boldsymbol{M}} \in \mathrm{Sym}^{-}, \end{aligned} \tag{4.76}$$

while for M2, M3 and M4 one need to add further constraints[2]. Another way to proceed is to always refer to the M1 model in the optimisation problem and verify a posteriori of the analysis whether the generalised force field identified also satisfies the hypotheses of the other material models. If that's the case, one can assert, by virtue of the static theorem of limit analysis, that the generalised force field is statically admissible even for the M2, M3 and/or M4 material. The analysis has to be repeated, in general, for every relevant direction of the horizontal actions.

[2]Since the constraint on the limited shear strength is a convex cone, the routine to be used in that case is the *ConicOptimization*, made available by *Wolfram Mathematica*®. In the case in which also the limited compressive strength is taken into account, the problem is generally convex and the *Convex Optimization* routine has to be used in *Wolfram Mathematica*®.

4.5 Summary and conclusive remarks

In this chapter a method for the stability assessment of masonry domes, which is based on the static theorem of limit analysis and makes use of the thin shell model is presented. The method searches for the equilibrium state that maximises the safety level within the set of statically admissible internal forces. The strategy adopted is very simple and it is borrowed from the well-known flexibility method used in the mechanics of beams. A suitable number of redundant internal forces is selected. All the internal force components are expressed in terms of a given set of basis functions, chosen among the trigonometric functions. The linear system of equilibrium equations is solved by keeping the redundant components as free parameters. A constrained optimisation problem is solved that searches for the minimum of a suitable cost function related to the safety level. The independent variables of the optimisation problem are the coefficients of the linear combination of known basis functions used for the redundant internal force components. The solution is pursued numerically by two different solution procedures. In the first one, the finite difference method is used; the other makes use of the collocation method. The optimisation problem is tackled by defining a suitable linear cost function and ending with a convex semidefinite optimisation problem. In the case vertical loads only are acting an expressly developed iterative method searches for the minimum thickness and thus for the minimum eccentricity of the internal actions. On the contrary, when also horizontal loads are present the optimisation is aimed at finding the maximum horizontal loads that can act on the dome, once the load direction is identified.

Although the application intended for this technique refers mainly to the safety level assessment of masonry domes and searches for the 'best' generalised force field in the sense of geometrical safety factor or greatest lateral load multipliers, it can possibly be exploited in several ways. For example, by playing with the constraints of the optimisation problem, one could search for generalised force fields having different features. One application would be, for example, to look for generalised force fields that satisfy conditions that account for the real cracking pattern in an existing dome.

Chapter 5

Case studies

In this chapter, the application of the *Statically Admissible Shell Forces* (SASF) analysis technique, described in Chapter 4, is illustrated with reference to a couple of case studies. The first case study is the spherical dome with an oculus on top. The second case study is the dome of Pisa Cathedral, a dome with a peculiar oval plan and ogival profile. The safety of the dome is assessed with and without horizontal loads and the influence of different material hypotheses on the results obtained for the case of the dome of Pisa Cathedral is also investigated.

5.1 Spherical dome with top opening

This section addresses the case of a spherical dome having a middle surface of radius $R = 10\,\mathrm{m}$ and a constant thickness $2h = 1\,\mathrm{m}$. The dome has a top opening whose radius is equal to $r = 1.5\,\mathrm{m}$ provided with a reinforcing ring. The dome is considered to be made of bricks with joints orthogonal to the middle surface of the shell. The parametric equations describing the middle surface of the dome are given in cylindrical coordinates, with the function describing the surface being (the dome is centred in the origin of the reference system)

$$\mathfrak{h}(\alpha, z) = \sqrt{R^2 - z^2}, \tag{5.1}$$

with $0 \leq \alpha \leq 2\pi$, $z_0 = 0\,\mathrm{m}$ and $z_1 = \sqrt{R^2 - r^2}$.

As shown in Chapter 4, for spherical geometry with normal joints, since the equilibrium equation $(4.4)_6$ is an identity, the procedure involves the identification of three redundant force components instead of two: t^{11}, t^{31} and m^{11}.

5.1.1 Geometrical safety factor for vertical loads: minimum thickness

The first analyses are carried out considering the dome subjected only to vertical loads, as shown in Figure 5.1. For this problem, termed P1, the goal is to find the maximum GSF by searching for the minimum admissible thickness of the dome. The analyses are performed by minimising the horizontal overall thrust at the base of the dome for different thickness values. The minimum thickness for which a feasible solution of the optimisation problem

exists is the admissible thickness. As already specified, the M1 model is adopted for all the analyses involving only vertical loads.

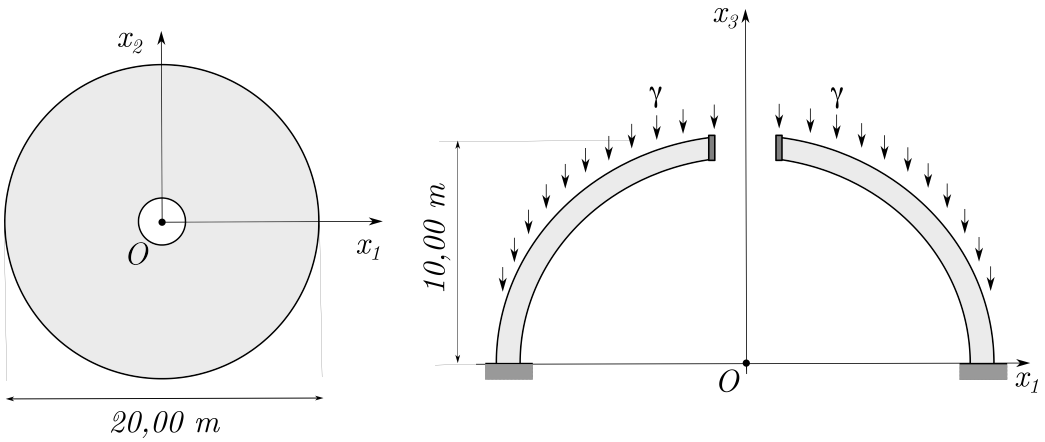

Figure 5.1: Scheme of the mechanical problem: spherical dome under vertical loads.

Convergence analysis

The analyses are carried out for different numbers of basis functions in order to check the convergence of the method. As shown in Figure 5.2, by increasing the number of basis functions the maximum of the absolute value of the eccentricity decreases as expected, while the time taken by the optimisation routine increases. The solution described in the following corresponds to the far-right point with 36 basis functions.

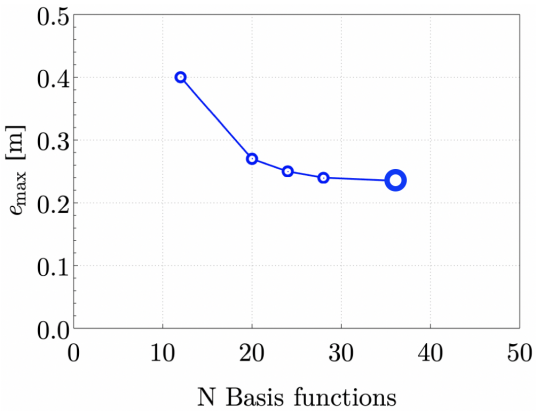

Figure 5.2: Convergence analysis: number of basis functions vs maximum eccentricity (in absolute value).

The optimised generalised internal force field

The generalised internal force field found by the method is described by analytical expressions and can be thus evaluated everywhere in the domain. Given the symmetry of the problem

the search for the optimal force field has been performed by setting $n = 0$, thus forcing the axial symmetry around x_3. The solution shown in the following has been obtained by setting $m = 8$. Moreover, also the reactions provided by the reinforcing ring, H_0 and M_0 have been chosen by the algorithm. Then, the minimisation problem involved optimising 17 basis functions for each redundant component and two boundary forces, resulting in a total of 36 coefficients. The optimisation grid has 20×40 equally spaced points. The optimal values of the parameters which are different from zero (17 coefficient for $t^{\langle 11 \rangle}$) are shown in Table 5.1. The transverse hoop shear force turns out to be null for the optimal solution. The optimal values for the boundary coefficient are $H_0 = 500.000$ and $M_0 = -10.686$.

$U_{(1,1)} = 0.000$	$U_{(1,2)} = -130.047$	$U_{(1,3)} = -1312.980$	$U_{(1,4)} = 547.740$
$U_{(1,5)} = 744.458$	$U_{(1,6)} = -296.0.35$	$U_{(1,7)} = -105.008$	$U_{(1,8)} = 31.674$
$U_{(1,9)} = 1.815$	$U_{(1,10)} = 886.932$	$U_{(1,11)} = -392.724$	$U_{(1,12)} = -1178.500$
$U_{(1,13)} = 486.287$	$U_{(1,14)} = 336.803$	$U_{(1,15)} = -122.496$	$U_{(1,16)} = -20.273$
$U_{(1,17)} = 3.932$			

Table 5.1: Spherical dome under vertical loads: optimal values of the coefficients.

The optimisation algorithm takes around 10 seconds to run on a MacBook Pro 16" 2019 with an Intel Core i9 2,3 GHz processor and 32 GB RAM. The generalised internal force field components different from zero are shown in Figure 5.3. A vertical section of the force fields diagrams is shown in Figure 5.4.

Admissibility conditions: eccentricity and principal membrane forces

To check the admissibility of the generalised internal force field, as anticipated in Chapter 4, a dense mesh of $n_\alpha^{check} \times n_z^{check}$ is adopted, with $n_\alpha^{check} = 1080$ and $n_z^{check} = 330$, for a total of 356400 points. In this way, the maximum distance between two points is around 6 cm in the circumferential direction and around 3 cm in the meridian direction. These distances are of the same order as the average bricks' dimensions and are assumed to be adequate for the case at hand. Thus, in the following, the expression 'everywhere in the domain' means in each of the 356400 points of the 'check grid'.

The maximum of the absolute value of the eccentricity, which is linked to the geometric safety factor, is 23.5 cm. In other words, the dome would have been stable even with a thickness of only 47 cm, resulting in a geometric safety factor of 2.13 since the thickness of the dome is 1 m. Although the case of the closed sphere is different from this one, the present result is not far from the minimum theoretical thickness found by Heyman, and equal to $h_{min} = 0.042R$. The maximum modulus eccentricity surface is shown in Figure 5.5. The principal membrane forces are, as expected, everywhere compressive as shown in Figure 5.6, where $f^{\langle 1 \rangle}$ and $f^{\langle 2 \rangle}$ denote, respectively, the maximum and the minimum principal force.

It should be noted that the solution found satisfies the zero tensile strength assumption along all directions passing through a generic point on the middle surface. Therefore, as this solution totally ignores possible beneficial effects due to the finite tensile strength of the bricks or effects related to texture, it should be recognised as fairly conservative.

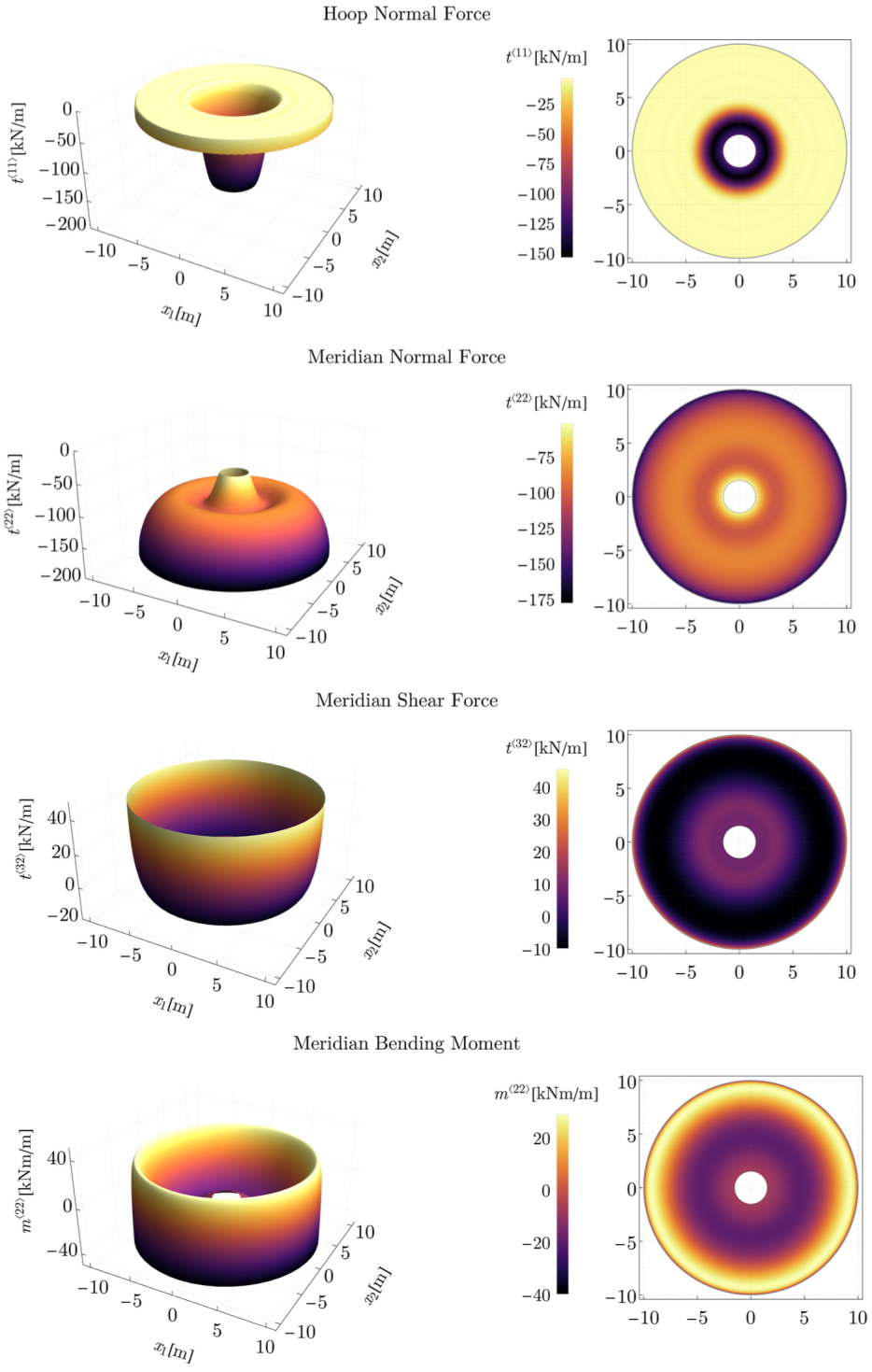

Figure 5.3: Spherical dome under vertical loads: optimal generalised force components.

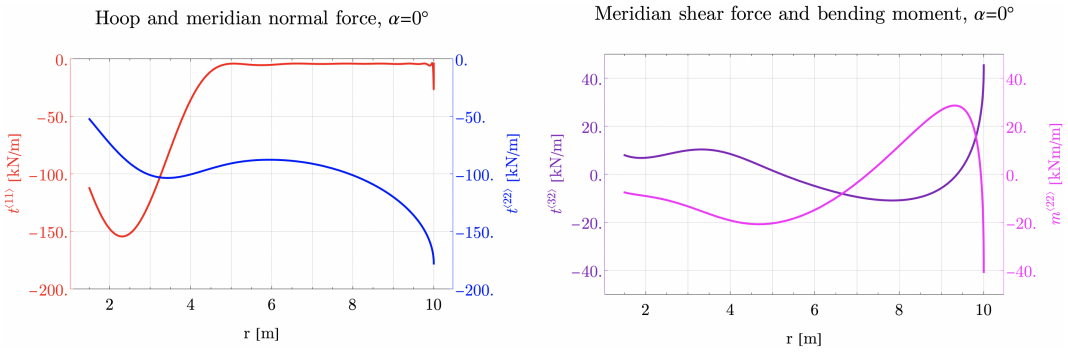

Figure 5.4: Membrane normal forces (left), meridian transverse shear and meridian bending moment (right) on the vertical section $\alpha = 0°$ ($r = x_1$).

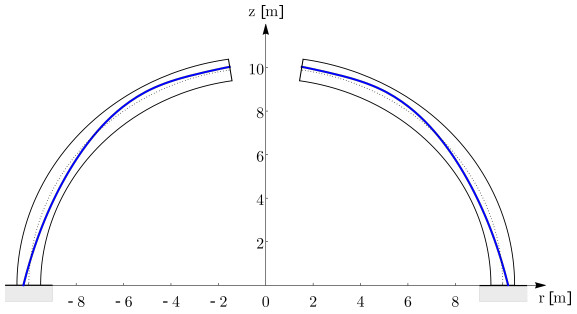

Figure 5.5: Maximum modulus eccentricity surface on a vertical section.

Although the optimisation procedure imposes the admissibility conditions on a finite set of points it is a remarkable feature of the method to return a solution that is everywhere compatible with the material constraints. In this regard, a remark on the admissibility condition is in order. In the context of standard Heyman hypotheses, the solution found by the optimisation method is considered statically admissible regardless of the magnitude of compressive and shear stresses. From a mechanical standpoint, one wants to check if the maximum compressive and shear stresses are compatible with those commonly admissible for the masonry material. The compressive stresses are evaluated by assuming a stress block distribution within the thickness of the shell. The maximum stress resulted to be equal to 3.3 MPa a value that could be compatible with a good masonry. Moreover, the maximum stress is located around the top oculus since a high horizontal thrust is required at the crown. However, the maximum stress decreases rapidly resulting less than 1.0 MPa from about 80 cm below the top opening. The maximum friction coefficient required for equilibrium is around 0.26, a value that is also fully compatible with the friction coefficient of historical masonry. It is therefore observed that the solution found adopting the M1 model is also statically admissible for the other material models described in Chapter 3.

Equilibrium error evaluation

The error in the optimal solution of the equilibrium problem can be easily evaluated everywhere in the domain since the solution is explicit. By writing the equilibrium system of

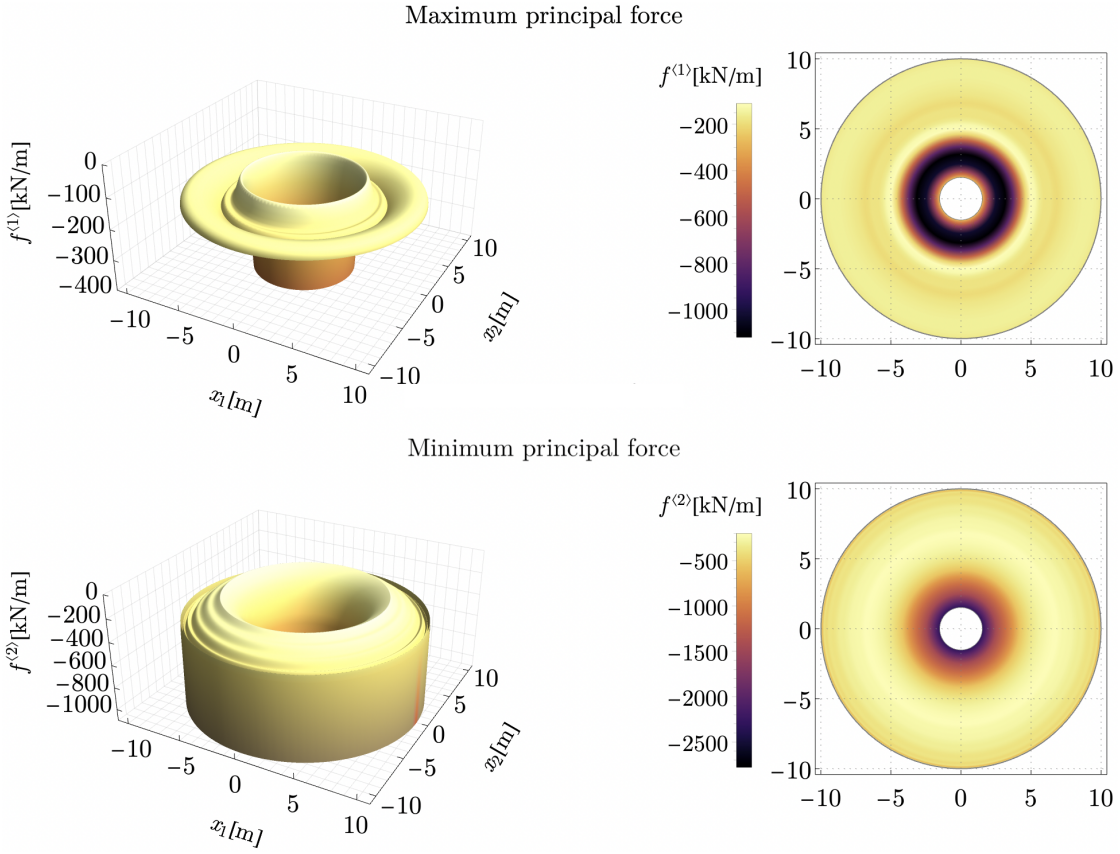

Figure 5.6: Principal membrane forces (for vertical loads).

equations in dimensionless form, the loading vector $\underset{\sim}{\boldsymbol{l}} = (\tilde{b}^1, \tilde{b}^2, \tilde{b}^3, \tilde{c}^1, \tilde{c}^2, \tilde{c}^3)$ is defined, where $\tilde{b}^k$, $\tilde{c}^k$ are the dimensionless components corresponding to b^1, b^2, b^3, c^1, c^2, c^3 (in the problem at hand $\tilde{c}^1 = \tilde{c}^2 = \tilde{c}^3 = 0$). The error is estimated by computing the residuals r^i of the six dimensionless equilibrium equations and comparing them with the norm of the load vector $\underset{\sim}{\boldsymbol{l}}$, that is

$$err^i = \frac{r^i}{\|\underset{\sim}{\boldsymbol{l}}\|}, \qquad i = 1, \ldots, 6. \tag{5.2}$$

The residuals r^i can be interpreted as the components of fictitious load distribution to be added to the real one in order to exactly fulfil the local equilibrium equations.

The highest error is located close to the free boundary of the domain and it is equal to around 2% in a narrow region around the top of the dome (red region in Figure 5.7). The maximum error on each component in the green region on Figure 5.7 is less than 1%.

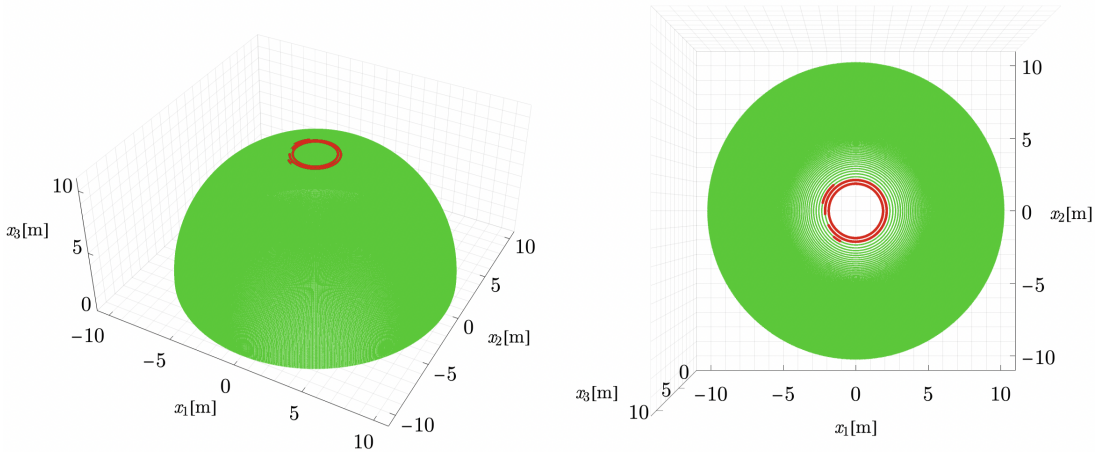

Figure 5.7: Maximum errors in the equilibrium equations.

5.1.2 Maximum lateral load multiplier for horizontal loads

The second set of analyses is carried out considering the dome subjected both to vertical and horizontal loads, as shown in Figure 5.8. In this kind of problem, termed P2, the purpose is to find the maximum lateral load multiplier. The analyses are carried out by maximising λ adopting the M1 model.

Convergence analysis

The analyses are carried out for different numbers of basis functions in order to check the convergence of the method. As shown in Figure 5.9, by increasing the number of basis functions the maximum lateral load multiplier increases as expected, while the time taken by the optimisation routine also increases. The solution described in the following corresponds to 35 basis functions, which represents a good compromise between accuracy achieved and time taken.

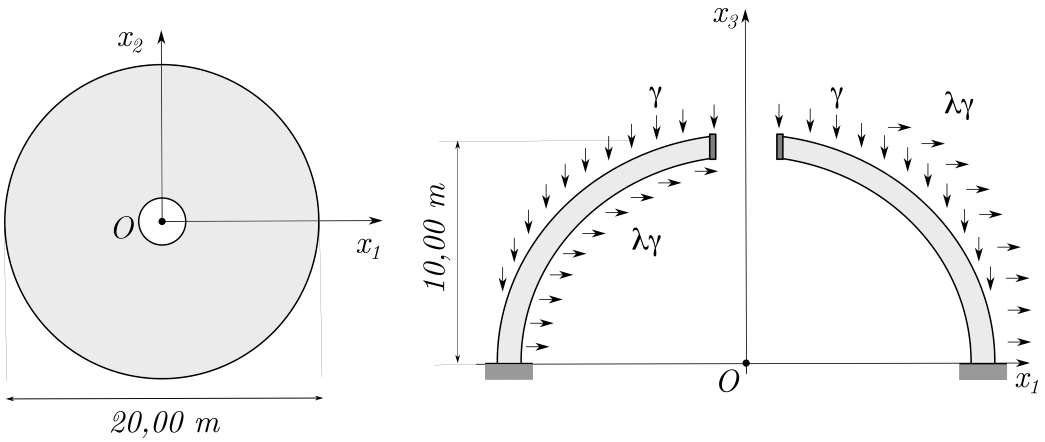

Figure 5.8: Scheme of the mechanical problem: spherical dome under vertical and horizontal loads.

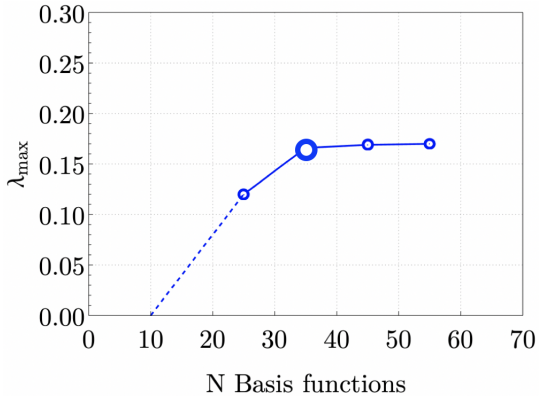

Figure 5.9: Convergence analysis: number of basis functions vs maximum lateral load multiplier.

The optimised generalised internal force field

The solution obtained by setting $n = 2$ and $m = 3$ for t^{11}, $t^{31} = 0$ and $m^{11} = 0$ is shown here because it is more regular compared to solutions in which also t^{31} and m^{11} have been optimised and at the same time it manages to reach a fairly high maximum load multiplier. In solving problem P2, the thickness of the dome is set to the real thickness in order to maximise the lateral load multiplier. The optimisation grid has 20×40 equally spaced points. The optimal values of the parameters which are different from zero (35 coefficient for $t^{\langle 11 \rangle}$) are shown in Table 5.2. The optimal values for the boundary coefficient are $H_0 = 119.510$ and $M_0 = -6.784$, while the maximum lateral load multiplier turns out to be $\lambda_{max} = 0.166$.

$U_{(1,1)} = -39.411$	$U_{(1,2)} = 61.369$	$U_{(1,3)} = -6.961$	$U_{(1,4)} = -6.107$
$U_{(1,5)} = 7.376$	$U_{(1,6)} = 28.303$	$U_{(1,7)} = -2.291$	$U_{(2,1)} = -0.022$
$U_{(2,2)} = 0.035$	$U_{(2,3)} = 0.004$	$U_{(2,4)} = -0.004$	$U_{(2,5)} = -0.004$
$U_{(2,6)} = 0.017$	$U_{(2,7)} = 0.001$	$U_{(3,1)} = 0.005$	$U_{(3,2)} = -0.008$
$U_{(3,3)} = -0.003$	$U_{(3,4)} = 0.001$	$U_{(3,5)} = 0.003$	$U_{(3,6)} = -0.004$
$U_{(3,7)} = -0.001$	$U_{(4,1)} = 26.716$	$U_{(4,2)} = -42.205$	$U_{(4,3)} = 2.499$
$U_{(4,4)} = 4.840$	$U_{(4,5)} = -2.357$	$U_{(4,6)} = -20.482$	$U_{(4,7)} = 0.878$
$U_{(5,1)} = -12.010$	$U_{(5,2)} = 19.100$	$U_{(5,3)} = -1.423$	$U_{(5,4)} = -2.266$
$U_{(5,5)} = 1.344$	$U_{(5,6)} = 9.336$	$U_{(5,7)} = -0.486$	

Table 5.2: Spherical dome under vertical and horizontal loads: optimal values of the coefficients.

The membrane force components are shown in Figure 5.10, the transverse meridian shear and meridian bending moment are shown in Figure 5.11, while the other generalised force components are zero. Two vertical sections of the internal force components diagrams are also shown in figure Figure 5.12 and Figure 5.13. The distributions of internal forces at $z = 0\,\mathrm{m}$ and at $z = 5\,\mathrm{m}$ are also shown in the diagrams plotted in Figure 5.14 and Figure 5.15 respectively.

Admissibility conditions: eccentricity and principal membrane forces

The diagram of the maximum modulus eccentricity surface on two vertical sections, on $\alpha = 0°$ and $\alpha = 90°$, respectively, are shown in Figure 5.16. Even for this load condition, as expected, the principal membrane forces are compressive, as shown in Figure 5.17. It must be said that, for the solution found, the maximum compressive stress would be excessive from a physical point of view, as it turns out to be $\sigma_{min} = -126\,\mathrm{MPa}$. Also, the friction coefficient required would be greater than one. However, the optimal solution found is perfectly admissible according to the material model M1. A deepening on this aspect is carried out for the case of the dome of Pisa cathedral.

Equilibrium error evaluation

The error in the optimal solution of the equilibrium problem is evaluated in the same way as for vertical loads. In the green region in Figure 5.18, the maximum error is less than 1%.

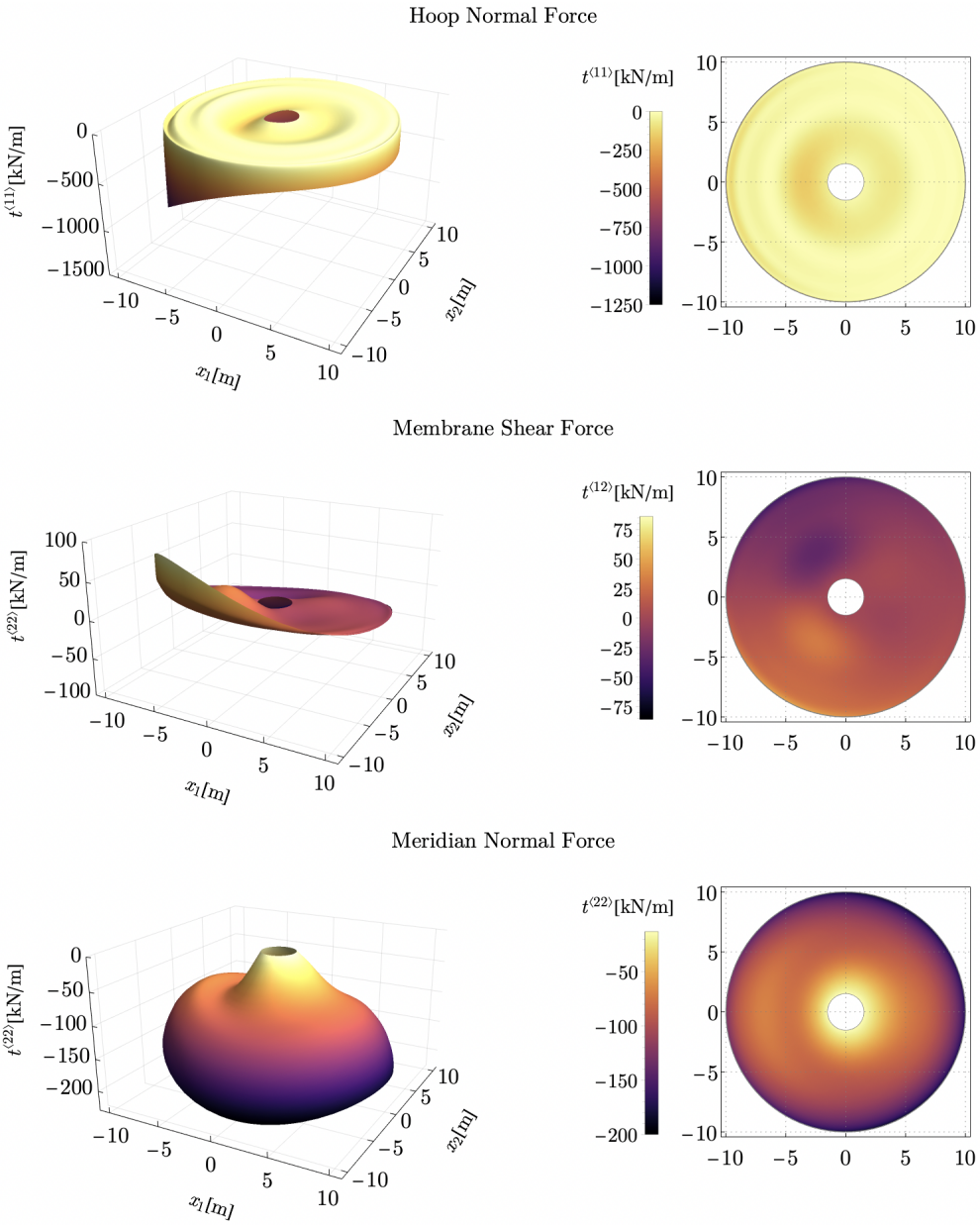

Figure 5.10: Spherical dome under vertical and horizontal loads: optimal membrane force components.

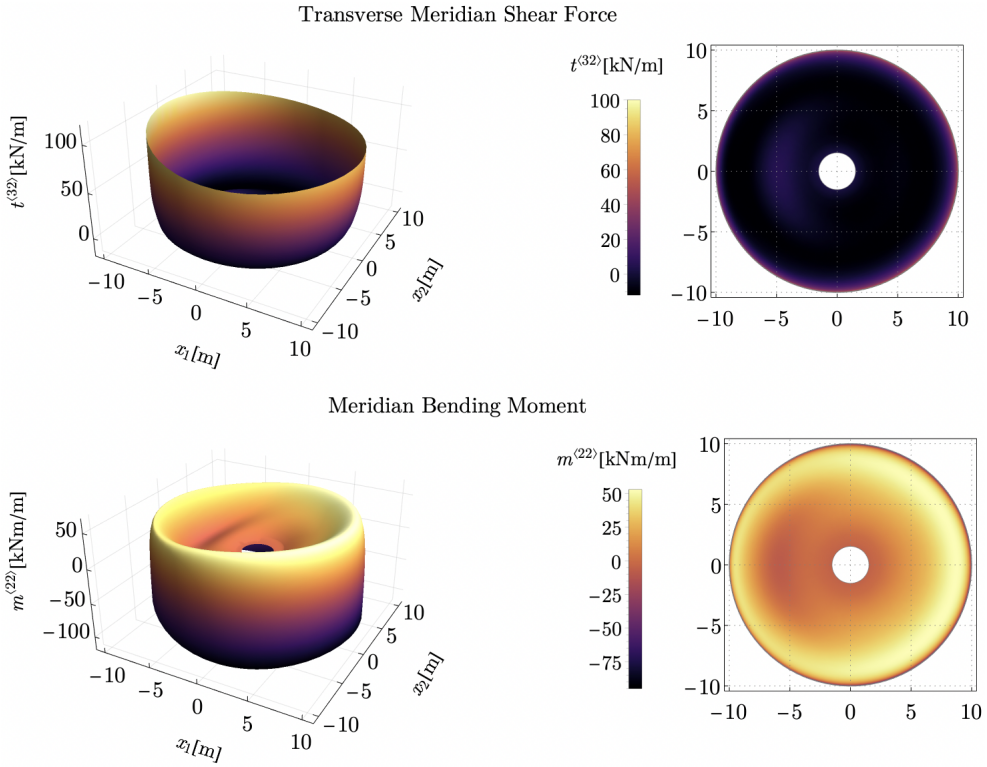

Figure 5.11: Spherical dome under vertical and horizontal loads: optimal meridian transverse shear and bending moment.

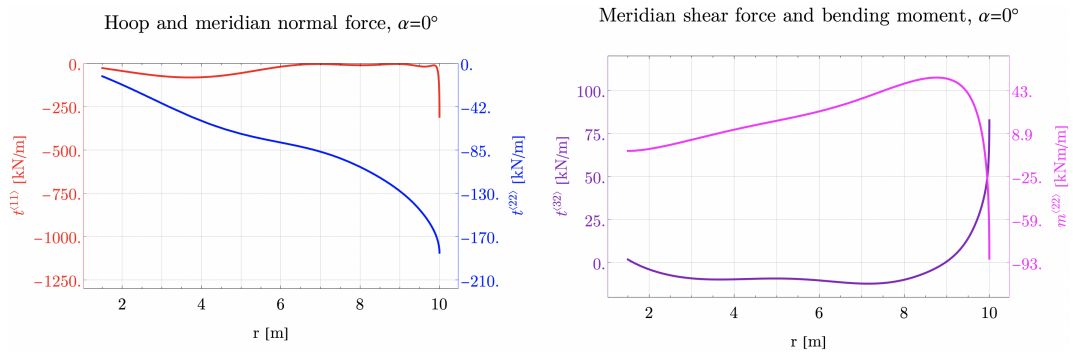

Figure 5.12: Membrane normal forces (left), meridian transverse shear and meridian bending moment (right) on the vertical section $\alpha = 0°$ ($r = x_1$).

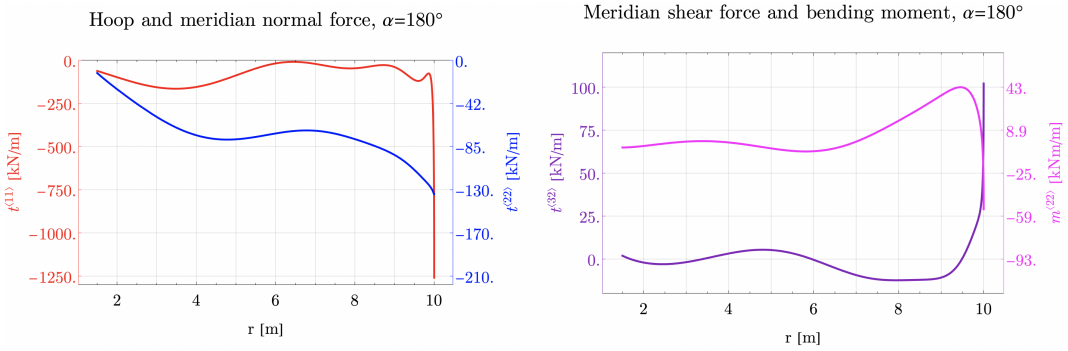

Figure 5.13: Membrane normal forces (left), meridian transverse shear and meridian bending moment (right) on the vertical section $\alpha = 180°$ ($r = -x_1$).

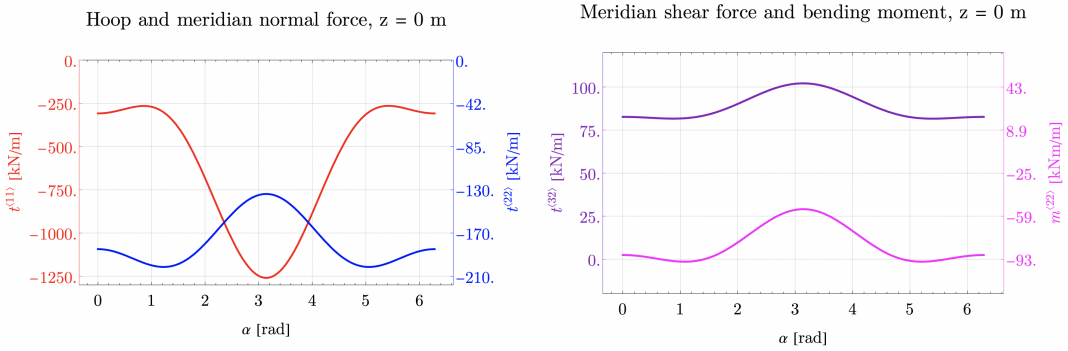

Figure 5.14: Membrane normal forces (left), meridian transverse shear and meridian bending moment (right) on $z = 0\,\mathrm{m}$.

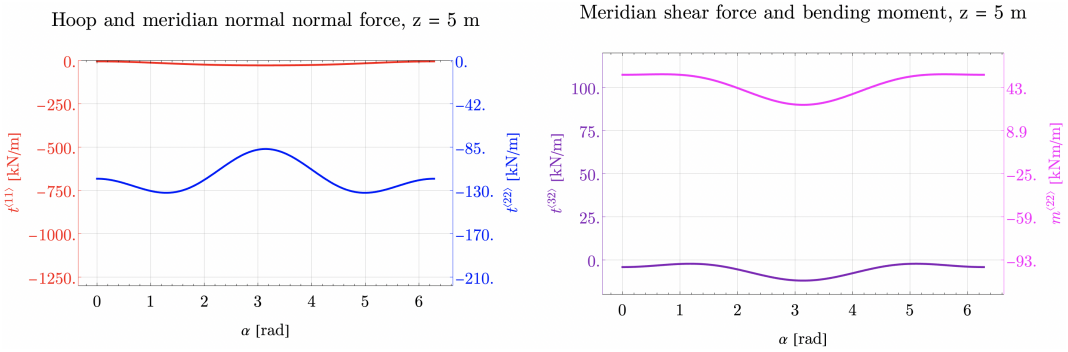

Figure 5.15: Membrane normal forces (left), meridian transverse shear and meridian bending moment (right) on $z = 5\,\mathrm{m}$.

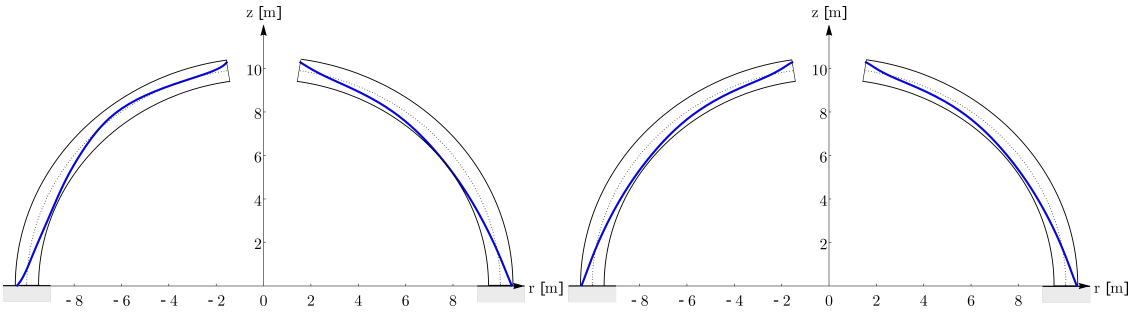

Figure 5.16: Maximum modulus eccentricity surface on two vertical sections at $\alpha = 0°$ (left) and $\alpha = 90°$ (right).

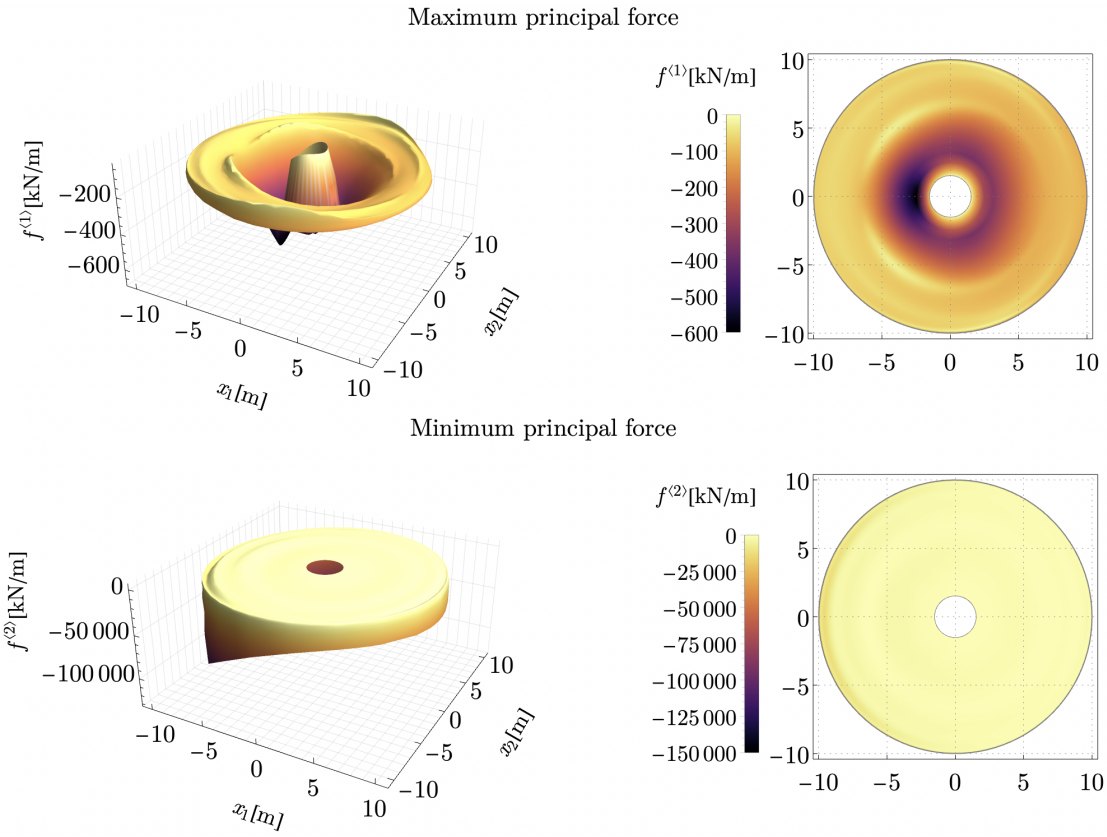

Figure 5.17: Principal membrane forces (for vertical and horizontal loads).

Close to the top oculus, in the yellow region, the maximum error increases up to a maximum of 10%. Along the edge the error is zero, strictly speaking, as the boundary conditions are exactly fulfilled. Nevertheless, since the equilibrium differential equations must hold at a distance arbitrarily close to the edge, the local error made on the equilibrium differential equations has been checked also along the edge where it reaches some 39% in a narrow region at the top of the dome (red region in Figure 5.18). In this regard, it is worth observing that the additional load that should be applied along the top edge to restore equilibrium has a negligible resultant, less than 0.6% of the total horizontal load.

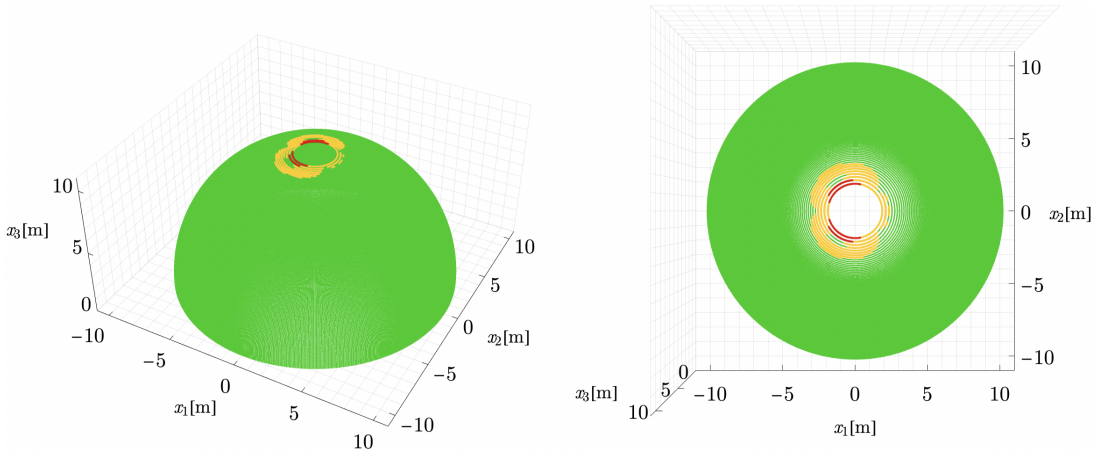

Figure 5.18: Maximum errors in the equilibrium equations.

5.2 The dome of Pisa Cathedral

The dome of Pisa Cathedral is an extremely interesting construction from many points of view. In this section, only the results of the analysis are presented, as the case study has already been described in Chapter 2.

By adopting the parametric representation in cylindrical coordinates (4.35), the middle surface of the dome is described by the function

$$\mathfrak{h}(\alpha, z) = \frac{\left(d + \sqrt{e^2 - z^2}\right)\left(f + \sqrt{g^2 - z^2}\right)}{\sqrt{\left(d + \sqrt{e^2 - z^2}\right)^2 \sin^2(\alpha) + \left(f + \sqrt{g^2 - z^2}\right)^2 \cos^2(\alpha)}}, \tag{5.3}$$

being $d = -5.57\,\mathrm{m}$, $e = 13.99\,\mathrm{m}$, $f = -8.11\,\mathrm{m}$, $g = 15.43\,\mathrm{m}$ dimensional constants depending on the shape of the surface.

5.2.1 Geometrical safety factor for vertical loads: minimum thickness

The first analyses are carried out considering the dome subjected only to vertical loads, as shown in Figure 5.19. For this problem, termed P1, the goal is to find the maximum GSF

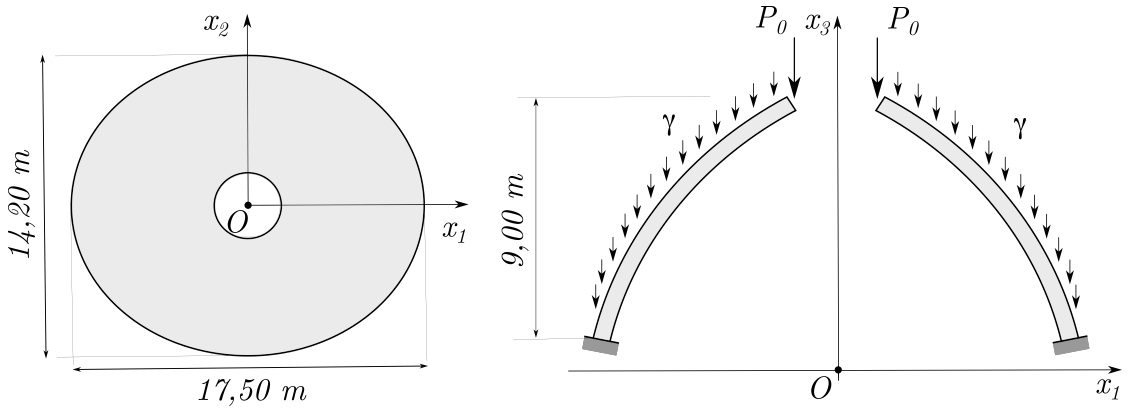

Figure 5.19: Scheme of the mechanical problem: dome of Pisa Cathedral under vertical loads.

by searching for the minimum admissible thickness of the dome. The analyses are performed by minimising the horizontal overall thrust at the base of the dome for different thickness values. The minimum thickness for which a feasible solution of the optimisation problem exists is the admissible thickness. As already specified, the M1 model is adopted for all the analyses involving only vertical loads.

Convergence analysis

The analyses are carried out for different numbers of basis functions in order to check the convergence of the method. As shown in Figure 5.20, by increasing the number of basis functions the maximum of the absolute value of the eccentricity decreases as expected, while the time taken by the optimisation routine increases. The solution described in the following corresponds to the far-right point with 65 basis functions, which represents a good compromise between accuracy achieved and time taken.

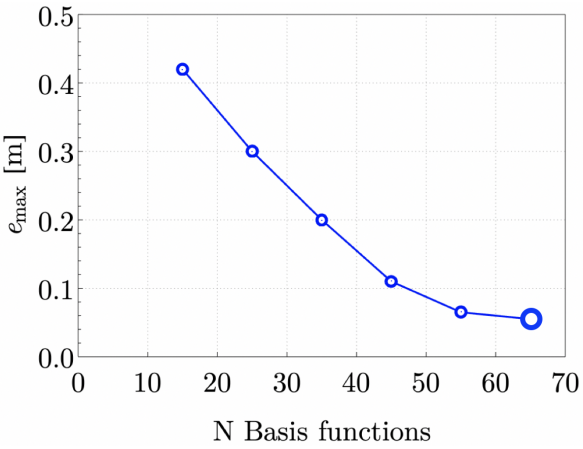

Figure 5.20: Convergence analysis: number of basis functions vs maximum eccentricity (in absolute value).

The optimised generalised internal force field

The solution shown has been obtained by setting $n = 2$ and $m = 6$ corresponding to 65 basis functions for each redundant component and a total of 130 coefficients to be optimised. The optimisation grid has 20×40 equally spaced points. The optimal values of the parameters which are different from zero (38 in total) are shown in Table 5.3.

$U_{(1,1)} = -456,449$	$U_{(1,2)} = 794,745$	$U_{(1,3)} = -258,252$	$U_{(1,4)} = -247,176$
$U_{(1,5)} = 109,704$	$U_{(1,6)} = 11,640$	$U_{(1,7)} = -5,266$	$U_{(1,8)} = 185,639$
$U_{(1,9)} = 520,836$	$U_{(1,10)} = -208,630$	$U_{(1,11)} = -76,700$	$U_{(1,12)} = 35,404$
$U_{(1,13)} = -0,188$	$U_{(5,1)} = -288,897$	$U_{(5,2)} = 510,484$	$U_{(5,3)} = -134,077$
$U_{(5,4)} = -176,973$	$U_{(5,5)} = 61,821$	$U_{(5,6)} = 12,881$	$U_{(5,7)} = -3,502$
$U_{(5,8)} = 93,335$	$U_{(5,9)} = 348,003$	$U_{(5,10)} = -112,196$	$U_{(5,11)} = -62,472$
$U_{(5,12)} = 21,276$	$U_{(5,13)} = 0,875$	$V_{(1,2)} = 0,012$	$V_{(1,3)} = -0,020$
$V_{(1,4)} = 0,020$	$V_{(1,5)} = -0,012$	$V_{(1,6)} = 0,005$	$V_{(1,7)} = -0,001$
$V_{(5,2)} = -0,010$	$V_{(5,3)} = 0,018$	$V_{(5,4)} = -0,021$	$V_{(5,5)} = 0,016$
$V_{(5,6)} = -0,008$	$V_{(5,7)} = 0,002$		

Table 5.3: Dome of Pisa Cathedral under vertical loads: optimal values of the coefficients.

The optimisation algorithm takes around 40 seconds to run on a MacBook Pro 16" 2019 with an Intel Core i9 2,3 GHz processor and 32 GB RAM. The membrane force components, the transverse shear components and the moment components are shown in Figure 5.21, Figure 5.22 and Figure 5.23 respectively. Two vertical sections of the internal force components diagrams are also shown in Figure 5.24 and Figure 5.25. The distributions of the internal forces at $z = 4\,\text{m}$ and at $z = 8\,\text{m}$ are shown in the diagrams plotted in Figure 5.26 and Figure 5.27 respectively.

Admissibility conditions: eccentricity and principal membrane forces

To check the admissibility of the generalised internal force field, as anticipated in Chapter 4, a dense mesh of $n_\alpha^{check} \times n_z^{check}$, with $n_\alpha^{check} = 720$ and $n_z^{check} = 300$, for a total of 216000 points, is adopted. In this way, the maximum distance between two points is around 7 cm in the circumferential direction and around 3 cm in the meridian direction. These distances are of the same order as the bricks' dimensions and are assumed to be adequate for the case at hand. Thus, in the following, the expression 'everywhere in the domain' means in each of the 216000 points of the 'check grid'.

The maximum of the absolute value of the eccentricity, which is linked to the geometric safety factor, is 5.5 cm. In other words, the dome would have been stable even with a thickness of only 11 cm, resulting in a geometric safety factor of 5.45 since the real thickness of the dome is 60 cm. At the structure' scale the maximum modulus eccentricity surface and the middle surface are almost indistinguishable (see Figure 5.28). Comparing these results with some previous analyses [Aita et al., 2017d], [Bennati et al., 2020], [Barsi et al., 2022], it is shown how the widening of the equilibrium possibilities given to the structure by the introduction of the bending moments could make a huge difference in the evaluation of its

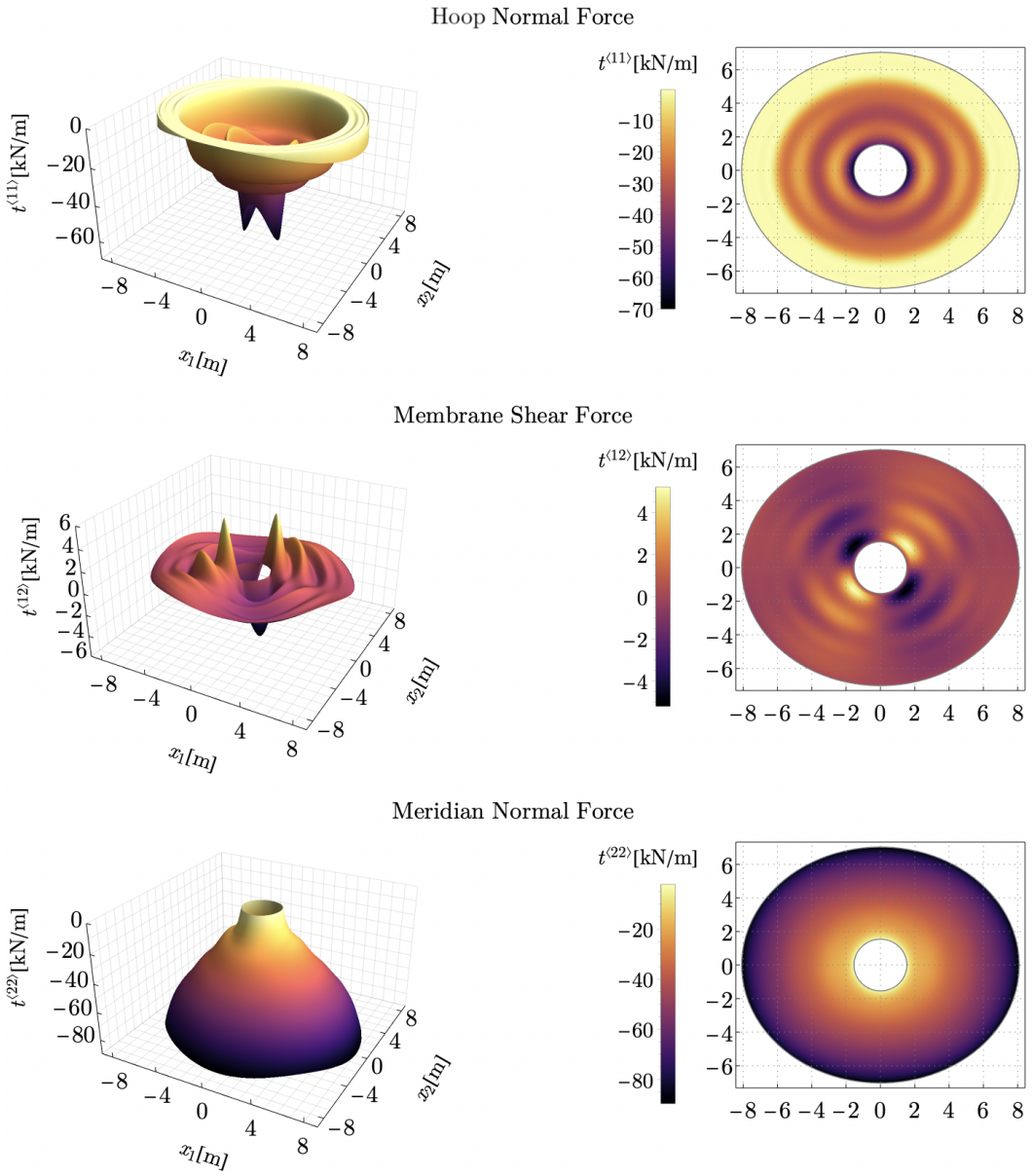

Figure 5.21: Dome of Pisa Cathedral under vertical loads: optimal membrane force components.

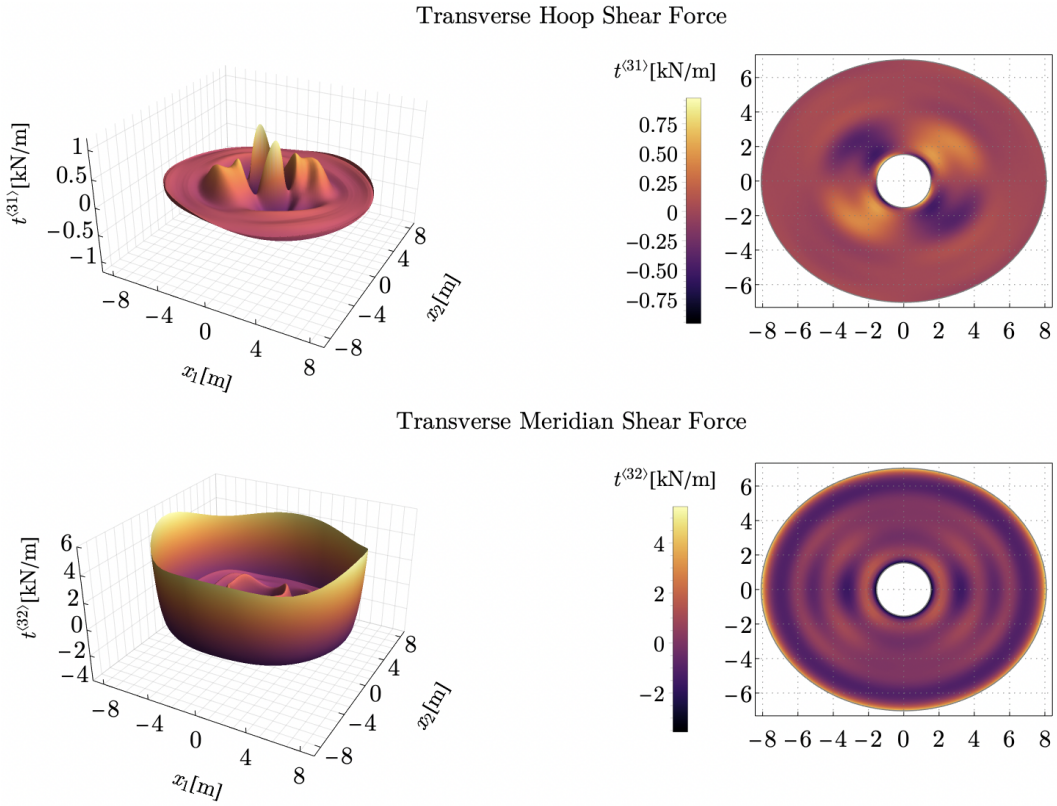

Figure 5.22: Dome of Pisa Cathedral under vertical loads: optimal transverse shear components.

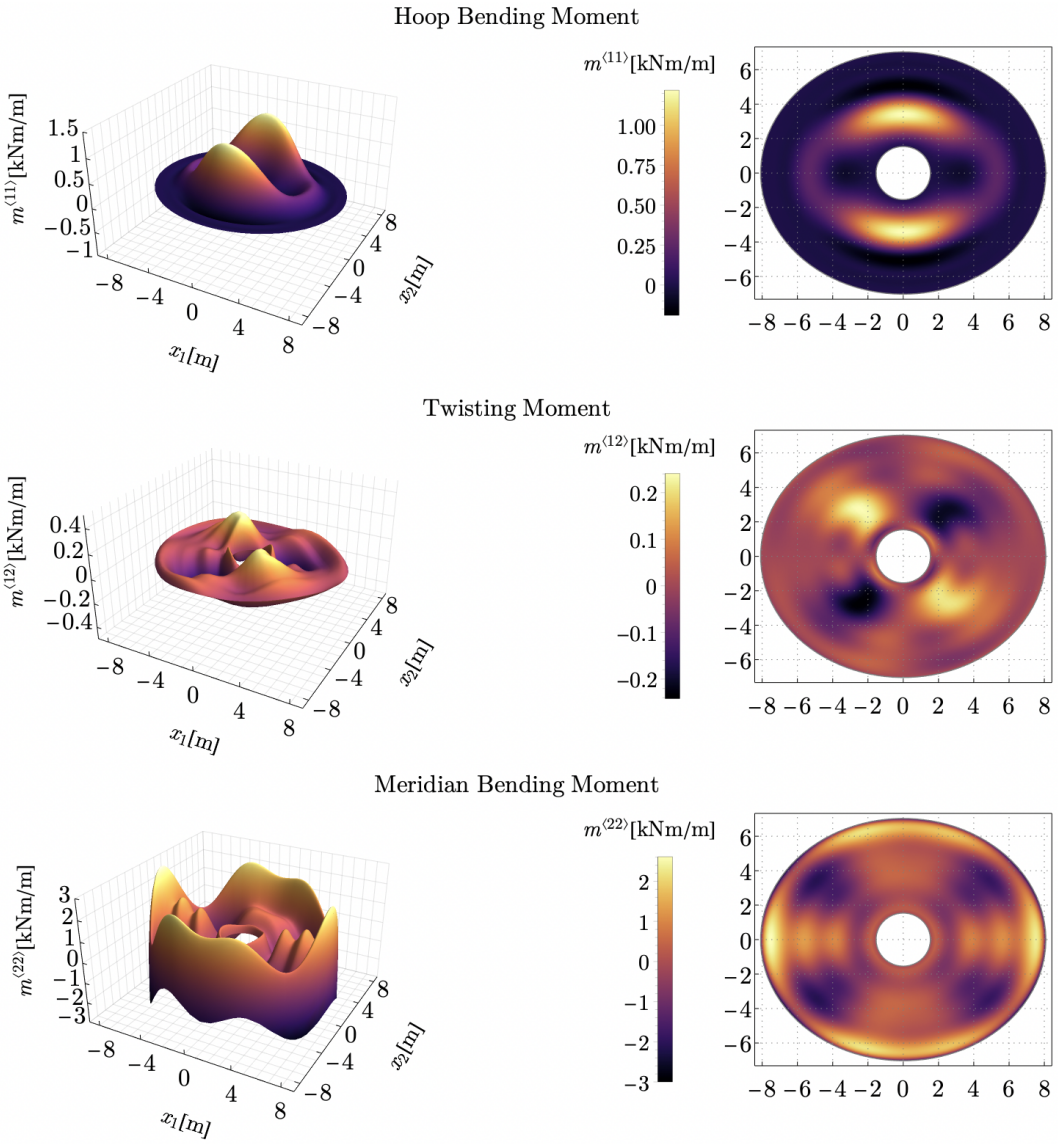

Figure 5.23: Dome of Pisa Cathedral under vertical loads: optimal moment components.

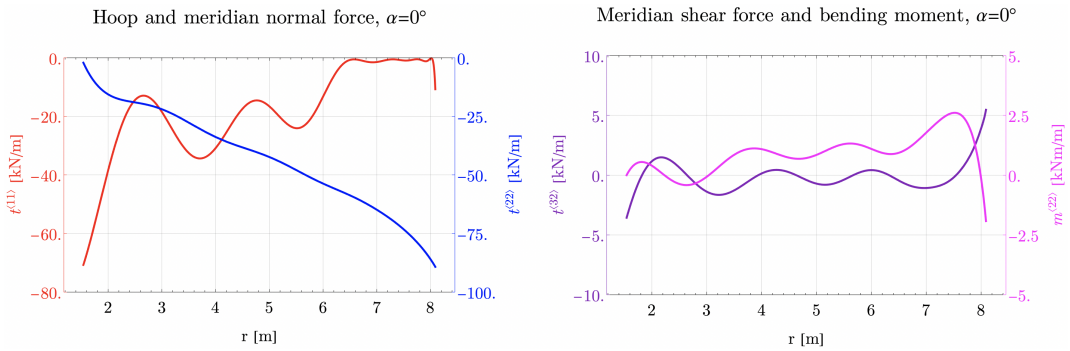

Figure 5.24: Membrane normal forces (left), meridian transverse shear and meridian bending moment (right) on the vertical section $\alpha = 0°$ ($r = x_1$).

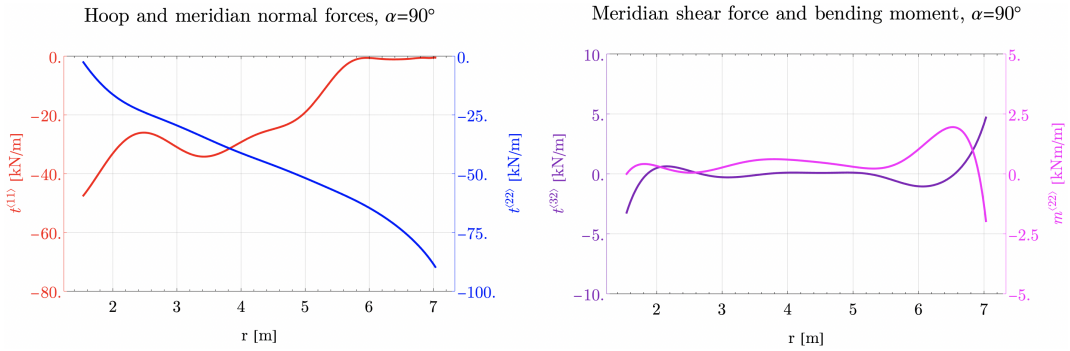

Figure 5.25: Membrane normal forces (left), meridian transverse shear and meridian bending moment (right) on the vertical section $\alpha = 90°$ ($r = x_2$).

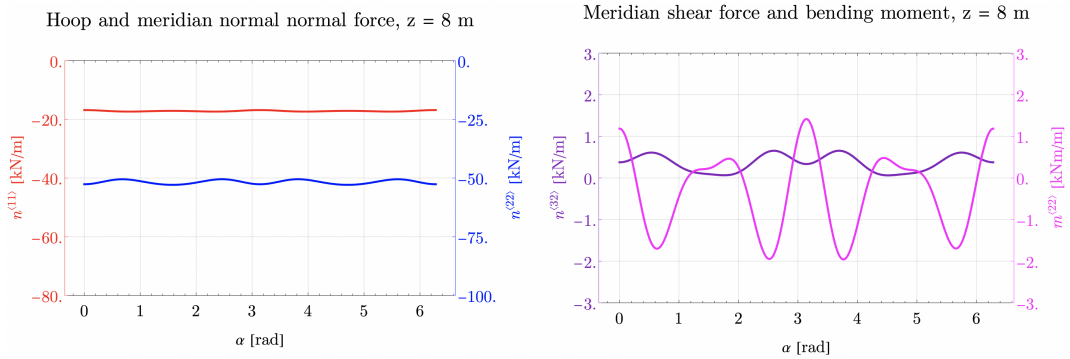

Figure 5.26: Membrane normal forces (left), meridian transverse shear and meridian bending moment (right) on $z = 4\,\mathrm{m}$.

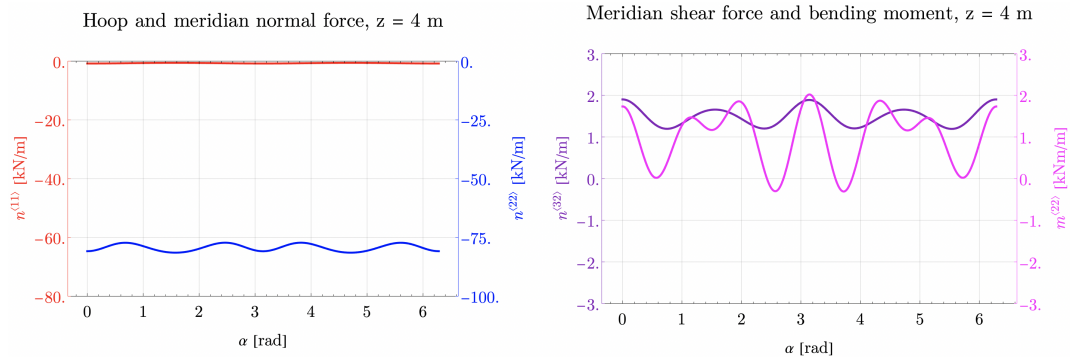

Figure 5.27: Membrane normal forces (left), meridian transverse shear and meridian bending moment (right) on $z = 8\,\mathrm{m}$.

stability. The principal membrane forces are, as expected, everywhere compressive as shown

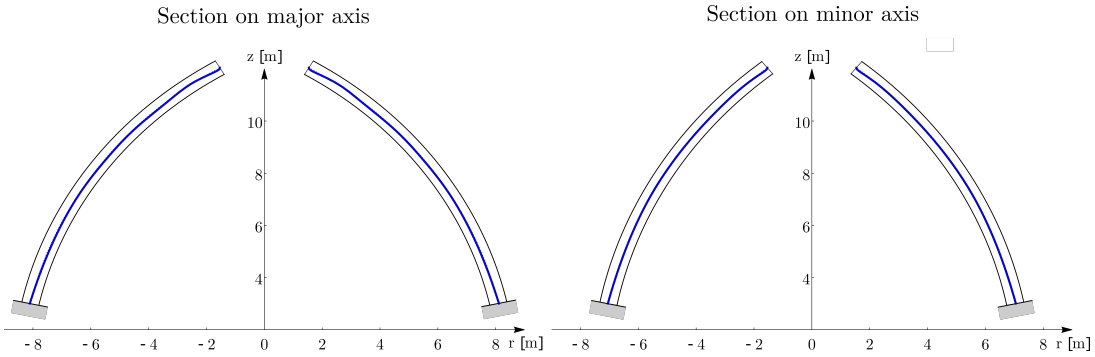

Figure 5.28: Maximum modulus eccentricity surface on two vertical sections at $\alpha = 0°$ (right) and $\alpha = 90°$ (left).

in Figure 5.29, where $f^{\langle 1\rangle}$ and $f^{\langle 2\rangle}$ denote, respectively, the maximum and the minimum principal force.

For the dome of Pisa Cathedral, the maximum stress is equal to 1.3 MPa a value that is fully compatible with a common masonry. This is due to the fact that the distribution of the internal forces is characterised by a very low eccentricity and thus the shell forces are distributed on almost the whole thickness. The maximum friction coefficient required for equilibrium is around 0.36, a value that is also fully compatible with the friction coefficient of historical masonry, except for the boundary region, where a value of around 0.86 is required. A remark concerning the friction limits is in order here. In the region of the introduction of the external boundary loads (i.e. boundary conditions) the friction coefficient required is given simply by the geometry of the dome and the direction of the external load: if the load is in the friction cone then the shear resistance is sufficient, otherwise it is not.

The simple adoption of the point-wise Coulomb friction law could lead to the erroneous conclusion that the dome is not stable, while a failure due to shear near the oculus is never observed in real domes, even when the load is introduced outside the friction cone. This is due essentially to the incompatibility of a possible local collapse mechanism which would require a sliding through the interior of the dome that is prevented by the orientation of the joints

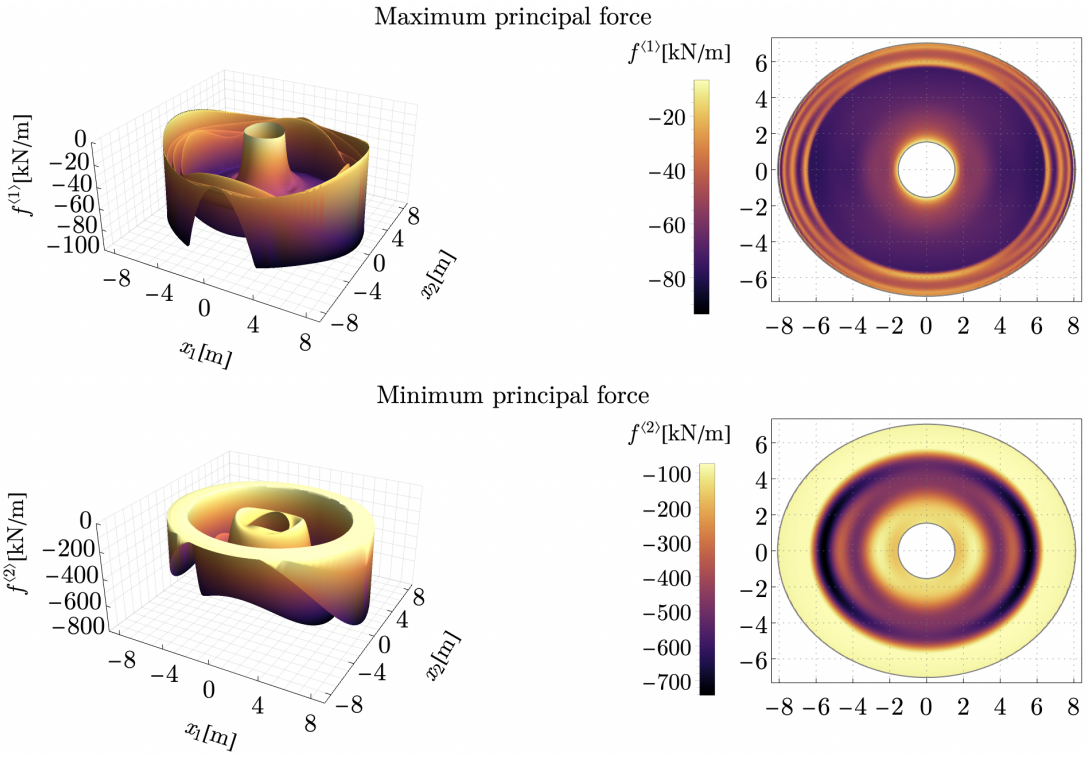

Figure 5.29: Principal membrane forces (for vertical loads).

(that for this reason cannot be vertical) and the consequent development of circumferential compressive forces in the upper ring. Thus, the simple introduction of the Coulomb friction law in the admissibility conditions requires some sort of consciousness to avoid considering ordinary situations like this as potentially unsafe. However, when the shear collapse is due to horizontal forces, the preceding considerations should be carefully reconsidered.

Equilibrium error evaluation

The error in the optimal solution of the equilibrium problem is evaluated as for the case of the spherical dome. The highest error is located close to the free boundary of the domain and it is equal to around 9% in a narrow region around the top of the dome (red region in Figure 5.30). This is likely due to a boundary layer effect in the numerical solution of the PDAE, a topic that will deserve further investigation. However, the error is very contained for our purpose given also the uncertainties in the evaluation of the load itself. Moreover, the error decreases very quickly going away from the free edge. To give an idea, the maximum error on each component in the range $3\,\mathrm{m} \leq z \leq 11.87\,\mathrm{m}$ is less than 1% (the green region on Figure 5.30). In addition, the global equilibrium of each ring delimited by two parallels is satisfied exactly except for truncation errors.

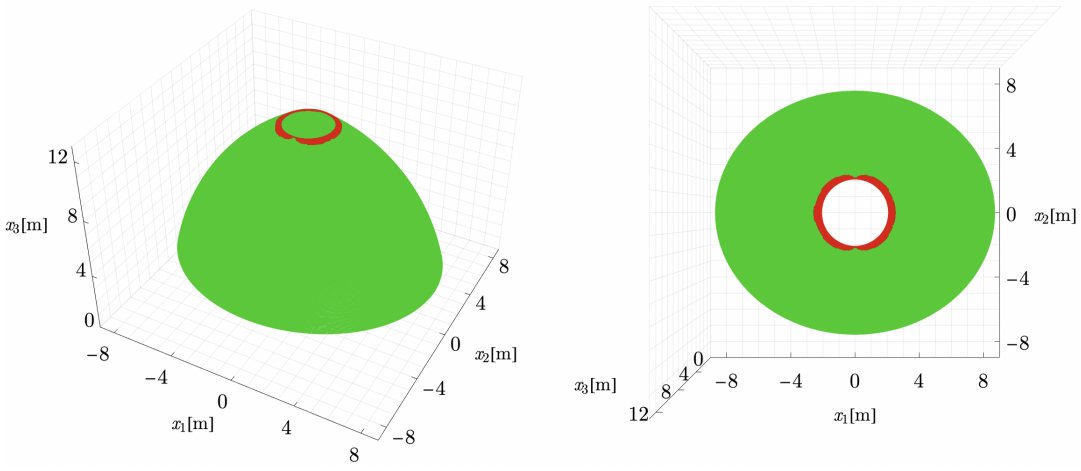

Figure 5.30: Maximum errors in the equilibrium equations.

The effect of a strengthening ring

The eccentricity diagrams that are shown in Figure 5.28 highlight that the highest values of the eccentricity are near the top opening, and this is due to the introduction of the boundary load as a pure vertical loading. As already said, if a strengthening ring is present around the opening or the dome can exchange internal forces with the overlying structures, it is possible for a horizontal thrust H_0 to develop as a boundary load. This is also well explained by Durand-Claye in [Durand-Claye, 1880], as shown in Figure 5.31. The effect of

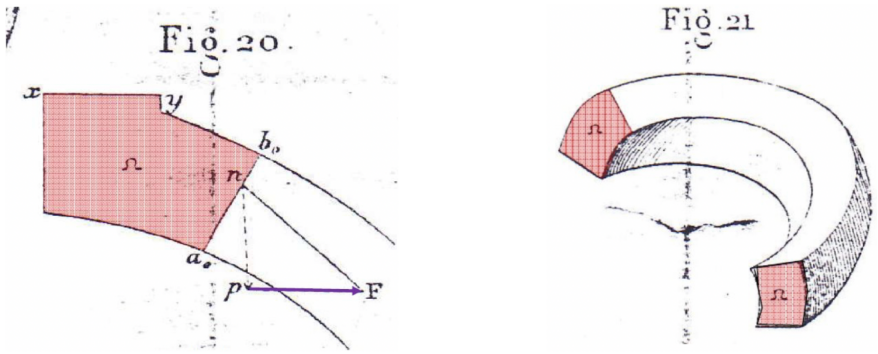

Figure 5.31: Horizontal component of boundary load due to what Durand-Claye called *anneau supérieure*, i.e. the strengthening ring (from [Durand-Claye, 1880], colours added to original).

such horizontal thrust is beneficial for the dome, as the eccentricity diagram may follow more closely the middle surface of the dome. By setting the horizontal thrust H_0 such that the resultant of the boundary load is tangent to the middle surface near the oculus, the analysis yields a solution that is better than the previous one in terms of the maximum eccentricity, as shown in Figure 5.32. In this case, the maximum of the absolute value of the eccentricity is only 3.3 cm and thus the minimum thickness is just 6.6 cm resulting in a GSF equal to 9.1. Obviously, this is an ideal situation in which the thrust assumes an optimal value, but

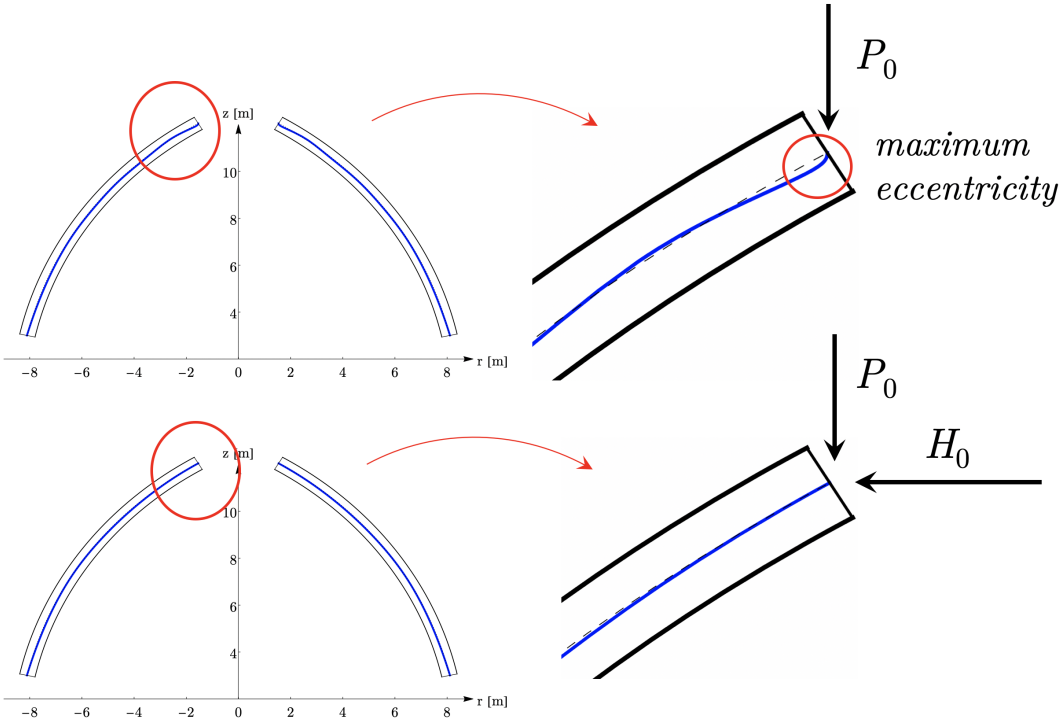

Figure 5.32: Differences between the eccentricity diagrams with and without horizontal thrust.

it shows the beneficial effect that a strengthening ring may have on the safety of the dome.

5.2.2 Maximum lateral load multiplier for horizontal loads

The second set of analyses is carried out considering the dome subjected both to vertical and horizontal loads, as shown in Figure 5.33. The horizontal loads act along the r axis, rotated

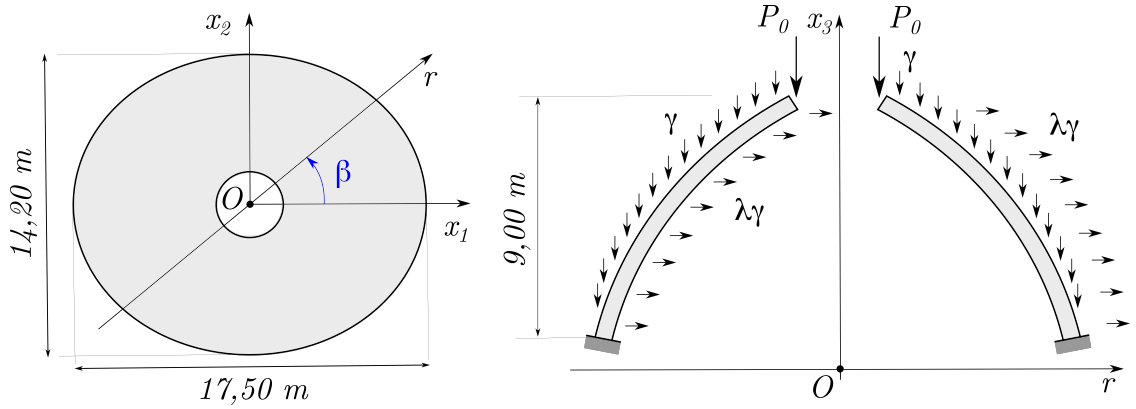

Figure 5.33: Scheme of the mechanical problem: dome of Pisa Cathedral under vertical and horizontal loads.

by an angle β with respect to the x_1 axis. The analyses are carried out by maximising λ

adopting, as a first hypothesis, the M1 model. Then, some considerations regarding the influence of a limited compressive and shear strength are carried out.

Convergence analysis

Also for the case of horizontal loads, the analyses are carried out for different numbers of basis functions in order to check the convergence of the method. As shown in Figure 5.34, by increasing the number of basis functions the maximum lateral load multiplier increases as expected, but with a slow trend, while the time taken by the optimisation routine increases more sensibly. The solution described in the following corresponds to the point with 45 basis functions, which represents a good compromise between accuracy achieved and time taken.

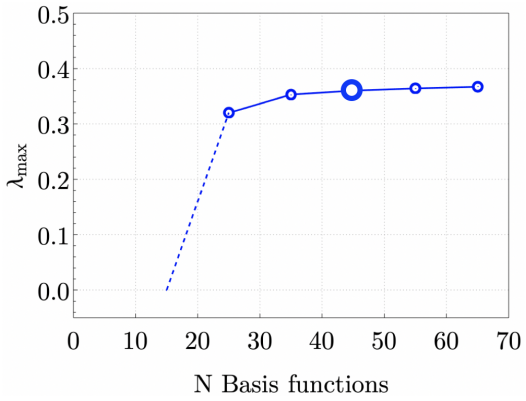

Figure 5.34: Convergence analysis: number of basis functions vs maximum lateral load multiplier.

The optimised generalised internal force field

The solution has been obtained by setting $n = 2$ and $m = 4$ for t^{11} and setting $m^{11} = 0$. This is due to the fact that the solution is more and more irregular as the basis functions for the hoop bending moment increase. In solving problem P2, the thickness of the dome is set to the real thickness in order to maximise the lateral load multiplier. The problem involves 45 basis functions for the normal hoop force redundant component and thus a total of 45 coefficients to be optimised. The optimisation grid has 20×40 equally spaced points. The optimal values of the parameters which are different from zero (45 in total) are shown in Table 5.4 and the optimal value of the lateral load multiplier is $\lambda_{max} = 0.360$.

Since the dome is not axisymmetric, the maximum lateral load multiplier changes with the direction of the horizontal actions, as shown in Figure 5.35. The solution in the case $\beta = 0°$ (horizontal actions along the x_1 direction), for which the maximum lateral load multiplier is $\lambda_{max} = 0.360$, is shown in the following. Concerning these results, it should be noticed that, even in the most restrictive case, where the horizontal loads are oriented in the weaker direction of the dome, the maximum lateral load multiplier is $\lambda_{max} = 0.245$, a value that is likely larger than the maximum real one of the earthquakes that could have interested the structure since its building in the 12^{th} century. This may be indicative of how reliance

$U_{(1,1)} = -99,515$	$U_{(1,2)} = 164,490$	$U_{(1,3)} = -10,898$	$U_{(1,4)} = -33,185$
$U_{(1,5)} = 1,290$	$U_{(1,6)} = 10,252$	$U_{(1,7)} = 92,953$	$U_{(1,8)} = -5,556$
$U_{(1,9)} = -5,868$	$U_{(2,1)} = 0,012$	$U_{(2,2)} = -0,031$	$U_{(2,3)} = -0,065$
$U_{(2,4)} = 0,007$	$U_{(2,5)} = 0,009$	$U_{(2,6)} = 0,054$	$U_{(2,7)} = -0,018$
$U_{(2,8)} = -0,037$	$U_{(2,9)} = 0,001$	$U_{(3,1)} = -0,161$	$U_{(3,2)} = 0,272$
$U_{(3,3)} = 0,032$	$U_{(3,4)} = -0,059$	$U_{(3,5)} = -0,004$	$U_{(3,6)} = -0,027$
$U_{(3,7)} = 0,159$	$U_{(3,8)} = 0,018$	$U_{(3,9)} = -0,011$	$U_{(4,1)} = 100,526$
$U_{(4,2)} = -168,360$	$U_{(4,3)} = 1,736$	$U_{(4,4)} = 36,992$	$U_{(4,5)} = -0,539$
$U_{(4,6)} = -1,615$	$U_{(4,7)} = -98,412$	$U_{(4,8)} = 1,417$	$U_{(4,9)} = 6,854$
$U_{(5,1)} = -49,317$	$U_{(5,2)} = 83,627$	$U_{(5,3)} = -2,240$	$U_{(5,4)} = -18,613$
$U_{(5,5)} = 0,571$	$U_{(5,6)} = 1,527$	$U_{(5,7)} = 49,409$	$U_{(5,8)} = -1,820$
$U_{(5,9)} = -3,334$			

Table 5.4: Dome of Pisa Cathedral under vertical and horizontal loads: optimal values of the coefficients.

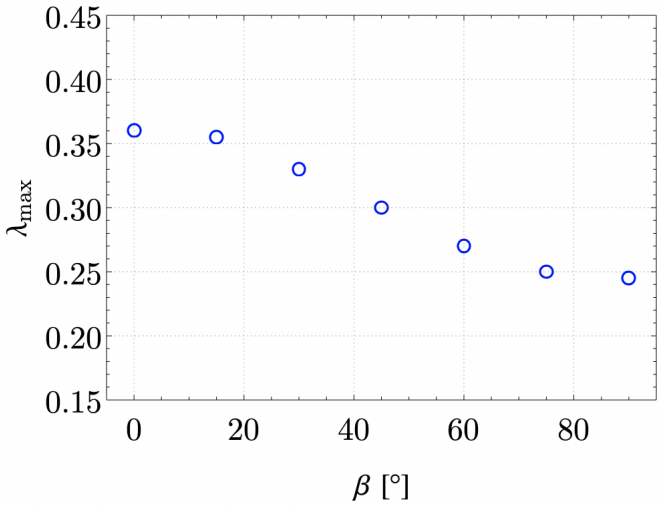

Figure 5.35: Maximum lateral load multiplier as a function of β.

on the shell resources of the masonry dome is essential when particular types of loads act on the structure.

The membrane force components, the transverse shear components and the moment components are shown in Figure 5.36, Figure 5.37 and Figure 5.38 respectively. Two vertical sections of the force fields diagrams are also shown in Figure 5.39 and Figure 5.40. The distributions of the internal forces at $z = 4\,\mathrm{m}$ and at $z = 8\,\mathrm{m}$ are shown in the diagrams plotted in Figure 5.41 and Figure 5.42 respectively.

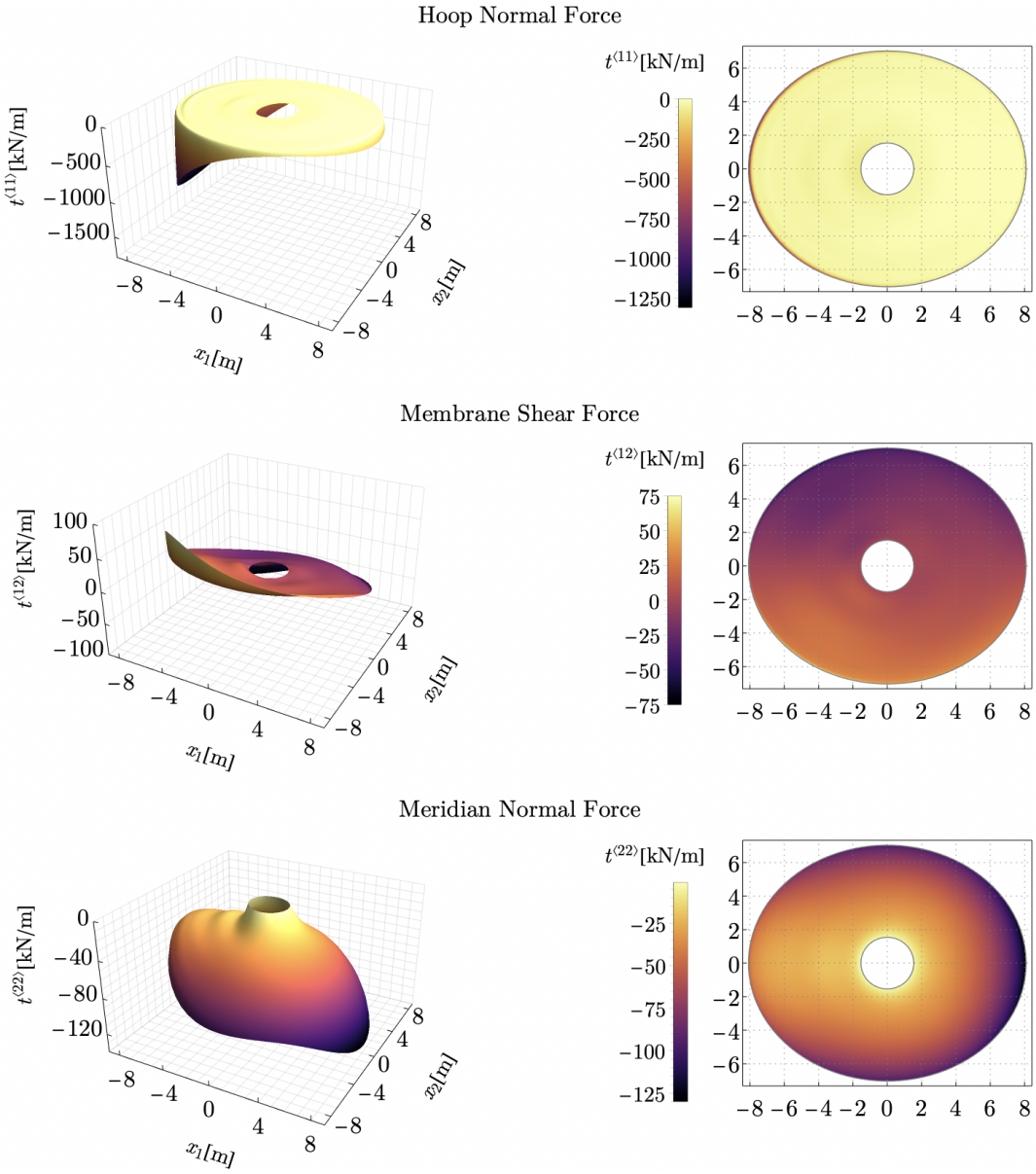

Figure 5.36: Dome of Pisa Cathedral under vertical and horizontal loads: optimal membrane force components.

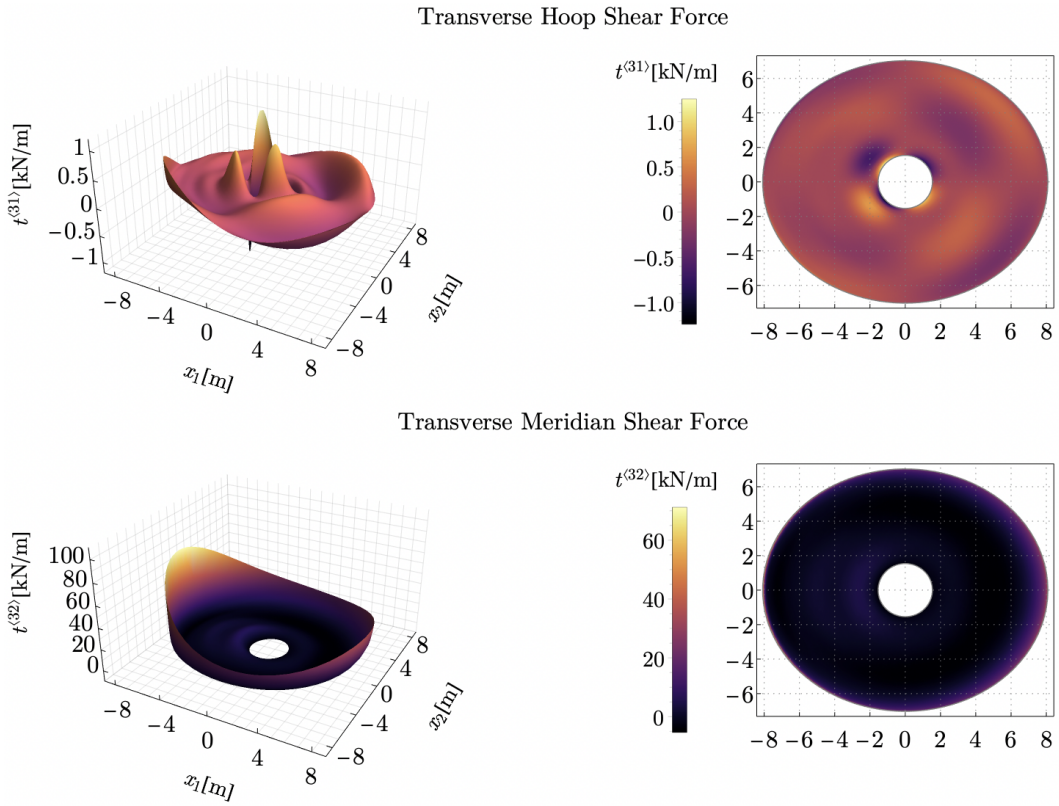

Figure 5.37: Dome of Pisa Cathedral under vertical and horizontal loads: optimal transverse shear components.

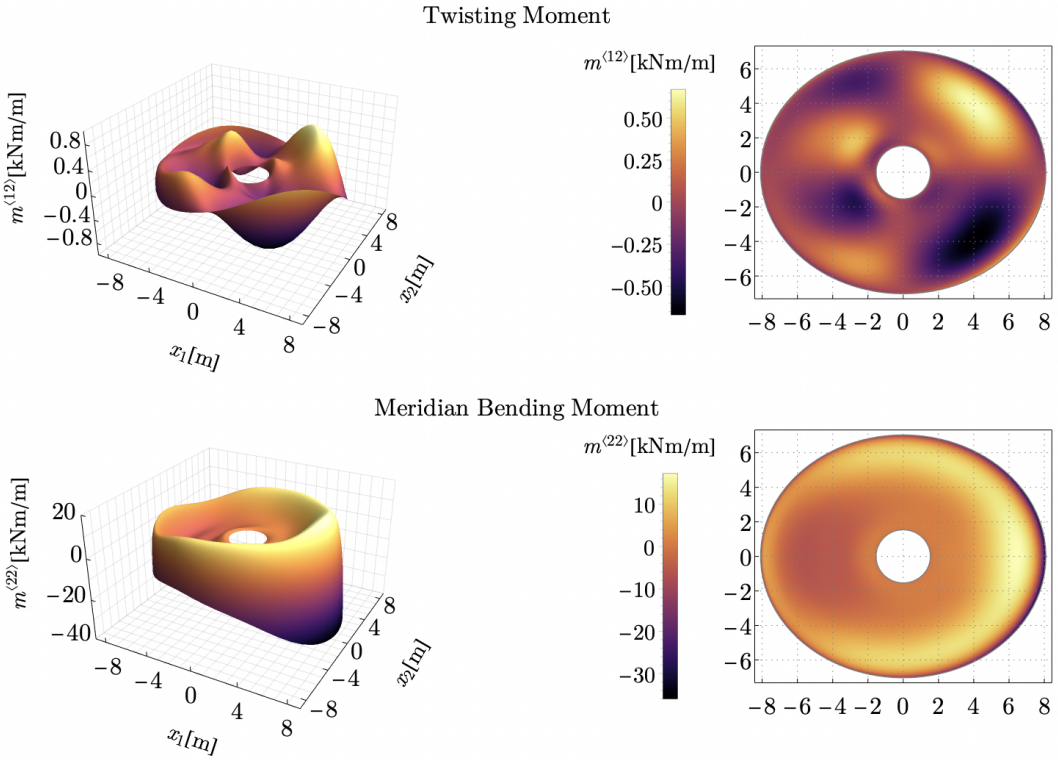

Figure 5.38: Dome of Pisa Cathedral under vertical and horizontal loads: optimal moment components.

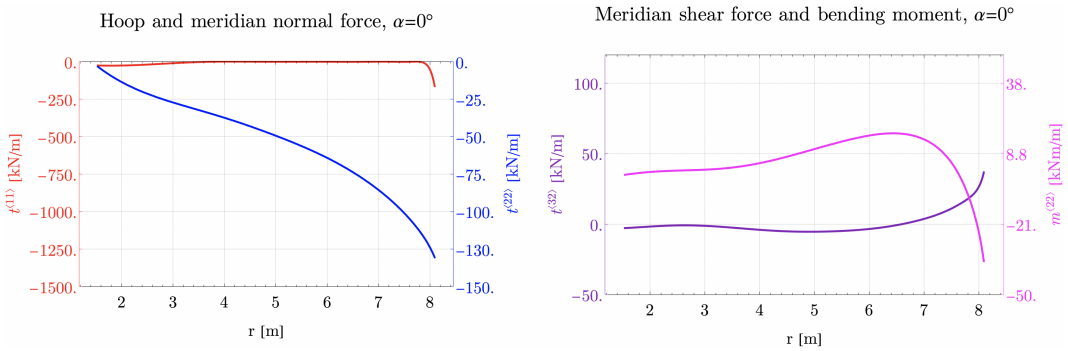

Figure 5.39: Membrane normal forces (left), meridian transverse shear and meridian bending moment (right) on the vertical section $\alpha = 0°$ ($r = x_1$).

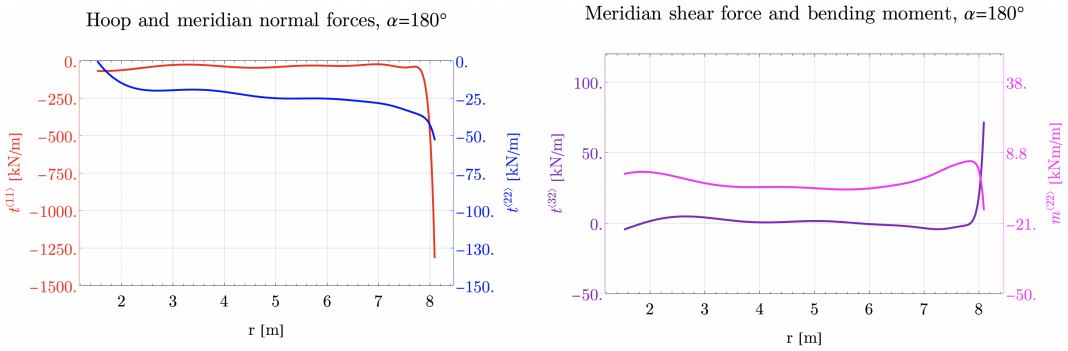

Figure 5.40: Membrane normal forces (left), meridian transverse shear and meridian bending moment (right) on the vertical section $\alpha = 180°$ ($r = -x_1$).

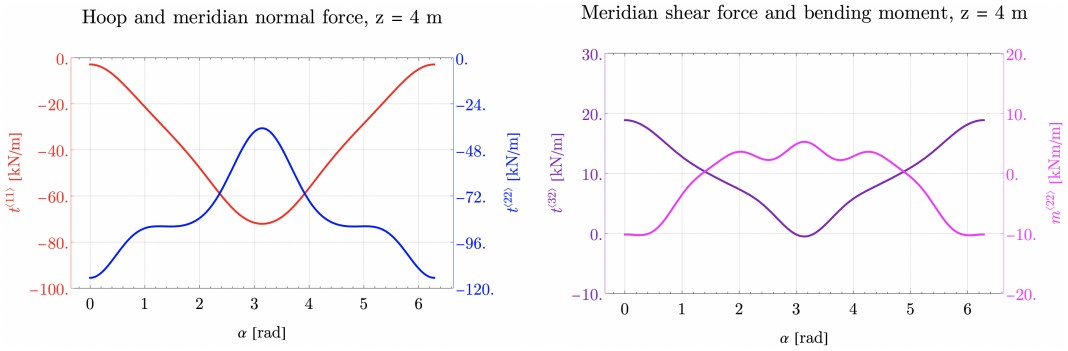

Figure 5.41: Membrane normal forces (left), meridian transverse shear and meridian bending moment (right) on $z = 4\,\mathrm{m}$.

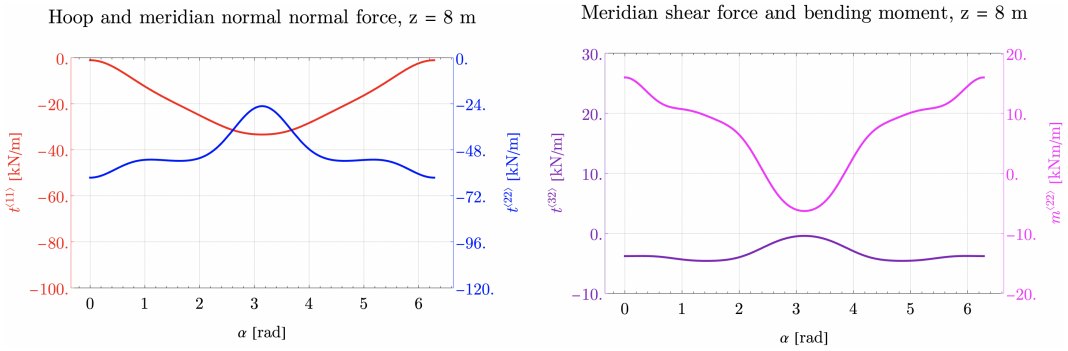

Figure 5.42: Membrane normal forces (left), meridian transverse shear and meridian bending moment (right) on $z = 8\,\mathrm{m}$.

Admissibility conditions: eccentricity and principal membrane forces

The diagram of the maximum modulus eccentricity surface on two vertical sections on major and minor axes is shown in Figure 5.43. Even for this load condition, as expected, the

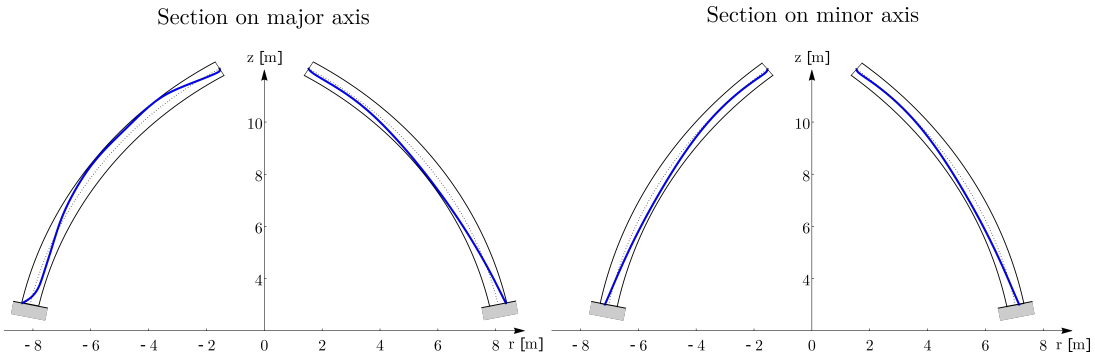

Figure 5.43: Maximum modulus eccentricity surface on two vertical sections at $\alpha = 0°$ (left) and $\alpha = 90°$ (right).

principal membrane forces are compressive, as shown in Figure 5.44.

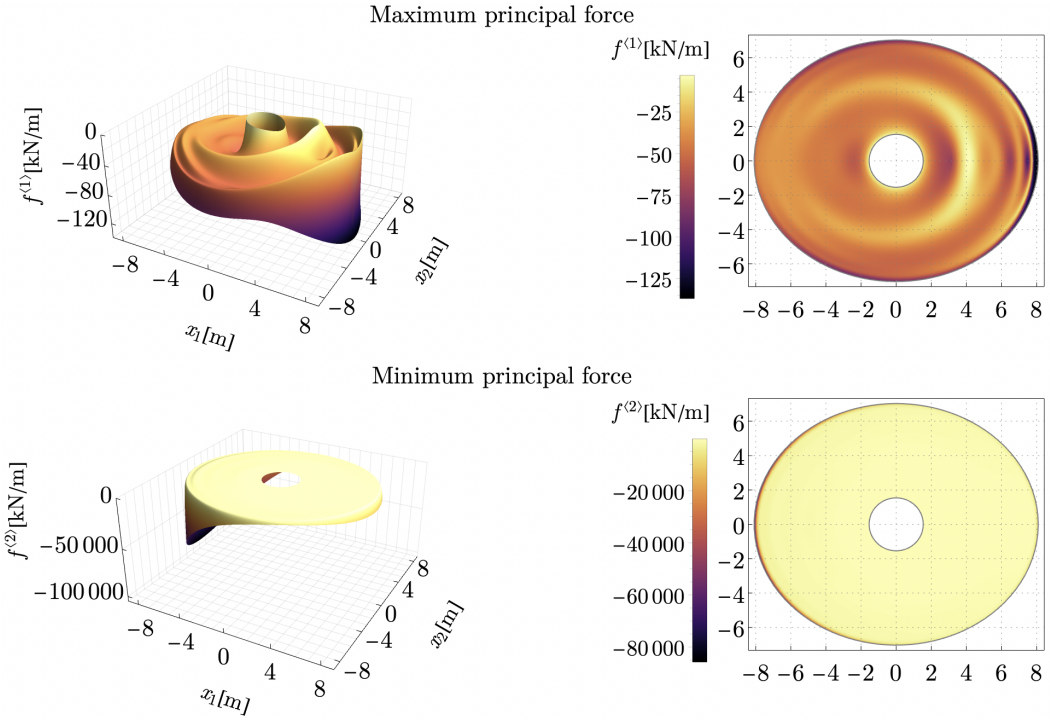

Figure 5.44: Principal membrane forces (for vertical and horizontal loads).

Equilibrium error evaluation

The error in the optimal solution of the equilibrium problem for $\beta = 0°$ and M1 model is evaluated in the same way for vertical loads. The highest error is located close to the free

boundaries of the domain and at the base and it is equal to 7% in a narrow region around the top of the dome and at the base (red regions in Figure 5.45). Moreover, the error decreases very quickly going away from the red regions. To give an idea, the maximum error on each component is less than 1% in the green region on Figure 5.45.

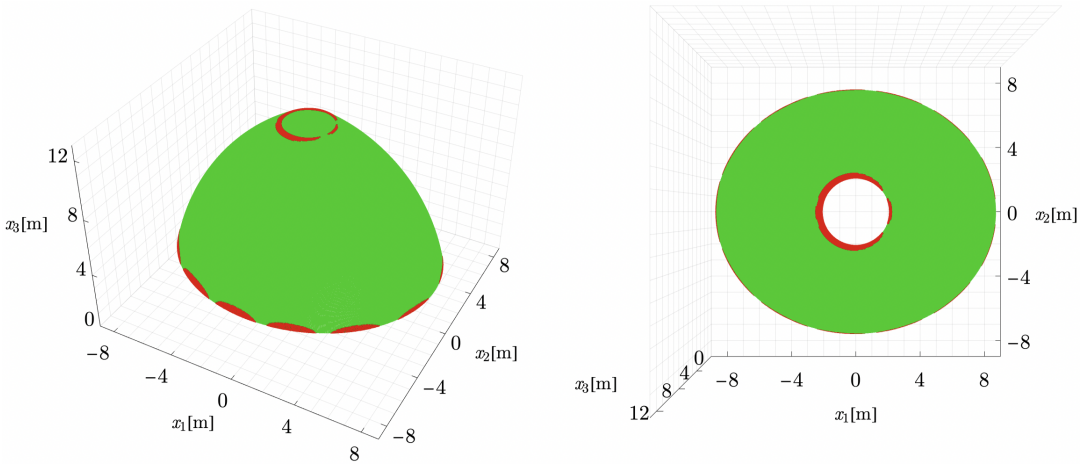

Figure 5.45: Maximum errors in the equilibrium equations.

Influence of a limited compressive strength

In case of horizontal loads, the optimal solution found by adopting the material model M1 is perfectly admissible. However, from a physical point of view, the maximum compressive stress turns out to be greater than 140 MPa which is out of reach of any masonry material. For this reason, a solution for which the maximum stress is lower than a certain value is sought. To this end, the optimisation problem (4.73) is slightly modified by adding a constraint on the maximum compressive force (adopting the M3 model). In particular, $t^{\langle 11\rangle} \geq \hat{t}^{\langle 11\rangle}$ is set, where $\hat{t}^{\langle 11\rangle}$ is a (negative) limit value on the hoop normal compressive force. By performing the analysis for different values of $\hat{t}^{\langle 11\rangle}$ the maximum stress is reduced as shown in Table 5.5. It is observed that in the range $(-50\,\mathrm{kN\,m^{-1}}, -30\,\mathrm{kN\,m^{-1}})$ the maximum lateral

$\hat{t}^{\langle 11\rangle}$	σ_{min}	λ_{max}
$-300\,\mathrm{kN\,m^{-1}}$	$-32\,\mathrm{MPa}$	0,360
$-100\,\mathrm{kN\,m^{-1}}$	$-11\,\mathrm{MPa}$	0,355
$-50\,\mathrm{kN\,m^{-1}}$	$-5\,\mathrm{MPa}$	0,345
$-30\,\mathrm{kN\,m^{-1}}$	$-3\,\mathrm{MPa}$	0,110

Table 5.5: Maximum stress as a function of $\hat{t}^{\langle 11\rangle}$ with $h = 30\,\mathrm{cm}$.

load multiplier decreases rapidly while the maximum stress decreases more slowly. This may be indicative of the fact that a compressive strength between 3 and 5 MPa may be required, at least locally, in order to make equilibrium to the external loads and is, therefore, a sign

that the actual compressive strength, which is not an issue in the case of vertical loads, may be important when horizontal loads act on the dome.

Influence of the shear resistance

The shear strength for the generalised internal force field illustrated before is such that the required friction coefficient would be larger than unity. To evaluate the influence of the shear strength on the maximum lateral load multiplier, the M2 model is adopted to carry out the analysis. Based on the considerations on the shear strength in Chapter 3, the shear failure criterion is required to be satisfied only along the meridian direction with zero cohesion. For the case in which horizontal loads are directed along the x_1 axis, i.e. $\beta = 0°$, Table 5.6 shows the maximum lateral load multiplier as a function of the friction coefficient. As it is seen,

ϕ	25°	30°	35°	40°	45°
μ	0,47	0,58	0,70	0,84	1,00
λ_{max}	0,100	0,114	0,130	0,148	0,168

Table 5.6: Maximum lateral load multiplier as a function of the friction angle for $\beta = 0°$.

the maximum lateral load multiplier in case the shear strength is bounded is significantly lower than the one that has been found with the M1 model.

In case the horizontal actions act along the x_2 axis, i.e. $\beta = 90°$, and assuming the friction angle equal to $\phi = 35°$, the maximum lateral load multiplier is $\lambda_{max} = 0.120$, which is close to the case of $\beta = 0°$. This shows that when the shear resistance is the condition that leads to collapse the lateral load multiplier is little influenced by the direction of the horizontal loads despite the fact that the dome' shape is not axisymmetric.

Statically admissible generalised internal force field for limited compressive and shear strength

Assuming the material has bounded compressive and shear strength (that is, by adopting the M4 model), one is interested in finding the maximum lateral load multiplier corresponding to a stable condition. Assuming the compressive strength equal to $f_c^{min} = -6\,\text{MPa}$ and the friction angle equal to $\phi = 35°$, the analyses are carried out for the weaker direction of the horizontal loads, $\beta = 90°$. The maximum lateral load multiplier satisfying all constraints is $\lambda_{max} = 0.120$ with the maximum compressive stress equal to $|\sigma_{min}| = 5.5\,\text{MPa}$. It is seen how the maximum lateral load multiplier is equal to the case of M2 model. This multiplier, although much less than the one found neglecting both compressive and shear strength, is more in line with the maximum expected peak ground acceleration in the Pisa area, and, despite all the restrictions on the material, it is higher by more than 50 % of the maximum found with TNA and TSA, which instead are carried out assuming Heyman's hypotheses.

5.3 Summary and conclusive remarks

The SASF method, introduced in Chapter 4, has been employed for the analysis of two case studies: the spherical dome and the dome of Pisa Cathedral. The method has proven able to provide useful estimations about the dome's safety level under different hypotheses on the material. Firstly, the analyses have been carried out with and without horizontal loads, assuming the M1 model. Then, some considerations on Heyman's hypotheses have been added for the case of the dome of Pisa Cathedral. It is recognised that the results obtained have consistently improved with respect to those obtained with both the application of TNA and TSA. This is likely due to the fact that the method removes important limitations of both techniques, considering all the resources of the shell for making equilibrium to the external loads. Moreover, also the evaluation of the influence of different hypotheses on the material resistance has been taken into account, highlighting that compressive and shear strength could both play a crucial role in the evaluation of the safety level of a dome subjected to horizontal actions.

Conclusions

The present thesis addressed the safety assessment of masonry domes with respect to possible collapse conditions. The theoretical and numerical studies mainly focused on the investigation of analysis methods operating within the framework of limit analysis. The domes were considered loaded upon by both vertical and horizontal force distributions: the former accounted for gravitational loads, while the latter were thought as representative in some sense of the seismic actions. The dome shapes considered in the thesis went far beyond the basic case in which the dome is shaped like a 'solid of revolution'. More complex forms were addressed as, for example, the oval-shaped domes, which required further effort to adapt and refine the analytical tools and numerical techniques needed for studying their stability.

The thesis refers to the rich and nowadays still active stream of research that has been developing in Europe over the last three centuries to address and solve the problem of determining the safety level of masonry domes against possible collapse. In this regard, a historical review of the approaches used since the 17^{th} century has been conducted, alongside with a concise survey of the recent literature on the subject. The review culminated with Jacques Heyman's seminal contribution by showing how most historical approaches find their theoretical justification in the context of the modern formulation of limit analysis and how, for this reason, they could be usefully revised and adopted even nowadays.

Two analysis methods drawn from the literature were critically investigated: the Thrust Network Analysis and the Thrust Surface Analysis. The two well-established methods, which are often employed today for the limit analysis of masonry vaulted structures, were presented along with the mechanical hypotheses they are based on. Since in the literature these two methods are sometimes thought to have common aspects, a question that arises naturally is whether the two methods are somehow related and, if so, under what assumptions the correlation holds. To investigate this issue a detailed comparison between TNA and TSA was conducted, which represents one of the original parts of the thesis. The analysis confirmed that the joints between blocks in the TNA must be vertical in order for the two methods to be theoretically comparable. Under this hypothesis, the relationships linking thrust networks to thrust surfaces were investigated to check the feasibility in practice of a possible method combining thrust networks and thrust surfaces.

Starting from a subdivision of the dome into a finite number of the blocks, the results obtained from the TNA were used to identify a thrust surface. Specifically, the closeness to the centres of pressure identified by TNA is used as a criterion to select a surface, among some predetermined classes, that could be thought of as 'corresponding' to the original thrust network. The proposed methodology has been applied to the case in which the dome of Pisa Cathedral is subjected to vertical loads only. The analyses clearly have shown that

the closeness of the surface to the centres of pressure doesn't ensure its admissibility and that a decisive role is played by the surface's shape. Furthermore, a comparison of the equilibrium states defined by the thrust network and the admissible thrust surface that most closely approximates the centres of pressure showed appreciable differences in the distribution of internal forces, even though the network and surface are geometrically very close. In conclusion, the illustrated counterexample seems to raise major doubts about the possibility of establishing in practice a correspondence between the network and the surface, when considering the dome as a set of blocks of finite size and thus, that a combined use of the two techniques is not easily exploitable. However, there remain some aspects that deserve further investigation. One of them is whether a more refined criterion including, for example, surface curvatures, can be set up to identify admissible surfaces starting from optimised thrust networks. Another issue is whether optimised solutions obtained from independent applications of TNA and TSA could yield closer equilibrium states.

The investigation on TNA and TSA methods was concluded by applying them to the case in which the dome of Pisa cathedral is subjected to horizontal as well as vertical loads. The analyses showed that the restrictions imposed on the equilibrium states that can be explored by these two methods lead to unsatisfactory estimates of the maximum collapse multiplier. This is the main reason why the rest of the research work presented in this thesis has been addressed to the development of a new analysis method, able to overcome these limitations.

The proposed method models the dome as a thin shell and, like TNA and TSA, it is able to cope with domes having generic shapes, not necessarily axisymmetric. The adoption of a thin shell model has been accurately motivated and the hypotheses on which the method is based were highlighted. The classical theory of thin shells has been recalled in detail as well as the fundamental theorems of limit analysis, which have been further specialised to the case of shells. Different failure criteria have been considered to evaluate the influence of different material assumptions on the results. The method searches for an optimal distribution of internal shell forces to assess the safety of the dome by virtue of the static theorem of limit analysis. The adopted procedure is inspired by the well-known flexibility method used to solve statically indeterminate beam systems. The equilibrium problem for a shell, which is always statically indeterminate, is rendered determinate by choosing a certain number of redundant force components and expressing them as a series of known functions. The equilibrium problem for the effective system is solved in terms of the coefficient of the series, by considering the redundant forces as external loads and by exploiting the linearity of the system. Three techniques have been employed to solve the equilibrium sub-problems. A finite-differences scheme has been specifically developed for domes expressed in cylindrical coordinates. Moreover, by exploiting the symbolic computation capability of *Mathematica*®, the collocation method has also been implemented. Finally, the results obtained have been compared with the ones obtained by the finite element method. All three methods showed good agreement in the results. The good convergence properties of the finite difference scheme and collocation method have been verified. Once the effective system has been solved, the procedure finds the values of the coefficients of the series by setting up an optimisation problem, which minimises a certain cost function related to the safety factor.

The method has been applied to two case studies: the dome of Pisa Cathedral and the spherical dome. The minimum admissible thickness turned out to be as low as 11 cm for the

dome of Pisa Cathedral in the case it is loaded upon by vertical actions only. Compared to the dome's actual thickness of 60 cm, this result yields a lower bound estimate of the geometric safety factor for vertical loads equal to roughly 5.5. The comparison of this result, with some previous estimates obtained through the application of the TSA, showed that the change in the structural scheme has a significant effect on the geometric safety factor, which resulted more than tripled. It has also been shown that a reinforcing ring placed around the opening can have a beneficial effect on the safety of the dome. Indeed, assuming a sufficiently high horizontal thrust at the crown (made possible by assuming a state of uniform compression in the reinforcing ring), the minimum thickness falls down to 6.6 centimetres, i.e., the surface of the maximum eccentricities deviates a little more than 3 centimetres from the average surface. The possibility for the dome to make equilibrium to the vertical loads by membrane internal forces suggests that the form chosen by the builders of the dome of Pisa cathedral is particularly suited to cope with gravitational loads and that the master builders of the time possessed a profound knowledge, resulting from intuition and experience, of the mechanics of these structures.

In the case of a spherical dome with a top opening subjected to vertical loads, the minimum thickness was found to be 4.7 % of the radius when the width of the top opening is 1.5 metres. This result is very close to Heyman's minimum theoretical thickness of 4.2 % of the radius for the case of a spherical dome with a closed top. Nevertheless, strong differences are observed between the distribution of the internal forces in the two cases. A first set of analyses has been carried out under the standard Heyman's hypotheses for horizontal loads. The maximum lateral load multiplier for the open spherical dome resulted to be $\lambda_{max} = 0.166$. The maximum collapse multiplier obtained for the dome of Pisa Cathedral lies within the range $\lambda_{max} = 0.24 - 0.36$, depending on the direction of the loads as the dome is not axisymmetric.

For the case study of the dome of Pisa Cathedral, a parametric analysis of the maximum lateral load multiplier was performed by relaxing Heyman's hypotheses, i.e., by varying the compressive and shear strength. The results obtained seem to show that it can be individuated a threshold value for the compressive strength, of the order of common masonry compressive strength values, above which the horizontal load multiplier is practically unaffected. On the contrary, for compressive strength below the threshold value, an abrupt drop in the horizontal load multiplier is observed. This finding suggests that when the masonry of the dome is weak or strongly damaged greater care should be taken in assessing the collapse of the dome. The maximum collapse multiplier resulted to be considerably affected by the limited shear strength of the masonry. As a first step towards the definition of a suitable shear failure criterion, the classical Mohr-Coulomb criterion was adopted along the directions orthogonal to uninterrupted mortar joints, which for the case study coincided with the meridians.

The limitation on the shear strength led to a significant decrease in the maximum horizontal multiplier, which turned out to be more sensitive to the friction angle than to the direction of the external load. In other words, for dominant horizontal actions, it seems that the shear strength cannot be fully disregarded, at least in some cases, when assessing the dome collapse. However, the most restrictive collapse multiplier estimate, obtained in the case both shear and compressive strength are limited, was equal to $\lambda_{max} = 0.120$. This value is about 50 % higher than those obtained with TNA and TSA, performed under the less

restrictive classical Heyman assumptions.

In conclusion, the methodological choice of modelling the dome as a shell seems to widen considerably the set of equilibrium configurations that can be effectively exploited for the safety assessment of the dome by means of the static theorem of limit analysis. The possibilities offered by the suitable combination of shell membrane and bending forces enable yielding a consistent increase in the safety factors compared to previous estimates determined by established methods working within the framework of limit analysis.

The expressly developed method can be applied to domes and vaults of arbitrary shape and general load distributions. The results obtained represent the first validation step of the method but are by no means ultimate. Further work will be devoted to improving the method by refining the optimisation procedure that searches for the maximum values of the safety factor. Moreover, the next steps of the research will address a thorough investigation of the safety assessment of domes under horizontal loads, as well as a comparison between theoretical and experimental results.

References

[Abeyartne, 2012] Abeyartne, R. (2012). Continuum mechanics volume II of Lecture Notes on The Mechanics of Elastic Solids. *web. mit. edu/abeyartne/lecture_ notes. html*, 11.

[Aita, 2003] Aita, D. (2003). *Analisi elastica non lineare e collasso di strutture ad arco in muratura*. PhD thesis, Università di Pisa.

[Aita et al., 2017a] Aita, D., Barsotti, R., and Bennati, S. (2017a). Explicit solutions for depressed masonry arches loaded until collapse — part I: a one-dimensional nonlinear elastic model. *Meccanica*, 52(4-5):989–1001.

[Aita et al., 2017b] Aita, D., Barsotti, R., and Bennati, S. (2017b). Explicit solutions for depressed masonry arches loaded until collapse — part II: a solution method for statically indeterminate systems. *Meccanica*, 52(4-5):1093–1106.

[Aita et al., 2017c] Aita, D., Barsotti, R., and Bennati, S. (2017c). A modern reinterpretation of Durand-Claye's method for the study of equilibrium conditions of masonry domes. In *AIMETA 2017-XXIII Conference The Italian Association of Theoretical and Applied Mechanics*, volume 3, pages 1459–1471. GECHI EDIZIONI.

[Aita et al., 2019] Aita, D., Barsotti, R., and Bennati, S. (2019). Studying the dome of Pisa cathedral via a modern reinterpretation of Durand-Claye's method. *Journal of Mechanics of Materials and Structures*, 14(5):603–619.

[Aita et al., 2017d] Aita, D., Barsotti, R., Bennati, S., Caroti, G., and Piemonte, A. (2017d). 3-dimensional geometric survey and structural modelling of the dome of Pisa cathedral. *The International Archives of Photogrammetry, Remote Sensing and Spatial Information Sciences*, 42:39.

[Angelillo et al., 2013] Angelillo, M., Babilio, E., and Fortunato, A. (2013). Singular stress fields for masonry-like vaults. *Continuum Mechanics and Thermodynamics*, 25(2):423–441.

[Angelillo et al., 2010] Angelillo, M., Cardamone, L., and Fortunato, A. (2010). A numerical model for masonry-like structures. *Journal of Mechanics of Materials and Structures*, 5(4):583–615.

[Angelillo and Fortunato, 2004] Angelillo, M. and Fortunato, A. (2004). Equilibrium of masonry vaults. In *Novel approaches in civil engineering*, pages 105–111. Springer.

[Anzellotti, 1985] Anzellotti, G. (1985). A class of convex non-coercive functionals and masonry-like materials. In *Annales de l'Institut Henri Poincaré C, Analyse non linéaire, Vol. 2*, volume 2, pages 261–307. Elsevier.

[Barsi et al., 2019] Barsi, F., Barsotti, R., and Bennati, S. (2019). Equilibrium of masonry sail vaults: the case study of a subterranean vault by Antonio da Sangallo the Elder in the "Fortezza Vecchia" in Livorno. In *Conference of the Italian Association of Theoretical and Applied Mechanics*, pages 2094–2103. Springer.

[Barsi et al., 2022] Barsi, F., Barsotti, R., and Bennati, S. (2022). Studying the equilibrium of oval-base pointed masonry domes: the case of Pisa cathedral. *International Journal of Masonry Research and Innovation*, 7(1-2):146–171.

[Barsotti and Bennati, 2018] Barsotti, R. and Bennati, S. (2018). A simple and effective nonlinear elastic one-dimensional model for the structural analysis of masonry arches. *Meccanica*, 53(7):1899–1915.

[Barsotti et al., 2017] Barsotti, R., Bennati, S., and Stagnari, R. (2017). Analytical determination of statically admissible thrust surfaces for the limit analysis of masonry vaults and domes. In *AIMETA 2017-XXIII Conference The Italian Association of Theoretical and Applied Mechanics*, volume 3, pages 1449–1458. GECHI Edizioni.

[Barsotti et al., 2021] Barsotti, R., Stagnari, R., and Bennati, S. (2021). Searching for admissible thrust surfaces in axial-symmetric masonry domes: Some first explicit solutions. *Engineering Structures*, 242:112547.

[Beatini et al., 2017] Beatini, V., Royer-Carfagni, G., and Tasora, A. (2017). A regularized non-smooth contact dynamics approach for architectural masonry structures. *Computers & Structures*, 187:88–100.

[Beatini et al., 2018] Beatini, V., Royer-Carfagni, G., and Tasora, A. (2018). The role of frictional contact of constituent blocks on the stability of masonry domes. *Proceedings of the Royal Society A: Mathematical, Physical and Engineering Sciences*, 474(2209):20170740.

[Becchi and Foce, 2002] Becchi, A. and Foce, F. (2002). *Degli archi e delle volte: arte del costruire tra meccanica e stereotomia*. Marsilio.

[Beltrami, 1882] Beltrami, E. (1882). Sull'equilibrio delle superficie flessibili ed inestendibili. *Memorie dell'Academia delle Scienze dell'Instituto di Bologna*, 3:217–265.

[Bennati et al., 2020] Bennati, S., Aita, D., Barsotti, R., Caroti, G., Chellini, G., Piemonte, A., Barsi, F., and Traverso, C. (2020). Survey, experimental tests and mechanical modelling of the dome of Pisa Cathedral: a multidisciplinary study. *International Journal of Masonry Research and Innovation*, 5(1):142–165.

[Benvenuto, 1991] Benvenuto, E. (1991). An introduction to the history of structural mechanics. volume ii: vaulted structures and elastic systems 1991; 307-554.

[Bigoni, 2012] Bigoni, D. (2012). *Nonlinear solid mechanics: bifurcation theory and material instability*. Cambridge University Press.

[Block and Ochsendorf, 2007] Block, P. and Ochsendorf, J. (2007). Thrust network analysis: a new methodology for three-dimensional equilibrium. *Journal of the International Association for shell and spatial structures*, 48(3):167–173.

[Block, 2009] Block, P. P. C. V. (2009). *Thrust network analysis: exploring three-dimensional equilibrium*. PhD thesis, Massachusetts Institute of Technology.

[Boothby, 2001] Boothby, T. E. (2001). Analysis of masonry arches and vaults. *Progress in Structural Engineering and materials*, 3(3):246–256.

[Bossut, 1778a] Bossut, C. (1778a). Nouvelles recherches sur l'équilibre des voûtes en dôme. *Mémoires de l'Académie Royale des Sciences de Paris*, 1778:587–596.

[Bossut, 1778b] Bossut, C. (1778b). Recherches sur l'équilibre des voûtes. *Mémoires de l'Académie Royale des Sciences de Paris*, pages 534–566.

[Bouguer, 1734] Bouguer, P. (1734). Sur les lignes courbes propres a former les voûtes en dome. *Mémoires de l'Académie Royale de Sciences de Paris*, pages 149–166.

[Chappuis, 1976] Chappuis, R. (1976). Utilisation du tracé ovale dans l'architecture des églises romanes. *Bulletin Monumental*, 134(1):7–36.

[Chen and Bagi, 2020] Chen, S. and Bagi, K. (2020). Crosswise tensile resistance of masonry patterns due to contact friction. *Proceedings of the Royal Society A*, 476(2240):20200439.

[Como, 2013] Como, M. (2013). *Statics of historic masonry constructions*, volume 1. Springer.

[Cosserat and Cosserat, 1909] Cosserat, E. and Cosserat, F. (1909). Theorie des corps deformables, paris: A. *Hermann et fils*.

[Cundall and Strack, 1979] Cundall, P. A. and Strack, O. D. (1979). A discrete numerical model for granular assemblies. *Geotechnique*, 29(1):47–65.

[Davini, 1993] Davini, C. (1993). *Lezioni sulla teoria dei gusci*. Istituto di Meccanica Teorica ed Applicata.

[De Chiara et al., 2019] De Chiara, E., Cennamo, C., Gesualdo, A., Montanino, A., Olivieri, C., and Fortunato, A. (2019). Automatic generation of statically admissible stress fields in masonry vaults. *Journal of Mechanics of Materials and Structures*, 14(5):719–737.

[Del Piero, 1989] Del Piero, G. (1989). Constitutive equation and compatibility of the external loads for linear elastic masonry-like materials. *Meccanica*, 24(3):150–162.

[Del Piero, 1998] Del Piero, G. (1998). Limit analysis and no-tension materials. *International Journal of Plasticity*, 14(1-3):259–271.

[Di Carlo et al., 2018] Di Carlo, F., Coccia, S., and Rinaldi, Z. (2018). Collapse load of a masonry arch after actual displacements of the supports. *Archive of Applied Mechanics*, 88(9):1545–1558.

[Di Pasquale, 1984] Di Pasquale, S. (1984). *Statica dei solidi murari: teoria ed esperienze*. Dipartimento di costruzioni.

[Drougkas et al., 2016] Drougkas, A., Roca, P., and Molins, C. (2016). Nonlinear micromechanical analysis of masonry periodic unit cells. *International Journal of Solids and Structures*, 80:193–211.

[Durand-Claye, 1866] Durand-Claye, A. (1866). *Note sur la vérification de la stabilité des voûtes de maçonnerie et sur l'emploi des courbes de pression*. E. Thunot.

[Durand-Claye, 1880] Durand-Claye, A. (1880). Vérification de la stabilité des voûtes et des arcs. application aux voûtes sphériques. In *Annales des ponts et chaussées*, volume 19, pages 416–440.

[Eddy, 1878] Eddy, H. T. (1878). *Researches in graphical statics*. D. van Nostrand.

[Ericksen, 1961] Ericksen, J. L. (1961). Conservation laws for liquid crystals. *Transactions of the Society of Rheology*, 5(1):23–34.

[Eringen, 2002] Eringen, A. C. (2002). *Nonlocal Continuum Field Theories*. Springer-Verlag New York.

[Fantin, 2017] Fantin, M. (2017). *Étude des rapports entre stéréotomie et résistance des voûtes clavées*. PhD thesis, Paris Est.

[Fantin and Ciblac, 2016] Fantin, M. and Ciblac, T. (2016). Extension of thrust network analysis with joints consideration and new equilibrium states. *International Journal of Space Structures*, 31(2-4):190–202.

[Fichera, 1973] Fichera, G. (1973). Boundary value problems of elasticity with unilateral constraints. In *Linear Theories of Elasticity and Thermoelasticity*, pages 391–424. Springer.

[Foce and Aita, 2003] Foce, F. and Aita, D. (2003). The masonry arch between «limit» and «elastic» analysis. a critical re-examination of Durand-Claye's method. In *Proceedings of the First International Congress on Construction History, Madrid*, pages 20–24.

[Fontana, 1694] Fontana, C. (1694). *Il Tempio Vaticano e la sua Origine*. Roma.

[Forgács et al., 2017] Forgács, T., Sarhosis, V., and Bagi, K. (2017). Minimum thickness of semi-circular skewed masonry arches. *Engineering Structures*, 140:317–336.

[Fraddosio et al., 2020] Fraddosio, A., Lepore, N., and Piccioni, M. D. (2020). Thrust surface method: An innovative approach for the three-dimensional lower bound limit analysis of masonry vaults. *Engineering Structures*, 202:109846.

[Fraternali, 2010] Fraternali, F. (2010). A thrust network approach to the equilibrium problem of unreinforced masonry vaults via polyhedral stress functions. *Mechanics Research Communications*, 37(2):198–204.

[Frézier, 1737] Frézier, A. (1737). *Théorie et pratique de la coupe des pierres et des bois pour la construction des voûtes et autres parties des bâtiments civils et militaires*, volume 1. J.-D. Doulsseker le fils.

[Fuentes, 2021] Fuentes, P. (2021). Graphical analysis of masonry domes. Historical approaches (1850–1920). In *History of Construction Cultures*, pages 394–401. CRC Press.

[Galassi et al., 2017] Galassi, S., Misseri, G., Rovero, L., and Tempesta, G. (2017). Equilibrium analysis of masonry domes. on the analytical interpretation of the Eddy-Lévy graphical method. *International Journal of Architectural Heritage*, 11(8):1195–1211.

[Giaquinta and Giusti, 1985] Giaquinta, M. and Giusti, E. (1985). Researches on the equilibrium of masonry structures. *Archive for Rational Mechanics and Analysis*, 88(4):359–392.

[Green and Laws, 1966] Green, A. E. and Laws, N. (1966). A general theory of rods. *Proceedings of the Royal Society of London. Series A. Mathematical and Physical Sciences*, 293(1433):145–155.

[Green et al., 1965] Green, A. E., Naghdi, P. M., and Wainwright, W. (1965). A general theory of a Cosserat surface. *Archive for Rational Mechanics and Analysis*, 20(4):287–308.

[Green and Zerna, 1992] Green, A. E. and Zerna, W. (1992). *Theoretical elasticity*. Courier Corporation.

[Grillanda et al., 2021] Grillanda, N., Chiozzi, A., Milani, G., and Tralli, A. (2021). Tilting plane tests for the ultimate shear capacity evaluation of perforated dry joint masonry panels. part I: Experimental tests. *Engineering Structures*, 238:112124.

[Gurtin et al., 2010] Gurtin, M. E., Fried, E., and Anand, L. (2010). *The mechanics and thermodynamics of continua*. Cambridge University Press.

[Heyman, 1966] Heyman, J. (1966). The stone skeleton. *International Journal of solids and structures*, 2(2):249–279.

[Heyman, 1967] Heyman, J. (1967). On shell solutions for masonry domes. *International Journal of Solids and Structures*, 3(2):227–241.

[Heyman, 1977] Heyman, J. (1977). *Equilibrium of shell structures*. Clarendon Press.

[Heyman, 2009] Heyman, J. (2009). La coupe des pierres. In *Third International Congress on Construction History, Brandenburg University of Technology Cottbus, Germany, 20th-24th May 2009*, page 1.

[Heyman, 2011] Heyman, J. (2011). The membrane analysis of thin masonry shells. In *Simposio internacional Bóveda tabicadas, Universidad Politécnica de Valencia*.

[Hooke, 1675] Hooke, R. (1675). The true mathematical and mechanical form of all manner of arches for buildings.

[Huerta, 2001] Huerta, S. (2001). *Mechanics of masonry vaults: The equilibrium approach*, pages 47–69. Universidade do Minho.

[Huerta, 2007] Huerta, S. (2007). Oval domes: History, geometry and mechanics. *Nexus Network Journal*, 9(2):211–248.

[Huerta, 2008] Huerta, S. (2008). The analysis of masonry architecture: A historical approach: To the memory of professor Henry J. Cowan. *Architectural Science Review*, 51(4):297–328.

[Huerta, 2010] Huerta, S. (2010). *Designing by Geometry. Rankine's Theorems of Transformation of Structures.*, pages 262–285. Outer Ediciones.

[Itskov, 2007] Itskov, M. (2007). *Tensor algebra and tensor analysis for engineers*. Springer.

[Karush, 2014] Karush, W. (2014). Minima of functions of several variables with inequalities as side conditions. In *Traces and Emergence of Nonlinear Programming*, pages 217–245. Springer.

[Kohn and Temam, 1983] Kohn, R. and Temam, R. (1983). Dual spaces of stresses and strains, with applications to hencky plasticity. *Applied Mathematics and Optimization*, 10(1):1–35.

[Kreyszig, 1991] Kreyszig, E. (1991). *Differential Geometry*. Differential Geometry. Dover Publications.

[Kuhn, 1982] Kuhn, H. W. (1982). Nonlinear programming: a historical view. *ACM SIGMAP Bulletin*, 31:6–18.

[Kurrer, 2018] Kurrer, K.-E. (2018). *The history of the theory of structures: searching for equilibrium*. John Wiley & Sons.

[Lebon et al., 2008] Lebon, G., Jou, D., and Casas-Vázquez, J. (2008). *Understanding non-equilibrium thermodynamics*, volume 295. Springer.

[Lévy, 1888] Lévy, M. (1888). *La statique graphique et ses applications aux constructions*, volume 1. Gauthier-Villars.

[Lubliner, 2008] Lubliner, J. (2008). *Plasticity theory*. Courier Corporation.

[Lucchesi et al., 1999] Lucchesi, M., Padovani, C., Pasquinelli, G., and Zani, N. (1999). The maximum modulus eccentricities surface for masonry vaults and limit analysis. *Mathematics and Mechanics of Solids*, 4(1):71–87.

[Lucchesi et al., 2021] Lucchesi, M., Pintucchi, B., and Zani, N. (2021). Intersection of convex cones as stress range for plane normal elastic bodies. In *Proceedings of 1st International Conference on Structural Damage Modelling and Assessment*, pages 87–101. Springer.

[Marmo et al., 2018] Marmo, F., Masi, D., and Rosati, L. (2018). Thrust network analysis of masonry helical staircases. *International Journal of Architectural Heritage*, 12(5):828–848.

[Marmo and Rosati, 2017] Marmo, F. and Rosati, L. (2017). Reformulation and extension of the thrust network analysis. *Computers & Structures*, 182:104–118.

[Mascheroni, 1785] Mascheroni, L. (1785). *Nuove Ricerche sull'equilibrio delle Volte*. Per Francesco Locatelli.

[Matthies et al., 1979] Matthies, H., Strang, G., and Christiansen, E. (1979). The saddle point of a differential program (for elastic-plastic theory). *Energy methods in finite element analysis.(A 79-53076 24-39) Chichester, Sussex, England, Wiley-Interscience*, pages 309–318.

[Milani et al., 2008] Milani, E., Milani, G., and Tralli, A. (2008). Limit analysis of masonry vaults by means of curved shell finite elements and homogenization. *International Journal of solids and structures*, 45(20):5258–5288.

[Milani and Cecchi, 2013] Milani, G. and Cecchi, A. (2013). Compatible model for herringbone bond masonry: Linear elastic homogenization, failure surfaces and structural implementation. *International Journal of Solids and Structures*, 50(20-21):3274–3296.

[Milani et al., 2007] Milani, G., Lourenço, P., and Tralli, A. (2007). 3d homogenized limit analysis of masonry buildings under horizontal loads. *Engineering Structures*, 29(11):3134–3148.

[Milankovitch, 1907] Milankovitch, M. (1907). Theorie der druckkurven. *Zeitschrift für Mathematik und Physik*, 55:1–27.

[Misseri et al., 2018] Misseri, G., DeJong, M. J., and Rovero, L. (2018). Experimental and numerical investigation of the collapse of pointed masonry arches under quasi-static horizontal loading. *Engineering Structures*, 173:180–190.

[Moseley, 1856] Moseley, H. (1856). *The mechanical principles of engineering and architecture*. Wiley and Halstead.

[Mousavian and Casapulla, 2020] Mousavian, E. and Casapulla, C. (2020). The role of different sliding resistances in limit analysis of hemispherical masonry domes. *Frattura ed Integrità Strutturale*, 14(51):336–355.

[Méry, 1840] Méry, E. H. (1840). Mémoire sur l'équilibre des voûtes en berceau. *Annales des Ponts et Chaussées*, 39:50–70.

[Naghdi, 1973] Naghdi, P. M. (1973). The theory of shells and plates. In *Linear theories of elasticity and thermoelasticity*, pages 425–640. Springer.

[Nodargi and Bisegna, 2021] Nodargi, N. and Bisegna, P. (2021). A new computational framework for the minimum thrust analysis of axisymmetric masonry domes. *Engineering Structures*, 234:111962.

[O'Dwyer, 1999] O'Dwyer, D. (1999). Funicular analysis of masonry vaults. *Computers & Structures*, 73(1-5):187–197.

[Panzeca and Polizzotto, 1988] Panzeca, T. and Polizzotto, C. (1988). Constitutive equations for no-tension materials. *Meccanica*, 23(2):88–93.

[Peng et al., 2018] Peng, B., Wang, D., Zong, G., and Zhang, Y. (2018). Homogenization strategy for brick masonry walls under in-plane loading. *Construction and Building Materials*, 163:656–667.

[Petracca et al., 2017] Petracca, M., Pelà, L., Rossi, R., Zaghi, S., Camata, G., and Spacone, E. (2017). Micro-scale continuous and discrete numerical models for nonlinear analysis of masonry shear walls. *Construction and Building Materials*, 149:296–314.

[Podio-Guidugli, 1991] Podio-Guidugli, P. (1991). *Lezioni sulla teoria lineare dei gusci elastici sottili*. Masson SpA.

[Poleni, 1748] Poleni, G. (1748). *Memorie Istoriche Della Gran Cvpola Del Tempio Vaticano, E De'Danni Di Essa, E De'Ristoramenti Loro, Divise In Libri Cinqve*. Nella Stamperia del seminario.

[Pucher, 1934] Pucher, A. (1934). Über den spannungszustand in doppelt gekrümmten flächen. *Beton und Eisen*, 33(19):298–304.

[Quarteroni and Quarteroni, 2009] Quarteroni, A. and Quarteroni, S. (2009). *Numerical models for differential problems*, volume 2. Springer.

[Salsa, 2016] Salsa, S. (2016). *Equazioni a derivate parziali: Metodi, modelli e applicazioni*, volume 98. Springer.

[Salvatori and Spinelli, 2018] Salvatori, L. and Spinelli, P. (2018). A continuum-discrete multiscale model for in-plane mechanical modeling of masonry panels. *Journal of Multiscale Modelling*, 9(03):1840004.

[Sanpaolesi, 1959] Sanpaolesi, P. (1959). Il restauro delle strutture della cupola della cattedrale di Pisa. *Bollettino d'Arte*.

[Schek, 1974] Schek, H.-J. (1974). The force density method for form finding and computation of general networks. *Computer methods in applied mechanics and engineering*, 3(1):115–134.

[Schwedler, 1859] Schwedler, J. (1859). Theorie der stützlinie. ein beitrag zur form und stärke gewölbter bögen. *Zeitschrift für Bauwesen", Bd*, 9(1859):109–126.

[Schwedler, 1863] Schwedler, J. (1863). Zur theorie der kuppelgewölbe. *Zeitschrift für Bauwesen*, 13:535–536.

[Schwedler, 1866] Schwedler, J. (1866). Die konstruktion der kuppeldächer. *Zeitschrift für Bauwesen*, 16:7–34.

[Shapiro, 2012] Shapiro, E. E. (2012). *Collapse mechanisms of small-scale unreinforced masonry vaults*. PhD thesis, Massachusetts Institute of Technology.

[Signorini, 1925a] Signorini, A. (1925a). Sulla pressoflessione delle murature. *Rend. Accad. Naz. Lincei*, 2:484–489.

[Signorini, 1925b] Signorini, A. (1925b). Un teorema di esistenza ed unicità nello studio dei materiali poco resistenti a trazione. *Rendiconti Accademia Nazionale Lincei*, 2:401–406.

[Simon and Bagi, 2016] Simon, J. and Bagi, K. (2016). Discrete element analysis of the minimum thickness of oval masonry domes. *International Journal of Architectural Heritage*, 10(4):457–475.

[Smith, 1984] Smith, C. (1984). East or west in 11th-century pisan culture: the dome of the cathedral and its western counterparts. *Journal of the Society of Architectural Historians*, XLIII:195–208.

[Stockdale et al., 2020] Stockdale, G. L., Sarhosis, V., and Milani, G. (2020). Seismic capacity and multi-mechanism analysis for dry-stack masonry arches subjected to hinge control. *Bulletin of Earthquake Engineering*, 18(2):673–724.

[Temam and Strang, 1980] Temam, R. and Strang, G. (1980). Functions of bounded deformation. *Archive for Rational Mechanics and Analysis*, 75(1):7–21.

[Tralli et al., 2014] Tralli, A., Alessandri, C., and Milani, G. (2014). Computational methods for masonry vaults: a review of recent results. *The Open Civil Engineering Journal*, 8:272–287.

[Trovalusci, 1992] Trovalusci, P. (1992). *Modelli matematici per la muratura a blocchi considerata come sistema dotato di struttura*. PhD thesis, Università di Roma, La Sapienza.

[Truesdell and Toupin, 1960] Truesdell, C. and Toupin, R. (1960). The classical field theories. In *Principles of classical mechanics and field theory/Prinzipien der Klassischen Mechanik und Feldtheorie*, pages 226–858. Springer.

[Villaggio, 2005] Villaggio, P. (2005). *Mathematical models for elastic structures*. Cambridge University Press.

[Wolfe, 1921] Wolfe, W. S. (1921). *Graphical analysis: a text book on graphic statics*. McGraw-Hill book Company, Incorporated.

[Zessin, 2012] Zessin, J. F. (2012). *Collapse analysis of unreinforced masonry domes and curving walls*. PhD thesis, MIT.